The Neutronic Design and Performance of the Indiana University Cyclotron Facility (IUCF) Low Energy Neutron Source (LENS)

Christopher M. Lavelle, M.S.

Accepted by the Graduate Faculty, Indiana University, in partial fulfillment of the requirements for the degree of Doctor of Philosophy.

Doctoral Committee:

_____

David V. Baxter, Ph.D., Chair

_____

Dobrin Bossev, Ph.D.

_____

John P. Carini, Ph.D.

_____

Erik B. Iverson, Ph.D.

_____

W. Michael Snow, Ph.D.

January 12, 2007

To Erin and Salvatore

Acknowledgements

I would like to thank my advisor David Baxter. His patience, intuition, and excitement have been a genuine inspiration. Without his careful guidance, this dissertation work would not have been possible. In fact, it is very likely that more than a few things may have ended up in Thomas Edison's pile of 10,000 things that do not work. He has my, and my family's, enduring gratitude and esteem.

My wife Erin deserves much credit for making this work possible. She has supported me graciously and without complaint all while going to school herself, working numerous jobs, and most recently, caring for our child while I scurried off to the lab for yet more science and that one more thing I should do before coming home. She is my inspiration and my joy.

There are numerous individuals at IUCF without whom many more things would be on the pile of things that do not work. The professionalism of the LENS group and IUCF faculty and staff make the IUCF a fantastic and productive place to work. I thank them for their attention to detail and many scientific discussions. I would also like to thank IUCF director Paul Sokol for his financial support during the completion of this work.

My mother and father were of great support during this stressful period, and deserve my thanks. Their love, sacrifice, and earnest advice have given me opportunities in life for which I will never be able to repay them.

Finally, my friends and colleagues Mark Leuschner and Nicholas Remmes shall not go without mention. Their insights into many of the physics questions and experimental conundrums that erupted during this dissertation work were of great value, and their advice on personal matters kept the ship sailing forward.

Abstract

Neutron scattering research is performed primarily at large-scale facilities. However, history has shown that smaller scale neutron scattering facilities can play a useful role in education and innovation while performing valuable materials research. This dissertation details the design and experimental validation of the LENS TMR as an example for a small scale accelerator driven neutron source.

LENS achieves competitive long wavelength neutron intensities by employing a novel long pulse mode of operation, where the neutron production target is irradiated on a time scale comparable to the emission time of neutrons from the system. Monte Carlo methods have been employed to develop a design for optimal production of long wavelength neutrons from the ^{9}Be(p,n) reaction at proton energies ranging from 7 to 13 MeV proton energy.

The neutron spectrum was experimentally measured using time of flight, where it is found that the impact of the long pulse mode on energy resolution can be eliminated at sub-eV neutron energies if the emission time distribution of neutron from the system is known. The emission time distribution from the TMR system is measured using a time focussed crystal analyzer. Emission time of the fundamental cold neutron mode is found to be consistent with Monte Carlo results. The measured thermal neutron spectrum from the water reflector is found to be in agreement with Monte Carlo predictions if the scattering kernels employed are well established. It was found that the scattering kernels currently employed for cryogenic methane are inadequate for accurate prediction of the cold neutron intensity from the system.

The TMR and neutronic modeling have been well characterized and the source design is flexible, such that it is possible for LENS to serve as an effective test bed for future work in neutronic development. Suggestions for improvements to the design that would allow increased neutron flux into the instruments are provided.

Contents

Chapter 1

Introduction

> To lead you to an overwhelming question...
> Oh, do not ask,"What is it?"
> Let us go and make our visit.
>
> —————————————————
> T. S. Eliot
> *The Lovesong of J. Alfred Prufrock*

1.1 Overview

The neutron is a unique tool for the study of materials. The fundamental proper-
ties of the neutron, charge neutrality and possession of a magnetic moment, allow
for a variety of scattering techniques that elucidate material structure and dynam-
ics. In addition, our precise knowledge of these fundamental values for the neutron
have become a vital probe of advanced theories of subatomic nuclear matter. Since
the discovery of the neutron, sources of neutrons have become much more intense.
Nevertheless, the inefficiency with which neutrons are produced has always meant
that neutron science is an intensity limited technique. Rapid progress in the field of
neutron scattering has been made possible by long wavelength neutrons produced in
cold moderators and the associated instrumentation employing low energy neutrons

[1, page 4].
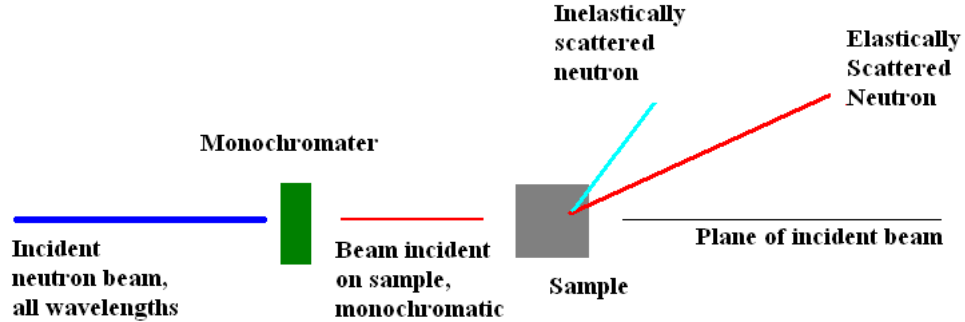
Figure 1.1: An cartoon of a neutron scattering experiment. An incident neutron beam comprised of all wavelengths is made monochromatic by a monochromater, which is then incident on a sample. The neutron may scatter elastically (no change in wavelength, represented as same color) or inelastically (change in wavelength, represented as a change in color). The angle relative to the plane of the incident beam of an elastically scattered neutron encodes structural information of the sample. A change in wavelength of the incident neutron encodes dynamical information as the neutron exchanges energy with the sample.

The art of preparing neutron fields for research has become a truly cross-disciplinary venture, requiring an understanding of the nuclear physics, condensed matter and optics involved in the production and transport of neutrons. An understanding of the functional role of the neutron in fields such as fundamental physics, condensed matter, engineering, biology or medicine is also required because the intended use of the neutron field is a large factor in the choices made during the design process. This dissertation intends to add to the progress in neutron scattering research by detailing the motivation, design, and experimental benchmarks of a long wavelength pulsed neutron source at Indiana University.

This chapter will focus on some of the advances made possible by neutron scattering to exemplify the importance of neutron sources in modern research. We will then discuss the motivation of the LENS source in a historical context in Chapter 2 followed by a discussion of some of the nuclear and transport physics in chapters

3 and 4 which underly the fundamental results of the Monte Carlo design analysis presented in chapter 5. The fundamental performance of the neutronic model is outlined at the end of Chapter 5 and leads directly to the experimental benchmarks of the neutron source, which are discussed in Chapter 6. A presentation of advanced topics in neutronics that could be employed to enhance performance of the neutron source completes the dissertation in Chapter 7.

The neutron is an excellent probe of materials, complimentary to x-rays, for many reasons.

- Slow neutron energies (0.1 meV to 1 eV) are comparable to material excitations, such as phonons, giving dynamical information. Slow neutron de Broglie wavelengths, which can extend from .2 to $>20\mathring{A}$, are comparable to interatomic and intermolecular spacings giving structural information.

- Isotopic variation in atomic structure leads to very different interactions cross-sections between isotopes of the same element. The portion of the sample to which the experiment is sensitive can be selected by isotopic substitution in the sample itself, in the surrounding medium, or both.

- Cross-sections are not regular across various atomic numbers, allowing one to "see" light atoms next to heavy ones.

- The magnetic moment of the neutron is a sensitive probe of magnetic systems, and allows the neutron to be polarized.

- Neutrons have no electric charge, allowing them to penetrate deeply into complex samples and sample environments

- Neutron beams and instruments cover a wide range of parameter space in energy and wavelength.

- Neutrons scatter directly from nuclei, in contrast to x-rays, which see the much larger electron structure.

- The general theory of low energy neutron interactions with atoms is well understood as a point interaction, which allows the straightforward interpretation of results [2].

Some of the fundamental properties of the neutron are detailed in Table 1.1.

Mass	$939.56563 \pm .00008[\frac{MeV}{c^2}]$
Mean lifetime	$885.7 \pm 0.8[\text{seconds}]$
Magnetic moment	$(-1.9130427 \pm .0000005)\mu_N$
Electric dipole moment	$< 0.63 \times 10^{-25}[e \cdot cm]$
Charge	$(-0.4 \pm 1.1) \times 10^{-21}e$
Spin	$-\hbar/2$

Table 1.1: Fundamental properties of the Neutron [3].

1.2 Examples of Neutrons At Work

A brief discussion of a few significant achievements in the field of condensed matter and biophysics demonstrates the power of the information gained via neutron scattering. We begin with a discussion of the dispersion relation of liquid helium, which was experimentally verified with inelastic neutron spectroscopy. Next, we discuss the ribosome, an organelle essential to the fabrication of proteins within living cells. Small Angle Scattering (SANS), which is to be the flagship instrument at LENS, helped elucidate the structure of the ribosome using a high resolution *contrast variation* technique, which is unique to neutrons. Finally, a survey of some essential work on high temperature superconductor material structure guided by neutron diffraction will complete this section.

1.2.1 Superfluid Helium Dynamics

A demonstration of neutron scattering in the understanding of dynamics comes from work on the dispersion relation of superfluid helium. Central to this work is the ability of the neutron to exchange energy with inelastic excitations in a solid, a topic we will find essential for the production of low energy ($\sim$meV) neutrons. Early work by Placzek and Van Hove [4] showed how neutrons could directly probe the phonon spectrum in solids. The extension of this work to liquids was well suited to the analysis of excitations in superfluid He II.

Landau [5, 6] showed that experimental results for specific heat of He II could be explained by assuming 2 kinds of excitations. He proposed the long wavelength excitations in He II were dominated by phonons, described by Bose-Einstein statistics. Higher k dispersion, on length scales comparable to interatomic spacings, were to be dominated by "rotons", described by Boltzmann statistics [7]. Phonon dispersion is given by $E(k) = ck$, where c is the speed of sound in the liquid. Roton dispersion is described by $E(k) = \Delta + \frac{(k-k_o)^2}{2\mu}$, where Δ and k_o are parameters describing the excitation and μ is the effective mass of the roton.

Feynman [8] and Feynman and Cohen [9] gave the quantum mechanical explanation of Landau's empirical insights. They assumed that sufficiently below the λ-point, He II could be regarded as a quantum mechanical system weakly perturbed from its ground state. In this regime, the primary excitations are quantized pressure waves (phonons) and quantized vortices (rotons), described as a quantum analog of "smoke rings". Cohen and Feynman [10] showed how cold neutrons could directly probe the proposed dispersion relation. If the energy of the incoming neutron is low compared to the roton energy, they proposed the linear phonon dispersion would dominate. If the energy of the incoming neutron was comparable to k_o, the roton excitation mean energy, roton dispersion would dominate, giving rise to a *roton min-*

imum in the dispersion relation. If the temperature of the He is low enough below the λ-point, the background due to He I is completely suppressed and the number of elementary excitations is low. In this regime, the neutron is more likely to produce an excitation than absorb one. A cold neutron, whose energy is close to the energy of these excitations, is expected to sharply exchange a single quantum of energy with the liquid.

Several groups set about measuring this effect, and two distinct approaches were used. The first method was to look at the shift of the neutron energy spectrum as it passed through He II [11]. A spectrum of neutrons was filtered through 8" of beryllium cooled by liquid nitrogen to give a sharp edge in the neutron spectrum at the $\sim 4\mathring{A}$ "bragg cutoff". After passing the spectrum through He II, the shift of this edge gives the magnitude of the average excitation at the cutoff energy. Different filters, and the later addition of a chopper, give the excitation energy as a function of incident neutron wavelength. Results of the this experiment, showing the sharp change in energy, are shown in Figure 1.2.

A more direct approach was taken by Henshaw [12] and Yarnell and coworkers [13, 14], where crystal analyzers were employed to define a monoenergetic incident neutron beam. A second analyzer determines the energy of the scattered neutron, thus measuring the neutron energy exchange directly. The results of Yarnell [14], shown in Figure 1.3, essentially prove the phonon-roton theory of elementary excitation dynamics in superfluid He II. It is interesting to note that cold neutrons are produced in a very similar fashion to what occurs in these experiments. At LENS, we will show how thermal neutrons lose energy via excitation of elementary excitations in a cryogenic solid, shifting portions of the neutron energy spectrum to lower energies.
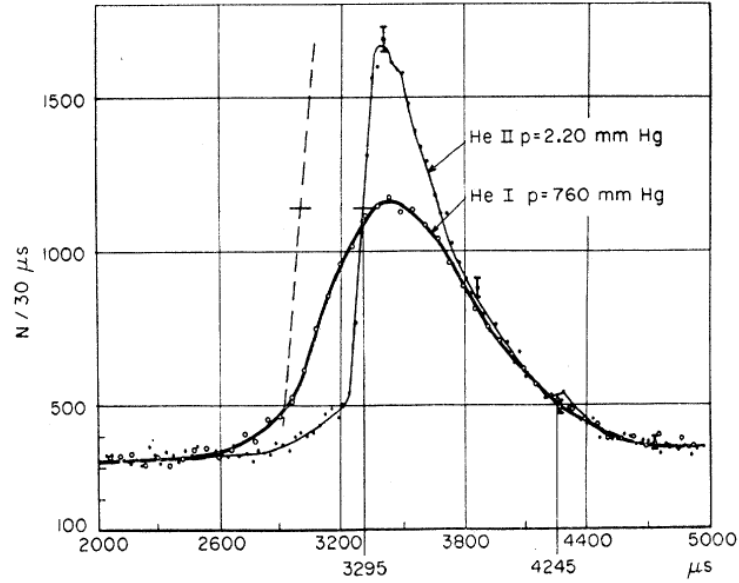
Figure 1.2: Results from the Palevsky measurements showing the sharp energy exchange of He II, which is not observed from He I. The incident spectrum is shown as the dashed line. From [11].
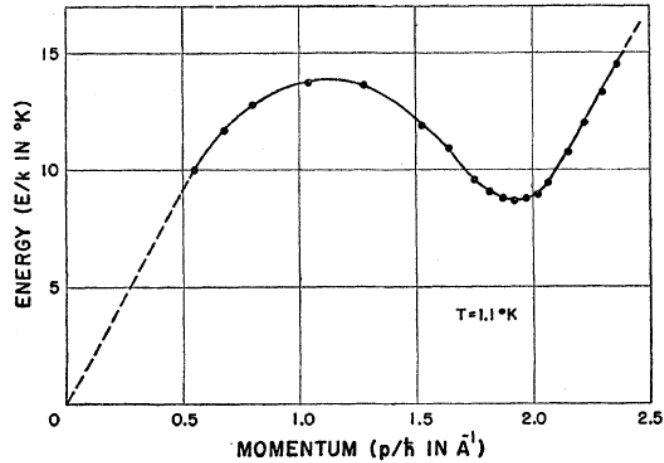
Figure 1.3: These results from the Yarnell measurements validate the phonon-roton quantum excitation model of He II. The slope of the dashed segment is the speed of sound in the liquid, which describes the long wavelength behavior of the system. As wavelengths get shorter, quantized vortices, or rotons, dominate, giving the *roton minimum*. Higher above k_o, phonons again dominate. From [14].

1.2.2   Ribosome Structure

The ribosome was discovered in 1956. Within a short time, much of the general function was understood [15], where of principle importance is that the ribosome is the protein factory in all living organisms. The ribosome is composed of two main units, identified by their sedimentation coefficient. The ribosome (70S) is composed of a 50S and 30S subunit, themselves a mixture of protein and RNA. The subunits are each a long macromolecular chain composed of protein and RNA with a complex folding structure. While much of the role played by the ribosome in the cell is understood, the structure of the macromolecular machinery of the organelle was not understood until very recently. How the ribosome machinery functions to accomplish protein production is also not clearly understood, and linking structure and function is of primary importance to molecular biology [16].

Investigation of ribosome structure is well suited to neutron small angle scattering (SANS), as opposed to other techniques, for a variety of reasons. The size and complexity of the molecule complicates the interpretation and resolution of x-ray results. NMR results are limited to smaller structures, and cannot resolve the entire macromolecule. Crystal diffraction studies require single crystals of large molecular weight that are technically difficult to produce.

SANS has advantages because of high resolution contrast variation and the wide range of sample conditions and particle sizes accessible to this technique [16]. Contrast variation exploits the huge difference in scattering lengths of hydrogen (H) and deuterium (D). This can be done in a number of ways [15, 17], but essentially the technique isotopically substitutes H and D in the sample so that the average scattering length of certain elements of the sample are matched to the background's scattering length. Thus, the difference between the background and the signal is due only to the structure that has been selected for study. There is a similar contrast

technique for x-ray scattering, but SANS is capable of resolving a much wider range of contrast than is possible with x-rays. In addition, matching the information from SANS with the results of other techniques can greatly inform the interpretation of SANS data. An excellent example of this comes from the work of Svergun and Nierhaus [18].
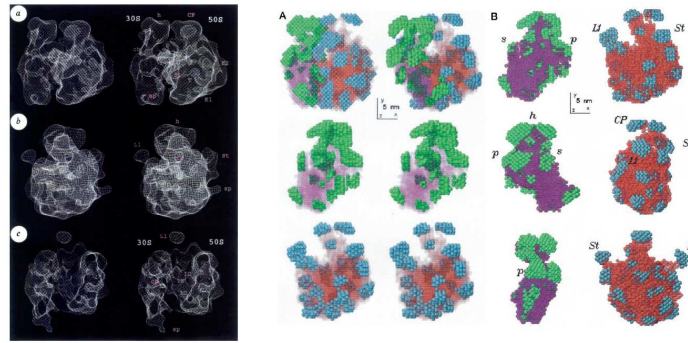
Figure 1.4: *Left:* The results of cryo-EM for the surface structure of the ribosome, from [19]. *Right:* Using a surface envelope informed by the cryo-EM results, determination of the protein and RNA structure within the ribosome is possible by contrast variation small angle neutron scattering. Green and blue solid spheres represent proteins and magenta and red semi-transparent bodies represent RNA. From [18].

Previous results on ribosome structure from cryo-electronmicroscopy (cryo-EM) has lead to a well defined outer surface of the ribosome in *E. Coli* [19]. Because the compositional RNA and protein molecules of the subunits are understood, it is possible to derive the locations of those molecules within the ribosome using SANS. This is accomplished by using a genetic algorithm to model various configurations of the molecular structure at low spatial resolution ($\sim 4\mathring{A}$) until an optimal match between the predicted SANS result and the measured SANS result is achieved. Svergun and Nierhaus used 42 different contrasts for this work, including SAXS (Small Angle X-ray Scattering). Contrast was achieved in the SANS work by deuterating both the solution and the *E. Coli* bacteria itself. Their stunning and beautiful re-

sults are shown in Figure 1.4 along side the cryo-EM results that informed the SANS structural study. By matching contrast variation studies with biochemical modeling, SANS can produce new insights into macromolecular structure. SANS is one of the key techniques in the LENS instrument suite. We note that relatively low resolution experiments such as this are well suited to the long pulse time structure of the LENS source.

1.2.3 Structure of High T_c Superconductors

The enormous potential of superconductivity ranges from electrical wires that do not dissipate energy to trains that can travel effortlessly on a cushion of magnetic fields. The quest to understand high temperature superconductors is an important challenge in condensed matter physics, and further progress in this field will rest on the ability of physicists to associate structure and composition with accurate models of the superconducting mechanism in solids. Neutron scattering experiments have provided a number of key insights into the structure and microscopic properties of these materials.

I Antiferromagnetic order in YBCO

There are several types of magnetism in solids [20, chap. 31-34]. A schematic example of ferromagnetism, antiferromagnetism, and ferromagnetic ordering is displayed in Figure 1.5. *antiferromagnetism* (AF), where the spin vectors of various atoms in the lattice anti align relative to one another, is of central importance to the superconducting mechanism in the YBCO series of high T_c superconductors. Above a certain critical temperature, the spins in the solid are thermally disordered. As the temperature is lowered, the thermal disorder is reduced in favor of magnetic ordering. The onset of AF is called the Neél temperature. Near the Neél point, the

magnetization, susceptibility, and zero-field specific heat are all well characterized by a power law, given by Equation 1.1 for the sublattice magnetization, where T_N is the Neél point.

$$M(T) \sim (T_N - T)^\beta \tag{1.1}$$
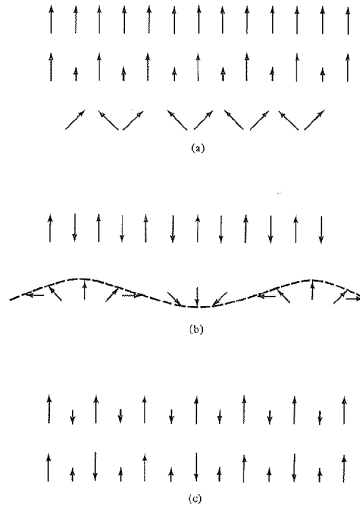
Figure 1.5: Various types of spin vector arrangements leading to A) Ferromagnetic order, characterized by alignment of the spin vectors on each site, B) Antiferromagnetic order, characterized by the anti-alignment of spin vectors on each site, and C) Magnetization arising from ferromagnetic ordering, where anti-aligned spins of different magnitude lead to a net magnetic field in the solid. The sinusoidal alignment in (B) is representative of the magnetic ordering in Chromium. From [20].

The discovery of the onset of superconductivity above 77K was first achieved [21, 22] in 1987 in $(Y_{1-x}Ba_x)_2CuO_4$ (YBCO), a class of compounds called *cuprates.* The fast pace of discoveries around this period, coupled with conflicting results on LaBCO compounds (which were direct precursors to the YBCO compounds) left open many questions of magnetic ordering and structure [23]. The question of whether or not AF plays a role in these compounds was still unresolved and well suited to neutron diffraction, where the onset of the Neél point can be observed directly [24]. Magnetic ordering forms a superlattice which, in analogy with bragg

scattering, will diffract neutrons by interactions between the spin vector at the lattice site and the neutron magnetic moment. By observing the onset of the magnetic bragg peak with temperature, the superlattice vector along which the AF planes are aligned can be determined. An example of the onset of AF in YBCO is shown in Figure 1.6.
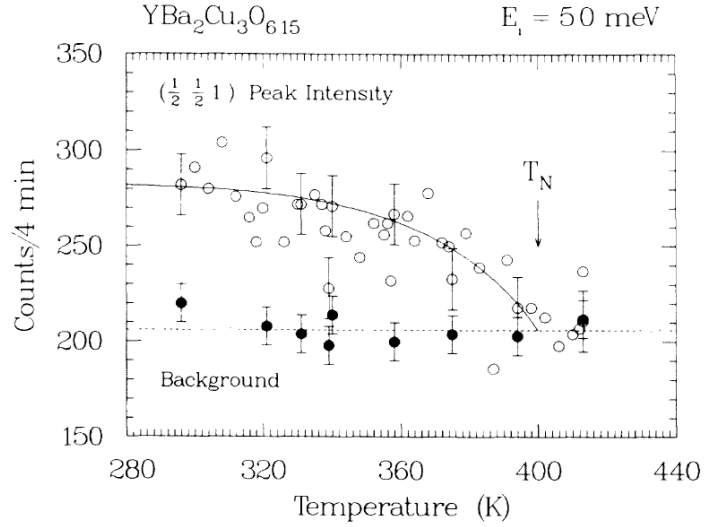
Figure 1.6: By observing the onset of the magnetic superlattice via diffraction with 50 meV neutrons, Tranquada and coworkers [24] were able to establish the presence of anti-ferromagnetism in the YBCO series of high T_c superconductors. From [24].

II Spin Stripes in Cuprate Model Systems

Cuprates are stable over a wide range of x in forms like $(Y_{1-x}Ba_x)_2CuO_4$ or $La_{2-x}Ba_xCuO_4$ (LBCO). In LBCO, the substitution of Ba for Sr raises T_c from 30K to 40K, and the substitution of Y for L lead directly to the YBCO discovery of high T_c. One of the mysteries of these compounds was the anomalous suppression of high T_c supercon-ductivity in LaSrCuO when $x \sim \frac{1}{8}$, first observed by Moodenbaugh *et. al* [23] and shown in Figure 1.7.

The value of x essentially determines the hole concentration in the sample. Results from x-ray diffraction (which is sensitive to charge where the neutron is not)
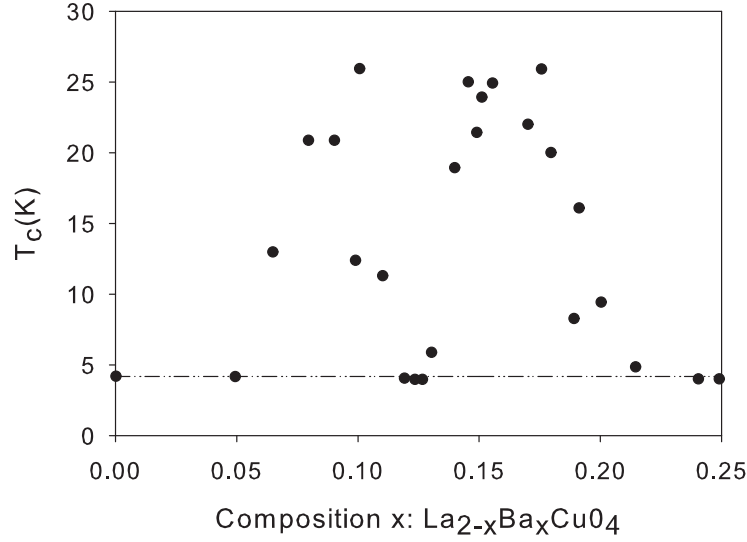
Figure 1.7: The onset of superconductivity in LBCO, a precursor to high T_c YBCO, has an anomalous suppression as a function of composition. Points along the dashed line have T_c onset below 4.2K. This effect became known as the "$\frac{1}{8}$ problem". Adapted from [23].

following the discovery of the "$\frac{1}{8}$ problem" had shown that the $\frac{1}{8}$ factor is closely related to the ratio of holes to charge carriers [25]. Subsequent research showed that x is also indicative of a structural phase transition [26, 27]. The CuO_2 structure transitions from low temperature orthorhombic (LTO) to low temperature tetragonal (LTT) as one crosses $x \sim .125$ from above. Both the LTO-LTT transition and proper hole concentration are essential to reproducing the $\frac{1}{8}$ suppression of high T_c.

An explanation of this suppression emerged from the study of a model cuprate system $La_{1.6-x}Nd_{0.4}Sr_xCuO_4$ by Tranquada and coworkers [28]. This system generally models the physics of the CuO_2 layer, and the partial doping with Nd locks in the LTT structure across a wider band of temperatures than would normally occur. The displacement of the oxygen moments out of the plane of the lattice leads to magnetic scattering at values of q commensurate with x. Thus, by observing scattering along the reciprocal lattice AF ordering plane $(\frac{1}{2} + q, \frac{1}{2} + q, 0)$ one can observe the value of q directly in a diffraction experiment using a triple axis spectrometer. A triple axis

spectrometer can give high resolution definition of the incoming neutron wavevector $\vec{k}$ and equally high resolution on measurement of the scattered vector, $\vec{k}'$. The results of the study, showing clear evidence of structure along the modulated (110) plane, are shown in Figure 1.8.
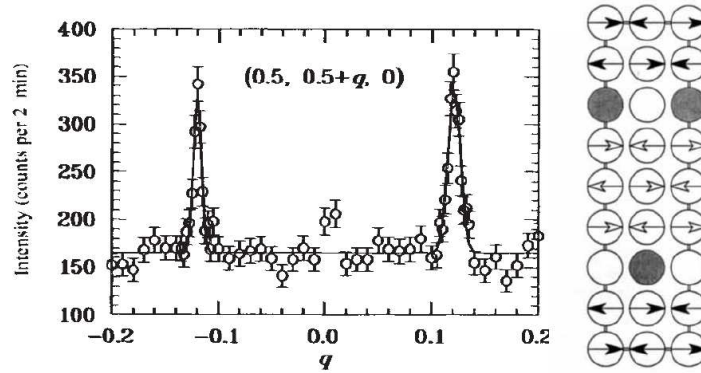
Figure 1.8: *Left:* The results of neutron diffraction show a clear indication of a structure at $q \sim x \sim .12$, measured using a triple axis neutron spectrometer where the $La_{1.48}Nd_{0.4}Sr_{0.12}CuO_4$ sample is in the LTT state at 11K. *Right:* A cartoon of the charge and spin stripes in the cuprate copper oxide layers at the metal sites. Magnetic moment vectors are indicated by the arrows. On crossing a charge (open circle) and hole (dark circle) domain boundary, the vector direction changes by 180 degrees, as indicated by the change in arrow color. The line behind the outermost atoms in the drawing indicates the magnetic unit cell. From [28].

The interpretation of this structure is that the AF order takes the form of charge and spin stripes in domains separated by charge and hole boundary layers. In the LTO mode, the structures form a diagonal pattern, a configuration where displacement fluctuations are more weakly confined than in the LTT mode. In the LTT mode, the confinement is both horizontal and vertical, and thus confines the displacement fluctuations closer to the lattice sites than in the diagonal case. The effect is to "pin" the charge and spin stripe structure in place, increasing resistivity and destroying the superconductivity. This important investigation lead to a greater appreciation for the role of charge and spin fluctuations in the cuprate series of superconducting compounds. Investigations into the spin structure deep inside a

material are uniquely possible in neutron scattering. High resolution studies such as these have been of central importance for neutron scattering and most pulsed sources have focussed on these kinds of experiments.

Chapter 2

Neutron Sources

Which way
did you come from,
following dream paths at night,
while snow is still deep
in this mountain recess?

Ryokan

2.1 Overview

Neutrons play a role in many branches of physics and in society. The applications of neutrons range from the generation of power in nuclear reactors (with associated controversy which we will not presume to address here) to the type of nanostructure investigations we have discussed. Low energy neutrons, neutrons with $\sim$eV energies or less, are primarily used for these pursuits. However, without imaginative ways to free neutrons from their deep recesses within in nuclei, there would be no neutron scattering science to speak of.

Much of the progress in neutron science has come as neutron sources become more intense. One could even make the argument there is a direct correlation between source strength and discovery (Figure 2.1). As source strength has increased,

so has the number of articles per year mentioning the neutron in the American Physical Society's PROLA archive. The core flux of neutron sources has increased dramatically since the 1932 discovery of the neutron by Chadwick. Growth in the field of neutron science has been steady, even in the WWII years from 1939-1946 almost when almost all work on neutrons was classified, and in the 1960's, when much of the technical concerns of neutronics began to enter engineering journals. Today, over 700 articles per year are published involving neutrons in PROLA journals alone.
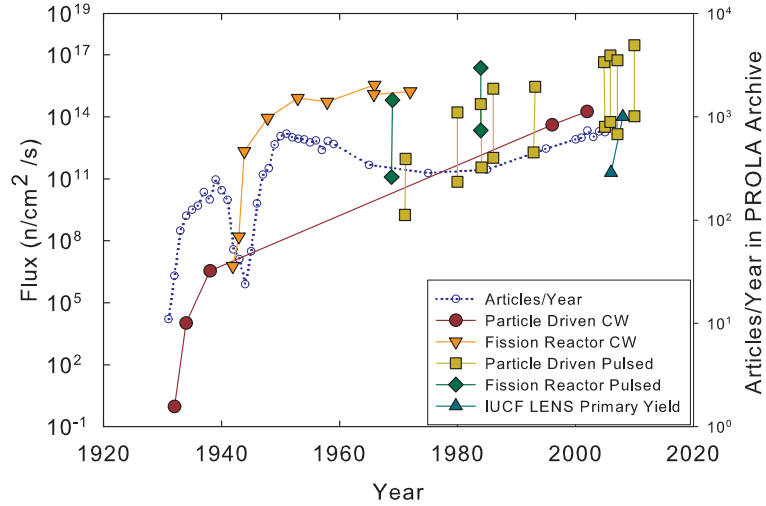
Figure 2.1: The core flux of neutron sources has increased dramatically since the 1932 discovery of the neutron by Chadwick. As source strength increases, so does the number of articles per year mentioning the neutron in the American Physical Society's PROLA archive.

Neutrons produced in the lab generally have a large amount of initial kinetic energy ($\sim$MeV or greater), which not only makes primary neutrons a highly penetrating form of radiation, it also makes removing that energy a source of significant limitation on cold source brightness. Another limitation on the science that can be done with neutrons is the relatively low amount of primary flux available compared to x-ray or charged particle beams. The core flux of neutrons available for research

will be intensity limited for the foreseeable future. The flux produced in research reactors seems to have reached a limiting value as early as 1970 (see Figure 2.1), though one never desires to rule out the possibility that innovation in these sources will lead to advances in flux. Accelerator sources have continued to follow a Moore's Law path, continuously increasing in power since their inception in the early 1980's, but each facility is more costly than the previous. The recently constructed SNS facility at Oak Ridge will be the world's most powerful neutron source, but carries an initial price tag of some $1,414,000,000. There is an upper limit to the flux at these facilities as well; issues of target shock present severe technological limitations to delivering ever greater intensities of proton beam to neutron production targets.

As a result of the neutron flux available, there is a balance in each type of source and instrument between intensity and resolution of the probes region of phase space. Each combination of neutron beam characteristics and instrument type investigates a specific region of phase space, trying to use the flux as efficiently as possible. This section will review two examples of existing neutron user facilities in the context of the benefits and drawbacks of each type of source. The NIST NCNR will serve as an example of a reactor based source and the IPNS at Argonne National Laboratory will be an example of an accelerator based pulsed source. We will comment on the dominance of European sources in the field of neutron scattering, and discuss the recent construction of SNS facility. Finally, we will show how the IUCF LENS facility will fulfill important roles as research user facility, educational institution, cold source development, and instrument development station in the context of the present facilities in the Unites States.

2.2 Units of Energy in Neutronics

Before discussing existing neutron sources in detail, a brief review of terminology is helpful. There are several units for discussing neutron energy, listed in Table 2.1. Regimes of energy are classified by the range and type of nuclear interactions that take place in Table 2.2 [29].

Quantity	Unit	Energy Relation (eV)	Abbrev.
Energy	Electron Volt	$\frac{1}{2}mv^2$	eV
Velocity	Meters per Second	$v = \frac{L}{t} = 1.39 \times 10^4\sqrt{E}$	m/s
Wavelength	Angstroms	$\lambda = \frac{h}{mv} = \frac{0.286}{\sqrt{E}}$	$\mathring{A}$
Temperature	Kelvin	$T = \frac{E}{k_b}$	K
Lethargy	Unitless	$u = ln(\frac{E_o}{E})$	-

Table 2.1: Commonly used units of measure in neutron science.

Classification	Energy (eV)
Ultra-cold (UCN)	$\leq 10^{-6}$
Cold	$10^{-6} \sim 25 \times 10^{-3}$
Thermal	$25 \times 10^{-3} \sim 125 \times 10^{-3}$ (5kT)
Epithermal	Neutrons out of thermal equilibrium with the moderator, but less than the energies where slowing down behavior dominates and resonance scattering is present.
Slowing down or Resonance	$10^0 \sim 10^5$ Breit-Wigner resonances dominate the cross-section
High Energy or Fast	E $\gtrsim 10^5$, typically associated with primary neutron flux.

Table 2.2: Common names for the energy regimes encountered in neutron science. Note over the 10 orders of magnitude in energy spanned by the neutron.

2.3 Making the Thermal Neutron Beam

Let us assume that we have an external source of neutrons from which we desire to produce a thermal neutron beam, without going into detail at this point about the

nature of that source. The stages in the process are *production*, *slowing down*, and *thermalization*, summarized in Table 2.3 and Figure 2.2. The process of preparing the thermal neutrons from primary neutrons is called *neutron moderation*. For neutron energies high above kT, elastic scattering is primarily responsible for moderation. A high energy neutron sees the moderator target atoms basically at rest, such that the recoiling target nucleus carries away some of the incident neutron energy, slowing down the neutron.

Stage	Energy Range	Physics involved
Production	MeV-GeV	Fission, Spallation, Nuclear and Photonuclear processes
Slowing Down	eV-MeV	Elastic collisions, Freely recoiling nucleus carries away neutron energy
Thermalization	meV-eV	Elastic collisions and excitations in materials bring neutrons into quasi-equilibrium with moderator material. Moderator nuclei often no longer free to recoil.

Table 2.3: Stages of the moderation process.

After successive slowing down collisions, the neutron energy becomes comparable to the moderator material temperature and to molecular binding energies. In this regime, the target nucleus is no longer free to recoil. Interaction with the collective motion of the atoms in the medium and the molecular degrees of freedom become the dominant modes of energy exchange. Once the neutrons slow to energies close to the material temperature, they come into a quasi-equilibrium defined by the condition that the neutrons are that are equally like to gain or lose energy in a collision in the medium (the *condition of detailed balance* [30]). The primary neutrons have now become thermal or cold neutrons in the medium. A medium employed for the purpose of slowing down neutrons is called a *moderator*. The total moderation process can take anywhere from 10's to 1000's of μs depending on the final neutron

energy and source characteristics.
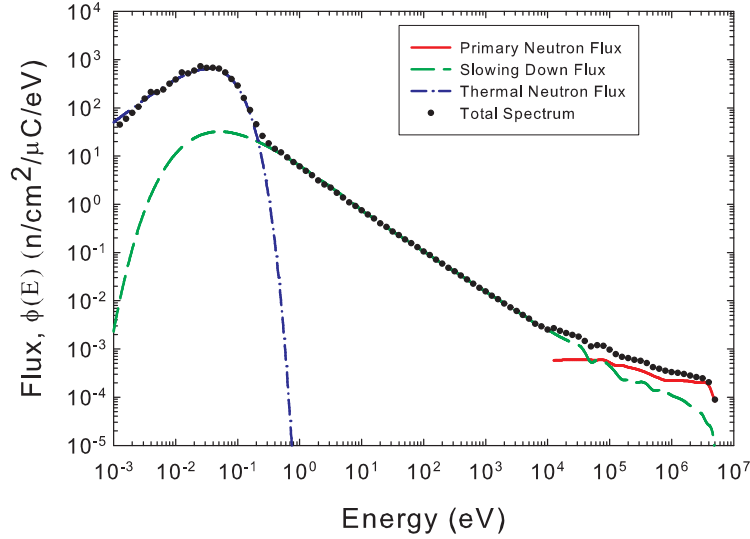
Figure 2.2: A sample energy spectrum from a simulation of neutron flux at a LENS sample position. The total flux of neutrons moderated by water at 300 K, shown in black dots, is a sum of the flux due to a direct contribution from the external source (solid red), flux due to neutrons undergoing slowing down via elastic collisions (dashed green), and thermalized flux in equilibrium with the water moderator (dash-dot blue).

Absorption preferentially removes lower energy neutrons raising the mean energy of the neutron flux and in effect warming the spectrum. There is also an important distinction to be made between neutron flux inside a medium and flux that has leaked out of the medium. Higher energy neutrons generally have have a longer mean free path than low energy neutrons, and so will preferentially leak out of the system. This causes leakage neutrons to have an appreciably harder neutron spectrum than neutrons in medium. In a material with low absorption, the low energy neutron spectrum is characterized by a Maxwellian energy distribution. However, the neutron flux emerging from the moderator is at a slightly higher temperature than the surrounding medium due to absorption. The neutrons will remain in the maxwellian distribution until they are absorbed or leak out of the moderator and into a beam line. At this point, a thermal neutron beam is no more complicated

than opening a hole in a lamp shade to create a collimated beam of light.

2.4 Types of Sources

We will now explore the specifics of the types of external sources of neutrons. There are four main ways to produce primary neutrons:

- Radioactive decay

- Nuclear fusion reactions

- Nuclear fission chain reactions

- Accelerator driven sources

Each method has its own technical challenges and merits. However, all these methods produce primary neutrons at MeV$\sim$GeV energies, 10-15 orders of magnitude above the $\gtrsim 5\mathring{A}$ wavelength (meV energy) ranges desired for scattering experiments at LENS.

Radioactive decay, such as in the Californium User Facility (CUF) at Oak Ridge or the IUCF Am-Be source, is a continuous source of neutrons [31]. For instance, at CUF spontaneous fission generates 2.3×10^9 n/s/mg of ^{252}Cf. Another method to generate neutrons is to use a source that radioactively decays via α particle emission, such as plutonium or americium, embedded in another material, such as beryllium, which produces neutrons via the (α,n) reaction. These processes are relatively inefficient and have the added disadvantage that they are composed of very hazardous radioactive materials. Nevertheless, radioactive decay sources play important roles in medicine, radiation damage testing, and detector calibrations. Before LENS became operational, the optimal low energy neutron detector bias and discriminator settings were determined with a paraffin moderated Am-Be source.

Fusion, while not a self sustaining source at present, has been used to generate neutrons via the (D,T) and (D,D) reactions in portable generators. Pulses of deuterium are accelerated into a target of tritium or deuterium to generate fusion neutrons. The process is very inefficient, $\sim 4 \times 10^{-5}$ n/deuteron for the (D,T) reaction [32], although it has the advantage of being a sealed commercial unit which is often highly portable. These sources have found roles radiography and in security applications, which fast neutron scattering and radiography signatures are used to detect explosives.

Fissionable materials, such as the fuel elements in a nuclear reactor, spontaneously fission at a low rate. However, when multiple fuel elements are brought together in a thermalizing medium, fission production can balance or exceed absorption because the probability to fission is much higher for thermal neutrons. The first self-sustaining nuclear reaction was created December 2, 1942. The famous experiment lead by Fermi in the at the University of Chicago Stagg Field squash court proved that a controlled, self-sustaining nuclear fission reaction was possible [33].

A reactor is essentially the balance of neutron production and absorption, both of which are proportional to flux, ϕ, which is simply illustrated mathematically. If one imagines the rate of fission is proportional to $A\phi$ and absorption is proportional to $B\phi$, then the time rate of change of total flux is roughly the difference between sources and sinks:

$$\frac{d\phi}{dt} \propto A\phi - B\phi \qquad (2.1)$$

This has a simple solution, that $\phi \sim \phi_o e^{\pm(A-B)t}$. The fraction of neutrons that multiply, or generate another neutron, is termed k_{eff}. If $\frac{A}{B} = k_{eff} > 1$, the reactor is *supercritical* and flux increases exponentially (a potentially dangerous scenario!). For $k_{eff} < 1$ the reactor is *subcritical*. Absorbers are adjusted to control the value of B to keep the reactor *critical*, $k_{eff} = 1$.

The field of reactor physics has progressed considerably since the Chicago experiment. Small reactors that serve primarily as sources of neutrons for experiments are called *research reactors*. They operate at low ($0.1 \sim 60$ MW) power output, not the > 1500 MW level characteristic of power reactors. The neutronics in research reactors are optimized for neutron beam extraction, as opposed to rare isotope production (breeder reactor) or power generation. There are more than 100 nuclear reactors in the United States today [34]. The political controversy associated with the processing and storage of the radioactive waste in spent fuel rods, as well as the extensive licensing requirements for reactors, has lead to a *de facto* moratorium on reactor construction in the United States. This is not the case in Europe, Asia, and Australia, where nuclear power is a dominant source of energy and new reactors are being built (though also not without controversy). There are also many more specialized research reactors and associated scattering instrumentation facilities in Europe. This, together with other factors, has lead to a clear European domination in neutron science over the past 20 years. Evidence of this dominance can be seen by comparing the network of research neutron sources available in Europe and North America (Figure 2.3).

Reactors have the advantage of producing high, continuous flux. However, because the source is always on, a higher background can develop in the scattering environment. Sensitive techniques may require the beam be transported over large distances using *neutron guides* to be free of this background. The number of high energy gamma rays per neutron is very high at a reactor [1], and monoenergetic beams

---

[1]Several measurements conducted in the 1970's [35, 36, 37] report values in the neighborhood of 6.5 prompt γ-rays per ^{235}U thermal neutron induced fission event with a mean energy of ~ 1 MeV per γ. The number of neutrons emitted into the system per fission depends on the geometry of the fuel cell, but can range from 1 to 3 neutrons per fission [38], giving between 2-6 γ-rays per neutron. Further still, 5.5 delayed γ-rays are emitted within the 5 seconds of the fission event [39], giving in the range of 4-10 γ-rays per neutron. A recent calculation by E.B. Iverson [40] on a detailed as built model of the 1 GeV proton spallation liquid mercury target at SNS shows approximately 3.4 γ rays per neutron. This calculation neglects the production of bremsstrahlung,

must be produced via inefficient mechanical choppers and crystal analyzers. If TOF
is to be employed, the beam must be further chopped to provide a the definite start
and duration of the neutron pulse. However, because the monochromator is the only
element of instrumental resolution (unlike TOF at a pulsed source), the attainable
resolution in energy can be very high. The application of cold sources to reactors
involves a complex feedback between the cold source and the flux in the reactor core
because the presence of an inhomogeneous cold source can effect the criticality of
the reactor. Also, because the of the high gamma flux in the reactor core there are
additional challenges in removing radiative heating of the cold source.

Figure 2.3: Neutron sources in Europe and North America, courtesy D.V.
Baxter.

Pulsed sources can be of a variety of types, including pulsed nuclear reactors
(which are relatively rare) such as IBR-II at Dubna. Accelerator based sources rely
on photoneutron production, nuclear (x,n) reactions, or spallation, though not all
accelerator based sources are pulsed. SINQ at PSI in Switzerland is a continuous
spallation source. Spallation refers to the acceleration of a proton to high energies so
that the proton can penetrate deep into a high Z target nucleus and break it apart,
creating a shower of neutrons. Spallation is a very efficient technique, generating

---

pair production, and florescence photons in the spallation reaction and subsequent particle transport. Lower energy γ-rays such as these are likely to be absorbed in the high z target itself after production, and so are not expected to have an impact on the neutron scattering instruments. While it is important to note that the γ-rays from neutron production are present in addition to γ radiation produced via thermal neutron capture in the system, one cannot help but compare these representative fission and spallation gamma yields to the gamma yield in the LENS ^{9}Be target at 5 MeV. The LENS target produces a meager ~ 0.1 γ-rays per neutron [41].

>10 n/proton. Primary neutron energies are also high enough to take advantage of neutron multiplying reactions like $(n, 2n)$ in beryllium in reflector design. Nuclear reactions are much less efficient, for instance the ^{9}Be(p,xn) reaction at 13 MeV is only $\sim 10^{-3}$ n/p efficient. The maximum achievable primary flux in accelerator based sources related only to the current of protons applied to the target, which itself is limited by technical concerns in the accelerator and stress in the target.

Pulsed sources have several advantages and a few disadvantages [32]. The source is off the majority of the time (low duty factor), so backgrounds are comparatively lower (when the beam is not on the target). The flux of epithermal neutrons is also much higher than in a reactor, which is useful for chemical excitation spectroscopy, and in many sources the number of gamma rays per neutron is also much less. The pulsed source is not without its disadvantages. The peak flux is similar to or exceeds a reactor source but the time averaged flux is much less, so TOF techniques are usually required. While one can effectively increase data efficiency by looking at multiple bandwidths from a single neutron pulse, it is a bit of a mixed bag. The emission time of a pulse of neutrons from the system after the proton pulse is a limiting factor in energy resolution, which can only be controlled with selective use of flux reducing neutron absorbers in the moderator some form of monochromatism. Also, the energy of the primary neutron flux is much higher than in any other artificial source of neutrons, leading to heightened concerns of material activation and thick biological shields around the production target.

2.5 The Research Reactor - NIST NCNR

The National Institute of Standards and Technology (NIST) Center For Neutron Research (NCNR) is home to one of the most prolific centers of neutron based research

anywhere in the world. The reactor first began operation at 10 MW in 1969 as the National Bureau of Standards Reactor (NBSR) [42]. The basic neutronic challenge at a research reactor of this type is to produce intense thermal fluxes that escape into beam lines while at the same time keeping the reactor critical. The fission cross-section goes as "$\frac{1}{v}$" with velocity, increasing by many times for low energy neutrons compared to fast neutrons. Thus, the thermal flux desired to maintain criticality is also needed for the scattering experiments.
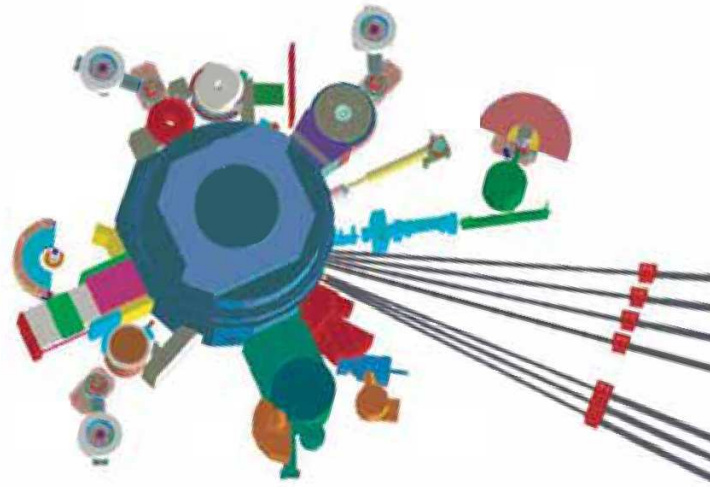
Figure 2.4: NIST NCNR Facility Layout. The reactor and cold source are enclosed in the central shielding monolith. Guided neutron beams transport neutrons to the Guide Hall instrumentation (right, not shown). Unguided instrumentation is necessarily closer to the reactor, where backgrounds are higher. From [43].

At NIST the balance between production, escape, and absorption is achieved via the use of split fuel elements in a neutron reflector. ^{235}U enriched fuel rods contain fuel above and below the center of the reactor to build up a high density of thermal neutrons in the center of the reflector. The fuel rods are inserted into a heavy water (D_2O) reflector, which thermalizes the fission neutrons with very low absorption. Penetrations extend along the center axis of the reactor to allow the thermal neutrons to leak out, as shown in Figure 2.5. Outside the reflector are

layers of biological and neutron background shielding materials.
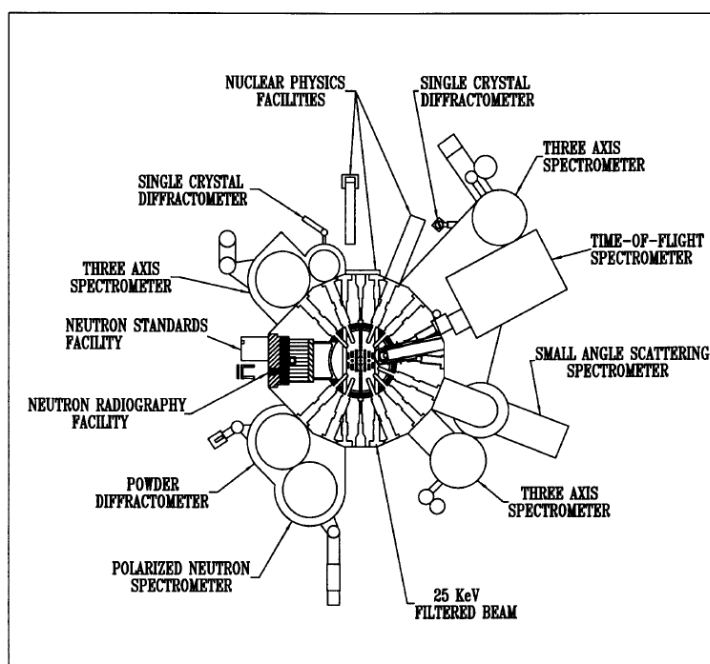
Figure 2.5: An internal schematic of the NBSR (now NIST NCNR) showing the arrangement of fuel elements relative to fuel core. From [42].

An excellent review of the instruments at NIST is provided in [44] and the articles therein. These include a variety of elastic and inelastic neutron scattering instruments, as well as novel instrumentation such as the activation analysis station where the gamma rays emitted by neutron capture are used to determine very low concentrations of isotopes in materials. Of chief importance to the continued competitiveness of the over 35 year old reactor was the addition of a cold neutron capability. The cold source allows existing, and also innovative new instruments, to probe new regions of phase space not available to neutron scattering with ambient temperature materials (Figure 2.6). A D_2O ice cold source was installed in 1987. A liquid H_2 source replaced this source in 1994, which increased cold neutron flux by over a factor of 10 compared to ambient temperature water[44]. The later advanced

cold source, installed in 2002 (Figure 2.7), improved this by a further factor of 3 [45] by using advanced Monte Carlo modeling to determine a more neturonically efficient geometry. This is an excellent example of the benefits of neutronic research: imagine the cost required to replace the NBSR with a 30 times more intense reactor!
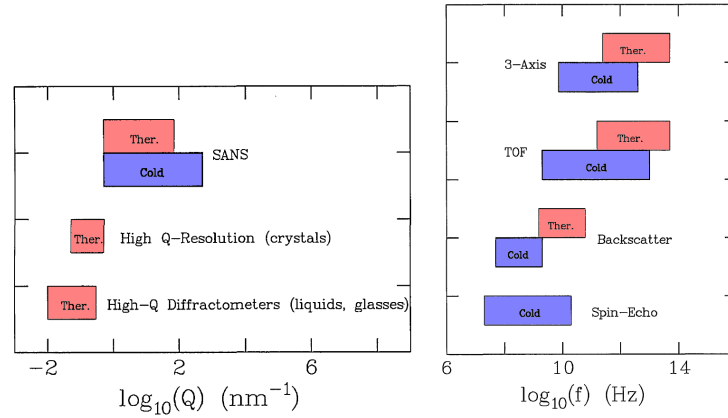
Figure 2.6: Cold neutrons enchance the range of phase space accessible to scattering instruments for *Left:* instruments that measure momentum transfer; *Right:* instruments that measure energy transfer. Adapted from [42].

Another central design concern at NIST is the immense heating of the cold source. Design calculations showed ~ 1400 Watts combined gamma and neutron heating in the moderator and cryogenic assembly, with at least 70% of the heat due to gammas. The disastrous potential for explosive radiolysis of many cryogenic materials, especially methane [46, 47], restrict cold sources in high power deposition environments to Liquid H_2 and D_2. The NIST cold source employs hydrogen at ~ 20 K [48].

A further important feature to the NIST cold source is the extensive use of neutron guides, which allows the extraction of high neutron flux from the core with minimal loss. In addition, longer flight paths increase the energy resolution of ToF instruments. A neutron guide exploits the coherent scattering of neutrons from a material. A material with high coherent scattering length appears as a uniform
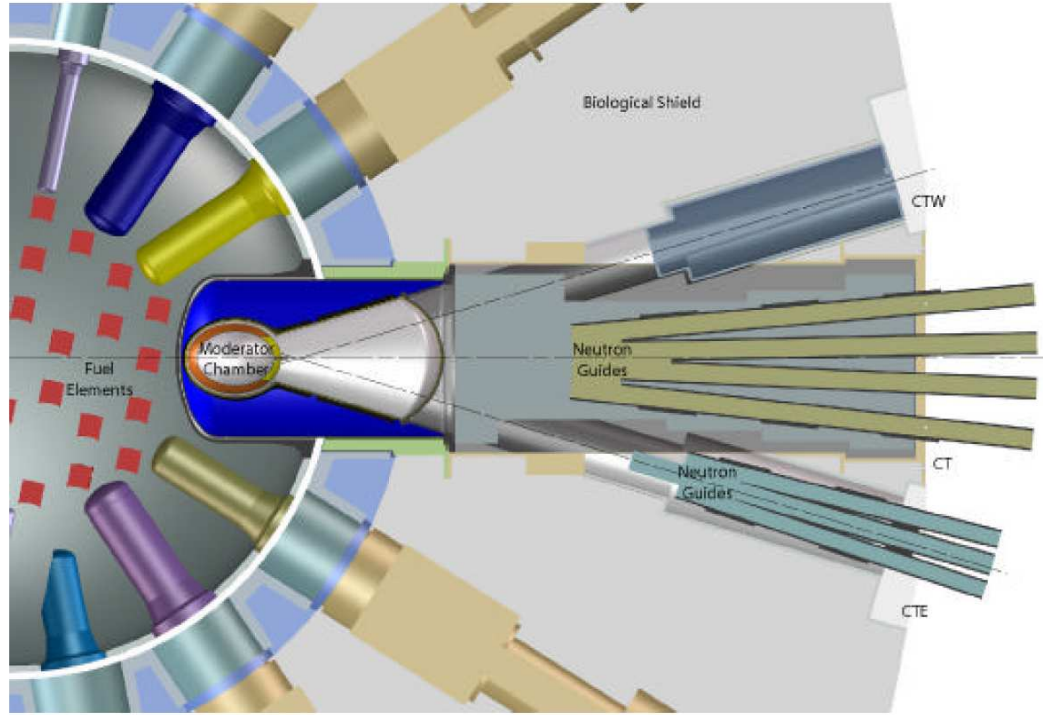
Figure 2.7: NIST Advanced Cold Source. Liquid H_2 cold source gives ~ 30 improvement in long wavelength flux relative to ambient temperature water. Cold neutron beams are guided to instruments, today over 60% of the neutron experiments use cold neutrons. From [48].

potential to the neutron, similar to an optical wave interacting with a change of refractive index. This leads to an "optical" index of refraction for neutrons, n.

$$n = 1 - \frac{\lambda^2 N a_{coh}}{2\pi}. \tag{2.2}$$

where λ is the neutron wavelength, N is the number of atoms per unit volume, and a_{coh} is the coherent scattering length. The index of refraction of nickel is typically used as a reference, m=1. In analogy to optics, there is a corresponding critical angle for neutron reflection, θ_c [49].

$$\theta_c = \lambda \sqrt{\frac{N a_{coh}}{\pi}} \tag{2.3}$$

Neutrons incident on a surface at less than critical angle (relative to the surface plane)

will only reflect, allowing the neutrons to be guided in reflecting tubes over long distances. On some instruments at LANSCE and SNS, > 80 m of guided neutron propagation has been accomplished, with losses much less than the $\frac{1}{r^2}$ expected without guides. The neutron guide overcomes the "lamp shade" method of neutron beam production by transporting a broader divergence of neutrons to the sample by total internal reflection of the long wavelength neutrons in the guide. At GPPD at IPNS, for instance, a guide gain of over a factor of 4 was obtained over an unguided beam line [50]. The main drawback of the use of guides is the expense; 1 meter of m=2 guide can cost $10,000.

Today, NIST has over 2000 visitors each year [43] and is a field leader in high quality neutron based research. The American Competitiveness Initiative legislation proposed by President George W. Bush in the 2006 State of the Union specifically enumerates increased funding to keep NIST NCNR one of the top neutron scattering facilities in the country for the foreseeable future.

2.6   The Pulsed Accelerator Source - IPNS

The Intense Pulsed Neutron Source (IPNS) began operations in 1981 after the ZING-P development program (ZING-P) [51]. As a result of the ZING-P program, 2 TOF instruments were developed (diffraction and inelastic spectrometer) and J. M. Carpenter earned a patent to the production target based neutron source [52]. ZING-P proved the concept was sound, and in 1981 the IPNS began user operations. Like NIST, IPNS is a national user facility made available to industry and academic research and maintained by a team of dedicated scientific and technical personnel. There is nominal, if any, cost to the typical academic user and hourly rates for instrument time for industrial users. Access to the resources of the facility are

controlled by a Program Advisory Committee (PAC), which reviews and selects proposed research for each instrument.
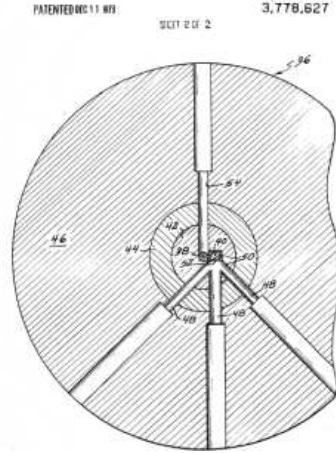
Figure 2.8: The Carpenter Target Moderator Reflector (TMR) neutron source concept, US Patent 3,778,627, which is a the model for all accelerator based neutron sources. A target is surrounded by neutron reflector with thermalizing moderators at the core to feed beam lines.

At IPNS a depleted uranium target produces ~15 n/p at 450 MeV proton energy via spallation reactions. Spallation neutrons are produced by high energy protons incident on a high Z target, producing a shower of neutrons via various internuclear cascade, breakup, and nuclear evaporation processes. These neutrons are of considerably higher energy than fission neutrons, requiring extensive shielding of the target referred to as a *monolith*.

The IPNS target is irradiated with $\sim 15\mu$A of time average current in bursts of <100 ns at 30 Hz [53]. A beryllium reflector returns some of the fast neutrons back to the moderators (also providing additional shielding), where they are then slowed to thermal energies and leak into beam lines. In addition, (n,2n) reactions in the beryllium reflector contribute to the total neutron yield [54, Chap. 2]. An outer graphite reflector and layers of neutron shielding further attenuate fast neutrons. Today there are cold 3 moderators at IPNS, liquid methane, solid methane, and solid methane with grooves, supplying 13 instruments (see Figure 2.9). Like NIST, each

instrument is a probe of a particular region of phase space. Unlike NIST, resolution for a number of instruments is determined by the pulse shape of the neutrons emitted from the moderator. To increase energy resolution, the emission time for neutrons must be reduced. One method to accomplish this is by using absorbers inside the moderator volume (poisoning) to reduce the lifetime of a neutron in the moderator. The second way this is accomplished is by lining the moderator's non-instrument faces with absorber (decoupling), which does not allow long lifetime low energy neutrons from the reflector into the moderator and defines a clear spatial eigenmode in the moderator (the buckling, see Section 5.4.5) by forcing the thermalized flux to zero at the edges. Unfortunately, both methods reduce flux considerably compared to coupled, poison free configurations.

Information on the specific capabilities of each instrument, as with most user facilities, is available via the facility web site, *http://www.pns.anl.gov/* . Argonne also maintains a general reference site for neutron scattering at *http://www.neutron.anl.gov/* .

The chief advantage of pulsed operation is that the instrument may make use of the entire pulse of neutrons simultaneously, as illustrated in Figure 2.10. In analogy to a spectrum of light, the incident neutron beam is "white", consisting of all wavelengths. At a continuous source all wavelengths arrive at all times. However, at a short pulsed source the time of flight is directly proportional to the wavelength [2] and resolution given by neutron emission time from the system. By looking at scattering in slices of time, one can divide the incident beam into its component wavelengths, as indicated by the colored bars on the plot. The energy resolution of the experiment is determined by the width of the bar, and the time required to achieve equivalent counts is determined by the total area of the bar. By viewing the

---

[2]We will find a need to challenge this perception for long pulses at LENS, see Sections 5.4.3, 5.8.4, and 6.3.2.
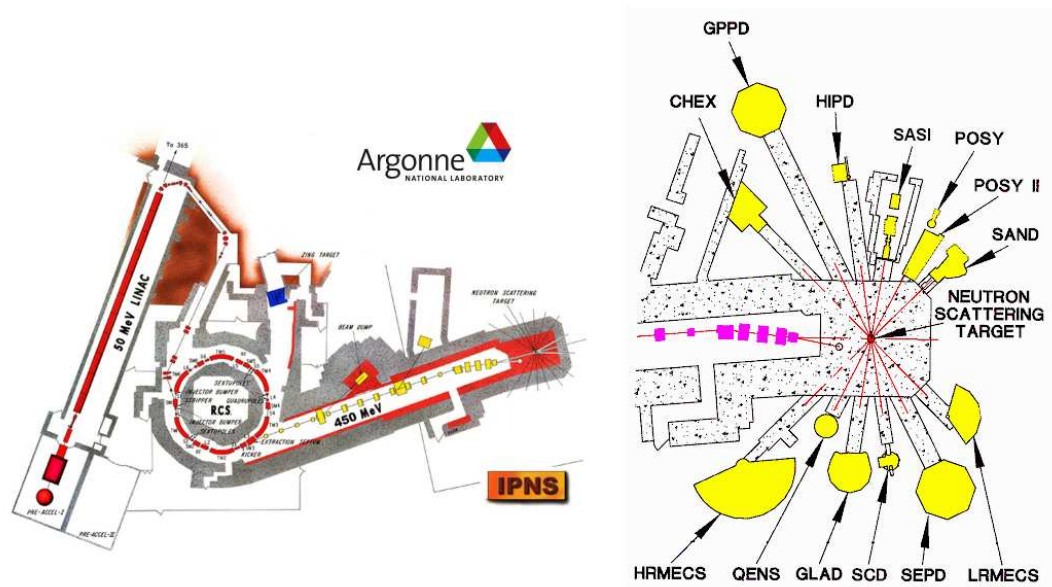
Figure 2.9: The layout of the IPNS accelerator, target, and instruments. The target is depleted uranium struck with 450 MeV protons, surrounded by a Beryllium reflector. Three cold moderators, liquid methane, solid methane, and solid methane with grooves feed the instruments. Adapted from *http://www.pns.anl.gov/*.

scattering in narrow slices of time, the effect due to incident neutrons of a certain color (wavelength) may be determined consecutively with all the other accessible colors.

Another advantage, and disadvantage, of the spallation source is the hardness of the spectrum. In a reactor, the majority of the neutrons have long lifetimes in the reactor and become well thermalized before escaping or absorbing in the system. This is not necessarily true for a spallation source, where the much higher energy spallation neutrons can penetrate meters of concrete. However, this is also a potential advantage, as there are higher fluxes of .1-10 eV neutrons for experiments. Neutrons of these energies are similar in energy to chemical bonds in molecules and can be employed in inelastic chemical spectroscopy experiments. The IPNS CHEX and HRMECS spectrometers are examples of such instruments. HRMECS, for example, uses a chopper to select 3-1000 meV beams of neutrons with high resolution in energy
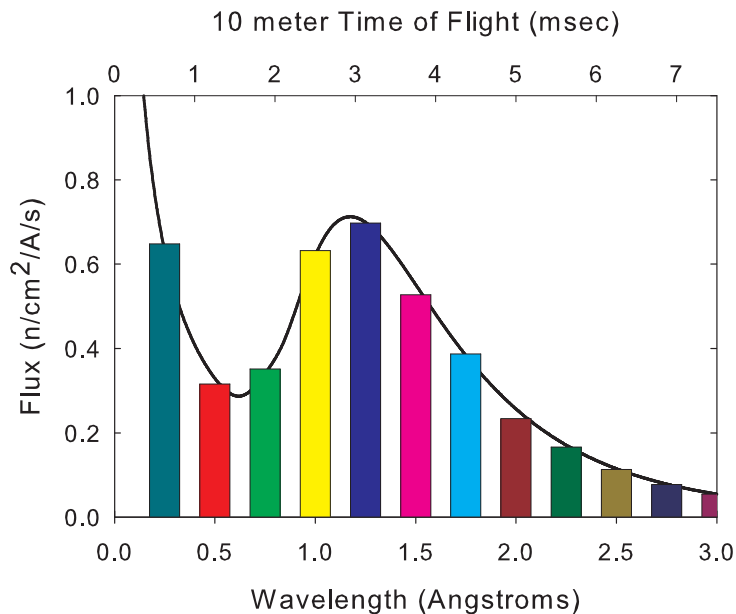
Figure 2.10: An incident neutron beam is white, consisting of all wavelengths in the spectrum. By viewing the scattering in narrow slices of time, as indicated by the colored bars on the chart, the effect due to incident neutrons of a certain color (wavelength) may be determined simultaneously to the other colors.

and scattering angle [55]. Guides are also employed at pulsed sources, where it has been shown that TOF energy resolution can be maintained provided that the critical angle is not too large [56]. Guide gains in intensity as high as a factor of 3 have been seen on the GPPD instrument [50]. This allows long flight paths, which increases time resolution considerably for a pulsed instrument.

The IPNS has a over a 20 year history as a successful and reliable DOE national user facility. It paved the way for instrumentation and cold neutrons at pulsed sources. Many of the neutronics and instrumentation concerns central to the success of the SNS were first mastered at IPNS.

2.7   The SNS

The Spallation Neutron Source (SNS) project at Oak Ridge holds much promise for the future of neutron scattering in North America. The SNS is a pulsed spallation

source, delivering up to 1 MW of GeV protons onto a liquid mercury target and producing ∼30 n/p. It is not a project based around an existing accelerator (like LANSCE, IPNS, or even LENS), but a dedicated user facility centered around the most powerful neutron source in the world. There will be several cold and ambient temperature moderators surrounded by a beryllium reflector which service 18 guided beam lines. Today, 2 instruments are functional while construction completes on the remaining site. A power upgrade to the accelerator and a second target station for long wavelength neutrons is planned as well. The facility completed initial construction in April 28, 2006, providing first beam to 2 instruments and a detector for benchmarking production [57].
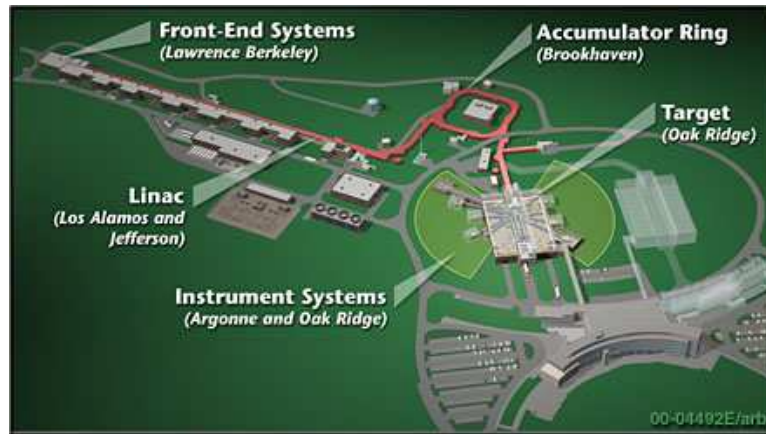
Figure 2.11: The SNS layout. The lab is constructed as an interagency collaborative project, with various national research centers responsible for different portions of the project. From *http://www.sns.gov*.

The SNS grew as an alternative to the proposed ANS 300 MW research reactor concept [58], which derailed in congress in 1995 due to cost and proliferation concerns. An alternative program costing $ 1 billion was called for, and an accelerator based source was ideal. The U.S. continues to lag behind Europe in neutron based materials sciences and the SNS hopes to restore a competitive capability to U.S. research and industry. The SNS brings many of the lessons of the past to instrument design. A frank report by the Office of Science and Technology Policy in 2002 reported that

fewer that 60% of U.S. instruments could be considered world class [59]. A key goal of the SNS is to provide a suite of instruments and sample environments that are each world class.
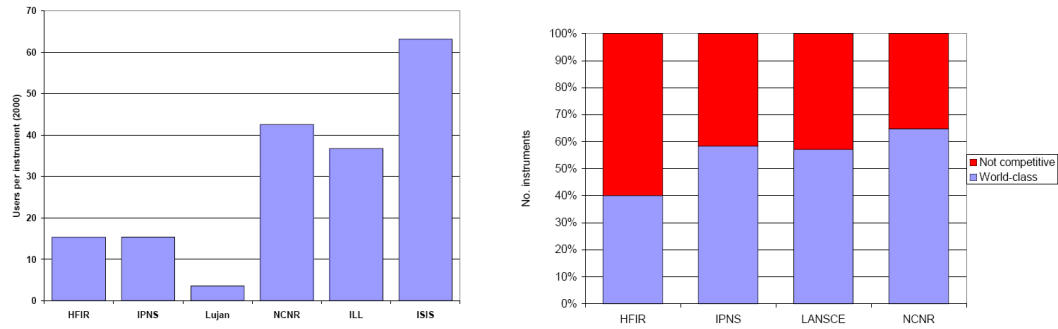
Figure 2.12: *Left:* U.S. lags behind in the number of users of neutron instruments. ILL and ISIS are European sources. *Right:* Many of the U.S. instruments are not competitive with those around the world. From [59].

2.8   LENS

We have shown how neutrons are important in many frontiers of science. We have also discussed the scientific and federal commitment to the future of neutron sciences in the United States. How can a university hope to be part of that growing trend in research and industry? The essence of the LENS project goals have been stated by in the literature.

> ...there is also a need for smaller sources at which new ideas may be explored and large amounts of beam time can be devoted to educating new users. In Europe, national-scale research reactor facilities provide a network of centers for these activities, but no similar network exists in North America. This presents a major obstacle to expanding the neutron scattering community in the Americas.
>
> D.V. Baxter *et. al* [60]

It is clear that the national user facility concept, based around beam time provided via peer review process, is a successful one in many cases [59]. However, users are at the mercy of beam conditions, a highly competitive peer review program, and limited access to the resource due to high demand for relatively few instruments. The Indiana University Cyclotron Facility (IUCF) Low Energy Neutron Source (LENS) project is a prototype for a new paradigm in neutron research - a source dedicated to the development of new techniques in neutronics, the development new ideas in scattering research, and the development of student educational experiences in the field of neutron scattering. We intend LENS to be capable of producing sufficient long wavelength neutron flux for research by operating a low temperature moderator (<10K) in a long pulse mode.

A main feature of such a small source will be its access to beam time and easily variable conditions (moderator type and temperature, proton pulse width, etc.), which will allow rapid prototyping in the source and of novel instruments such

as Spin Echo Small Angle Scattering (SESANS). In addition, the usefulness of the facility in the context of the national user facility base will be extended if colder neutron beams can be produced than are available elsewhere. The low radiation environment at a small source allows moderator materials and temperatures beyond those that are available at the more powerful sources. By focusing the research on long wavelength neutrons, the source and instruments can be optimized together to reach new regions of phase space in low-Q diffraction (SANS), refractometry, and spin-echo.

LENS will also be able to explore use the long pulse source (LPS) mode of operation. As we have discussed, neutron scattering is intensity limited. Clearly, if one irradiates the target 1000 times longer, one will produce 1000 times as many neutrons. However, as we discussed in Chapter 1, high resolution techniques such as powder diffraction and inelastic neutron spectroscopy have been important components of the research at modern user facilities. As a result, all modern pulsed spallation facilities employ short pulses. A small source such as LENS will be able to investigate long pulse instrumentation more cost effectively than making adjustments to a national user facility.

The LENS facility will also support local research at Indiana University. Low-Q diffraction with neutrons has provided unique insight into in polymer and biological sciences [59], such as we have seen in the case of the ribosome. A low Q SANS instrument, made possible by long wavelength neutrons from the colder moderators at LENS, will be a valuable resource to IU efforts in chemistry, biology, and physics. Also, the neutron source will support the Radiation Effects Research Program, increasing the fidelity of radiation damage assessments in electronics. Finally, it is possible to use the LENS target in the production of ultra-cold neutrons in support of fundamental physics research at IU.
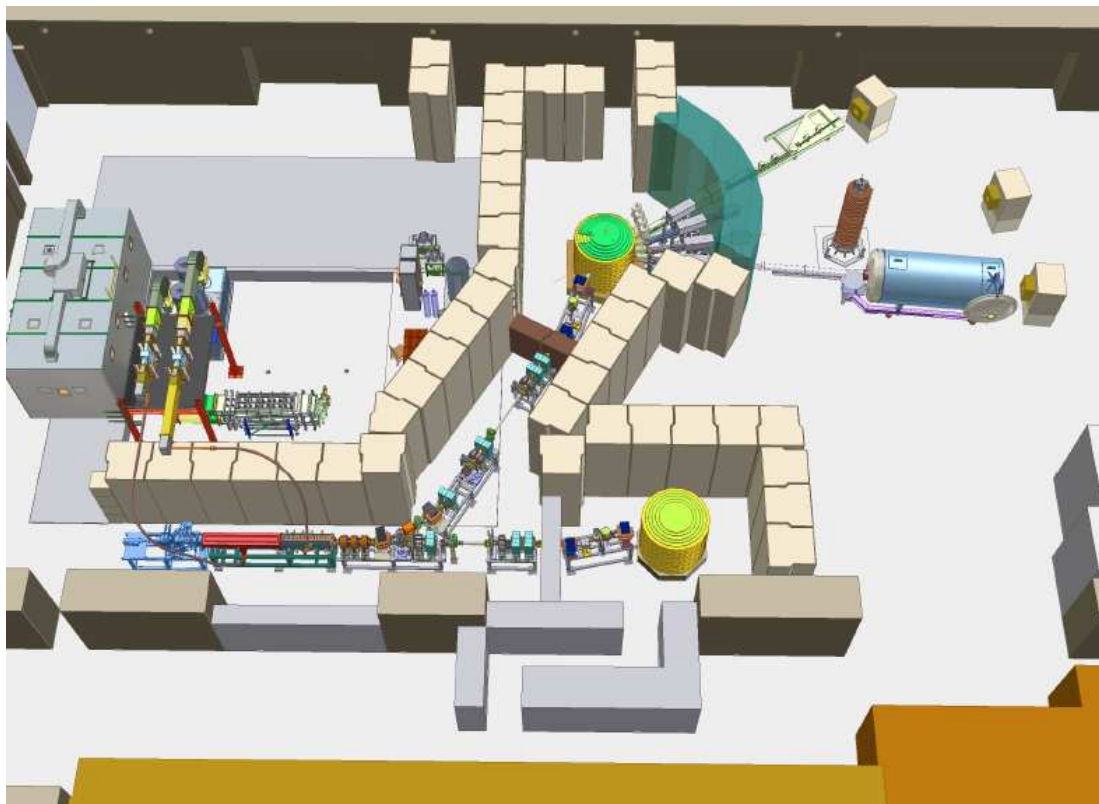
Figure 2.13: LENS Facility Layout. The facility consists of the accelerator, boosted to full power by klystron RF amplifiers, the Radiation Effects station, and the Science Station. The science station supports SANS, radiography (not shown), Spin-echo, and the ACORN experiment.

The IUCF LENS facility produced first neutrons December 15, 2004 and first cold neutrons on April 14, 2005. A power upgrade is underway to make LENS a moderate brilliance source of long wavelength neutrons in support of education, materials research, and instrument development. In addition, the benefits of the neutron source to local IU research interests will be significant.

Chapter 3

Neutron Interactions with Matter

> ...for it would be absurd if a
> student of nature ought to know
> what the sun or moon is but need
> not know any of their coincidents
> in their own right.
>
> Aristotle
> *Physics*

3.1 Introduction

We have reviewed some applications of neutron scattering to important problems in physics and biology as well as the major types of neutron sources. In this chapter, we will explore the basic neutron interactions with matter, including definitions of neutron flux, cross-section, and the physics underlying the general behavior of neutron cross-sections. In the next chapter, we will show how those interactions determine the general features of neutron transport.

3.2 Definition of Neutron Flux

In principle, the main quantity we seek to calculate in is the number of neutrons per unit volume (the neutron density), N, at a point in phase space specified by energy E, trajectory vector $\vec{\Omega}$, time, t, and position, $\vec{r}$. The neutron flux density (herein simply flux), ϕ, is an integral quantity representing the flow of neutron density through a a region of space. However, the definition of flux departs from definitions found in other branches of physics. It is a purely scalar quantity in units of $neutrons/area/time$, and there are a number of equivalent definitions to be found in the literature.

1. Neutron flux is the number of neutrons per unit time passing through an infinitesimal volume sphere divided by the area of that volume. [61] If $< N >$ is the mean number of neutrons, N, passing through a volume, $V = AL$, then

$$\phi = \frac{< N >}{At} \qquad (3.1)$$

2. Neutron flux is the number of track lengths (see Figure 3.1) per unit volume in a region of space. [62] If the mean track length is $< L >$ through a rectangular volume, the number of track lengths per unit volume per unit time is:

$$\phi = \frac{N < L >}{Vt} = \frac{N < l >}{At} \qquad (3.2)$$

where $< l >$ is an average fraction of the longest track through the region. For an infitesimal thin volume (i.e., a surface), $< l >= 1/ < \mu >$ where μ is the cosine between the neutron track and the surface normal.

3. The neutron flux multiplied by the probability per unit length of a reaction to occur, Σ, gives the reaction rate per unit volume,$\mathbb{R}$. [63] If r is the number of

reactions that occur in the volume, this definition implies

$$r = \Sigma \times N < L >= \Sigma \phi V t \tag{3.3}$$

$$\mathbb{R} = \frac{r}{Vt} = \Sigma \phi \tag{3.4}$$

where $\mathbb{R}$ is the reaction rate per unit volume.

4. The neutron flux as a function of speed $(v = |\vec{v}|)$ is equivalent to the density multiplied by the speed, $\phi(v, \vec{r}, t) = vN(\vec{r}, \vec{v}, t)$. [30]

$$< vN >= \frac{< L >}{t} \frac{N}{AL} = \frac{N < l >}{At} \tag{3.5}$$
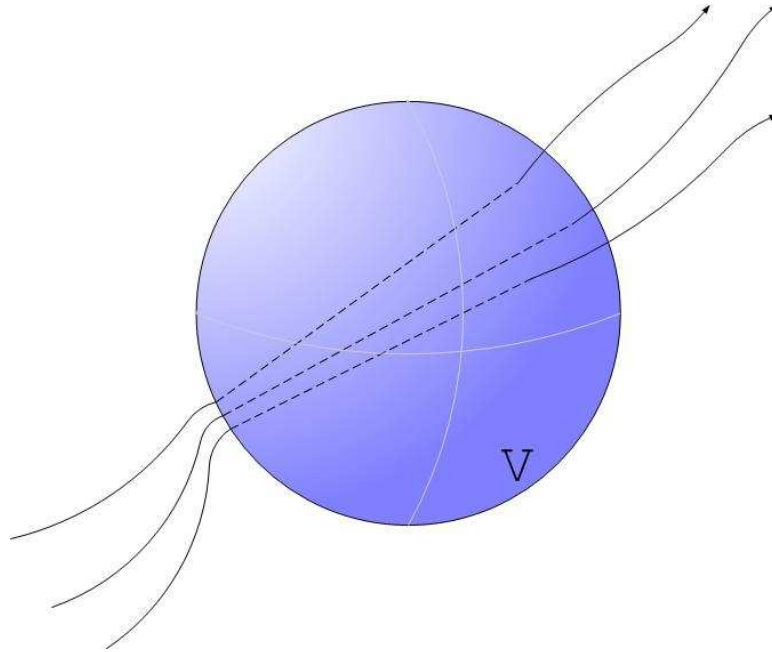
Figure 3.1: Definitions of flux: The dashed lines represent track lengths through the volume, V, and the solid lines represent to flow of neutron tracks that cross the surface of the volume. Equally, neutron flux can be described in terms of the number of tracks that cross the volume (definition 1) or the length of tracks through the volume (definitions 2 and 3).

Closely related to the scalar flux is the neutron vector current, $\vec{j} = \vec{v}N(\vec{r}, \vec{v}, t)$. Typically ϕ is a function of speed (or Energy E), trajectory ($\vec{\Omega}$), position ($\vec{r}$), and time (t) so that $\phi \rightarrow \phi(\vec{v}, \vec{r}, t) = \phi(\vec{r}, \vec{\Omega}, E, t)$. If a variable is omitted, it is implied to have been integrated out. In any presentation of flux it essential to clarify the bounds of the measurement integration in phase space. For example, one might be tempted to simply state "the flux is 10 $n/cm^2/s$", which implies $\int dt \int d\vec{\Omega} \int d\vec{r}\phi(\vec{r}, \vec{\Omega}, E, t)$ in units of $n/cm^2/s/eV$; however, the energy, position, time frame, and accepted trajectories of the measurement would be left unacceptably ambiguous unless specified.

3.3   Cross-section

Interactions are defined in terms of cross-sections, which represent the probability per unit phase space that an interaction occurs. The double differential cross-section is defined as [64]:

$$\frac{d^2\sigma}{d\Omega dE} = \frac{\text{neutrons scattered per unit time into energy } E \text{ to } E + dE, \, d\vec{\Omega} \text{ about } \vec{\Omega}}{\text{Incident neutron flux}}$$

(3.6)

Which is related by definition to the differential cross-section

$$\frac{d\sigma}{d\Omega} = \int_0^\infty dE \frac{d^2\sigma}{d\Omega dE}$$

(3.7)

and to the total cross-section:

$$\sigma = \int_{\text{all directions}} d\Omega \frac{d\sigma}{d\Omega}$$

(3.8)

The *microscopic* cross-section, σ given in units of barns (10^{-24} cm), represents the effective area of the target nucleus as viewed by the neutron. In radiation transport we employ the related *macroscopic* cross-section, Σ, which is given by the atom number density, n, multiplied by the microscopic cross-section,

$$\Sigma = n\sigma \tag{3.9}$$

where we note the that Σ has dimensions of inverse length.

As a neutron travels through a homogeneous medium, the probability to interact per unit length is a constant given by the ratio of the volume occupied by a density of scattering nuclei, n, to the total volume, V. We can show that this ratio is related to Σ and in turn the mean free path. The rate of change of neutron number per unit length due to an interaction with an atom a in the medium between x and $x + dx$ is a constant,

$$\frac{dN}{dx} = -C \tag{3.10}$$

where according to the above definition,

$$C = \frac{\text{volume occupied by scatters}}{\text{total volume}} = n\sigma = \Sigma \tag{3.11}$$

The constant is a negative since the interaction removes the neutron from its initial path. The number of neutrons interacting in the length dx is

$$dN = -Cdx = -n\sigma N dx = -\Sigma N dx \tag{3.12}$$

such that the number of uncollided neutrons remaining after a distance x is given by integration

$$N = N_o e^{-\frac{x}{\lambda}} = N_o e^{-\Sigma x} \tag{3.13}$$

Thus, the characteristic length scale for neutron interactions is set by the mean free path, $\lambda = \frac{1}{\Sigma}$.

We will wish to connect the nuclear cross-section with the nomenclature used in transport theory. The macroscopic cross-section per unit solid angle that the neutron scatters into $\vec{\Omega}$ to $\vec{\Omega} + d\vec{\Omega}$ is [1]

$$n\frac{d\sigma}{d\vec{\Omega}} = \Sigma(\vec{\Omega}' \bullet \vec{\Omega}) \tag{3.14}$$

and the macroscopic cross-section to scatter from energy E' into E to $E + dE$ as a function of angle is

$$n\frac{d^2\sigma}{d\vec{\Omega}dE} = \Sigma(E' \rightarrow E, \vec{\Omega}' \bullet \vec{\Omega}) \tag{3.15}$$

In transport theory one can often focus on energy exchange alone. Integrating over all possible scattering exit angles gives the macroscopic cross-section to scatter from energy E' to E

$$n\int d\vec{\Omega}\frac{d^2\sigma}{d\vec{\Omega}dE} = \int d\vec{\Omega}\Sigma(E \rightarrow E', \vec{\Omega} \bullet \vec{\Omega}') \equiv \Sigma(E' \rightarrow E) \tag{3.16}$$

3.4 Calculation of Cross-sections

The description of neutron interactions is contained in the cross-section, so we will address the general features of nuclear neutron cross-sections. We will then show how the neutron interacts with a system of scattering nuclei.

Understanding the production of neutrons at LENS will require knowledge of nuclear cross-sections over many orders of magnitude in energy. For example, the

---

[1]The implication here that $\Sigma(\vec{\Omega}', \vec{\Omega}) = \Sigma(\vec{\Omega}' \bullet \vec{\Omega})$ assumes that there is no preferred orientation to the medium. This is a manifestation of the *incoherent approximation* used in transport theory which we will discuss in Section 3.8. This assumption is not true for the case of crystalline scatterers, where interference effects result from the lattice structure of the medium.

total cross-sections for lead (^{208}Pb) is shown in Figure 3.2 and for hydrogen in Figure 4.3. The calculation of these cross-sections can be exceedingly complicated, such as in the interaction of neutrons with nuclei at high energy or of low energy neutron interactions with excitations in a solid, or extraordinarily simple, as in the case of a slow neutron interaction with a free nucleus. Let us first consider the total neutron cross-section of lead, which shows the important structural features of neutron cross-sections.
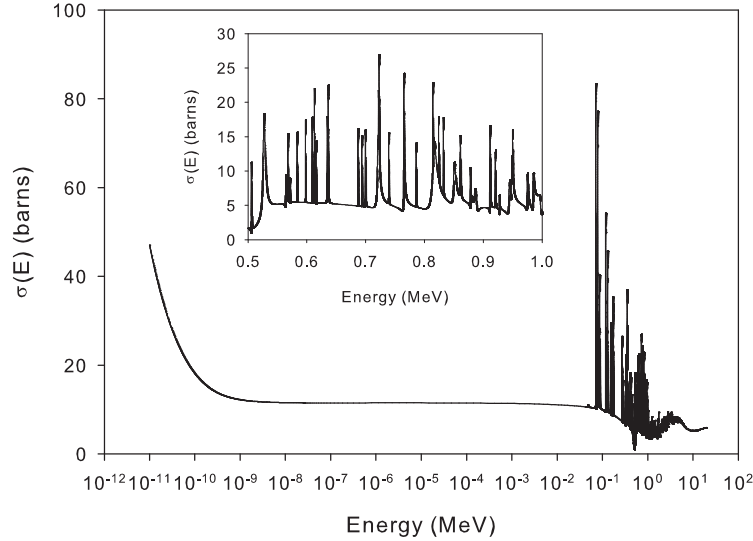
Figure 3.2: ^{208}Pb Cross-section, showing several dominant features. $\frac{1}{v}$ absorption behavior dominates for $E < 1eV$, a constant elastic cross-section is present into to the resonance region. Resonance scattering is present beginning at about 0.1 MeV, and is also shown in the inset plot. Above 10 MeV the resonances become so closely spaced that they form a continuum at the highest energies. Cross-section data from IAEA JENDF nuclear data set [65].

Starting from the lowest energies (0-1 eV), absorption dominates with a characteristic $1/v$ form. Elastic scattering in this regime is roughly constant, and represents *potential scattering* where the neutron does not interact with the internal structure of the nucleus, only the surface potential. This constant behavior continues up to about 500 KeV, after which the contribution from potential scattering is reduced. In the 1 eV to 10 MeV range there may be many sharp peaks in the cross-section called

resonances, shown in more detail in the inset of Figure 3.2. In resonance scattering the neutron energy is very close to a bound state in the target nucleus, which leads to a sharp peak in the scattering at the bound state energy. Off the resonance energy, potential scattering again dominates. At around 10 MeV, however, the resonances become so closely spaced in energy that they may not be distinguished from each other, forming a regime called the *continuum* or *unresolved resonance* region.

3.5 Scattering

For the neutron energies of interest to LENS we may discuss the physics of neutron interactions in a non-relativistic Schröedinger equation. For a 15 MeV neutron, relativistic γ is less than 2%, so relativistic corrections at energies less than this are negligible. The Hamiltonian is a sum of a free part, H_o, and potential part, V, with states specified by continuous eigenvalues ψ.

$$H|\psi >= (H_o + V)|\psi >= E|\psi >$$ (3.17)

Eigenvalues of the free Hamiltonian given by ϕ, such that the solution to the Schröedinger equation is given by the Lippmann-Schwinger equation,

$$|\psi >= |\phi > + \frac{1}{E - H_o \pm i\epsilon} V|\psi >$$ (3.18)

which becomes an integral equation in $|\psi >$ when addressed with a spatial "bra", $< \vec{x}|$ from the left.

$$< \vec{x}|\psi >=< \vec{x}|\phi > + \int d\vec{x}' < \vec{x}|\frac{1}{E - H_o \pm i\epsilon}|\vec{x}' >< \vec{x'}|V|\psi >$$ (3.19)

We note the solution is a sum of an altered wave and the initial wave. This leads naturally to a Green's function approach to solve for any V. The Green's function, G is given by

$$G_\pm(\vec{x}, \vec{x}') \equiv\ <\vec{x}|\frac{1}{E - H_o \pm i\epsilon}|\vec{x}' > \qquad (3.20)$$

where we define the planar wavefunctions as

$$<\vec{x}|\vec{k}> = \frac{e^{i\vec{k}'\bullet\vec{x}'}}{(2\pi)^{\frac{3}{2}}} \qquad (3.21)$$

and define the normalization such that

$$\int d^3x\ <\vec{k}|\vec{x}><\vec{x}|\vec{k}'> = \delta^{(3)}(\vec{k} - \vec{k}');\ \int d^3k\ <\vec{x}|\vec{k}><\vec{k}|\vec{x}'> = \delta^{(3)}(\vec{x} - \vec{x}') \quad (3.22)$$

We may evaluate Equation 3.20 as integral in the momentum basis to overcome the difficulties posed by the singularity in the scattering operator $\frac{1}{E-H_o\pm i\epsilon}$.

$$
\begin{aligned}
G_\pm(\vec{x}, \vec{x}') &= <\vec{x}|\frac{1}{E - H_o \pm i\epsilon}|\vec{x}' > & (3.23) \\
&= \int d\vec{k} \int d\vec{k}'\ <\vec{x}|\vec{k}><\vec{k}|\frac{1}{E - H_o \pm i\epsilon}|\vec{k}'><\vec{k}'|\vec{x}' > & (3.24) \\
&= \int d\vec{k}\ <\vec{x}|\vec{k}>\ \frac{1}{E - \frac{\hbar^2 k^2}{2m} \pm i\epsilon}\ <\vec{k}|\vec{x}' > & (3.25) \\
&= \frac{1}{(2\pi)^3} \int d\vec{k}\frac{e^{ik|x-x'|\cos\theta}}{E - \frac{\hbar^2 k^2}{2m} \pm i\epsilon} & (3.26) \\
& & (3.27)
\end{aligned}
$$

where θ is the angle between a vector connecting the observer ($\vec{x}$) to a point in the

scattering volume $(\vec{x'})$ and the momentum vector of the neutron, $\vec{k}$.

$$G_{\pm}(\vec{x},\vec{x'}) \quad = \quad \frac{1}{(2\pi)^3} \int d\theta \int dk 2\pi \sin\theta k^2 \frac{e^{ik|x-x'|\cos\theta}}{E - \frac{\hbar^2 k^2}{2m} \pm i\epsilon} \tag{3.28}$$

$$= \quad \frac{1}{(2\pi)^3} \int 2\pi i k dk \frac{1}{|x-x'|} \frac{e^{ik|x-x'|} - e^{-ik|x-x'|}}{E - \frac{\hbar^2 k^2}{2m} \pm i\epsilon} \tag{3.29}$$

$$= \quad \frac{2m}{\hbar^2}(2\pi i)^2 \frac{1}{(2\pi)^3} \frac{1}{|x-x'|} \frac{e^{\pm ik|x-x'|}}{2} \tag{3.30}$$

so that Green's function is given by:

$$G_{\pm}(\vec{x},\vec{x'}) = -\frac{2m}{\hbar^2} \frac{1}{4\pi} \frac{e^{\pm ik|\vec{x}-\vec{x'}|}}{|\vec{x}-\vec{x'}|} \tag{3.31}$$

The solution to the scattering problem is now given generally as an integration over the scattering volume

$$< \vec{x}|\psi> = <\vec{x}|\phi> -\frac{2m}{\hbar^2} \int d\vec{x'} \frac{e^{\pm ik|\vec{x}-\vec{x'}|}}{|\vec{x}-\vec{x'}|} <\vec{x'}|V|\psi> \tag{3.32}$$

It is convenient to restrict our consideration to *local* potentials, those that are diagonal in the position basis, such that $< \vec{x'}|V|\vec{x''}> = V(\vec{x'})\delta(\vec{x'}-\vec{x''})$. The observer is at a distence r from the scattering that is large compared with the volume of the scattering center, such that $|\vec{x}-\vec{x'}| \sim r - \hat{\vec{r}} \bullet \vec{x'}$. We restrict our analysis to G_+ solutions (outgoing free neutron wave vector),

$$< \vec{x}|\psi> \quad \rightarrow \quad <\vec{x}|\vec{k}> -\frac{1}{4\pi}\frac{2m}{\hbar^2}\frac{e^{ikr}}{r} \int d\vec{x'} e^{i\vec{k'}\bullet\vec{x'}} V(\vec{x'}) <\vec{x'}|\psi> \tag{3.33}$$

$$< \vec{x}|\psi> \quad = \quad \frac{1}{(2\pi)^{\frac{3}{2}}}[e^{i\vec{k}\bullet\vec{x}} + \frac{e^{ikr}}{r}f(\vec{k'},\vec{k})] \tag{3.34}$$

where

$$f(\vec{k'},\vec{k}) \equiv -\frac{1}{4\pi}(2\pi)^3\frac{2m}{\hbar^2} <\vec{k'}|V|\psi> \tag{3.35}$$

Strictly speaking, $|\psi>$ is a solution of the full Schröedinger equation, which is still unknown. However, if the potential is sufficiently weak so as not to greatly change the incident wave packet and the potential is of finite range we expect ψ to be well represented by plane waves (or a superposition of plane waves),

$$f(\vec{k}', \vec{k}) \approx -\frac{1}{4\pi}(2\pi)^3\frac{2m}{\hbar^2} < \vec{k}'|V|\vec{k} > \tag{3.36}$$

This is the *Born approximation*, which will be addressed later in this chapter.

We may ask "How is $f(\vec{k}', \vec{k})$ related to the cross-section?" The cross-section is the probability to scatter into a unit solid angle per unit time per unit incident beam. The incident beam flux is given by $\Phi = vN$, which for de Broglie waves is $\Phi = \frac{\hbar}{m}kN$. The outgoing plane waves are normalized per unit phase space as $\frac{e^{i\vec{k}\bullet\vec{x}}}{(2\pi)^3N}$, where $(2\pi)^3N$ is a volume element in phase space. The probability to transition per unit time from state $\vec{k}$ to final state $\vec{k}'$ (the transition rate $T_{k'k}$) is given by *Fermi's Golden Rule*:

$$T_{k'k} = \frac{2\pi}{\hbar}\rho_{k'}| < k'|V|k > |^2 \tag{3.37}$$

where $\rho_{k'}$ is *density of states*, the probability of finding a neutron of state k' with trajectory between $\vec{\Omega}$ and $\vec{\Omega}+d\vec{\Omega}$ per unit phase space. The density of states is given by

$$\rho_{k'}dE' = \frac{1}{(2\pi)^3N}k'^2dk'd\Omega \tag{3.38}$$

with

$$E' = \frac{\hbar^2k'^2}{2m} \rightarrow dE' = \frac{\hbar^2}{m}k'dk' \tag{3.39}$$

such that

$$\rho_{k'} = \frac{1}{(2\pi)^3N}k'\frac{m}{\hbar^2}d\Omega \tag{3.40}$$

We express the cross-section in terms of Fermi's golden rule as

$$\frac{d\sigma}{d\Omega} \equiv \frac{\text{Scattering per unit time}}{\text{Flux}} \tag{3.41}$$

$$\frac{d\sigma}{d\Omega} = \frac{T_{k'k}}{\Phi d\Omega} \tag{3.42}$$

$$= \frac{\frac{2\pi}{\hbar}\rho_{k'}|<k'|V|k>|^2}{\frac{\hbar}{m}kN} \tag{3.43}$$

$$= \frac{\frac{2\pi}{\hbar}\frac{1}{(2\pi)^3 N}k'\frac{m}{\hbar^2}d\Omega|<k'|V|k>|^2}{\frac{\hbar}{m}kN} \tag{3.44}$$

$$\frac{d\sigma}{d\Omega} = \frac{k'}{k}\left(\frac{m}{2\pi\hbar^2}\right)^2|<k'|V|k>|^2 \tag{3.45}$$

we note that

$$\frac{m}{2\pi\hbar^2}<k'|V|k> = f(k',k) \tag{3.46}$$

such that the cross-section is given by the absolute value of f, where f is the *scattering amplitude*. The ratio of k' to k in the expression comes from the phase space density of the incident and outgoing flux.

$$\frac{d\sigma}{d\Omega} = \frac{k'}{k}|f(k',k)|^2 \tag{3.47}$$

3.6   General Features of Neutron Cross-sections

In the next few sections we will elucidate the general physics underlying the neutron interactions pointed out earlier. However, if the interaction term $<k'|V|k>$ is constant (potential scattering) for moderate to low energy neutrons, $E < 10$ keV, we can already see that some of the general physics of the neutron cross-section are contained in Equation 3.45. In the case of inelastic scattering, there is an

exchange of energy with the scattering center, ε, such that total energy is conserved.

$$E' = E + \varepsilon \tag{3.48}$$

For a given final state energy energy, the inelastic scattering cross-section is

$$\frac{d^2\sigma}{d\Omega dE} = \frac{k'}{k}(\frac{m}{2\pi\hbar^2})^2| < k'|V|k > |^2\delta(E' - E - \varepsilon) \tag{3.49}$$

If the scattering is inelastic, it will depend on the interaction term multiplied by the $\frac{k'}{k}$, which was due to normalization. In the case where the scattering amplitude does not have a final neutron state dependence, such as absorption, the cross-section goes as the "$\frac{1}{v}$" law as we observe in low energy (E<1eV) neutron scattering. In the case of elastic scattering, no energy is exchanged ($|k'| = |k|$ and $\varepsilon = 0$) and the expression reduces to a constant, just as we observe in the lead and hydrogen cross-sections in the range from 1 eV to 10 KeV (Figures 3.2 and 4.3).

$$\frac{d\sigma}{d\Omega} = (\frac{m}{2\pi\hbar^2})^2| < k'|V|k > |^2 \tag{3.50}$$

3.6.1   Phase Shifts

We have been using a basis of plane waves specified in a position or momentum basis. The scattering can also be represented in in a basis of spherical waves, specified by eigenvalues of energy, angular momentum quantum number, and magnetic quantum number. This leads to the *method of partial waves*, which is important in the discussion of nuclear potential scattering. The wavefunction and normalization

in momentum and position basis is:

$$< \vec{k}|E,l,m> = \frac{\hbar}{\sqrt{mk}}\delta(E - \frac{\hbar^2 k^2}{2m})Y_l^m(\hat{k}) \tag{3.51}$$

$$< \vec{x}|E,l,m> = \frac{i^l}{\hbar}\sqrt{\frac{2mk}{\pi}}j_l(kr)Y_l^m(\hat{r}) \tag{3.52}$$

$$< E',l',m'|E,l,m> = \delta(E' - E)\delta_{l'l}\delta_{m'm} \tag{3.53}$$

We can write the scalar transition operator as a function of energy using the Wigner-Eckart Theorm:

$$< E',l',m'|T|E,l,m> = T_l(E)\delta_{l'l}\delta_{m'm} \tag{3.54}$$

When we apply this basis to the scattering function, we have

$$
\begin{aligned}
f(\vec{k'}, \vec{k}) &= -\frac{1}{4\pi}\frac{2m}{\hbar^2}(2\pi)^3 < \vec{k'}|T|\vec{k} > \tag{3.55} \\
&= -\frac{1}{4\pi}\frac{2m}{\hbar^2}(2\pi)^3 \sum_{l',m'}\sum_{l,m}\int dE \int dE' \times \\
&\quad < \vec{k'}|E',l',m' >< E',l',m'|T|E,l,m >< E,l,m|\vec{k} > \tag{3.56} \\
&= -\frac{4\pi^2}{k}\sum_{l,m}T_l(E)|_{E=\hbar^2 k^2/2m}Y_l^m(\hat{k'})Y_l^m(\hat{k}) \tag{3.57}
\end{aligned}
$$

If we identify the incident wave of energy E traveling the +Z direction only m=0 terms contribute to the scattering amplitude. Under these conditions, we have

$$
\begin{aligned}
f(\vec{k'}, \vec{k}) &= \sum_{l=0}^{\infty}(2l+1)(-\pi\frac{T_l(E)}{k})P_l(\vec{k'} \bullet \vec{k}) \tag{3.58} \\
f(\theta) &= \sum_{l=0}^{\infty}(2l+1)f_l(k)P_l(\cos\theta) \tag{3.59}
\end{aligned}
$$

If we expand Equation for large r, the outgoing wave function $< \vec{x}|\psi >$ is

$$j_l(kr) \approx \frac{e^{i(kr-l\pi/2)} - e^{-i(kr-l\pi/2)}}{2ikr} \tag{3.60}$$

$$< x|\psi > = \frac{1}{(2\pi)^{3/2}}[e^{ikz} + f(k)e^{ikr}/r] \tag{3.61}$$

$$< x|\psi > = \frac{1}{(2\pi)^{3/2}}\sum_l$$

$$(2l+1)\frac{P_l(\cos\theta)}{2ik}[[1 - 2ikf_l(k)]\frac{e^{ikr}}{r} - \frac{e^{-i(kr-l\pi)}}{r}] \tag{3.62}$$

so we see the scattering consists of a sum over partial waves indexed by l with the lth partial wave scattering amplitude $1 - 2ikf_l(k)$. In the time independent formalism there are no sources or sinks of probability density $|\psi|$ and the total current from incoming waves must equal the total current from outgoing waves.

$$\frac{d|\psi|}{dt} = \vec{\nabla} \bullet \vec{j} + \frac{\partial|\psi|}{\partial t} \tag{3.63}$$

$$\vec{\nabla} \bullet \vec{j} = -\frac{\partial|\psi|}{\partial t} = 0 \tag{3.64}$$

$$\int dV\vec{\nabla} \bullet \vec{j} = \oint \vec{j} \bullet d\vec{S} = 0 \tag{3.65}$$

From Equation 3.62 we see that the incoming wave expectation value is 1, therefore we express the outgoing wave amplitude as $S_l(E)$,

$$S_l(E) = 1 - 2ikf_l(k) \tag{3.66}$$

$$|S_l(E)| = 1 \tag{3.67}$$

A simple conventional expression for $S_l(E)$ which also satisfies this condition is

$$S_l(E) = e^{2i\delta_l(E)} \tag{3.68}$$

where we define δ_l to be the energy dependant phase shift of the lth partial wave, such that

$$f_l(k) = \frac{1}{k \cot \delta_l - ik} \tag{3.69}$$

$$f(\theta) = \frac{1}{k} \sum_{l=0}^{\infty} (2l+1) e^{i\delta_l} \sin \delta_l P_l(\cos(\theta)) \tag{3.70}$$

Recalling the optical theorem, we can reduce the scattering total cross-section to being due to a phase shift alone.

$$\text{Im}(f(0)) = \frac{k\sigma_t}{4\pi} \tag{3.71}$$

$$= \frac{1}{k} \sum_{l=0}^{\infty} (2l+1) \sin^2 \delta_l \tag{3.72}$$

$$\sigma_t = \frac{4\pi}{k^2} \sum_{l=0}^{\infty} (2l+1) \sin^2 \delta_l \tag{3.73}$$

3.6.2 Hard Sphere, Zero Energy, and Resonance Phase Shifts

To complete our description of neutron cross-sections, need to show that the interaction is constant at low energy and we need to discuss the origin of resonance behavior. This can be illustrated by solving for the phase shift for a hard sphere potential and an energy dependent "resonance" phase shift.

The hard sphere wave function is given exactly from the solution to the Schrödinger equation outside the range of the central potential. The radial Schrödinger equation is

$$\frac{d^2 u_l}{dr^2} + (k^2 - \frac{2mV(r)}{\hbar^2} - \frac{l(l+1)}{r^2}) u_l = 0 \tag{3.74}$$

where wavefunctions are $|\psi\rangle = \sum_l (2l+1) A_l(r) P_l(\cos(\theta))$ and solutions to the above

are $rA_l(r) = u_l(r)$. The potential for a hard sphere is

$$
\begin{aligned}
V(r) &= \infty \text{ for } r < a \qquad\qquad (3.75)\\
&= 0 \text{ for } r > a
\end{aligned}
$$

The wavefunction must go to zero on the surface of the sphere.

$$
\begin{aligned}
A_l(r) &= e^{i\delta_l}(j_l(kr)\cos\delta_l - n_l(kr)\sin\delta_l) \qquad\qquad (3.76)\\
\tan\delta_l &= \frac{j_l(ka)}{n_l(ka)} \qquad\qquad (3.77)\\
\tan\delta_0 &= -\tan(ka) \qquad\qquad (3.78)\\
\delta_0 &= ka \qquad\qquad (3.79)
\end{aligned}
$$

so that, using the optical therom for s-wave (l=0) scattering,

$$
\sigma_t = 4\pi a^2 \qquad\qquad (3.80)
$$

Thus, the total scattering cross-section goes as 4 times the geometric scattering (πa^2) for a hard sphere potential of radius a.

In the limit $E \to 0$ s-wave scattering dominates and Equation 3.74 reduces for any potential V (not necessarily hard sphere)

$$
\frac{d^2 u_o}{dr^2} = 0 \qquad\qquad (3.81)
$$

with the simple general solution of

$$
u_o(r) = \alpha(r - a) \qquad\qquad (3.82)
$$

where α is a constant. The radial wave function can be compared to the general solution for s-wave scattering at low k,

$$A_l(r) \;=\; e^{i\delta_l}(j_l(kr)\cos\delta_l - n_l(kr)\sin\delta_l) \tag{3.83}$$

$$A_o(r) \;=\; e^{i\delta_o}\left(\frac{\sin(ka)}{kr}\cos\delta_o + \frac{\cos kr}{kr}\sin\delta_o\right) \tag{3.84}$$

$$\;=\; e^{i\delta_o}\frac{1}{kr}\sin(kr+\delta_o) \tag{3.85}$$

Comparing the logarithmic derivative to the general solution as $r \to 0$, we see

$$\mathrm{Lim}_{k\to 0}\frac{u_o'}{u_o} = k\cot(kr+\delta_o) = \frac{1}{r-a} \tag{3.86}$$

$$k\cot(\delta_o) = -\frac{1}{a} \tag{3.87}$$

and from Equation 3.69

$$f_o = \frac{1}{k\cot\delta_o - ik} \tag{3.88}$$

$$\sigma_t = 4\pi\mathrm{Lim}_{k\to 0}|f_o|^2 = 4\pi a^2 \tag{3.89}$$

where a is termed the *scattering length*. So, in the limit of zero energy scattering, the result is identical to hard sphere scattering for any potential. This is because at low energy the neutron interacts only with the surface of the potential, not the internal structure. We also note that at low energy, the phase shift tends to a constant, showing the interaction term at low energy is a constant.

Resonance scattering is a consequence of an energy dependent phase shift. Let us imagine that there is a bound state, or resonance, at E_r. In the vicinity of the resonance, the scattering sharply peaks as the particles are trapped by the bound state. Off the resonance, the scattering is again hard sphere, as the centrifugal

barrier prevents deep penetration into the potential. Physically, this is due to a rapid increase in the phase shift of the neutron as the particle becomes trapped in the bound state. In this case, we expect very near the resonance that the scattering amplitude is imaginary (completely confined neutron, $\cot \delta_o|_{(E=E_r)} = 0$) and the phase shift falls off with a power series off the resonance.

$$\cot \delta_l(E) \approx \cot \delta_l|_{E=E_r} \ - \ \frac{d \cot(\delta_o)}{dE}|_{E=E_r}(E - E_r) + \dots \tag{3.90}$$

$$f_l(k) \ = \ \frac{1}{k}\frac{1}{\cot \delta_l + i} \tag{3.91}$$

$$\approx \ \frac{1}{k}\frac{1}{c(E - E_r) - i} \tag{3.92}$$

$$\sigma_l(E) \ = \ \frac{4\pi}{k^2}\frac{(2l+1)c^{-2}}{(E - E_r)^2 + c^{-2}} \tag{3.93}$$

where $c = \frac{d \cot(\delta_o)}{dE}|_{E=E_r}$ the cross-section of the lth partial wave resonance is $\sigma_l(E)$. This is a Cauchy Distribution, such that we interpret the half-width of the resonance peak as $\Gamma = 2/c$ and the peak location as E_r such that we have the Breit-Wigner resonance form:

$$\sigma_l(E) = \frac{4\pi}{k^2}\frac{(2l+1)(\Gamma/2)^2}{(E - E_r)^2 + (\Gamma/2)^2} \tag{3.94}$$

3.7   Fermi Pseudopotential

In the limit of low energy neutron scattering, the outgoing wave is not greatly altered from the incoming wave. That is to say that if we have plane waves incident, the outgoing wave will also be a plane wave. This is the first Born approximation, leading

to great simplifications in the calculation of $f \approx f_b$:

$$f_b(\vec{k}', \vec{k}) \approx -\frac{1}{4\pi}(2\pi)^3 \frac{2m}{\hbar^2} < \vec{k}'|V|\vec{k} > \tag{3.95}$$

$$f_b(\vec{k}', \vec{k}) = -\frac{1}{4\pi}(2\pi)^3 \frac{2m}{\hbar^2} \int d\vec{x}' < \vec{k}'|\vec{x}' >< \vec{x}'|V|\vec{x} >< \vec{x}|\vec{k} > \tag{3.96}$$

$$f_b(\vec{k}', \vec{k}) = -\frac{1}{4\pi} \frac{2m}{\hbar^2} \int d\vec{x}' e^{i\vec{\kappa} \bullet \vec{x}'} V(\vec{x}') \tag{3.97}$$

where the *momentum transfer* is $\vec{\kappa} = \vec{k} - \vec{k}'$. So the scattering is merely the fourier transform of the potential with respect to momentum.

We have shown that the scattering of low energy neutrons must go as the square of the scattering length, however, in the hard sphere limit the neutron wave function does not satisfy the Born condition that the wave form not be greatly altered by the scattering process. In fact, the wave form goes to zero at the surface of the sphere! Fermi proposed that we employ a simple form of the potential in the Born approximation that bears little resemblance to the nuclear potential, but still returns the correct form for the scattering. This is called the *Fermi pseudopotential* and goes as,

$$V(x) = a\delta(x) \tag{3.98}$$

such that when employed in the born approximation, the scattering becomes:

$$\frac{d\sigma}{d\Omega} = (\frac{m}{2\pi\hbar^2})^2 |\int V(x)e^{iq \bullet r}|^2 \tag{3.99}$$

$$= (\frac{m}{2\pi\hbar^2})^2 a^2 \tag{3.100}$$

From inspection of Equation 3.80, we have

$$b^2 = (\frac{m}{2\pi\hbar^2})^2 a^2 \tag{3.101}$$

$$V(x) = (\frac{2\pi\hbar^2}{m})b\delta(x) \tag{3.102}$$

where a is the *bound scattering length.* The potential should be the same in either the lab frame or the CM, so the bound scattering length is related to the free scattering length by the transformation,

$$\frac{b}{\mu} = \frac{b_{free}}{A} \rightarrow b = b_f \frac{A+1}{A} \tag{3.103}$$

where A is the mass of the scatterer in amu. The motivation behind the pseudopotential is that the scatterer is much smaller than the wavelength of the incident radiation. Thus, the neutron "sees" the scatterer much like a point in space. This is well satisfied for slow neutrons where nuclear radii and values of b are on the order of femtometers $(10^{-15}m)$ and the neutron wavelength is $10^{-10} \sim 10^{-8}m$. Values of b are typically somewhat larger than the geometric scattering (which would be given by the nuclear radius as πR^2) and are also spin dependant. A collection of experimental and theoretical values for nuclear radii are given in Figure 3.3, and for comparison values of the scattering length up to Zn are shown in Figure 3.4.
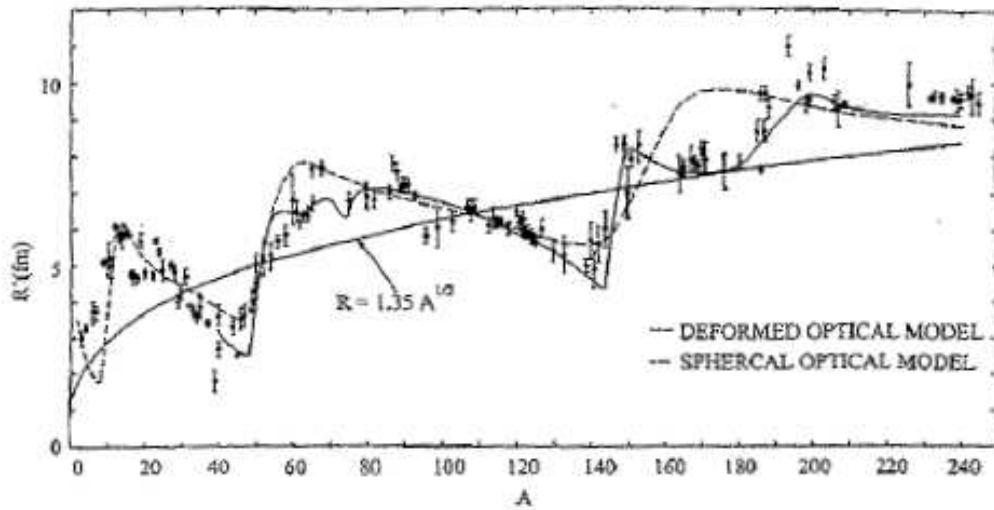
Figure 3.3: Theoretical and experimental values of the nuclear radius. From [66].
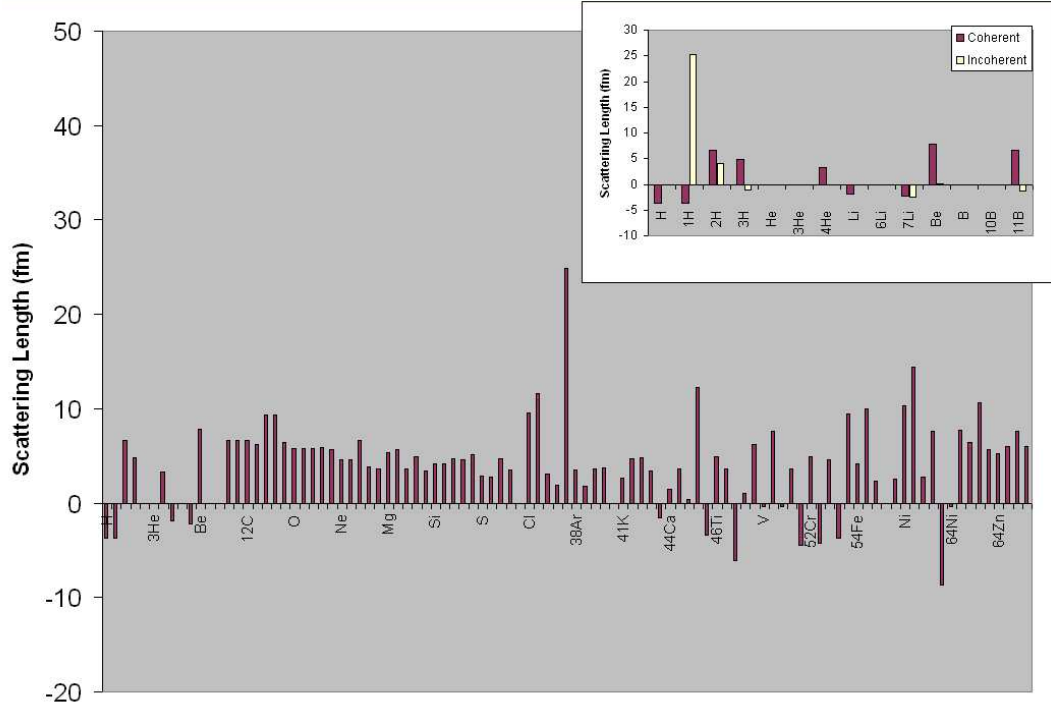
Figure 3.4: Experimental values of the scattering length. Unlike the geometric radius of the nucleus in Figure 3.3, note the distinct lack of a trend among the atomic numbers and isotopes. [67]

3.8   Van Hove and Detailed Balance

For neutron scattering at very low energy, the energy exchanged with the dynamics of a system of scatters can far exceed the energy exchanged in the nuclear scattering from a fixed nucleus. In our discussion of transport below about $\sim 10 eV^2$, these *molecular binding effects* will dominate the scattering. Thus, it is imperative to relate the scattering of the neutron at low energy from a system of scattering centers, first derived in detail by Van Hove [2].

We begin with a modification to the definition of the coordinates employed in the inelastic Born approximation. As stated, we assume that the exchange of energy with the individual scattering particle is much less than the energy exchange with the system S. We also imagine that the scattering vector is now $r + r'$ where r' is a vector

---
[2]In MCNP thermal scattering laws extend from 0 to 4 eV

describing the position of a scattering particle in a system, S, and similarly the time coordinate becomes $t + t'$. Finally, we add the quantum state of the system, $|n>$ with energy E_n, to the wave function and sum over all states of the system, weighted with a state occupation probability p_n, often described by Boltzman statistics.

$$\frac{d^2\sigma}{d\Omega dE} = \frac{m^3}{(2\pi)^2\hbar^6}\frac{k}{k_o}W(q)\delta(k^2 - k_o^2 + \frac{2m}{\hbar^2}(E - E_o)) \qquad (3.104)$$

$$\text{where } W(q) = |f_b(k', k)|^2 \; ; \; f_b \rightarrow [\int dr e^{iqr}V(r)]e^{iqr_j} \qquad (3.105)$$

where r_j is the position of particle j in S. Thermally averaging over all particles and quantum states of the system weighted by the occupation probability of the state, where $|n_o>$ is the initial state and $|n>$ is the final state.

$$< e^{iqr_j} > = \sum_{n_o} p_{n_o} \sum_n |\sum_{j=1}^N < n_o|e^{iqr_j}|n>|^2 \qquad (3.106)$$

so that the Born approximation applied to a system of N scattering particles is

$$\frac{d^2\sigma}{d\Omega dE} = \frac{m^3}{(2\pi)^2\hbar^6}\frac{k}{k_o}W(q) \times$$

$$\sum_{n_o} p_{n_o} \sum_n |\sum_{j=1}^N < n_o|e^{iqr_j}|n>|^2\delta(k^2 - k_o^2 + (\frac{2m}{\hbar^2}(E - E_o)) \qquad (3.107)$$

We can rewrite the scattering in terms of a portion that depends on the incident particle and the target particle (nuclear part) and a portion that depends on the

system static and dynamic structure (condensed matter part).

$$\frac{d^2\sigma}{d\Omega dE} \quad = \quad AS(q,\omega) \tag{3.108}$$

$$\text{where } \hbar\omega \quad \equiv \quad E - E_o \tag{3.109}$$

$$A \quad = \quad \frac{m^3}{(2\pi)^2\hbar^6}\frac{k}{k_o}W(q) \tag{3.110}$$

$$S(q,\omega) = \sum_{n_o} p_{n_o} \sum_n |\sum_{j=1}^{N} < n_o| \; e^{iqr_j}|n>|^2 \quad \delta(k^2 - k_o^2 + (\frac{2m}{\hbar^2}(E - E_o)) \tag{3.111}$$

If we link $S(q,\omega)$, in analogy with the role played by the potential in the Born approximation, with the Fourier transform of some function $G(r,t)$ we find an interesting result:

$$S(q,\omega) \quad = \quad \frac{N}{2\pi}\int e^{i(qr-wt)}G(r,t)drdt \tag{3.112}$$

$$G(r,t) \quad = \quad \frac{1}{(2\pi)^3N}\sum_{n_o}p_{n_o}\sum_n\sum_{l,j=1}^{N} \times$$

$$\int dqe^{-iqr} < n_o|e^{iqr}|n> e^{iE_nt/\hbar} < n|e^{iqr}|n_o> e^{-iE_{n_o}t/\hbar} \tag{3.113}$$

employing the Heisenberg representation, $f(t) = e^{\frac{iHt}{\hbar}}fe^{\frac{-iHt}{\hbar}}$

$$G(r,t) \quad = \quad \frac{1}{N} < \sum_{l,j=1}^{N}\int dr'\delta(r + r_l(0) - r')\delta(r' - r_j(t)) > \tag{3.114}$$

where $< \dots >$ indicates a thermal average. For $t = 0$, we retain the static conditions of the system. $G(r,t)$ is the *pair correlation function* of the system. In a classical system, it represents the density of the medium at point r and time t. In a quantum system, because of the non-commutativity of the position operators r and $r(t)$ the interpretation is the the correlation function represents the probability of finding

particle j at position r_j at time t if particle i was at r_i at time $t = 0$.

There are a few manipulations we will find convenient for future work. First, we may divide the scattering into a *self* part, where we consider the probability of finding the same particle at r at time t, and *distinct* part, representing the probability of finding a different particle at r at time t. Second, we can include an additional label for each scattering atom, such as spin state or isotope, via the scattering length. Finally, we may extract the detailed balance factor by writing $S(q, \omega)$ in terms of properly chosen dimensionless variables.

If we divide the summation in Equation 3.113 into a part with $i = j$ and a part with $i \neq j$ then we have

$$G(r, t) = G_s(r, t) + G_d(r, t) \tag{3.115}$$

$$G_s(r, t) = \frac{1}{N} < \sum_{l=j=1}^{N} \int dr' \delta(r + r_l(0) - r') \delta(r' - r_j(t)) > \tag{3.116}$$

$$G_d(r, t) = \frac{1}{N} < \sum_{l \neq j=1}^{N} \int dr' \delta(r + r_l(0) - r') \delta(r' - r_j(t)) > \tag{3.117}$$

In general, neutron scatting sites are further labeled by their scattering length, b, which can vary based on spin state or isotope, and are assumed here to completely uncorrelated. We can expand equation 3.113 to include variation in scattering length, and express it terms of an average over spin or isotopes, for $G \rightarrow \Gamma$;

$$\Gamma(r, t) = \frac{1}{N} < \sum_{l=j=1}^{N} \int dr' b_i(0) \delta(r + r_l(0) - r') b_j(t) \delta(r' - r_j(t)) > \tag{3.118}$$

$$\Gamma(r, t) = \bar{b^2} G_s(r, t) + \bar{b}^2 G_d(r, t) \tag{3.119}$$

where $\bar{b}$ denotes the isotope or spin average over the scattering lengths in the sample.

We can divide this into a *coherent* and *incoherent* part of the scattering

$$S(q,\omega)_{coh} = \bar{b}^2 \frac{N}{2\pi} \int e^{i(qr-wt)} G(r,t) dr dt \qquad (3.120)$$

$$S(q,\omega)_{inc} = (\bar{b^2} - \bar{b}^2) \frac{N}{2\pi} \int e^{i(qr-wt)} G_s(r,t) dr dt \qquad (3.121)$$

The power of the Van Hove correlation function is that if we understand the expectation value of the position of the particles in the system, we can infer the dynamic structure factor, $S(q,\omega)$, and more importantly, vice-versa. If we understand the scattering, we can infer the static and dynamic structure. The incoherent part is due to scattering from a single particle, and while the states available to scatter into are generally given by the specifics of the system, the incoherent part contains no information on the structure of the system as scattering from 2 sites averages to zero. In the coherent term, self and distinct terms are included, leading to the inclusion of interference from the structure of the scattering system. The relative magnitudes of each term in the cross-section is determined from the so-called *coherent* and *incoherent* scattering lengths,*b*,

$$b_{coh} = \bar{b} \; ; \; b_{inc} = \sqrt{(\bar{b^2} - \bar{b}^2)} \qquad (3.122)$$

The averaging process for the coherent scattering length allows for contrast variation. For instance the scattering length of hydrogen is -3.7 fm and for deuterium it is 6.7 fm [67]; the change of sign makes it possible to average out the coherent scattering completely. In thermalization studies in hydrogenous medium, the incoherent scattering cross-section of hydrogen is 45 times *larger* than the coherent scattering cross-section, so coherent scattering is typically neglected.

If p_{n_o} is given by $e^{-\epsilon/T}/Z$, we can show how to invert the scattering from scat-

tering from state $E \rightarrow E_o$ to $E_o \rightarrow E$ is given by

$$p_{n_o} = e^{\beta E'} \tag{3.123}$$

$$\frac{E'}{E}e^{-\beta E'}e^{\beta E}\frac{d^2\sigma}{d\omega dE'} = \frac{d^2\sigma}{d\omega dE} \tag{3.124}$$

$$\text{where } M(E,T) = Ee^{\beta E} \text{ and } \beta = \tfrac{1}{kT} \tag{3.125}$$

$$\text{and } n\frac{d^2\sigma}{d\omega dE_n} \equiv \Sigma(E' \rightarrow E, \mu) \tag{3.126}$$

$$\frac{\Sigma(E' \rightarrow E, \mu)}{M(E',T)} = \frac{\Sigma(E \rightarrow E', \mu)}{M(E,T)} \tag{3.127}$$

If we return to the Fourier transform of S_{inc}, having already performed the spatial transform $\chi_s(q,t) = \int dr e^{iqr} G_s(r,t)$, where χ_s is the *intermediate scattering function*

$$S_{inc}(q,\omega) = \frac{1}{2\pi}\int_{-\infty}^{\infty} dt e^{-i\omega t}\chi_s(q,t) \tag{3.128}$$

and replace t with $t + i/2T$ then

$$S_{inc}(q,\omega) = \frac{1}{2\pi}\int_{-\infty}^{\infty} dt e^{-i\omega(t+i/2T)}\chi_s(q,t+i/2T) \tag{3.129}$$

$$= \frac{1}{2\pi}e^{-\omega/2T}\int_{-\infty}^{\infty} dt e^{-i\omega t}\chi_s(q,t+i/2T) \tag{3.130}$$

$$= \frac{1}{T}e^{-\beta/2}\frac{1}{2\pi}\int_{-\infty}^{\infty} dt' e^{-i\omega t'}\chi_s(q,t'+i/2T) \tag{3.131}$$

$$\text{where } t' = Tt \text{ and } \alpha = \tfrac{q^2}{2MkT}$$

$$= \frac{1}{T}e^{-\beta/2}S_s(\alpha,\beta) \tag{3.132}$$

such that $S(\alpha,\beta)$ is the *scattering law*, or kernel, and gives the scattering from a system of particles. It is even in α and β and has the added feature of automatically satisfying detailed balance even if there are errors in the experimental determination of $S(\alpha,\beta)$. Analytic solutions to $S(q,\omega)$ are possible in certain approximate cases of the system, S, such as a free gas and a crystal lattice of harmonic oscillators.

3.9 Free Gas $S(q, \omega)$

In the free gas case, we assume there are no cooperative motions (no intermolecular interactions) and that the target atoms is completely free to recoil. This case is extremely important in Monte Carlo modeling because it represents the approximation used when the scattering laws are undetermined. In this semi-classical consideration, $r(t) = r(0) + pt$ where p is the momentum of the particle. We then have

$$S(q, \omega) = \frac{1}{2\pi} \int dt e^{-i\epsilon t} < e^{iq(r-r(t))} >_T \tag{3.133}$$

where $< \cdots >_T$ indicates a thermal average. Exploring the thermal average term,

$$< e^{iq(r-r(t))} >_T \quad = \quad < e^{iqr} e^{iHt} e^{-iqr} e^{-iHt} >_T \tag{3.134}$$

$$= \quad < e^{iH't} e^{-iHt} >_T \tag{3.135}$$

using e^{iqr} as the generator of translation.

$$< e^{iH't} e^{-iHt} >_T \quad = \quad < e^{i\frac{(\hbar p-q)^2 t}{2m}} e^{-i\frac{\hbar^2 p^2 t}{2m}} >_T \tag{3.136}$$

$$= \quad < e^{i\frac{(\hbar p-q)^2}{2m}t} e^{-i\frac{\hbar^2 p^2 t}{2m}} >_T \tag{3.137}$$

$$= \quad < e^{\frac{it}{2m}(-2\hbar pq + q^2)} >_T \tag{3.138}$$

$$\tag{3.139}$$

We define the thermal average for Boltzman statistics as

$$< \ldots >_T = \int f(p) < \ldots > d\vec{p} \tag{3.140}$$

$$f(p) = (\frac{1}{2\pi MT})^{\frac{3}{2}} e^{-\frac{p^2}{2MT}} \tag{3.141}$$

such that

$$
< e^{\frac{it}{2m}(-2\hbar pq + q^2)} >_T \; = \; \int (\frac{1}{2\pi MT})^{\frac{3}{2}} e^{-\frac{p^2}{2MT}} e^{\frac{it}{2m}(-2\hbar pq + q^2)} d\vec{p} \tag{3.142}
$$

$$
= \; (\frac{1}{2\pi MT})^{\frac{3}{2}} \int e^{-\frac{1}{2MT}(p^2 + 2\hbar ipqTt + q^2 itT)} 2\pi p dp \tag{3.143}
$$

$$
= \; (\frac{1}{2\pi MT})^{\frac{3}{2}} (2mT) e^{-\frac{q^2}{2mT}(iTt - 4\hbar^2 T^2 t^2)} \tag{3.144}
$$

Returning to the Fourier transform in energy,

$$
S(q, \omega) \; = \; \frac{1}{2\pi} \int_{-\infty}^{\infty} dt e^{-i\epsilon t} e^{-\frac{q^2}{2m}(Tt^2 - it)} \tag{3.145}
$$

$$
= \; \frac{1}{2\pi} \int_{-\infty}^{\infty} dt e^{-\frac{q^2 T}{2A}(t^2 - \frac{2A}{q^2 T} it(\frac{q^2}{2A} - \epsilon))} \tag{3.146}
$$

$$
= \; \frac{1}{2\pi} \int_{-\infty}^{\infty} dt e^{-\frac{q^2 T}{2A}[(t - \frac{iA}{q^2 T}(\frac{q^2}{2A} - \epsilon))^2] + \frac{A^2}{q^4 T^2}(\frac{q^2}{2A} - \epsilon)^2} \tag{3.147}
$$

$$
= \; \frac{1}{2\pi} \sqrt{\frac{2A}{q^2 T}} e^{\frac{-q^2 T}{2A} \frac{A^2}{q^4 T^2}(\frac{q^2}{2A} - \epsilon)^2} \tag{3.148}
$$

where we have used the fact that the contribution from the imaginary path is zero.
Finally, we can write this in terms of the scattering law, where

$$
\alpha \; = \; \frac{q^2}{2AT} \tag{3.149}
$$

$$
\beta \; = \; -\frac{\epsilon}{T} \tag{3.150}
$$

$$
S(\alpha, \beta) \; = \; \frac{e^{-\beta}}{T} S(q, \epsilon) \tag{3.151}
$$

$$
S(\alpha, \beta) \; = \; \sqrt{\frac{A}{2\pi q^2 T}} \frac{e^{-\frac{1}{2}\beta}}{T} e^{\frac{(\alpha - \beta)^2}{4\alpha}} \tag{3.152}
$$

$$
S(\alpha, \beta) \; = \; \frac{1}{2\sqrt{\pi \alpha}} e^{-\frac{\alpha^2 + \beta^2}{4\alpha}} \tag{3.153}
$$

$$
\text{where } \frac{d^2\sigma}{d\Omega dE} \; = \; \sigma(E \to E', \mu) = \frac{4\pi a^2}{2kT} \sqrt{\frac{E'}{E}} S(\alpha, \beta) \tag{3.154}
$$

This result is important in thermalization work because it represents the scattering due to translational motion of any size molecule if there are no inelastic interactions with the neutron and if there are no interactions between the molecules of the ensemble. It was used by Wigner to determine the analytic solution of transport equation for neutrons in hydrogenous a proton gas [30]. It also satisfies detailed balance explicitly, so the solution to the transport equations will be guaranteed to return a Maxwellian when absorption is low.

3.10 Harmonic Crystal $S(q, \omega)$

A surprisingly general, and widely applicable scattering law can be determined from the analysis of the harmonic crystal $S(\alpha, \beta)$. In this context, we refer to a lattice of scattering sites, each bound to their respective site by a harmonic force, such that the solid may be viewed as a collection of excited harmonic oscillator states.

We begin with the scattering cross-section in the Van Hove formalism as

$$\sigma(E' \rightarrow E, \Omega' \rightarrow \Omega) = \frac{k}{k'} \int_{-\infty}^{\infty} e^{-\frac{i\beta t}{\hbar}} \sum_{i} \sum_{f} \rho_i |<f| \sum_{\nu} \vec{a_\nu} e^{i\vec{\kappa} \bullet \vec{r_\nu}} |i>|^2 \delta(\epsilon - W_f + W_i)$$

(3.155)

where $\vec{a_\nu}$ is the creation/annhilation operator acting along the unit vector of the excitation ν, and ρ_i is the statistical occupation probability of the initial state i. We have written this in terms of the final and initial states of the system, however we may also write the state of the system as a sum over harmonic oscillator states with $\vec{O} = \vec{a_\nu} e^{i\vec{\kappa} \bullet \vec{r_\nu}}$

$$\sigma = \frac{1}{2\pi\hbar} \frac{k}{k'} \sum_{i} \rho_i \int_{-\infty}^{\infty} e^{-\frac{i\beta t}{\hbar}} \sum_{\nu} \sum_{\nu'} \sum_{f} |<i|\vec{O_\nu}^\dagger|f><f|\vec{O_{\nu'}}^\dagger|i> e^{\frac{i(w_f - w_i)t}{\hbar}} dt$$

(3.156)

$$\sigma = \frac{1}{2\pi\hbar} \frac{k}{k'} \sum_i \rho_i \int_{-\infty}^{\infty} e^{-\frac{i\beta t}{\hbar}} \sum_\nu \sum_{\nu'} \sum_f | < i | \vec{a_\nu} e^{-i\vec{\kappa}\bullet r_\nu(0)} \vec{a_{\nu'}} e^{-i\vec{\kappa}\bullet r_\nu(t)} |^2 e^{\frac{i(w_f - w_i)t}{\hbar}} dt$$

(3.157)

$$\sigma = \frac{1}{2\pi\hbar} \frac{k}{k'} \sum_i \rho_i \int_{-\infty}^{\infty} e^{-\frac{i\beta t}{\hbar}} \sum_\nu \sum_{\nu'} Q_{\nu\nu'}(\kappa, t) dt \qquad (3.158)$$

where we define $Q_{\nu\nu'}(\kappa, t)$ as

$$Q_{\nu\nu'}(\kappa, t) = \sum_f | < i | \vec{a_\nu} e^{-i\vec{\kappa}\bullet r_\nu(0)} \vec{a_{\nu'}} e^{-i\vec{\kappa}\bullet r_\nu(t)} |i > |^2 e^{\frac{i(w_f - w_i)t}{\hbar}} dt \qquad (3.159)$$

We also see that, once again, we can at this point separate the expression into a coherent sum over $\nu \neq \nu'$, and an incoherent sum over $\nu' = \nu$. We assume that incoherence dominates in the *incoherent approximation*. We introduce harmonic oscillator position coordinates in terms of the ν scatter's position, $\vec{R_\nu}$, a time dependence, t, an excitation number, λ, and a time dependent displacement from $\vec{R_\nu}$, $\vec{q_\lambda}(t)$

$$\vec{r_\nu}(t) = \vec{R_\nu} + \sum_\lambda C_{\nu\lambda} \vec{q_\lambda}(t) \qquad (3.160)$$

where excitation λ has energy $\hbar\omega_\lambda$. $Q_{\nu\nu'}(\kappa, t)$ averaged over the ensemble is also referred to as the *intermediate scattering function*, χ, the Fourier transform of which gives $S(\alpha, \beta)$.

$$\chi_{\nu\nu'}(\kappa, t) = < Q_{\nu\nu'}(\kappa, t) >_T \quad = \quad < i | \vec{a_\nu} e^{-i\vec{\kappa}\bullet r_\nu(0)} \vec{a_{\nu'}} e^{-i\vec{\kappa}\bullet r_\nu(t)} |i >_T \qquad (3.161)$$

substituting the position coordinates, and moving to states summed over λ, we have

$$\chi_{\nu\nu'}(\kappa, t) = < n_\lambda | e^{-i\vec{\kappa}\bullet(\vec{R_\nu} - \vec{R_{\nu'}})} e^{-i\vec{\kappa}\bullet\sum_\lambda C_{\nu\lambda}\vec{q_\lambda}(0)} e^{i\vec{\kappa}\bullet\sum_\lambda C_{\nu'\lambda}\vec{q_\lambda}(t)} |n_\lambda >_T \qquad (3.162)$$

$$\chi_{\nu\nu'}(\kappa, t) = e^{-i\vec{\kappa}\bullet(\vec{R_\nu} - \vec{R_{\nu'}})}\Pi_\lambda < n_\lambda | e^{-i\vec{\kappa}\bullet C_{\nu\lambda}\vec{q}_\lambda(0)} e^{i\vec{\kappa}\bullet C_{\nu'\lambda}\vec{q}_\lambda(t)} | n_\lambda >_T \tag{3.163}$$

We introduce the harmonic oscillator position in term s of creation and annihilation operators, such that

$$H = \frac{1}{2M}(p^2 + M^2\omega^2 q^2) \tag{3.164}$$

$$q(t) = \frac{i}{\sqrt{2M\omega}}(a^\dagger(0)e^{-i\omega t} - a(0)e^{i\omega t}) \tag{3.165}$$

Two useful identifies for operators A and B for Equation 3.163 are

$$e^A e^B = e^{A+B+\frac{1}{2}[A,B]} \tag{3.166}$$

$$< i|e^{A+B}|i >_T = e^{\frac{1}{2}<i|(A+B)^2|i>_T} \tag{3.167}$$

which allows us to write the thermal average over the position operators, where Z_λ is the occupation probability of a state of energy $\hbar\omega_\lambda$

$$< n_\lambda | \ldots | n_\lambda > = e^{\frac{1}{2}[(\vec{\kappa}\bullet\vec{C_{\nu\lambda}})^2 + (\vec{\kappa}\bullet\vec{C_{\nu'\lambda}})^2]<n_\lambda|q_\lambda^2(0)|n_\lambda> + (\vec{\kappa}\bullet\vec{C_{\nu\lambda}})(\vec{\kappa}\bullet\vec{C_{\nu'\lambda}})<n_\lambda|q_\lambda(0)q_\lambda(t)|n_\lambda>}$$

$$\tag{3.168}$$

$$< n_\lambda | q_\lambda(0)^2 | n_\lambda > = \frac{1}{2\omega_\lambda}\frac{Z_\lambda + 1}{Z_\lambda - 1} \tag{3.169}$$

$$< n_\lambda | q_\lambda(0)q_\lambda(t) | n_\lambda > = \frac{1}{2M\omega}[< a^\dagger a >_T e^{i\omega t} + < aa^\dagger >_T e^{-i\omega t}] \tag{3.170}$$

$$= \frac{1}{2\omega_\lambda}(\frac{Z_\lambda}{Z_\lambda - 1}e^{i\omega t} + \frac{1}{Z_\lambda - 1}e^{-i\omega t}) \tag{3.171}$$

we substitute these relations into the expression for $\chi_{\nu\nu'}$ to find an expression for the

intermediate scattering function

$$\chi_{\nu\nu'} \quad = \quad e^{-i\vec{\kappa}\bullet(\vec{R}_\nu - \vec{R}_{\nu'})} e^{\sum_\lambda -\frac{1}{2}[(\vec{\kappa}\bullet\vec{C}_{\nu\lambda})^2 + (\vec{\kappa}\bullet\vec{C}_{\nu'\lambda})^2]\frac{1}{2\omega_\lambda}\coth(\frac{\omega_\lambda}{2T})} \tag{3.172}$$

$$\times e^{\sum_\lambda \vec{\kappa}\bullet\vec{C}_{\nu\lambda}\vec{\kappa}\bullet\vec{C}_{\nu'\lambda}\frac{1}{2\omega_\lambda}\frac{\cos(\omega_\lambda(t-\frac{i}{2T}))}{\sinh(\frac{\omega_\lambda}{2T})}} \tag{3.173}$$

$$\chi_{\nu\nu'} \quad = \quad e^{-\sum_\lambda \frac{1}{2}(\vec{\kappa}\bullet C_{\nu\lambda})^2 f(\omega_\lambda, T, t)} \tag{3.174}$$

$$\text{where} \quad f(\omega, T, t) = \frac{1}{\omega}\coth\frac{\omega}{2T} - \frac{\cos(\omega(t - \frac{i}{2T}))}{\sinh\frac{\omega}{2T}} \tag{3.175}$$

We approximate the summation over lattice sites by an integration over a frequency distribution, $g(\omega)$,

$$\sum_\lambda (\vec{\kappa}\bullet C_{\nu\lambda})^2 \rightarrow \kappa^2 \int_0^\infty d\omega g(\omega) \tag{3.176}$$

so the intermediate scattering function takes on the *gaussian representation*

$$\chi_{\nu\nu'} \quad = \quad e^{-\frac{1}{2}\kappa^2\Lambda(t)} \tag{3.177}$$

$$\text{where} \quad \Lambda(t + \frac{i}{2T}) = \int_0^\infty \frac{d\omega}{\omega}g(\omega)(\frac{1}{\omega}\coth\frac{\omega}{2T} - \frac{\cos(\omega t)}{\sinh\frac{\omega}{2T}}) \tag{3.178}$$

In a pure harmonic crystal, the density of states represents the density of phonon excitations, and is typically Debye-like. However, by a suitable choice of $g(\omega)$, we can reproduce a surprising variety of scattering behavior beyond the pure crystal. If we use $g(\omega) = \delta(\omega)$, we return the scattering law for free gas. If $g(\omega) = \frac{1}{A}\delta(\omega - \omega_o)$, we return the scattering from an Einstein crystal. We also note $e^{-\frac{1}{2}\kappa^2\Lambda(0)}$ is the Debye-Waller factor, which represents the diffuse scattering due to mean square displacement from equilibrium position in the crystal. Finally, Eglestaff has shown that if we employ a Gaussian centered at zero, we can represent the scattering from the diffusive behavior of liquids. Further, any sum of these expressions may be used to model the scattering system. In essence, we employ an *effective phonon frequency*

distribution to describe the scattering.

Some examples of frequency spectra [68] used to generate the ENDF-B cross-sections for our Monte Carlo work are shown in Figures 3.5 and 3.6. Figure 3.5 shows the frequency spectra of some typical ambient temperature reflector materials. Beryllium shows Debye-like behavior at low energy, tending to anharmonic effects at higher energy. Graphite has a set of phonon excitations extending over a broad range. Liquid water molecules tend to be localized by successive collisions with their neighbors, leading to an effective mean square displacement coupled to the harmonic and rotational excitations of the excitations within the molecule itself. Also of interest for comparison is Zirconium Hydride (ZrH), where light hydrogen atoms are bound to heavy zirconium sites in the lattice, leading to a close approximation of the Einstein Crystal. The acoustic and optical modes are separated in energy, but both show quadratic slopes leading into a discrete delta-function excitation.
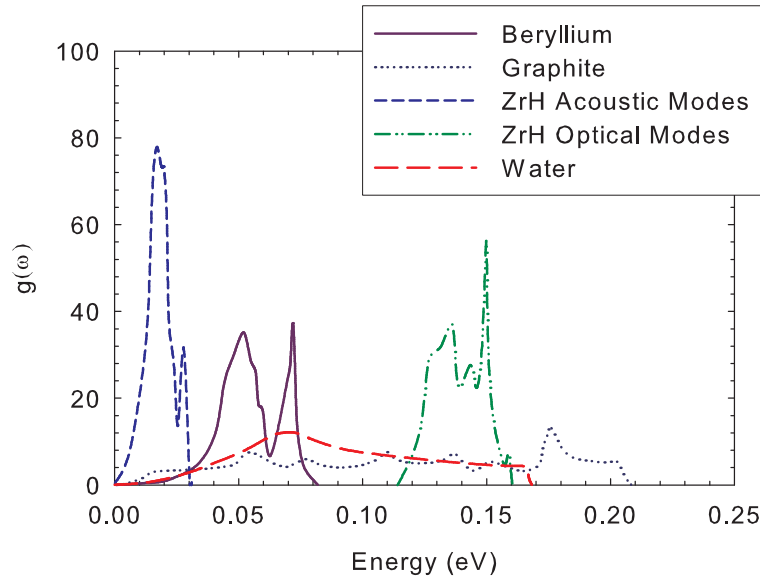
Figure 3.5: Reflector materials frequency spectra

Figure 3.6 show the frequency spectra of some cold moderator materials. Liq-

uid hydrogen and deuterium find prolific use in spallation and reactor source cold moderators. While the liquid does show similar shape to the water curve, the range of excitations is much lower, giving a high density of excitations in the range of cold neutron energies. Liquid methane is similar, apart form the inclusion of diffusive motions, which we note as $\rho(0) \neq 0$. Finally, solid methane shows Debye-like behavior at low energy, however the density of excitations at low energy is far greater than the liquid state.
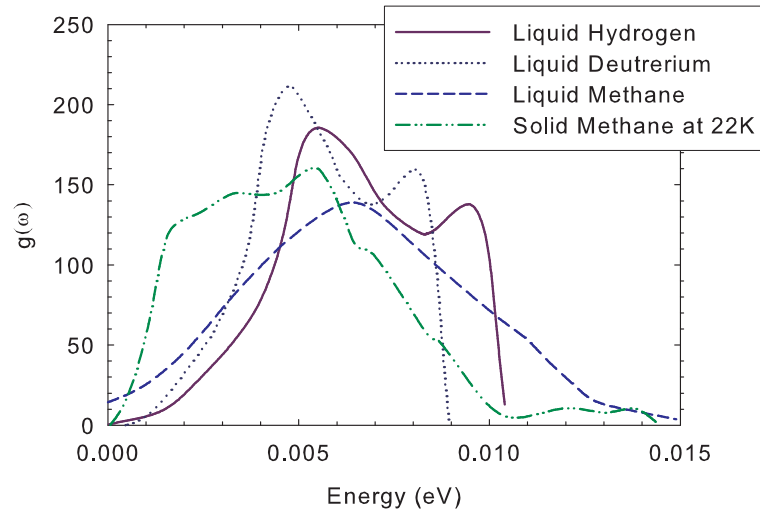
Figure 3.6: Cold moderator materials frequency spectra

Chapter 4

Transport

> The softest of stuff in the world
> Penetrates quickly the hardest;
> Insubstantial, it enters
> Where no room is.
>
> Lao Tzu
> *Tao Te Ching*

4.1   Boltzmann Equation

This chapter will explore how the energy spectra of neutrons are closely tied to the interactions in the medium. The integro-differential Boltzmann equation, familiar from kinetic theory [69], relates the flow of neutrons to the interactions that occur in the medium. In general, the neutron problem involves first understanding the interactions that occur, then solving for the Boltzmann equation for the neutron density to understand the neutron transport [30]. The Boltzmann equation is a balance equation of sources and sinks of neutron density. If we imagine a differential element of phase space, comprised of a box at $\vec{r}$ of infinitesimal phase space volume $d\vec{r}dEd\vec{\Omega}$, and consider all ways in which neutrons may enter or leave the box we have

the following set of terms, illustrated in Figure 4.1,

General Form

$$(\text{Rate of Change of Flux}) = (\text{Sources})\text{-}(\text{Sinks}) \tag{4.1}$$

Time Rate of Change Operator

$$\frac{d}{dt}N(\vec{r}, \vec{v}, t) = (\frac{1}{v}\frac{\partial}{\partial t} + \vec{\Omega} \bullet \vec{\nabla})\phi(\vec{r}, \vec{v}, t) \tag{4.2}$$

Sources - Inscatter

The rate of scattering into the box of phase space is the integral over all phase space that takes a neutron from an arbitrary point in momentum space to the box under consideration. This is an essential term, and complicates the solution of the Boltzmann equation tremendously as there is a wide range of dynamic interactions that take place for different energies and materials. The cross-section to scatter into the box is given generally over all space by $\Sigma(E' \to E, \vec{\Omega}' \to \vec{\Omega}, t)$

$$\int_0^\infty dE' \int d\vec{\Omega}' \Sigma(E' \to E, \vec{\Omega}' \to \vec{\Omega}, t)\phi(E', \vec{r'}, \vec{\Omega}', t) \tag{4.3}$$

Sources - Internal Sources

Reactions such as the fission reaction or the ^{9}Be(n,2n) produce neutrons. They are specified in terms of the reaction cross-section, Σ_{prod} and the mean number of neutrons created in the reaction, $f(E)$.

$$S_{internal}(E, \vec{r}, \vec{\Omega}, t) = \int_0^\infty dE\phi(E, \vec{r}, \vec{\Omega}, t)f(E)\Sigma_{prod}(E, t) \tag{4.4}$$

Sources - External Sources

A general time dependant external source of neutron flux is given by S

$$S(E, \vec{r}, \vec{\Omega}, t) \tag{4.5}$$

Sinks - Outscatter

Closely related to the inscatter term is the outscatter term, given by the sum over all reactions in the box of phase space that preserve the *existence* of the neutron, excluding fission. The outscatter cross-section is given by

$$\Sigma_s(E, \vec{\Omega}, t) = \int dE' \int d\vec{\Omega}' \Sigma(E' \rightarrow E, \vec{\Omega}' \rightarrow \vec{\Omega}, t) \tag{4.6}$$

$$\Sigma_s(E, \vec{\Omega}, t)\phi(E, \vec{\Omega}, t) \tag{4.7}$$

Sinks - Absorption

Finally, we group together the the reaction rate of all terms that destroy, or absorb, the neutron.

$$\Sigma_a(E, \vec{\Omega}, t)\phi(E, \vec{\Omega}, t) \tag{4.8}$$

Boltzmann Equation for Neutrons

The terms for rate of change, sources, and sinks are added together to form the transport equation. The role each term plays is indicated schematically in Figure

4.1.

$$
(\frac{1}{v}\frac{\partial}{\partial t} + \vec{\Omega} \bullet \vec{\nabla})\phi(\vec{r},\vec{v},t) + (\Sigma_s(E,\vec{\Omega},t) + \Sigma_a(E,\vec{\Omega},t))\phi(E,\vec{\Omega},t) =
$$
$$
\int_0^\infty dE' \int d\vec{\Omega}' \Sigma(E' \to E, \vec{\Omega}' \to \vec{\Omega}, t)\phi(E',\vec{r'},\vec{\Omega}',t) + S(E,\vec{r},\vec{\Omega},t)
$$

$$(4.9)$$
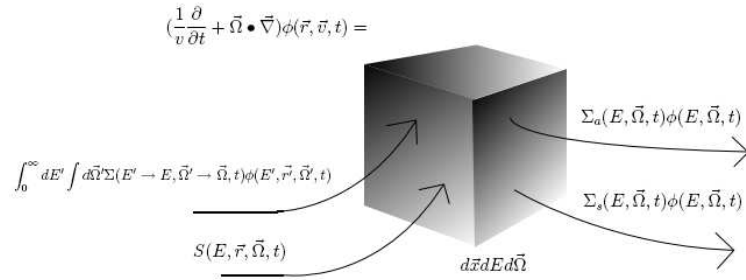
Figure 4.1: Illustration of the processes in transport

The conditions under which the Boltzmann equation is valid is are [70]:

1. At higher energy (much greater than chemical binding energies) neutron motion can be described in terms of well-defined collisions with independent nuclei

2. Neutron density is low such that interactions between free neutrons are neglected.

3. Particles travel is straight paths between collisions; Probability of collision per unit length is constant in bulk medium

4. The time required for an interaction to occur is short compared with all other transport processes

The requirement that the collisions be independent is challenged in the approach to equilibrium, when the target atoms are linked together by chemical bonds. A

thorough discussion of the validity of the Boltzmann equation for neutrons on a coarse grained phase space is found in Yip [71].

4.2 Non-relativistic Kinematics

The energy loss mechanism in slowing down is chiefly due to elastic scattering of neutrons from target nuclei in the moderator material. The >1 eV primary neutrons are of energies much greater than the thermal energy of the target atoms, and so the target atoms are considered to be at rest. In this case the neutron can only lose energy in a collision, as the neutron transfers a portion of its translational kinetic energy to the target atom via s-wave potential scattering. The energy of the neutron after
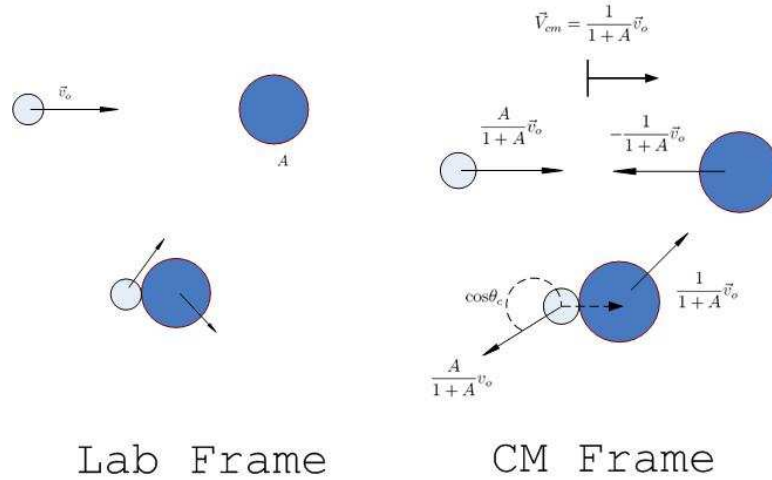
Figure 4.2: Elastic collision kinematics in the lab frame and CM frame. *Top: Before the collision Bottom:* After the collision.

a collision with the target atom is determined entirely by the scattering angle. In the center of mass (CM) frame the linear momentum is zero, and we consider elastic scattering such that the total kinetic energy is conserved. These 2 conservation laws are all we need to develop the scattering kernel for slowing down. Let us begin by first considering neutron (mass $A = 1$) with velocity $\vec{v}_o$ in the lab frame incident on

a target atom of mass A at rest in the lab frame, as shown in Figure 4.2. The center
of mass velocity, $\vec{V}_{cm}$, is

$$\vec{V}_{cm} = \frac{1}{1+A}\vec{v}_o \qquad (4.10)$$

Which in turn gives the center of mass velocity of the neutron before the collision,
$\vec{v}_n^c$

$$\vec{v}_n^c = \frac{A}{1+A}\vec{v}_o \qquad (4.11)$$

and the target, $\vec{v}_t^c$,

$$\vec{v}_t^c = -\frac{1}{1+A}\vec{v}_o \qquad (4.12)$$

In the CM frame the total linear momentum is zero, fixing the target velocity in
terms of the neutron velocity.

$$\vec{v}_t^c = -\frac{1}{A}\vec{v}_n^c \qquad (4.13)$$

After the collision, the velocities are $\vec{v}_n^{c\prime}$ and $\vec{v}_t^{c\prime}$, also related via Equation 4.13.
The momentum relation is inserted in the conservation of kinetic energy expression,
which allows us to write the final neutron energy in the center of mass in terms of
the initial neutron energy.

$$(v_n^c)^2 + A(v_t^c)^2 = (v_n^{c\prime})^2 + A(v_t^{c\prime})^2 \qquad (4.14)$$

$$\frac{A}{1+A}v_o^2 = (v_n^{c\prime})^2(1+\frac{1}{A}) \qquad (4.15)$$

$$(v_n^{c\prime})^2 = \frac{A}{1+A}v_o^2 \qquad (4.16)$$

Finally, we see that the outgoing neutron energy is uniquely related to the scattering angle through the transformation back to the lab frame.

$$\vec{v}_n^L = \vec{v}_n{}^c\prime + \vec{V}_{cm} \tag{4.17}$$

$$v_n^{L^2} = (v_n{}^c\prime)^2 + V_{cm}^2 + 2v_n{}^c\prime V_{cm}\cos\theta_c \tag{4.18}$$

$$(v_n^L/v_o)^2 = \frac{E}{E_o} = \frac{A^2 + A + 2A\cos\theta_c}{(1+A)^2} \tag{4.19}$$

where the scattering angle in the CM frame is θ_c. The center of mass scattering angle is related to the lab frame scattering angle as

$$\cos\theta_L = \frac{v_n\cos\theta_c + V_{cm}}{|\vec{v}_n + \vec{V}_{cm}|} \tag{4.20}$$

$$\cos\theta_L = \frac{v_n\cos\theta_c + V_{cm}}{\sqrt{v_n^2 + V_{cm}^2 + 2v_nV_{cm}\cos\theta_c}} \tag{4.21}$$

$$\cos\theta_L = \frac{A\cos\theta_c + 1}{\sqrt{A^2 + 1 + 2A\cos\theta_c}} \tag{4.22}$$

We note from Equation 4.19 that the neutron loses energy in the lab frame. In addition, for isotropic scattering there is an equiprobable range of energy loss. In the case of hydrogen, $A = 1$, the neutron has the ability to lose anywhere from none to all of its energy in a *single* collision. For $A \neq 1$, the energy loss range decreases in width as A increases. For hydrogen, $A = 1$, Eqns. 4.19 and 4.22 reduce to particulary pleasant set of expressions, which form the basis of a proton recoil method of fast neutron spectroscopy.

$$\cos\theta_L = \cos\frac{\theta_c}{2} \tag{4.23}$$

$$E = E_o\cos^2\frac{\theta_c}{2} = E_o\cos^2\theta_L \tag{4.24}$$

Isotropic scattering in the CM frame (which is accurate to better than 1% for

hydrogen [30, chap. 8.2]) allows us to average over all scattering angles to find the mean energy loss per collision. We write Equation 4.19 as

$$\frac{E'}{E} = \frac{1}{2}(1 + \alpha\prime) + \frac{1}{2}(1 - \alpha\prime)\cos\theta_c \tag{4.25}$$

where $\alpha\prime$ is $(\frac{A-1}{A+1})^2$. [1] We can determine the mean energy change by integrating Equation 4.19 over all possible exit angles, weighted by the probability that we scatter into a given angle and energy. For isotropic scattering, that probability is $\mathbb{P}(\theta_c) = \frac{1}{4\pi}$. The mean fraction of energy lost per collision, $\zeta = < \frac{E}{E_o} >$, is given by

$$\zeta = \int \sin\theta_c d\theta_c \int d\phi \mathbb{P}(\theta_c)\frac{E}{E_o}(\theta_c) \tag{4.26}$$

$$\zeta = \int \sin\theta_c d\theta_c \int d\phi \frac{[\frac{1}{2}(1 + \alpha\prime) + \frac{1}{2}(1 - \alpha\prime)\cos\theta_c]}{4\pi} \tag{4.27}$$

$$\zeta = \frac{1}{2}(1 + \alpha\prime) \tag{4.28}$$

It is appropriate at this point to introduce the unit of *lethargy*, u, defined as:

$$u = \ln(\frac{E_o}{E}) \tag{4.29}$$

such that

$$\phi(E)|\frac{dE}{du}| = \phi(u) \rightarrow E\phi(E) = \phi(u) \tag{4.30}$$

where E_o is an arbitrary reference energy. Lethargy is a more compact unit for expressing energy because of the wide range of energy spanned in neutron slowing

---

[1]There is an unfortunate collision in reactor physics nomenclature for α. Here it is a factor related to the difference between the mass of the neutron and the target atom,$(\frac{A-1}{A+1})^2$. In Chapter 3, α is the dimensionless momentum transfer, $\frac{q^2}{2Ak_bT}$. Further still, α is used as the leakage parameter of the $\frac{1}{E}$ component of the flux in Section 4.4. Thus, we will employ the somewhat nonstandard nomenclature of $\alpha\prime$ to represent $(\frac{A-1}{A+1})^2$ throughout this chapter.

down. We can express lethargy change in terms of energy as:

$$\frac{E'}{E} = e^{u-u'} \tag{4.31}$$

We note that lethargy change varies between 1 and $\alpha\prime$, giving the range of lethargy change as $1 - \alpha\prime$.

As we solve for the energy spectrum of the slowing down flux in the next section, the probability a collision transfers the neutron from lethargy u' to lethargy u is will be useful. This is the scattering kernel for slowing down,

$$\Sigma(u' \to u) = \frac{\Sigma_s(u')e^{u'-u}}{1 - \alpha\prime} \text{ for } u - \ln\frac{1}{\alpha\prime} \le u' \le u \tag{4.32}$$

$$\text{else } 0 \tag{4.33}$$

which is non-zero only in the range of kinematically allowed lethargy change. This is the scattering kernel for slowing down. For hydrogen, scattering to zero energy is theoretically possible in a single collision, and Σ becomes

$$\Sigma(u' \to u) = \Sigma_s(u')e^{u'-u} \text{ for } -\infty \le u' \le u \tag{4.34}$$

4.3   Energy Distribution of Slowing Down Flux

We are now in a position to use the results of the kinematical analysis in the transport equation to determine the energy spectrum of slowing down flux. The transport equation of a homogenous hydrogen medium with a steady state source is:

$$[\Sigma_s(u) + \Sigma_a(u)]\phi(u) = \int_{-\infty}^{u} du'\Sigma_s(u')e^{u'-u}\phi(u') + S(u) \tag{4.35}$$

We assume elastic scattering and absorption dominate the transport, so the total cross-section is $\Sigma(u) = \Sigma_s(u) + \Sigma_a(u)$. The *collision density* is the number of collisions per unit volume per unit time, expressed as $\Phi(u) = \Sigma(u)\phi(u)$, We define the *slowing down density*, $q(u)$, as the number of neutrons slowed lower than lethargy u per unit time.

$$q(u) = \int_{-\infty}^{u} du' \Sigma_s(u') e^{u'-u} \phi(u') \tag{4.36}$$

We can express the transport equation in terms of the slowing down and collision densities quite simply as:

$$\Phi(u) = q(u) + S(u) \tag{4.37}$$

Differentiation of the slowing down expression gives

$$\frac{d}{du} q(u) = e^{-u} \frac{d}{du}[\mathbb{Q}(u) - \mathbb{Q}(-\infty)] - e^{-u} \int_{-\infty}^{u} du' \Sigma(u') e^{u-u'} \phi(u') \tag{4.38}$$

where $\mathbb{Q}(u) = \int du \Sigma(u) e^u \phi(u)$. Thus, the differentiation becomes:

$$\frac{d}{du} q(u) + q(u) = \Sigma_s(u)\phi(u) \tag{4.39}$$

Similarly, if we differentiate the transport equation,

$$\frac{d\Phi(u)}{du} = \frac{dq(u)}{du} + \frac{dS(u)}{du} \tag{4.40}$$

Our goal now is to eliminate the slowing down expression in favor of a single differential equation in flux as a function of lethargy. Substitute for $\frac{dq}{du}$ in the differentiated transport equation.

$$\frac{d\Phi(u)}{du} = c(u)\Phi(u) - q(u) + \frac{dS(u)}{du} \tag{4.41}$$

where $c(u) = \frac{\Sigma_s(u)}{\Sigma(u)}$. Next, eliminate $q_{(}u)$ by rearranging the transport equation and substituting:

$$\frac{d\Phi(u)}{du} = c(u)\Phi(u) - (\Phi(u) - S(u)) + \frac{dS(u)}{ds} \tag{4.42}$$

$$y(u) = \Phi(u) - S(u) \tag{4.43}$$

$$\frac{dy(u)}{du} + (1 - c(u))y(u) = c(u)S(u) \tag{4.44}$$

which is a differential equation solved by means of integrating factor to give a general relation for flux as a function of slowing down for any source or Σ.

$$\Phi(u) = S(u) + \int_{\infty}^{u} S(u')c(u')e^{\int_{u'}^{u}[1-c(u'')du'']}du' \tag{4.45}$$

A conventional situation in the case of hydrogen is one where elastic scattering is constant in energy $(\Sigma_s(E) = \Sigma_s)$, capture goes as $\frac{1}{v}$, and the source is a delta function, $S(u) = Q\delta(u)$:

$$\Sigma_s(v) = \Sigma_s \tag{4.46}$$

$$\Sigma_a(v) = \Sigma_{ao}\frac{v_o}{v} \tag{4.47}$$

In this case, we may evaluate Eqn 4.45 directly, seeking a solution for all $u \neq 0$.

$$\Phi(u) = Qc(0)e^{\int_0^u[1-c(u'')]}du'' \tag{4.48}$$

$$\Phi(u) = Qc(0)e^{\int_0^u \frac{\Sigma_a(u)}{\Sigma_a(u)+\Sigma_s(u)}}du'' \tag{4.49}$$

Focusing on the integral term,

$$\int_0^u \frac{\Sigma_a(u)}{\Sigma_a(u) + \Sigma_s(u)} du'' = \tag{4.50}$$

$$\int_{v_o}^v \frac{\Sigma_{ao}\frac{v_o}{v}}{\Sigma_{ao}\frac{v_o}{v} + \Sigma_s}|\frac{du}{dv}|dv = \tag{4.51}$$

$$2\ln(\frac{v(\Sigma_s + \Sigma_{ao})}{\Sigma_s v + \Sigma_{ao}v_o}) \tag{4.52}$$

This yields the solution for slowing down flux in hydrogen with $\frac{1}{v}$ capture. This is generally valid from 1 eV to 10 keV.

$$\Phi(u) = Qc(0)e^{2\ln(\frac{v(\Sigma_s+\Sigma_{ao})}{\Sigma_s v+\Sigma_{ao}v_o})} \tag{4.53}$$

$$\Phi(u) = Qc(0)(\frac{v(\Sigma_s + \Sigma_{ao})}{\Sigma_s v + \Sigma_{ao}v_o})^2 \tag{4.54}$$

$$\phi(u) = \frac{Q\Sigma_s v^3(\Sigma_s + \Sigma_a)}{(\Sigma_s v + \Sigma_a v_o)^3} \tag{4.55}$$

A very important result is revealed for $\Sigma_a \rightarrow 0$. As absorption is small compared to elastic scattering, the flux tends to a $1/E$ distribution.

$$\text{Lim}_{\Sigma_a \rightarrow 0}\phi(u) = \frac{Q}{\Sigma_s} \tag{4.56}$$

$$\phi(E) = \frac{Q}{\Sigma_s E} \tag{4.57}$$

4.4 Approach to Equilibrium

The above method makes several assumptions about the hydrogen cross-section, shown in Figures 4.3. The assumption that Σ_s is constant in energy and capture goes as $1/v$ are well satisfied on the range from 1 eV to 10 keV. Outside this range, the scattering cross-section becomes more complicated. At high energy, s-wave scattering may no longer dominate such that the elastic scattering is no longer isotropic in the

lab frame. At low energy the energy loss mechanism is no longer dominated by collisions with a target atom at rest and free to recoil as collective motions of the target atoms become important.
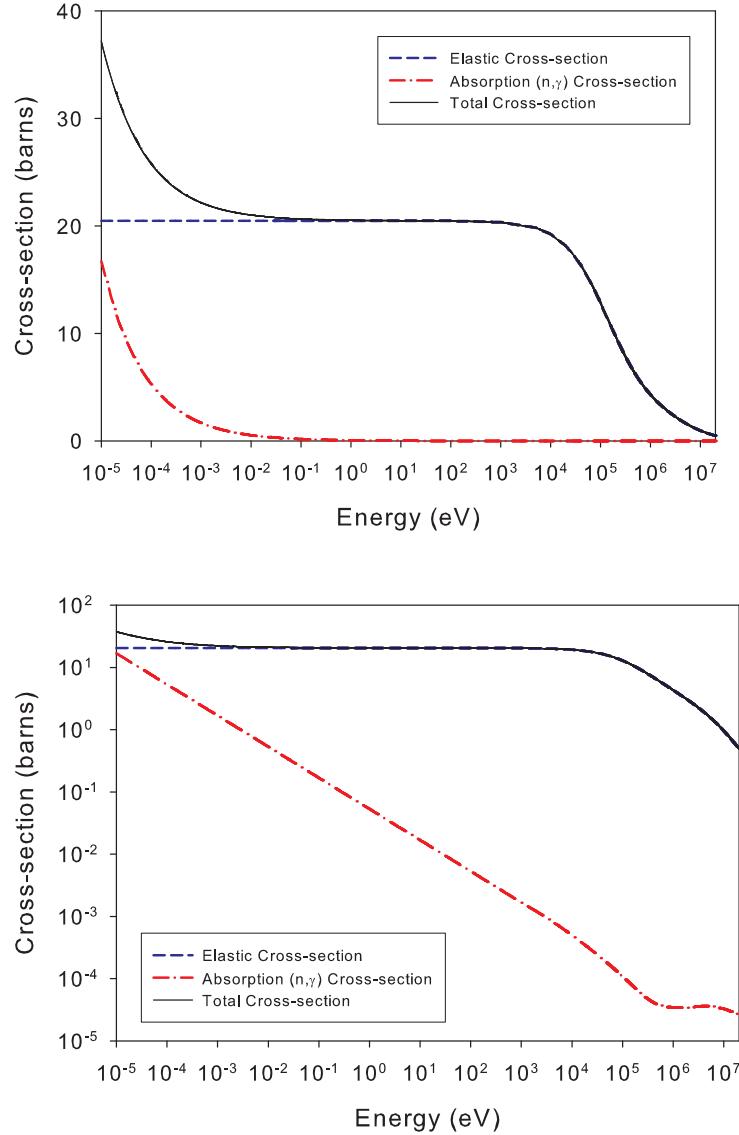

Figure 4.3: Top: Hydrogen total cross-section linear scale, **Bottom:** Hydrogen total cross-section logarithmic scale. Note the dominance of elastic scattering over absorption at higher energies.

As can be seen in Figure 2.2, the ranges over which thermalized flux, slowing down flux, and production flux are defined are related to the dominating physics,

however the relationship is not precise. The production flux mixes with the slowing down flux, though these neutron groups are easily distinguished mathematically (although neutrons themselves are indistinguishable!) as a source term (no collisions have occurred since the neutron was "born" into the system) and a term undergoing collisions where energy can only be lost. We have evaluated this second case to give the $1/E$ form of slowing down flux.

The slowing down flux does not necessarily sharply cutoff and the $1/E$ form by itself does not follow the physical boundary condition that $\phi(E)$ is not infinite as $E \to 0$. For low absorption, the slowing down flux overlaps the Maxwellian at ~ 100 meV region before attenuating strongly with decreasing energy (see Figure 2.2). The Maxwellian term originates from the neutrons that are as likely to gain energy from a collision as they are to lose it, where as slowing down neutrons can only lose energy in a collision, assuming most of the atoms are free to recoil. Thus, the number of atoms which the neutron can collide with such that $v_{target} \ll v_{neutron}$ reduces as the neutron energy tends to thermal energies. The form for the slowing down flux can be shown for $A \neq 1$ to be proportional to $\frac{1}{1+\frac{k_b T}{E}}$ near the Maxwellian mean energy [30].

Analytic solutions to the transport equation become excessively cumbersome to elucidate the physics as the constant Σ_s condition is relaxed in favor of more realistic cross-sections, but slowing down in atomic hydrogen gas can be solved numerically. The cross-section for an atomic hydrogen gas is calculated from free gas $S(\alpha, \beta)$ to be:

$$
\begin{aligned}
\Sigma(E' \to E) &= \frac{\Sigma_s}{E'} e^{\varepsilon' - \varepsilon} \mathrm{erf}\sqrt{\varepsilon'} \quad \text{for } \varepsilon > \varepsilon' \\
\Sigma(E' \to E) &= \frac{\Sigma_s}{E'} \mathrm{erf}\sqrt{\varepsilon'} \qquad \text{for } \varepsilon < \varepsilon'
\end{aligned}
\tag{4.58}
$$

where $\varepsilon = (E' - E)/k_b T$ represents the energy exchange in units of thermal energy [30, Chap. 3]. The reduced transport equation, Equation 4.59 is then a Fredholm Equation of the first kind, solvable by a matrix inversion numerical procedure [72].

$$[\Sigma_a(E) + \Sigma_s(E)]\phi(E) = \int_0^\infty dE'\Sigma(E' \to E)\phi(E') + S(E) \qquad (4.59)$$

$$\bar{\Sigma}_{ij} = \int_{E_j}^{E_i} dE\Sigma(E_i \to E_j) \qquad (4.60)$$

$$\Sigma_i\phi_i = \bar{\Sigma}_{ij}\phi_j + S_i \qquad (4.61)$$

The transition matrix $\bar{\Sigma}_s$ can be inverted to yield the results shown in Figure 4.4. The flux tends to a maxwellian at low energy, but there is a transition region between $1/E$ and Maxwellian behavior. In experimental results, this intermediate region is treated using the "effective temperature" model [30], which approximates the neutron flux by a Maxwellian plus a slowing down term multiplied by a "joining function", $\Delta(E)$.

$$\phi(E) = \phi_{thermal}(E) + \phi_{slowing}(E) \qquad (4.62)$$

$$\phi_{thermal}(E) = N_o\frac{E}{E_o^2}e^{-\frac{E}{E_o}} \qquad (4.63)$$

$$\phi_{slowing}(E) = \frac{N_s}{E^{1+\alpha}}\Delta(E) \qquad (4.64)$$

where $E_o = k_bT_{eff}$ is the *effective temperature* of the thermalized neutron flux. It will be slightly warmer that the surroundings due to the preferential absorption of the low energy neutron flux, and preferential leakage of high energy flux. If the medium is finite, α can be greater than the analytic solution because the neutrons have not collided enough times before escaping to reach the lowest energies. Thus, α is termed the "leakage parameter".

An interesting place the leakage parameter finds application is in planetary

geoscience. Spallation neutrons produced by cosmic radiation incident on the moon's surface produces a source of leakage neutrons. An orbiting satellite can detect these neutrons, and relate the neutron flux intensity to the average atomic number of the lunar soil below the satellite [73].

At the transition between the Maxwellian and the slowing down flux, an asymptotic analytic solution to the transport equation [30] valid across this range, but not as $E \to 0$ is

$$\phi_{slowing}(E) \quad = \quad N_s \frac{1}{E - 2kT} \text{ asymptotic solution for } E \to large \quad (4.65)$$

To be physically realistic, the joining function must physically satisfy the conditions that $\Delta(E) \to 0$ as $E \to 0$ and $\Delta(E) \to$ constant as $E \gg kT$. Several workers have developed successful forms for $\Delta(E)$

$$\Delta_{Wescott}(E) \quad = \quad \frac{1}{1 + (E/E')^7} \quad (4.66)$$

$$\Delta_{Carpenter}(E) \quad = \quad \frac{1}{1 + e^{-\frac{\lambda - \lambda_o}{\lambda_1}}} = \frac{1}{1 + e^{\frac{a}{\sqrt{E}} + b}} \quad (4.67)$$

Wescott initially used the very sharp cutoff $\Delta_{Wescott}$ as a for the joining function to tabulate integral contributions of epithermal flux to foil activation experiments at reactors [74, 75]. Carpenter and coworkers found greater success in fitting high resolution neutron TOF spectra for pulsed sources with a more pliable equation, due to Taylor [76], which allows for a shallower cutoff. At LENS, we will employ the form of Carpenter for the joining function.

For completeness, it is also important to mention the results of Wigner and Wilkens [30] on this topic. While the above exact solution has been solved numerically in Figure 4.4, it has also been solved in a functional form. The results clearly
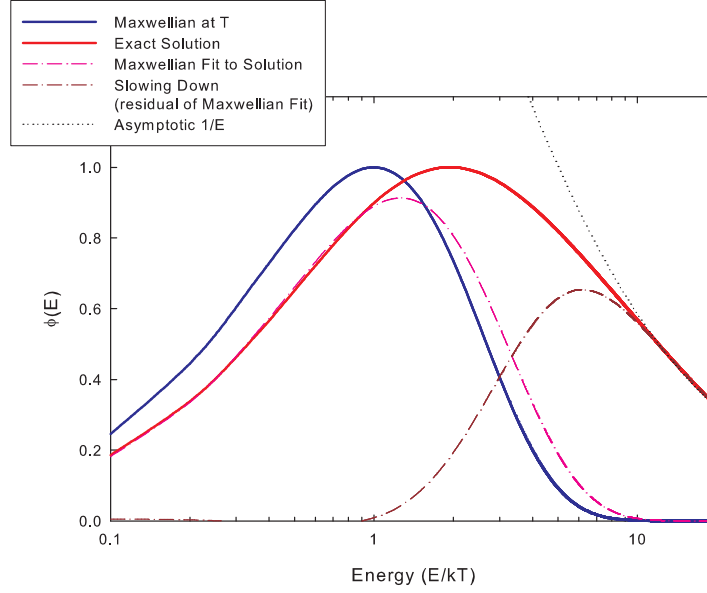
Figure 4.4: Exact numerical solution to proton gas, $\frac{1}{v}$ absorption ($\frac{\Sigma_a}{\Sigma_f} = 0.2$)

display the role played by absorption, where we define $\Gamma = \frac{\Sigma_a}{\Sigma_f}$ and we employ a dimensionless velocity variable $x = \frac{v}{\sqrt{2kT}}$. There are 2 solutions for the neutron density:

$$N_1(x) \sim \frac{1}{x^2} \frac{e^{-2\Gamma/x}}{1 + \Gamma/x} \tag{4.68}$$

$$N_2(x) \sim x^2 \frac{e^{-x^2 + 2\Gamma/x}}{1 + \Gamma/x} \tag{4.69}$$

where N_1 describes large x and N_2 describes small x. N_2 is a Maxwellian shifted to higher effective temperatures by absorption.

Another important issue is wether or not the neutron beam is *well thermalized*, meaning the neutrons have come to a complete equilibrium with their homogenous surroundings. In all that has come previously, we have assumed that this is the case. In pulsed accelerator sources the preferential leakage of high energy flux leads to spectra that are appreciably hardened compared to spectra in the medium. In the case where there is a sharp temperature discontinuity, such as the interface

between cold moderator and reflector, the solution will be a sum of 2 Maxwellians at temperatures on the order of the medium temperatures. A 2 Maxwellian solution that overlaps in space is also a better fit to solutions inside a moderating medium [77]. Because the LENS moderator is thin, we expect some transmission and leakage of both thermal and cold neutron energies to be significant, leading to a similar 2 Maxwellian solution when a cold moderator is employed. Thus, the flux at sample positions in the LENS beam lines is to be described by a 2 Maxwellian form, with a joining function that tends to a constant at high energy

$$\phi(E) = N_1 \frac{E}{E_1^2} e^{-\frac{E}{E_1}} + N_2 \frac{E}{E_2^2} e^{-\frac{E}{E_2}} + \frac{N_s}{1 + e^{\frac{a}{\sqrt{E}} + b}} \frac{1}{E^{1+\alpha}} \qquad (4.70)$$

or, in terms of lethargy flux

$$\phi(u) = E\phi(E) = N_1 (\frac{E}{E_1})^2 e^{-\frac{E}{E_1}} + N_2 (\frac{E}{E_2})^2 e^{-\frac{E}{E_2}} + \frac{N_s E^{-\alpha}}{1 + e^{\frac{a}{\sqrt{E}} + b}} \qquad (4.71)$$

4.5 Conclusion

We have reviewed the definitions of flux, current, cross-section, and scattering kernel. We have employed these descriptions of interactions and neutron flow into the transport equation to derive the essential description of the flux from high energy to low energy. We found that the primary neutrons will assume a distribution characteristic of the source, but will then slow down, giving an energy spectrum that varies as $1/E$. As equilibrium is reached with a moderator, we demonstrated that the flux must assume a Maxwellian, although at a higher temperature than the medium due to leakage and absorption. Finally, we demonstrated the essential description of a cutoff function between slowing down and equilibrium behavior.

In the next section, we will employ Monte Carlo techniques to determine an

optimized configuration of a neutron source for the production of cold neutrons from a high energy primary neutron source. Beyond the design and construction of this configuration, we will describe measurements of the performance of the system as constructed.

Chapter 5

Methods in the Design of LENS

> The White Rabbit put on his spectacles. "Where shall I begin, please your Majesty?" he asked.
>
> "Begin at the beginning," the King said gravely, "and go on till you come to the end: then stop."
>
> Lewis Carroll
> Alice in Wonderland

5.1 Introduction

The design of the LENS source began as early as 2003, and continued over an intense design and development schedule leading to a working prototype neutron source in 2004. This chapter will describe the Monte Carlo methods used to optimize the configuration of the LENS production target, neutron reflector, cold moderator, shielding, and beam lines.

The objectives of the Monte Carlo neutronic design analysis are:

- High yield of cold neutrons for experiments

- Low moderator temperatures ($\leq$10K)

- High yield of primary neutrons with low activation hazard

- Impulse neutron response that is comparable to, or shorter than, the proposed proton pulse width of 1 ms or less

The design discussion progresses somewhat chronologically, reflecting the order in which optimizations were made, beginning with considerations of moderator material and coupling energy, which lead into discussions of target and reflector geometry relative to the moderator, and we end with a discussion of shielding calculations and neutronic performance of the *as built* configuration.

5.1.1 The Monte Carlo Method

A precise definition of the Monte Carlo method is elusive, as it encompasses a wide variety of approaches to problem solving in physics. A brief and general definition might simply be that any method of problem solving that relies on random numbers or random events to arrive at a solution is a Monte Carlo method. Monte Carlo methods have a rich and varied history; as early as 1777 Monte Carlo methods have been used to determine π. French naturalist Georges Buffon dropped a needle on paper (a random event) with parallel lines on it, counting the fraction of times the needle crossed a line. If the width of the lines are as wide as the length of the needle, the probability the needle crosses a line is $2/\pi$.

Our goal is far more complicated. We seek to determine the transport of neutron and gamma radiation (and others forms as necessary) in an arbitrary geometry. Presuming the geometry or cross-sections are far too complicated to attempt an analytic solution, we could solve for the transport either by deterministic or Monte Carlo methods. Deterministic methods would rely on dividing the geometry into small regions (discrete ordinates) and solving for the *average* integro-differential

transport in each region. As the regions get progressively smaller, a more exact solution is approximated across the whole geometry [78, 1-2]. Monte Carlo methods calculate the value of specific quantities over a specific region of phase space, and as such are solutions to the integral transport equation even though no transport equations are necessary. In a neutron Monte Carlo simulation each particle follows an independent random path through the geometry, and we simply count, or *tally*, how many times a particle enters the region of phase space of interest to determine the value of the flux integrated over the region. This is particularly well suited to design problems, where we seek to investigate the impact of changes in the geometry to specific regions of phase space.

An important distinction must be made in this work between *precision* and *accuracy*. The precision of a Monte Carlo is related only to the number of trials - the more trials run the better the probability of the event's occurrence is known. Results generally follow Poission statistics for Monte Carlo, such that the statistical error of the tally is related to the population of Monte Carlo tracks in the region as $\frac{1}{\sqrt{N}}$, where N is the number of tracks. The accuracy of the Monte Carlo is only as good as the input - if the cross-sections, geometry, or methods of calculating neutron trajectory are inaccurate so may be the result. Thus, it is possible to have a very precise but inaccurate answer if one is not cautious. The stability of the result and its associated statistical variance is referred to as *convergence*. Convergence means that the change in the value of a calculated quantity is small as more trials are run. In all our Monte Carlo work, we seek accuracy, precision, and a high degree of convergence. We will comment on this only when it proves difficult to achieve one of these 3 vital factors of a Monte Carlo simulation.

5.1.2 MCNP

The primary software used to perform the Monte Carlo is MCNP (Monte Carlo N-Particle). MCNP evolved out of the need to simulate neutral radiation transport in the Manhattan Project into a modern workhorse in all manner of radiation transport applications. The code is developed and maintained by at Los Alamos National Laboratory with export control provided by the RSICC at Oak Ridge National Laboratory. There are 2 similar, but competing versions of the code; MCNP, which simulates neutron, gamma, and electron transport up to 150 MeV; and MCNPX, which augments MCNP's capabilities by the addition of physics models for GeV processes and has the ability to simulate many more types of charged particles and secondary particles. MCNP5 is used for most work presented in this dissertation although in general we have not seen any great discrepancy when comparing results from the two codes. VISED for windows is used for all geometry visualizations.

5.1.3 Computing Resources

Simulations were run on a variety of systems, including 2 and 3 GHZ desktop PC's running Windows XP, the IU RS/6000 supercomputer using MPI on an AIX operating system, and latest on the IU AVDD-0 parallel machine, using MPI over a UNIX operating system. An installation is currently in development on the newest IU machine, Big Red. Apart from the tremendous advancements in the number of Monte Carlo particles run on the MPI machines versus the local desktop PC's, we have not seen variations in results that would lead us to suspect the individual installation of MCNP/X is a serious issue. However, it is notable that over factor of 100 enhancements in computational speed were achieved on the MPI systems. As new versions of MCNP are released, and IU computing resources expanded, we also expanded our simulation abilities to match. Table 5.1 shows the various systems and

versions of the code employed in the design efforts.

Table 5.1: Computing systems employed in design work.

System	Type	OS	Installation	Dates
2 GHZ	PC	WindowsXP	MCNP4C2, MCNPX 2.5 Beta	2002-2005
3 GHZ	PC	WindowsXP	MCNP5, MCNPX	2006
LIBRA Cluster	>80 CPU IBM RS/6000	IBM AIX w/MPI	MCNP4c2	2004-2005
AVIDD-O	>250 CPU in three different types of systems	UNIX w/ MPICH	MCNP5, MCNPX 2.5	2005-2006
Big Red (in development)	> 1000 cpu	UNIX	MCNP5	2007

5.2 Proton Delivery System

Neutron production at LENS truly begins with the accelerator. The LENS project employs the existing Accsys PL-7 Radiofreqency Qudrupole/Drift Tube Linac (RFQ/DTL) [79, 80], recovered from the preaccelerator to the cooler injector synchrotron at IUCF [81]. The accelerator was refurbished for high current and high duty factor operation, which included rotating the vanes by 90 degrees to switch from accelerating H^- to H^+, and increasing the water cooling of the system to handle 6 kW [82]. The initial operating energy for LENS remains at 7 MeV.

The proton injector ion source (PIJ) creates a high current H^+ beam for acceleration in the PL-7. The PIJ uses 1.2 kW of 2.45 GHZ microwave energy [82] generated by a magnetron to ionize hydrogen gas in a vacuum chamber. The plasma is confined by magnetic fields and extracted electrostatically. The resulting 22 mA of 25 keV protons is well matched by beam optics to the acceptance of the RFQ.

The proton beam from the ion source is pulsed (providing the pulsed neutron beam) by turning on the RFQ amplifiers after the ion source pulse has come to full current. The rise time of the proton pulse is about 3 μs, and maximum pulse width is 300 μs. Maximum pulse width is limited by the 12 425 MHZ tube amplifiers used to power the RFQ. The klystron upgrade program for the amplifiers intends to reduce the rise time to $\sim$ 1 ms, and extend the maximum pulse width to $\sim$ 700 μs in the very near future. Pulse width in the new system will be limited by the AC power available to the klystrons.
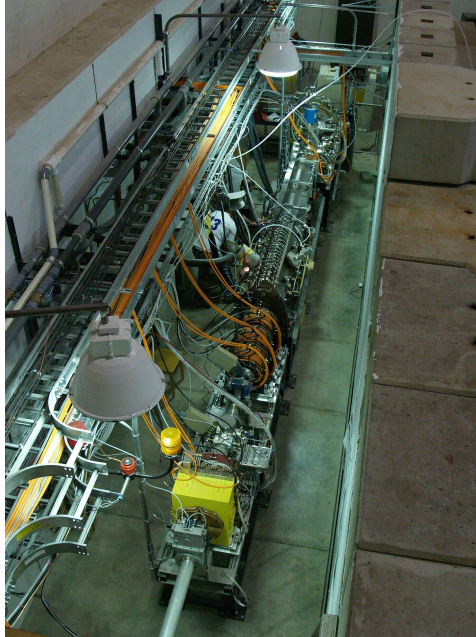
Figure 5.1: Image of LENS Accelerator PL-7 RQF/DTL. Taken by H.O. Meyer.

The RFQ/DTL is a commercial accelerator capable of accelerating protons or deuterons up to 7 MeV, and with additional DTLs, up to higher energies. Over the next year, a new DTL will be added to increase proton energy to 13 MeV and the addition of klystrons will increase the peak proton current to >20 mA from the present $\sim$7 mA. To avoid target activation via the ^{9}Be(p,t)^{7}Be reaction, the upgrade to full power operation will be restricted to 13 MeV, thus neutronic optimizations

focus on 13 MeV power levels.

Target thermal stress during the higher power operation will pose a significant issue, which is addressed by the proton transport beam line. The proton beam will be spread relatively uniform over the face of the target to ~50 cm^2 by 2 octupole magnets to reduce the point heating of the target. The proton beam line has 2 bends to keep backstreaming neutrons from the target out of line of sight of the accelerator to reduce fast neutron activation.

Present performance has ranged from 7-10 mA peak current at 15-30 Hz and 50-250 μs pulse width, with nominal conditions for experiments in this dissertation are 150 μs, ~7 mA, 15 Hz. The upgrade path for the accelerator calls for klystron installation to be complete by end of 2006, and 13 MeV upgrade complete by end of 2007. Final operating conditions will be 13 MeV protons with 50 mA peak current at 0.024 duty factor. For a beryllium target, these upgrades would represent a factor ~300 increase in the time average neutron flux produced in the target over the present nominal conditions.

5.3   Production Target

5.3.1   Production Targets Considered

The selection of neutron production target begins with consideration of the available data on neutron production. Higher energy beams ($E > 100$ MeV) generally have higher neutron yields per proton, as shown in Figure 5.2. However, the high energy neutrons associated with higher energy particle beam energies are generally at odds with the project goal of limited activation. The lower energy RFQ/DTL was identified for use in the project, so we focused our attentions on lower energy proton or deuteron for primary neutron production.
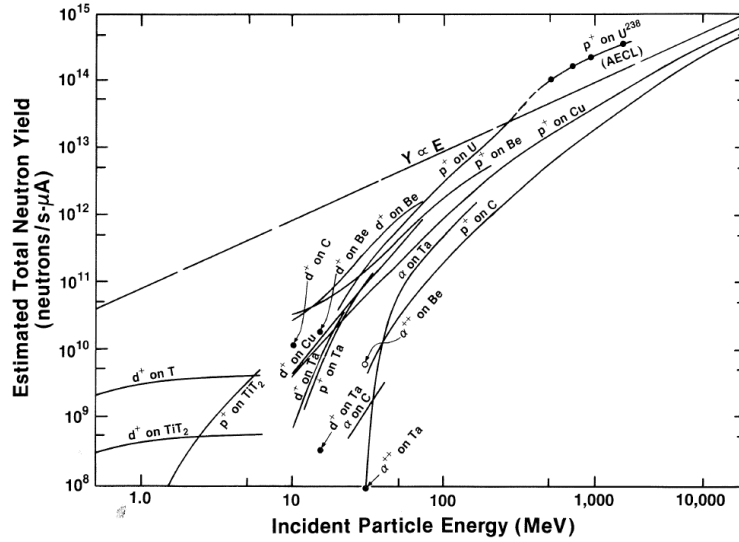
Figure 5.2: Neutron production from high energy charged particle beams. From [83]

.

Figure 5.3 shows neutron production from various lower energy particle beams on various targets. In the range of energies accessible to the RFQ/DTL, the ^{7}Li(p,n) reaction has the highest neutron yield, followed by the ^{9}Be(d,n), and then the ^{9}Be(p,n). However, as we have discussed, issues of target shock and technical considerations of accelerator capabilities complicate the selection of target material beyond simple considerations of yield. To assess the impact of material properties, a comparison of material properties and yields of lithium and beryllium targets are shown in Table 5.2.

5.3.2 Choosing Beryllium for the Target

Beryllium was chosen as the target material after comparing lithium and beryllium as potential targets for LENS. There are multiple considerations, including a desire balance high yield against keeping the penetrating high energy neutron and gamma radiation modest and a desire to avoid complicated target engineering if possible, while maintaining the high neutron yield.
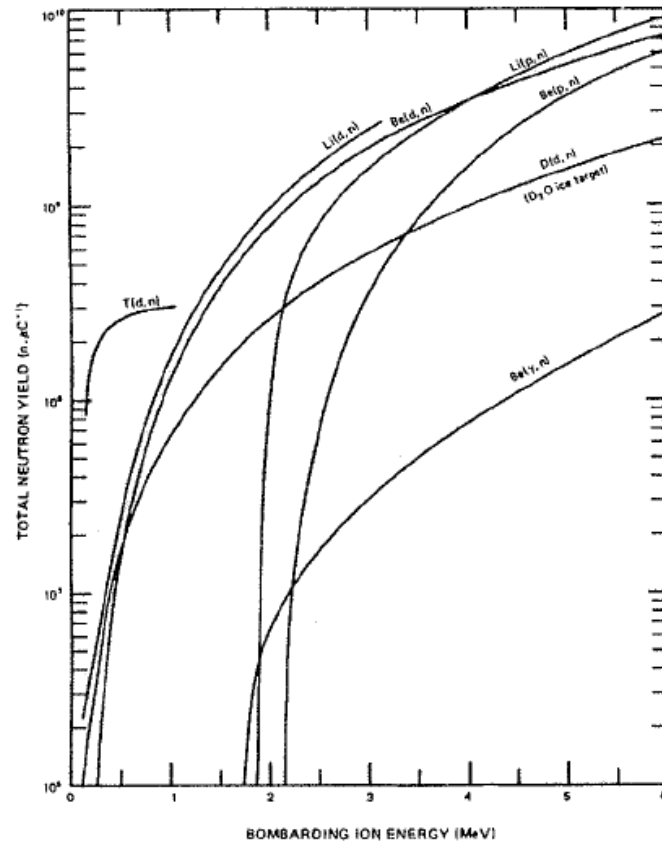
Figure 5.3: Neutron production from low energy charged particle beams. From [83].

Although Figure 5.3 shows for proton energy less than 8 MeV Li has the highest yield, experimental work by Lone and coworkers [86, 88] shows that as bombarding particle energy approaches energies greater than 10 MeV, the relative increase in neutron yield from (d,n) reactions decreases. This is an important technical concern for the LENS accelerator, as there is a potential to activate the accelerator vanes in the event of a beam loss (beam transmission is usually not 100%) if deuteron beam is employed. The average energy of neutrons produced in the (p,n) reaction is much less than in the (d,n) reaction (forward peaked high energy neutron flux results from deuteron elastic breakup), and so (p,n) reactions are favorable for a source that is designed to produce cold neutrons.

Proton reactions at low energy favor lithium from a consideration of neutron

Table 5.2: Physical Properties of Target Materials [84]. Yields are given at 10 MeV to represent a typical energy achievable with the proposed accelerator system.

Property	Lithium	Beryllium
Atomic Number	3	4
Isotope for Neutron Production	^{7}Li	^{9}Be
Natural Abundance of Production Isotope	92.5%	100%
Atomic Weight (g/mol)	6.941	9.01218
Melting Point (C)	180.54	1278
Boiling Point (C)	1342	2970
Specific Gravity	0.534	1.848
Specific Heat at 293 K (cal/deg mol)	5.92	3.93
Thermal Conductivity at 298.2 K (W/cm/K)	0.848	2.01
(p,n) Total Neutron Yield at 10 MeV (n/μC)	1.7×10^{10} [85]	2.5×10^{10} [86]
(p,n) Total Gamma Yield at 10 MeV (p/μC)	3.3×10^9[87]	1.8×10^8[87]
(d,n) Total Neutron Yield at 10 MeV (n/μC)	3.0×10^{10}[88]	3.6×10^{10} [88]

yield alone. However, as the facility moves to higher energies in the long term future, the yield from beryllium is superior to lithium. There are additional concerns with lithium, including its low melting point, high specific heat, and low heat conductivity of lithium. Compared to beryllium, lithium is a flimsy material that absorbs heat more readily, and that heat is more difficult to remove. A lithium target will also quickly blister or melt without aggressive target cooling. In contrast, beryllium is strong, more elastic than steel [84], does not oxidize in air, and has more favorable thermodynamic properties.

The short range of protons in materials at these energies (13 MeV protons stop in 1.3 mm of Be) implies the target must also form the vacuum seal between proton beam line and the rest of the TMR. Target stress has been analyzed for higher power operations, and the present design calls for the target to be 3 mm Be plate bonded to an Al substrate cooled with flowing water. To achieve the average dissipation rate needed (roughly 6 MW/m^2) the Al plate is designed to employ a hypervapotron cooling configuration [89] to dissipate an eventual average thermal load of up to 30

kW. The build up of hydrogen, and to a lesser extent helium, in the target can lead to embrittlement. Therefore, at full power operations periodic annealing of the production target, or sustained operation above 200 ^{o}C, will be necessary to prevent fracture.

A beryllium target and proton beams is ideal for LENS, but advanced lithium target engineering and strongly forward peaked (d,n) produced neutron beams are receiving strong support for medical applications, including Boron Neutron Capture Therapy (BNCT) and fast neutron irradiation of tumors. In these applications, intense strongly collimated beams of lower energy ($\sim$1-3 MeV) fast neutrons are desirable. However, much of the data available in the literature is of relative yields in limited angular ranges. The generation of neutron and gamma absolute yield data as a function of energy and angle for MeV charged particle beams is a strong component of the research. This information is vital for high fidelity neutronic modeling in this cross-over field of physics and medical research. We discuss the physics leading to source distributions employed in the LENS model in the next section.

5.3.3 The Physics of the ^{9}Be(p, xn) Reaction

There is a relative lack of experimental information on neutron production from 5-14.8 MeV. Energy and angle dependant probability distributions for 7 and 13 MeV ^{9}Be(p, xn) were calculated from nuclear physics considerations by H. Nann [90], and are required to provide the input for modeling with MCNP [62, 78]. Gamma rays from the $^9Be(p, \alpha)$ reaction were modeled as an isotropic source spread out uniformly over the target volume with energy 3.5 MeV [41].

I   Neutron Yield

Monte Carlo can only calculate the probability with which a given process occurs, so it is essential to also know the number of initial events. In the MCNP simulations, this is set by the total neutron yield. Figure 5.4 shows the total neutron yield from $Be(p, xn)$ across a region of proton energy accessible to the accelerator system. A fit to collected experimental data [91] on total 4π neutron yield from beryllium, Y_N as a function of proton energy, E_p in MeV, is given in Equation 5.1 and shown in Figure 5.4.

$$Y_N(E_p) = 3.42 \times 10^8 (E_p - 1.87)^{2.05} \text{ [n/}\mu\text{C]} \tag{5.1}$$

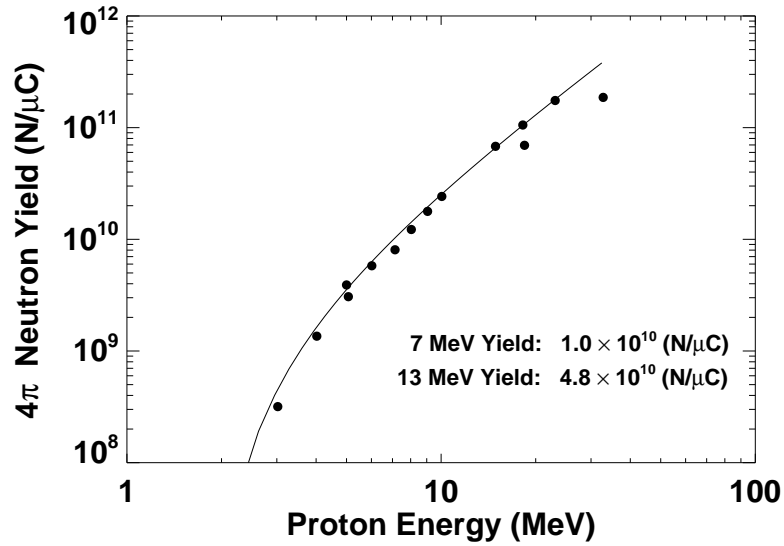**Figure 5.4:** Collected experimental data [91] on neutron yield from $^9Be(p, xn)$ reactions. Curve is equation 5.1

II   Reaction Channels

The three main channels for neutron production in the Be target are compound nucleus formation, direct charge exchange, and multi-body break up (where the $2\alpha+n$ system breaks up easily). Pre-equilibrium break up of the compound nucleus

leads to a high energy tail, while multi-body break up gives a distribution of lower energy neutrons. Both break up reactions are modeled isotropically. Direct charge exchange leads to forward peaking in the angular distribution [90]. As the energy of the protons increases, the number of excited states decaying to the ground state by lower energy neutron emission increases, leading to an increase in the low energy portion of the spectrum. There is a resonance with the excited state of $^{10}B^*$ at 2.56 MeV [92], leading to the pronounced peak in neutron production at this energy. The neutron spectrum at 0 degrees at 5,7,13, and 17.24 MeV is shown in Figure 5.7. A table of reaction channels and thresholds is given in Table 5.3. The $^{6}Li^*$ state at
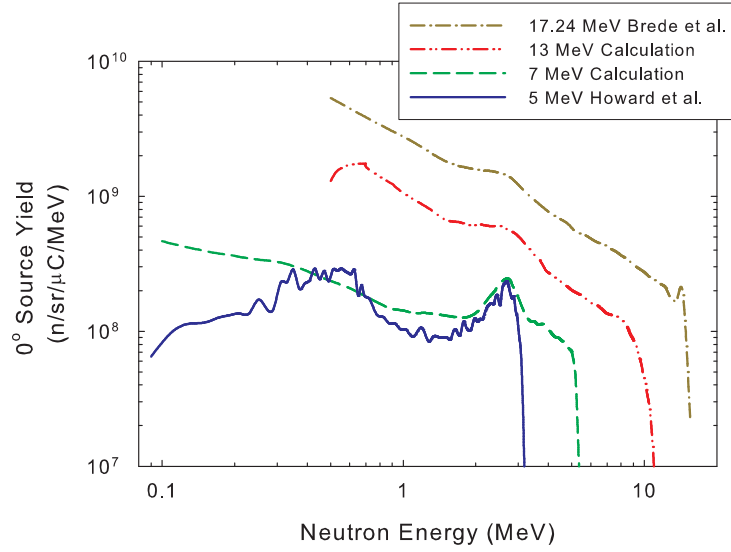
Figure 5.5: Neutron yield energy spectrum at 0 degrees at various proton energies, experiment [93, 94] and calculations [90].

3.56 MeV, where * indicates the residual nucleus is in an excited state, decays via gamma ray emission because decay via alpha emission is forbidden due to spin and parity conservation. Its emission rate has been observed in experiment by Guzek [41]. In addition, several secondary channels are sources of neutrons and alpha particles, and are included in Table 5.4.

Table 5.3: List of $^9Be(p,n)$ reaction channels.[†] denotes neutron production channel,[§] denotes secondary channel exists. [65]

Reaction Products	Q-Value (MeV)	Threshold (MeV)
$^{10}B + \gamma$	6.59	0.00
$^6Li + \alpha^{\S\dagger}$	2.23	0.00
$d + 2\alpha$	0.65	0.00
$^8Be + d$	0.56	0.00
$^9Be + p^{\S\dagger}$	0.00	0.00
$n + p + 2\alpha^{\dagger}$	-1.57	1.75
$^8Be + n + p^{\dagger}$	-1.59	1.85
$^9Be + n^{\dagger}$	-1.85	2.06
$^5He + p + \alpha$	-2.46	2.74
$^5Li + n + \alpha^{\S\dagger}$	-3.54	3.93
$^7Li +^3 He$	-11.2	12.5
$^7Be + t$	-12.1	13.4
$t +^3 He + \alpha$	-13.7	15.2
$^7Li + p + d$	-16.7	18.6
$^8Li + p + d$	-16.9	18.8
$^6Li + p + t$	-17.7	19.7

Table 5.4: Secondary Channels, [*] Denotes residual nucleus in excited state. Decay of secondary channel residual nuclei also leads to neutron and α production.

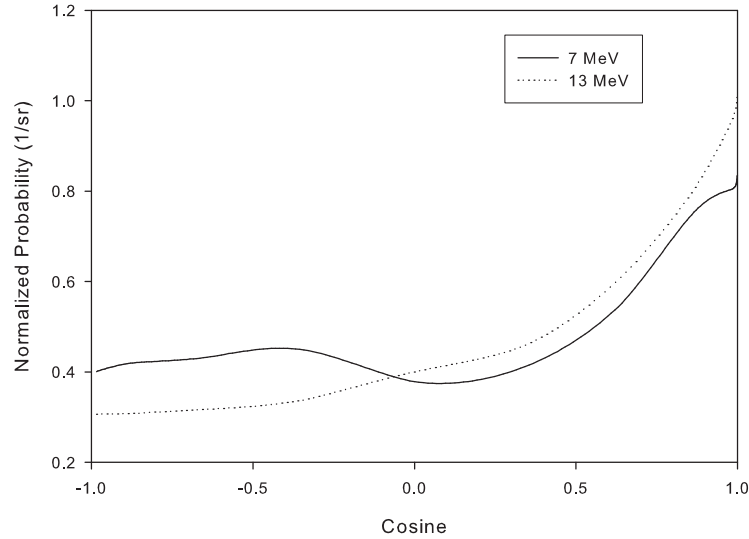| $^9Be + p \rightarrow$	$\alpha +^6 Li^* + \gamma_{3.56\text{MeV}}$	
	$\alpha +^6 Li^* \rightarrow p+^5He;$	$^5He \rightarrow n + \alpha$
	$\alpha +^6 Li^* \rightarrow n +^5 Li;$	$^5Li \rightarrow p + \alpha$
	$\alpha +^5 Li + n;$	$^5Li \rightarrow p + \alpha$
	$^9Be^* + p \rightarrow \alpha +^5 He;$	$^5He \rightarrow n + \alpha$

Figure 5.6: Angular probability distribution used in MCNP input. Integral under each curve normalized to 1.

5.3.4 MCNP Source Terms

Figure 5.7 shows the energy probability distribution for 7 MeV protons and Figure 5.8 for 13 MeV protons on beryllium [90] used in the MCNP simulations. The angular distributions (integrated over all energy) are given in Figure 5.6. In the course of this work, sources were also calculated at 11 MeV, 22 MeV, and a final source at 3 MeV source was generated from the data presented in [41].

5.4 Elements of Cold Moderator Design

In Chapter 2, we have shown how cold neutrons have significantly improved instrument performance and expanded the range of science and materials that can be studied with neutrons. Before discussing the specifics of the LENS cold neutron optimization, it is appropriate to discuss some general characteristics of cold neutron moderators currently in use.
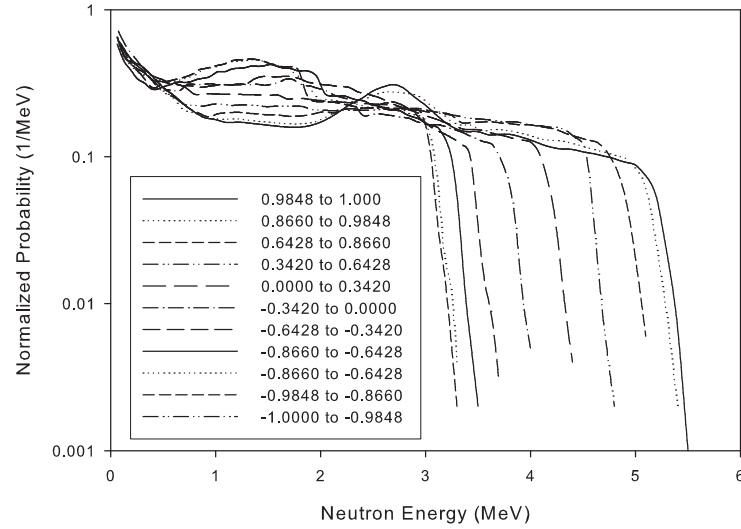
Figure 5.7: Calculated energy probability distribution used in MCNP input for E_p=7 MeV at each angle. Integral under each curve normalized to 1.
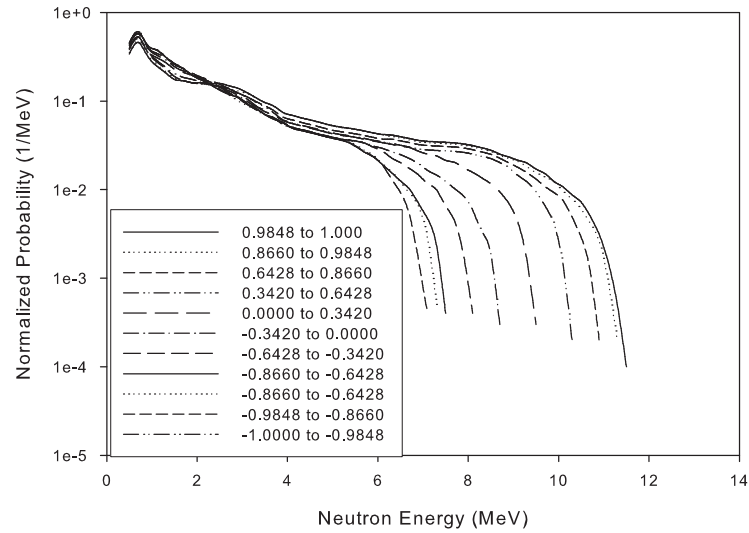

Figure 5.8: Calculated energy probability distribution used in MCNP input for E_p=13 MeV at each angle. Integral under each curve normalized to 1.

5.4.1   Reflectors

The first accelerator based neutron sources consisted of fast neutron sources situated near a bare neutron moderator [95]. Although this provided a source of thermal neutrons due to the moderator alone, it is far from the most efficient geometry. Once a neutron leaves the moderator, it escapes the system entirely. By introducing material around the moderator, called a reflector, some of the flux from the target will enter or reenter the moderator in the course of its random walk. The optimized LENS reflector has been shown via Monte Carlo to enhance cold neutron brightness by over factor of 5. For comparison, the experimentally optimized configuration of Inoue in Japan [96] found lower enhancements in the thermal neutron flux using a reflector. They report enhancements of factors of 3 for BeO, 2 for graphite, and 1.5 for paraffin material used as a reflector for a decoupled moderator configuration.

Fortunately, the reflected neutrons are generally traveling quite fast ($> 10^5 m/s$), and the distances between collisions on the order of cm, so the additional time to emit from the system due to scattering in the reflector can be quite small. One important exception to this is the case of a highly non-absorbing moderator, where thermal neutron diffusion is non-zero. In this case, the lifetime of the slow neutrons in the reflector is long compared to the neutron emission time from the moderator, and special techniques of decoupling and poisoning must be employed to reduce emission times. The emission time requirements are dependent on the instrumental application, requiring instrument designers and neutronics scientists to work together to optimize the global cold source and instrument package.

5.4.2   Moderators

The moderator design controls the neutron flux that reaches the instruments, as well as the energy resolution of those instruments if the source is pulsed. As moderators

are cooled, the number of neutrons per unit energy at low energy increases, increasing the phase space density of a neutron beam. Cooling the moderator cools the neutron flux until a well-thermalized saturation intensity is reached, where the ability of the moderator to cool the neutrons is balanced by absorption and leakage. Various moderator materials have limits to the lowest energy neutrons that can be reached based on the threshold of incoherent inelastic excitations in the material [96], which provides a second limitation to the intensity of neutrons at low energy. If our goal is to provide high intensity of low energy flux, we must have a moderator which is capable of cooling the neutron spectrum to low effective temperatures, which means a high density of low energy states to exchange energy with the neutron gas, as well as a material with low neutron absorption and high scattering cross-section.

5.4.3   Emission Time and Energy Resolution

A vital characteristic of moderators at pulsed sources is the emission time. For a pulsed source without choppers, the energy resolution of the TOF technique is controlled by the emission time. This can be shown mathematically, where the energy, E, as a function reduced time of flight, $t - \bar{t}(E)$, and flight path L gives an expression of the energy resolution, ΔE. The energy resolution is the smallest change in energy that can be resolved with the instrument.

$$E = \frac{1}{2}m(\frac{L}{t - \bar{t}(E)})^2 \tag{5.2}$$

$$(\Delta E)^2 = (\delta t)^2(\frac{\partial E}{\partial t})^2 + (\delta L)^2(\frac{\partial E}{\partial L})^2 + (\delta\bar{t}(E))^2(\frac{\partial E}{\partial\bar{t}(E)})^2 \tag{5.3}$$

where $\bar{t}$ represents the average time for a neutron of energy E to leave the moderator. It is a function of both the proton pulse width and the emission time distribution from the moderator. δt is the time resolution of the experiment, set by the integration

time of the instrument, the emission time required to emit neutrons of energy E from the moderator, and the proton pulse.

$$(\delta t)^2 = (\Delta t_{proton})^2 + (\Delta t_{emission})^2 + (\Delta t_{instrument})^2 \sim \tau^2 \qquad (5.4)$$

If we assume that no cross-terms are present and that $\Delta t_{emission}$ is the dominant term, we can derive a form for the energy resolution of a pulsed instrument. We need to define a term to quantify $\Delta t_{emission}$, which we will call $\tau_x(E)$, where $\tau(E)$ the energy dependant width of x fraction of the neutron pulse (i.e., $\tau_{0.5}$ is the FWHM, see Figure 5.12). Neutron pulse shapes have a characteristic form, an example of which comes from the work of Ikeda and Carpenter [76]. Figure 5.12 shows the describes $\tau(E)$ calculated in simulation for long pulse and short pulse modes of operation of LENS, and shows the calculated energy resolution of LENS for a 150 μs proton pulse and a detector at 610 cm. We note that energy resolution is better than 10 % only for neutron energies less than 30 meV.

A useful metric is τv, which is a characteristic length scale for the flight path. For flight paths where $L = tv \gg \tau v$, we may neglect $\bar{t}$, and Equation 5.3 reduces to

$$\frac{\Delta E}{E} = \frac{2\tau}{t} \qquad (5.5)$$

We see from Figure 5.12 that at 25 meV $\tau_{0.5} \sim 300 \mu s$ and $v = 2200 m/s$ so $\tau v = 66 cm$, a significant fraction of the 570 cm prototype flight path. Thus, we cannot neglect the effect of emission time on the instrumental resolution.

When this is the case, the instrumental energy resolution then becomes more complicated. We can rearrange the expression to show the impact of the $\bar{t}$ term (which is often neglected for short pulse sources), keeping first order terms in the
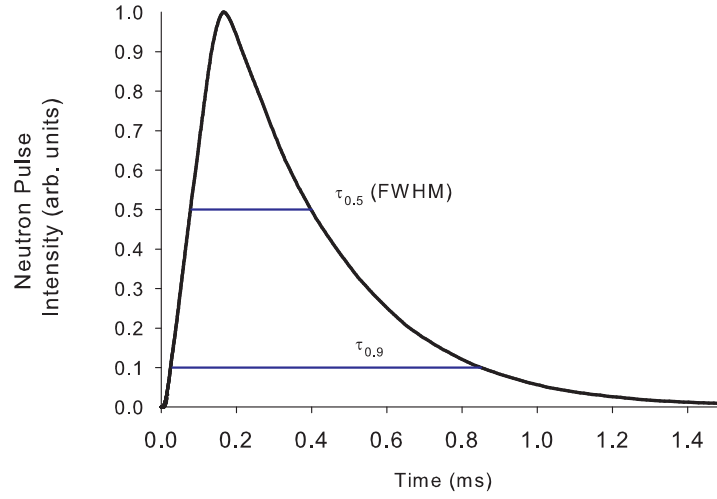
Figure 5.9: Figure showing the meaning of τ_x for a typical neutron pulse shape
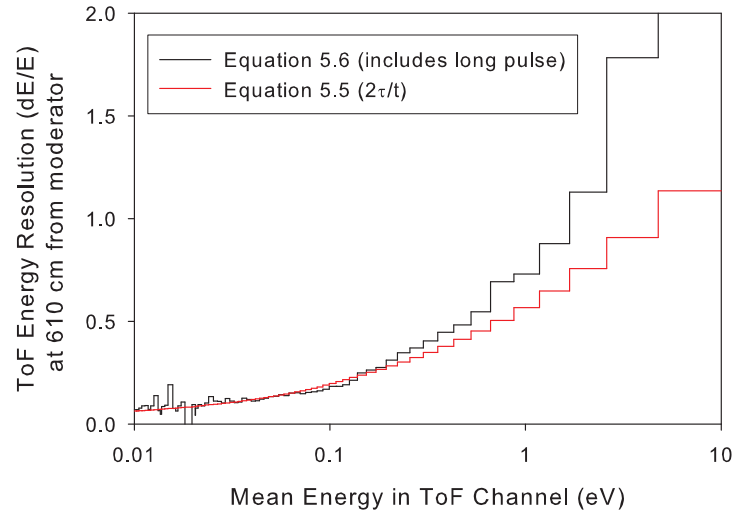
Figure 5.10: Simulated Energy Resolution at LENS for a 150 μs proton pulse and a detector 610 cm from the moderator face.

Figure 5.11: Figure showing τ_x for an instantaneous proton pulse. The saturation at high energy for the long pulse figure is due to the long pulse mode of operation.

Figure 5.12: Figure showing τ_x at LENS for a 150 μs proton pulse

derivative, and neglecting errors in the determination of $\bar{t}$ and L,

$$\frac{\Delta E}{E} = \frac{2\tau}{t - \bar{t}} \frac{1}{1 - \frac{2E}{t-\bar{t}} \frac{d\bar{t}}{dE}} \tag{5.6}$$

$$\frac{\Delta E}{E} \approx \frac{2\tau}{t}(1 + \frac{\bar{t}}{t} + \frac{2E}{t - \bar{t}} \frac{d\bar{t}}{dE} + \frac{1}{2}(\frac{2E}{t - \bar{t}} \frac{d\bar{t}}{dE} + \frac{\bar{t}}{t})^2) \tag{5.7}$$

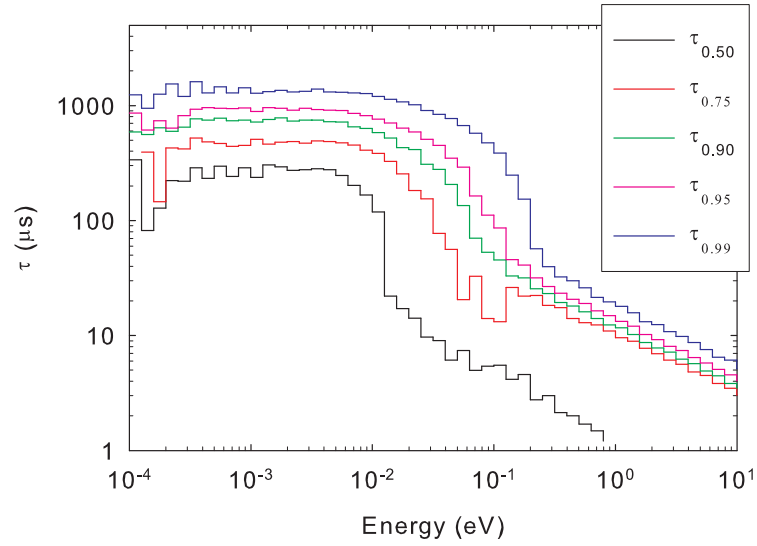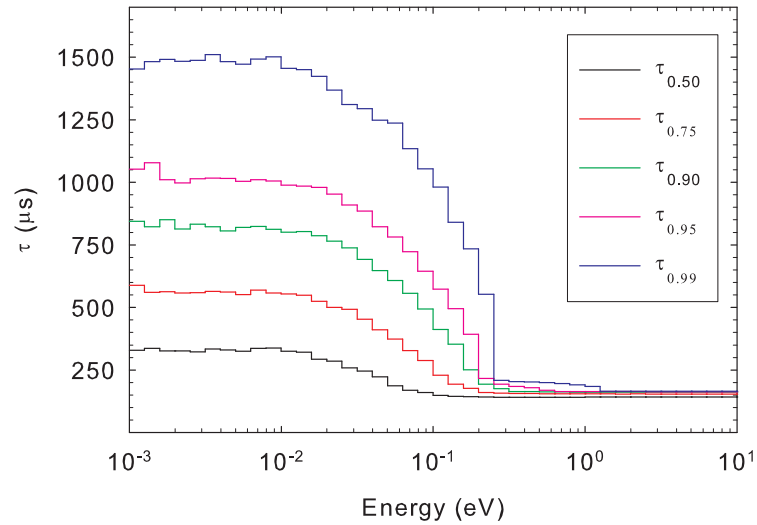Let us explore Equation 5.7 for a moment. For $t \sim \bar{t}$, energy resolution will be quite poor. For rapid change of $\bar{t}$ with E, which can occur in the 10-1000 meV regime, energy resolution will also suffer. The sensitivity to the derivative requires that determination of $\bar{t}$ must be done carefully. To first order, $\frac{2\tau}{t}$ is retained, thus as fight paths are increased to increase t, energy resolution is increased. For instrument designs, this increase in resolution must be balanced against the $1/r^2$ falloff (unless guides are employed) in intensity. As we will discuss in Section 5.4.5, τ can be controlled neutronically, but this is not an option for LENS to operate in the coupled mode.

5.4.4   Emission Time - the Collision Perspective

The concept of emission time can be understood from the perspective of the number of collisions required for a neutron to first achieve a certain energy range (production term), and the number of collisions during which the neutron remains at that energy (storage term). If we imagine the time independent flux as a sum of the energy distribution of the neutron flux at the ith collision, $\phi_i(E)$ we have an expression

$$\phi(E) = \sum_{i=0}^{N} \phi_i(E) \tag{5.8}$$

where $i = 0$ is the neutron source flux. We may naturally calculate $\phi_i(E)$ in Monte Carlo, as shown in Figures 5.13 and 5.14 calculated in the moderator volume. In

Figure 5.13 the quantity calculated is the fraction of integral flux at the ith collision out to 300 collisions for several energy groups, as given by

$$\frac{\int_a^b dE\phi_i(E)}{\sum\limits_{i=0}^{300} \int_a^b dE\phi_i(E)} \tag{5.9}$$

In this analysis, we see that the primary and fast flux becomes slowing down flux
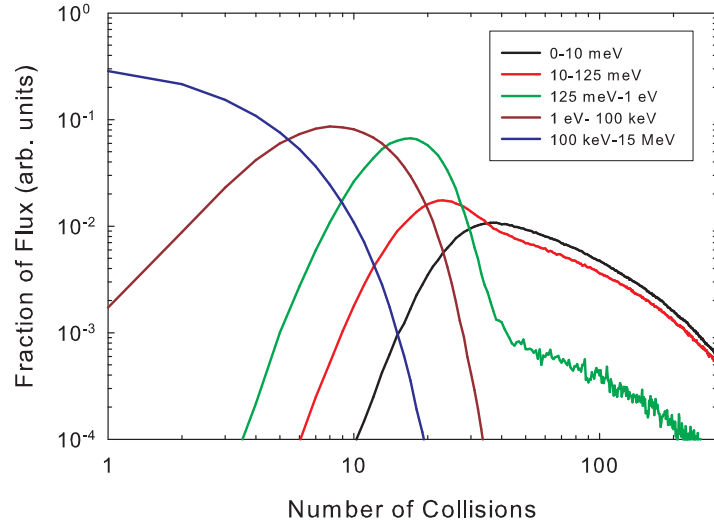
Figure 5.13: Collision analysis in integral energy groups. The mean number of collisions required to reach a given energy peaks around a mean value. Equilibrium flux (0-125 meV) has a long tail to the collision distribution as further collisions do not change the mean energy of the flux. The intensity of the flux in the equilibrium groups decreases with increasing collision number due to leakage of neutrons from the system and absorption.

after about 5 to 18 collisions (half width in Figure 5.13). Mean free paths are on the order of 3 cm in water, and velocity of a 1 MeV neutron is 1.4×10^7 m/s, so moderation collisions would take on the order of tens of ns. Thus, any emission time structure in this regime is completely washed out by a long pulse mode of operation. A 1 eV neutron travels at about 1.4×10^4 m/s, and lasts about 10 to 30 collisions, at a 7.3 mm mean free path, and so has an emission time of about 5-15 μs. Finally,

for cold neutron flux, which travels at about 700 m/s for a 2.5 meV neutron and undergoes from 20-105 collisions at a 2 mm mean free path, will have an emission time from 60 to 300 μs.

The next figure shows the energy distribution versus number of collisions in the moderator volume. Here we see the fast flux slows down as a power law path (straight line on logscale plot) to the equilibrium group (0.1-100 meV). The equilibrium group persists for long times (large collision number), but the $\sim$100 meV part decays away faster than the $\sim$2.5 meV part due to leakage. At large collision number, $N > 150$, the low energy tail decays faster than the high energy tail, representative of spectral warming due to preferential absorbtion of the low energy flux.

An essential issue of background is implied by these figures. The neutron flux persists at low levels even out to very large collision numbers ($N > 300$), which implies that a 25 meV neutron, even with mean free paths as small as 1 cm, may still persist for over 1300 μs. Thus, if a highly penetrating fast neutron escapes into the scattering hall, it will undergo several hundred collisions before absorbing. At LENS we seek backgrounds on the order of detector dark current, and these neutrons would create a strong background signal. For this reason instruments tend to have absorbing shielding near their detectors.

5.4.5   Decay of fundamental mode

It has been shown that if the moderator is large enough to develop a fundamental spatial eigenmode (with Maxwellian flux of mean velocity v_o) then the flux in the fundamental mode decays separably and exponentially ($\phi(E,t) \propto \phi(E)e^{-\lambda t}$) after reaching a maximum [30, 97]. For neutrons $<.25$ meV (>1.0 $\mathring{A}$) rise times are typically quite steep compared to decay times, we can assume the decay constant, λ, is a the most central factor in TOF energy resolution. This decay constant is given
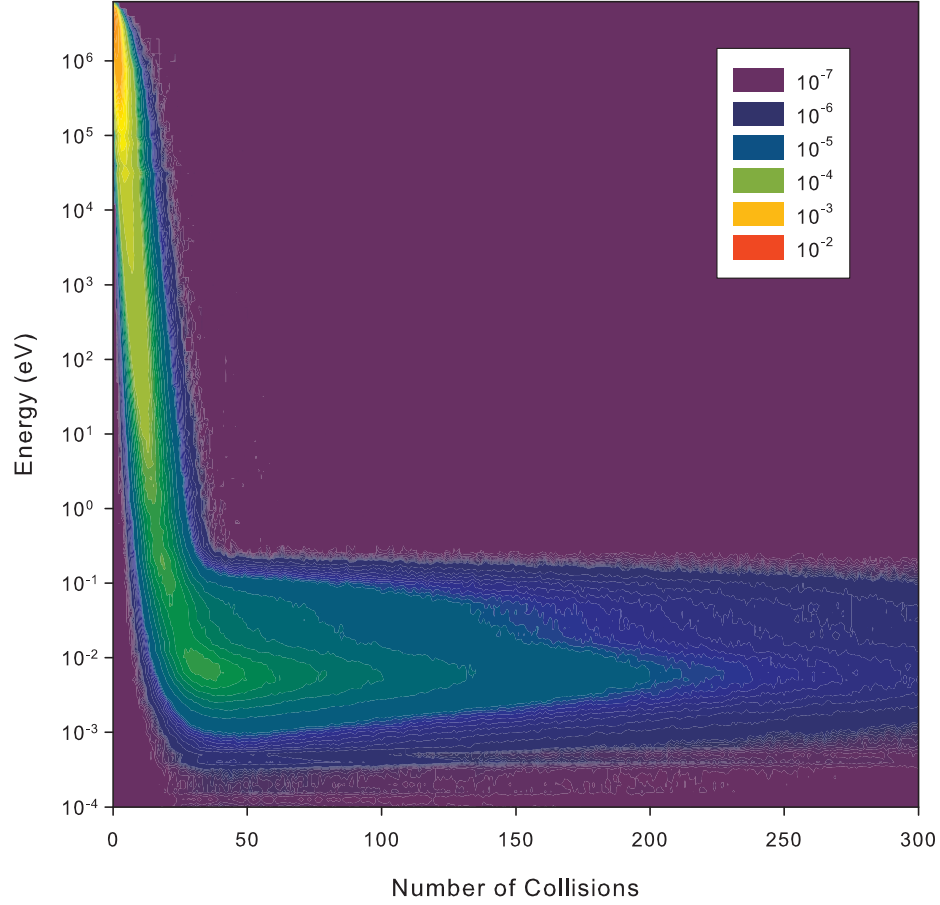
Figure 5.14: Collision analysis for flux averaged over the moderator volume. The 0th collision is the source flux. As the neutrons collide, they lose on average $\frac{1}{2}$ of their energy in each collision with hydrogen. As the neutrons reach thermal energies, they remain in a quasi-equilibrium for $\gtrsim 30$ collisions. The equilibrium condition is defined by neutrons that are equally likely to gain or lose energy, so the energy does not change greatly as collision number increases. The energy is static, but the flux decreases with increasing collision number as neutrons leak out of or absorb in the moderator volume. In addition, the thermal neutron flux feeding the moderator from the reflector decays with increasing collision number for the same reason.

by

$$\lambda = v_o \Sigma_a + D_o B^2 - C_d B^2 \qquad (5.10)$$

where Σ_a is the absorption macroscopic cross-section at the neutron maxwellian velocity v_o, D_o is the diffusion coefficient, C_d is the diffusion cooling coefficient, and

B is the spatial eigenvalue, or *buckling*. For a rectangular decoupled moderator where the flux is forced to zero at the edges, $B^2 = \frac{\pi^2}{(x+y+z)^2}$, where x,y, and z are the dimensions of the rectangle. If the moderator is arbitrarily large, there is a location Z_o relative to the center of the moderator beyond which neutrons no longer efficiently diffuse back to the region of the moderator viewed by the beam line. For convenance, Z_o is often chosen to be a certain multiple of the diffusion length of the medium. For a infinite slab of finite thickness z a rectangular moderator would have $B^2 = \frac{\pi^2}{(2Z_o+z)^2}$

Equation 5.10 allows us to readily interpret how we may influence moderator performance. First, we have control over the absorption of the moderator, not only via choice of moderator medium, but also by inserting absorbers into the moderator volume directly, in a technique known as *poisoning*. We also have control over the size of the moderator buckling, by using absorbers to define the location at which the low energy neutron flux is forced to zero, in a technique called *decoupling*. The use of absorbers to control the flux and emission characteristics must be carefully weighed against the intensity loses in the absorbers.

The diffusion term refers to the ability of neutrons of low energy to leak out of the moderator, which is necessary to make the thermal neutron beam. It is related to the inverse of mean free path between elastic collisions. If the mean free path is very short, then there will be too many collisions for the neutrons to leak out efficiently. If it is very long, the number of energy reducing collisions before leakage will be reduced.

The diffusion cooling term is related to the second moment of the energy exchange cross-section, $\Sigma(E' \rightarrow E)$, and represents the ability of neutrons to scatter from higher energies to the fundamental mode energies. If the diffusion cooling coefficient is high enough, or the diffusion term low enough, then we have a situation

known as diffusive cooling, where there is a build up of of low energy neutrons in a region of phase space due to leakage of high energy neutrons (with longer diffusion lengths) out of the medium. Because neutrons in the core of the moderator will have lower energies, and shorter diffusion lengths, we expect the highest density of lowest energy neutrons to be in the core. If we open a hole in the moderator, as in so called *reentrant cavity* type moderators, any neutrons entering the hole will have an infinite diffusion length ($D_o = 0$), and we will have access to the diffusive cooled flux in the core.

These have been, of course, very general considerations. The application of diffusion cooling to crystalline systems (where mean free paths can vary wildly as a function of energy) is somewhat problematic, and the measurement of the C_d term has also proven elusive for a number of cases [30]. However these general consideration should prove sufficient for understanding neutronic aspects of moderators, given the general predilection to Monte Carlo methods of calculating emission times.

5.4.6   Moderator State of the Art

There are many different moderator materials in use at facilities around the world, ranging from ambient temperature moderators like water, heavy water and polyethylene to cryogenic moderators like liquid hydrogen, and solid methane. Exotic cryogenic moderators, like combinations of liquid hydrogen and solid polyethylene particles, or hydrogen rich organic compounds such as mesethylene, ammonia, and propane have been tested as moderators in high radiation environments. The more traditional ambient temperature moderators like polyethylene and water have higher energy flux, but also very well defined characteristics.

A collection of neutron spectra measured on different types of moderator materials is shown in Figure 5.15. While it is certainly the case that the surrounding

geometry has a *significant* impact on spectral shape and total neutron yield, these spectra have been normalized to peak at unity so that their shapes and mean energy may be more easily compared.
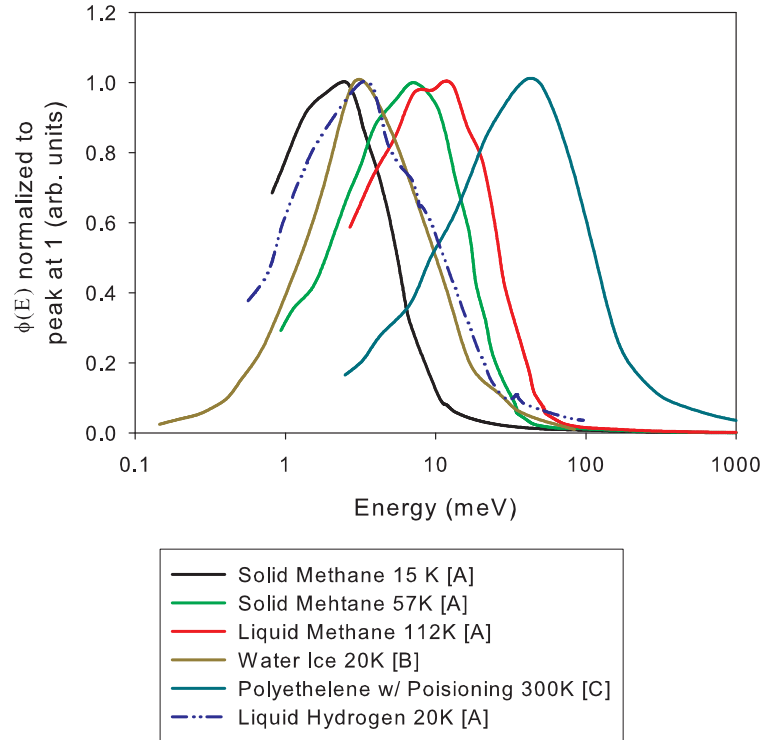
Figure 5.15: Neutron spectrum from various moderators. Cold methane is the best performer. Spectra taken from A)[98], B)[95], C)[99]

One of the first experimental treatments of cold neutron production was done by Whittemore and McReynolds in 1961 [95]. Despite over 40 years on the subject of cold neutron production, their 2 central results remain unchanged. 1) Cryogenic methane is the brightest cold moderator 2) Cavity-type configurations have higher total cold neutron yields than slab configurations. A more recent quantification of the superiority of methane [96] shows that as materials are cooled, a limiting effective temperature of the neutron gas is reached that is representative of the threshold of inelastic excitations in the material. Figure 5.16, adapted from their results, shows

methane has the lowest effective neutron temperature of any material to date due to its high density of hydrogen and high density of low energy excitations.
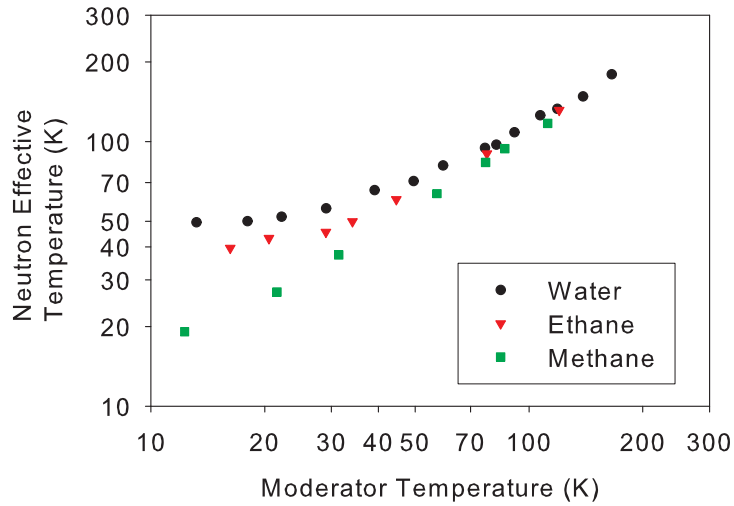
Figure 5.16: Temperature dependence of cooled neutron flux as a function of moderator temperature, adapted from Inoue [96]. Methane has the lowest effective neutron temperature of any material to date due to its high density of hydrogen and high density of low energy excitations.

So why is methane in limited use at sources around the world? Unfortunately, high primary neutron flux and cold solid moderators are mutually exclusive at present. The world's most intense neutron sources cannot employ methane because of the phenomena of *radiation damage.*

There are 2 main forms of radiation damage due to fast neutron irradiation, and both can lead to catastrophic results. The first form, known as *Wigner Energy*, which is attributed to the 1957 fire in the graphite reflector of the Windscale reactor in Britain [100]. The resulting fire destroyed the reactor core before burning out, where it sits in the same state today. Only recently have methods using remote handling equipment been developed to decommission the site, at a cost of over $50 million dollars.

Wigner energy occurs primarily in the graphite reflectors used in nuclear reac-

tors. High intensity radiation flux can dislodge atoms in the solid lattice into higher energy non-equilibrium positions. When the atoms recombine during annealing the additional energy is released in the form of heat. While we do not expect this type of radiation damage to play a large role in LENS, it is an example of the important pragmatic role radiation damage plays in neutron production.

The second form of radiation damage, very important to the LENS cryogenic methane moderator, occurs when the organic molecules making up a moderator are decomposed by the incident radiation. The breakdown of the moderator material has an adverse affect on cold neutron yield [76]. Worse still, if a sufficient density of free radicals build up in the moderator a sudden explosive recombination of the by-products is possible [47]. Radiation damage concerns are typically alleviated by periodic annealing of the moderator, but at high intensity sources the build up of damage is too fast to be successfully and productively relieved by periodic annealing. The lower energy primary neutron spectrum produced in the LENS target is expected to greatly reduce this problem, allowing more complex materials to be tested as moderators and allowing the production methane moderator to run longer at lower temperatures.

5.5   TMR Neutronics

In the design of the LENS cold moderator we must balance high cold neutron yield against radiation damage and heating, and limit emission time to less than 1 ms. LENS intends to run in a *long pulse mode*, which is to say that the proton beam will illuminate the target for a time that is comparable to neutron lifetimes in the system. Also, developing a competitive source intensity is paramount, so LENS will employ a *coupled* moderator configuration. It is also known that cavity configurations

can enhance flux, but at the outset this was not considered due the complicated fabrication of such a configuration.

The LENS prototype cold moderator is a rectangular slab configuration enclosed by a cylindrical reflector. Ease of fabrication for the reflector water vessel also forced the use of generally cylindrical geometries for the reflector, though nothing a priori excludes other geometries, and spherical models were used in early design work. Central to this analysis is the cold methane scattering law, where we employ the best available model of incoherent approximation low temperature scattering from methane [101], see Figure 5.17. We employ the standard scattering laws for ambient temperature water, graphite, and heavy water where appropriate. We use free gas model to describe the behavior where standard scattering laws are unavailable. While we presume the scattering laws to be of sufficient quality to facilitate these calculations and optimizations, later we will demonstrate some shortcomings of these kernels.
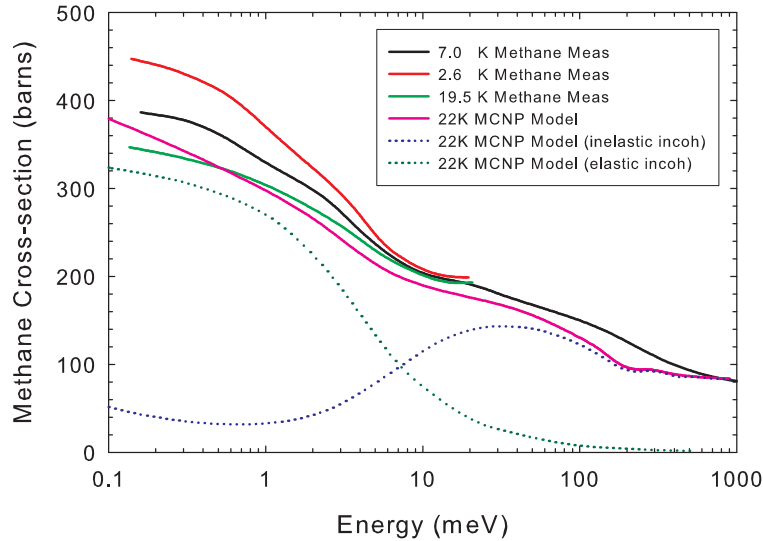

Figure 5.17: Comparison of *smeth22k* total cross section [101] to measurements of Grieger [102] on total methane cross-section.

We will focus the neutronic calculations presented here to the optimizations

leading to the final general configuration of moderator, target, and reflector (TMR). Calculations entail:

- A cylindrical reflector of radius and material to be determined enclosing a slab moderator

- 22 K Methane Moderator in coupled configuration

- Proton target behind moderator, separated by premoderator material, in line of sight of neutron beam lines and illuminated by 13 MeV protons

- Premoderator optimal thickness and material to be determined

- Beam port configuration and moderator slab geometry to be determined

- Aluminum Structural Material

We naturally must limit our discussion to the most central material, neglecting the less intense or difficult to fabricate configurations that were considered. Some of those designs considered included [103]

- Premoderators: Light Water, Heavy Water, Beryllium, Graphite, Aluminum

- Reflectors: Light Water, Heavy Water, Beryllium, Graphite, Lead, Bizmuth

- Configurations: 30,45,60,90 degree proton beam/target angle with 0 or ± 20 degree angle between proton target and moderator

- Neutron Beam Ports: up to 16×16 at $0, \pm 20, \pm 30$ degrees to moderator normal

- Proton Target Vessels: Dimensions up to 12x16x16 cm

- Moderator Vessels: Dimensions up to $16 \times 16 \times 5$ cm, including aluminum and vacuum layers surrounding the moderator

5.5.1   Moderator Thickness

Calculations using a simplified model of infinite plane, finite thickness slabs of 22 K solid methane moderator were used to determine the sensitivity of cold neutron brightness to methane thickness using the *smeth22k* kernel [101]. If cold neutrons are to be produced directly from the primary fast neutron flux, then the optimal thickness of methane is about 5 cm. However, if the moderator is designed to couple to thermal neutrons produced in the reflector (10-500 meV), then the methane can be much thinner, on the order of just a few cm. Calculations showing these results are given in Figure 5.18. This result can be understood from the fact that the mean free path of 1-10 meV neutrons in low temperature solid methane is on the order of 1.5-2.0 mm [102], so unless the moderator is thin attenuation of the cold flux in the moderator itself will be strong.

A thinner moderator is advantageous because it greatly reduces neutronic heating from fast neutrons and allows the moderator to be thin enough to avoid a strong temperature gradient across its thickness, eliminating the need for aluminum foam or similar structures. Figure 5.19 shows the relative probability to produce cold neutrons of various energies from a beam of incident 100 meV neutrons, where a broad maximum is observed from 1 to 2 cm for the production of cold neutrons. To minimize neutron and gamma heating and the thermal gradient, 1 cm was chosen as the thickness of the methane moderator.

The moderator area was chosen to be 12 cm by 12 cm because no gain in cold neutron intensity was seen for larger moderator in simulations of reflector/moderator configurations, see Figure 5.20. There is a saturation in the cold neutron leakage from the moderator as a function of moderator area at 12×12 cm^2. Simulations of the spatial distribution of thermal and cold flux across the leakage surface of the moderator show a relatively flat distribution. Full details of the simulated perfor-

mance can be found in Section 5.8.
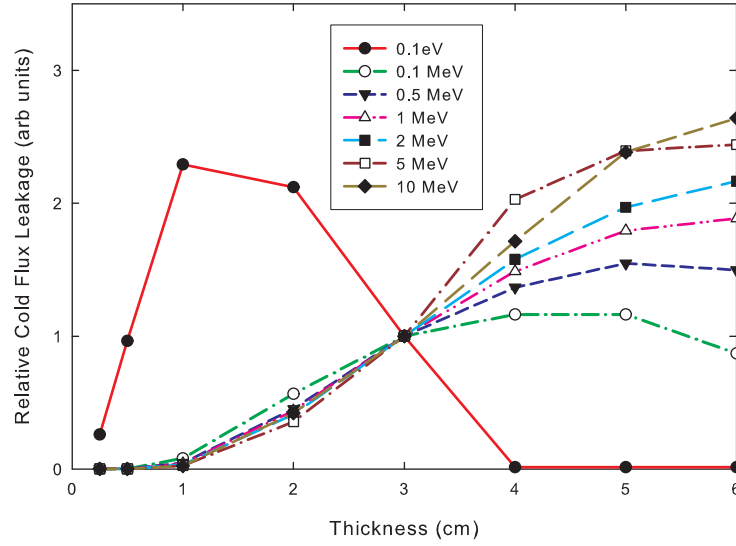

Figure 5.18: Efficiency of fast and thermal neutrons to generate cold neutrons as a function of methane thickness.
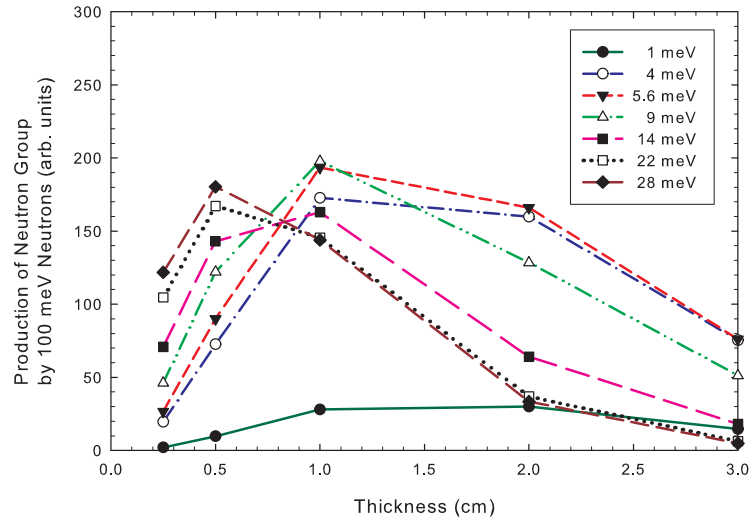

Figure 5.19: Simulated efficiency of various energy of cold neutron production from the exit face of infinite slab, finite thickness methane for 100 meV pencil neutron beam incident on one side. A broad 1-2 cm maximum is observed for production of cold neutron groups.
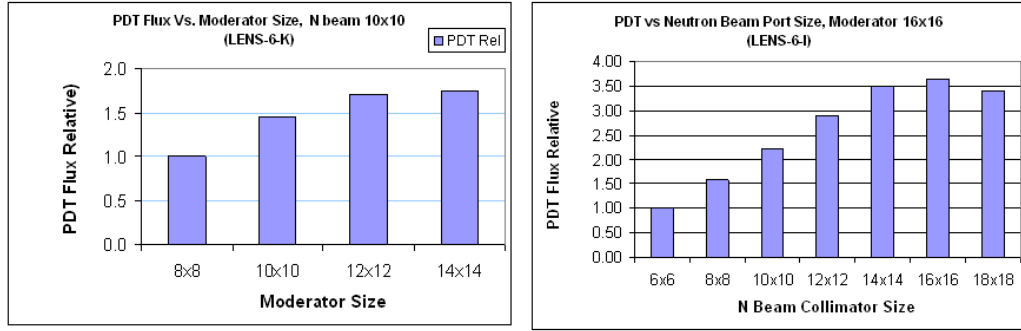
Figure 5.20: Relative cold neutron flux at sample position as a function of moderator area and beam pipe diameter [103].

5.5.2 Realistic Cylindrical Geometry

The *As Built* TMR neutronic MCNP model is shown in Figures 5.22 and 5.23. The TMR consists of a cylindrical light water reflector surrounding the beryllium target and solid methane moderator. The relatively thin, 12x12x1 cm^3, solid methane moderator is strongly coupled to the thermal neutrons produced from the reflector. The reflector is separated from the shielding matrix by a borated decoupling layer whose main purpose is to reduce activation in the high purity lead gamma radiation shield outside the reflector. The present design includes more vacuum space surrounding the moderator than is optimal in order to facilitate experimental studies of various neutronic changes (such as changes in premoderator, moderator geometry, poisons, etc.) at the present very low power levels. We will show later that a gain of a factor of up to 1.3 (Figure 5.24) is possible if this gap is reduced, and that present constructed configuration is almost a factor of 2 lower in cold neutron brilliance than our optimized configurations (Figure 5.26).

For a neutron source with strong coupling of the thermal neutron field between the moderator and the reflector, the reflector is employed as both a reflector *and* a thermal neutron source. It is known that coupled moderator geometries increase cold neutron brightness considerably [104, 105, 106]. Calculations of reflector materials in

model spherical geometries investigated the ability of various materials to produce high thermal neutron flux in the center of the reflector as a function of neutron energy and reflector radius.

Results are shown in Figure 5.21 for a 40 cm sphere with an isotropic point source at the center. For neutron energies lower than about 3.5 MeV, light water is the best reflector material. However, as the hydrogen cross-section falls off above this energy, beryllium is superior. Light water was chosen for the LENS reflector because of cost concerns regarding beryllium and the fact that the source will initially employ lower energy 7 MeV proton beam. The use of a beryllium reflector remains under consideration as a future upgrade and could increase brightness.

The reflector design configuration is a cylinder of light water 25 cm in radius, 50 cm tall enclosing the production target and moderator. The moderator is located in the center of the reflector, upstream from the production target. No cold flux gain is realized from increasing the water reflector radius beyond 20 cm, but calculations indicate that the optimal beryllium reflector radius is 25 cm, so the cylinder was enlarged to accommodate a beryllium upgrade.

5.5.3   Water and Vacuum around the Moderator

To maximize thermal neutron density in the moderator, vacuum gaps between moderator and reflector should be minimized. However, the desire to maintain flexibility in experimental moderator designs led us to relax this constraint considerably in the present design. The present design, (shown in Figure 5.23) has a vacuum gap between the water premoderator and moderator of 5.5 cm, and varies on all other sides of the moderator (the minimum side gap is 4.4 cm). The premoderator layer thickness is 1.85 cm.

To investigate the impact of this oversize vacuum space on performance, the
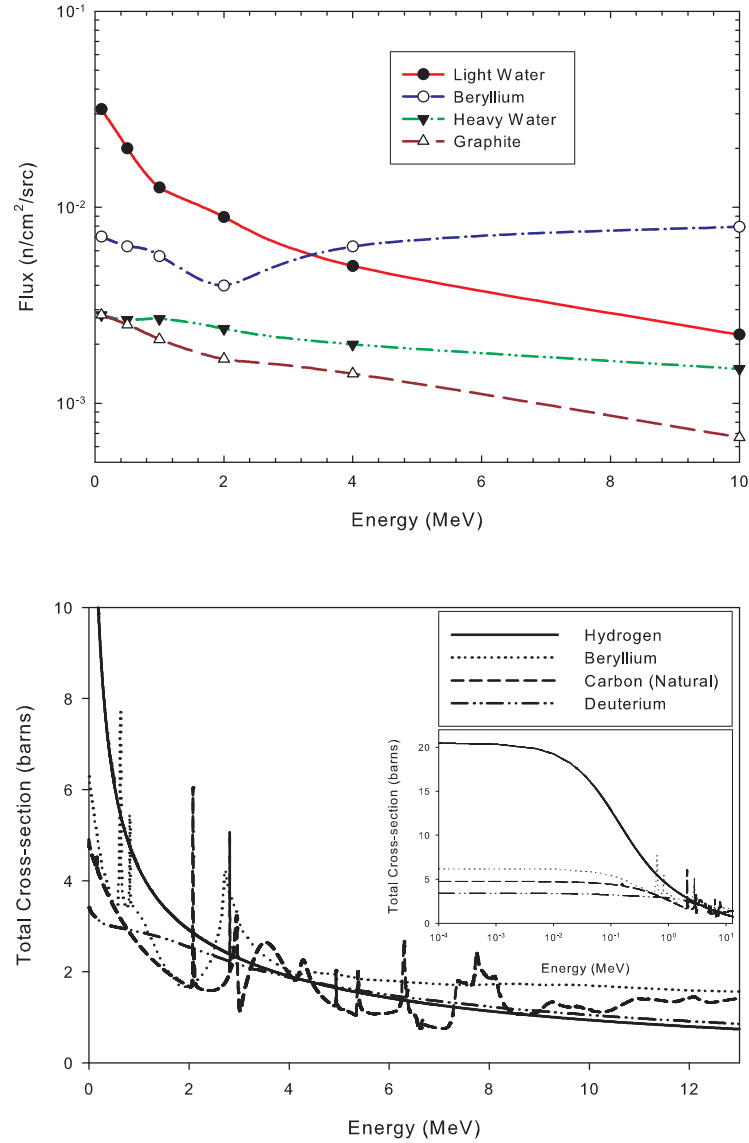
Figure 5.21: *Top:* Efficiency to generate thermal neutron flux at the core of the reflector as a function of primary neutron energy per source neutron in the simulation. *Bottom:* Reflector material total cross-sections. Note that cross-section of hydrogen is less than beryllium for $E > 4$ MeV, making it a better reflector in this energy regime. Below this regime, hydrogen's cross-section is clearly superior (see insert).

target-moderator void gap was reduced (water layer increased) in simulations of the cold methane moderator. The effect of other vacuum gaps on the sides and below the moderator was investigated by reducing these gaps to a uniform 2 cm and 1 cm.
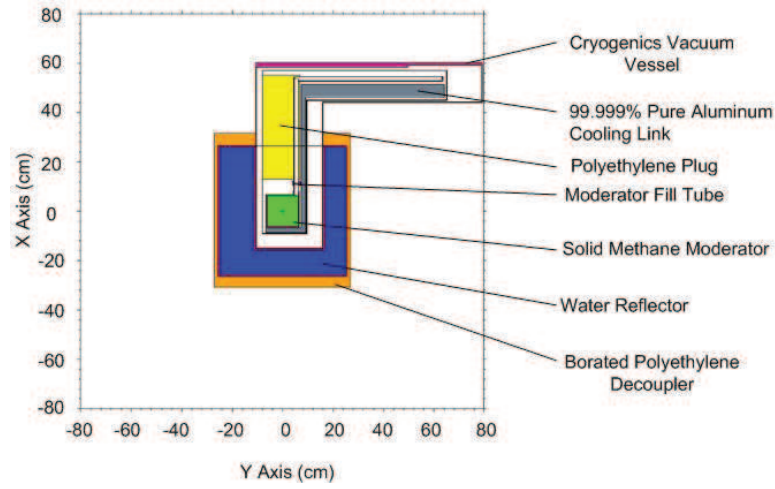
Figure 5.22: YX Planar view of the TMR geometry. The 12x12 cm methane slab is at the center, connected to the helium refrigerator (not shown) by the 99.999% purity aluminum cold link. The water reflector surrounds the moderator and the polyethylene plug above the moderator compensates for the void introduced into the water by the cryogenics systems. Biological shielding layers are not shown for clarity, but are included in the simulations.
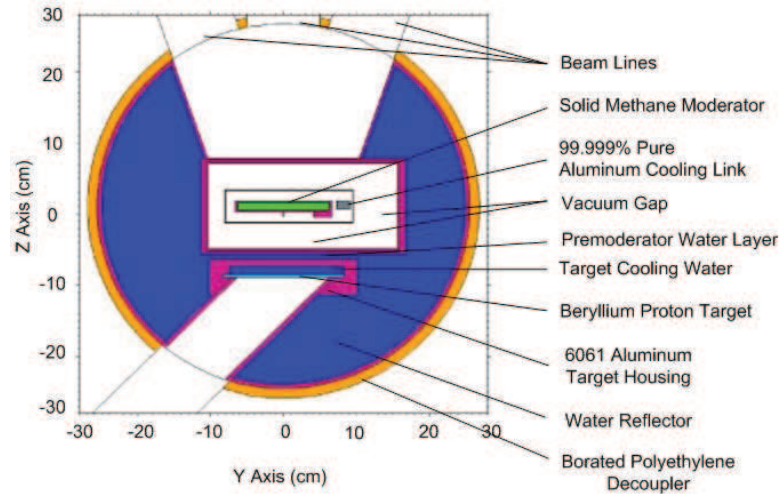
Figure 5.23: YZ Planar view of the TMR geometry. The 1 cm thick methane moderator is at the center, forward of the target and target cooling. The target and moderator are surrounded by a light water reflector of radius 25 cm, decoupled from the shielding layers by a 5 cm thick borated poly layer. Biological shielding layers are not shown for clarity, but are included in the simulations.

Results for the leakage flux (neutrons that escape the TMR system) on the central beam line at the 5.7 m sample position are shown in Figures 5.24 and 5.25. The

shape of the neutron energy spectra in these configurations show that the increased water near the moderator reduces the slope of the $\frac{1}{E}$ component of the flux (the slope gives the leakage exponent, which is proportional to the escape probability of neutrons from the TMR) and increases the flux at 1 eV (the moderator coupling which is proportional to the total level epithermal flux in the moderator, roughly independent of the primary neutron source type or moderator material) [83], due to reduced leakage of slowing down flux in these configurations. Up to a 30% increase in the integrated yield below 10 meV is possible simply by reducing the size of the vacuum gaps or by inserting polyethylene into the existing vessel. Increasing the premoderator beyond 4.85 $\sim$ 5.85 cm reduces integrated cold neutron leakage.
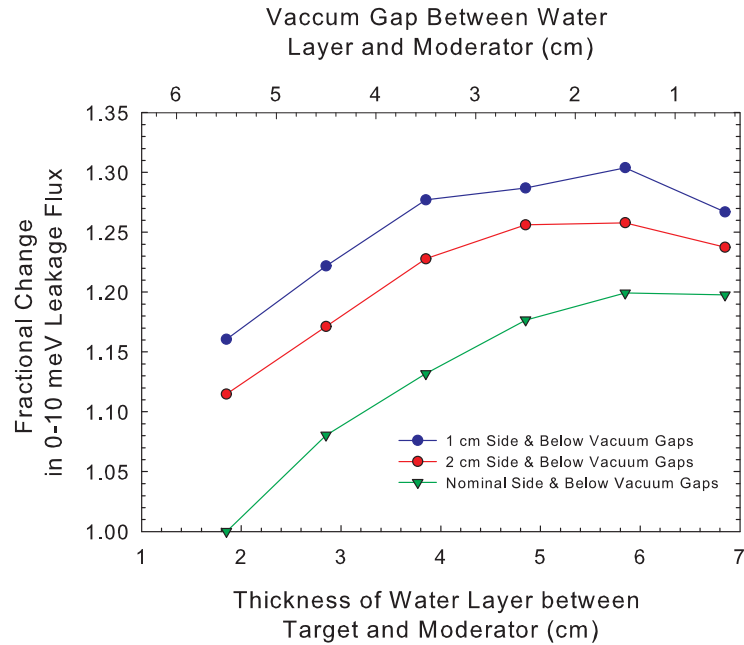
Figure 5.24: A simulation of the cold flux leakage enhancement on the central beam line expected from increasing the thickness of reflector material between the target and moderator. The enhancement is greater if voids along the sides and below the moderator are reduced to a minimal 1 cm from the moderator vessel surface.
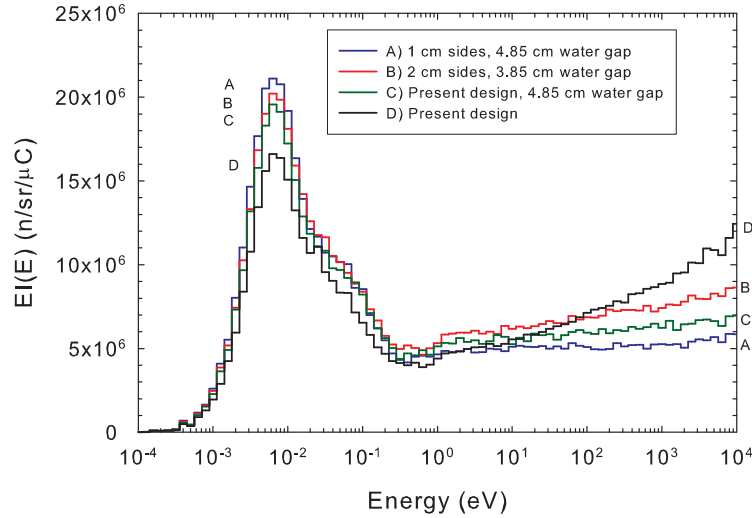
Figure 5.25: Simulations of neutron energy spectra for representative configurations from Figure 5.24 show the impact of water premoderator layer thickness and vacuum gap thickness on cold neutron leakage flux. The optimal Case (A) minimizes vacuum gaps and optimizes premoderator thickness. Case (B) has less cold flux than Case (A) due to enlarged side gaps. Case (C) is similar, where present design's current side gap thickness is unchanged and premoderator layer alone is optimized. Case (D) is the present design, where the high leakage from the TMR causes the slope of the 1-10^4 eV flux to increase while at the same time reducing coupling between the moderator and reflector.

5.5.4 Neutronic Impact of Departures from Optimal Configuration

Some features of the realistic design model were modified in the constructed configuration due to various pragmatic constraints and to allow for the possibility of a 5 cm thick moderator during early moderator studies. These changes were incorporated into a new *As Built* neutronic configuration for comparison to experiments. Changes to the optimized geometry include:

- Higher fidelity target cooling system model, more accurate target position in reflector.

- Introduction of larger cryogenic vacuum cavity

- Exclusion of largeer amount of water between target the vacuum cavity

- Reversal of aluminum rod bend void into the neutron beam path

- Reduced size of polyethylene plug in cryogenic gallery with more accurate rendering of cryogenic gallery.

- Higher fidelity elemental composition of structural materials

- Use of borated epoxy/lead pellet material instead of pure lead in thin lead layer.

- Inclusion of SANS collimation

- Beam line shielding not included as it was not constructed for the prototype TMR.

- New MCNP Geometry highly modular for easy modification, although not as computationally efficient.

The impact of the departures from the neutronic design can be seen in the leakage flux on the central beam, shown in figure 5.26, for 13 MeV proton energy. The cold flux ($E < 10$ meV) is a factor of 1.80 down from the neutronically optimized design, and a factor of 1.49 down from the "realistic" optimized neutronic design. The main culprit in the deviation is the combination of decreased thickness of water gap and larger amount of vacuum space around the moderator as we have discussed . The dependence of horizontal and vertical gaps is weaker than the sensitivity to the water gap. In the previous section we have shown how increasing it can restore 30% of the lost flux. Another major contribution is from the approximate model of target cooling as water jets in the design geometries, which effectively surround the production target with much less aluminum than is practical. In the design model,
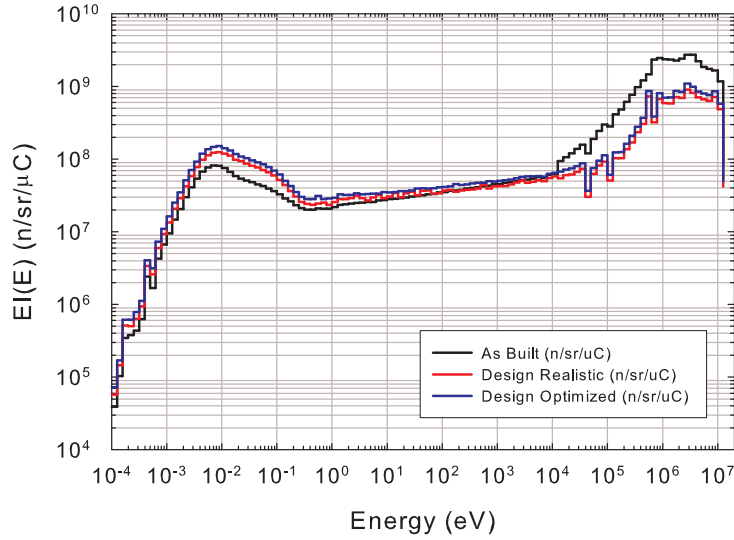
Figure 5.26: Neutron Spectra for 13 MeV proton on each beamline at 570 cm from the moderator face.

the aluminum surrounds the target. The missing water can be seen in the increase in uncollided neutron flux at the MeV energies in the as built model. Finally, the target is translated a bit farther forward in the design geometry, allowing for more water behind the target to reflect the backscattered neutron flux. We shall see in the next chapter that the as built configuration accurately models the constructed TMR as confirmed by experiments.

5.6 Calculation of Cryogenic Radiation Load

The heat deposited by neutron and gamma radiation in the moderator and in the cryogenics linkages will be removed by a CryoMech PT410 commercial He refrigerator [107]. Bench tests with the moderator and an electrical heater connected to the moderator vessel showed that the PT410 can achieve temperatures below 10 K provided that the heat load applied to the vessel is less than 3 Watts (see Table 5.5). To achieve a comparable level of radiation heating in simulation, we need to optimize

Applied Heat (W)	Lower Cooling Link Section Temp(K)	Moderator Vessel Temp (K)
0.0	3.8	4.9
1.0	5.9	7.3
2.0	7.2	8.9
3.0	8.3	10.2
4.0	9.1	11.3
5.0	10.0	12.3

Table 5.5: Cryogenics response to applied heat. To ensure sub 10 K temperatures are achievable, the total radiative heating of the cryogenics must be less than 3.0 Watts.

the location of the cryogenics within the TMR and then optimize the geometry of the cryogenic linkages themselves.

The two major considerations are streaming neutrons and radiation heating from neutrons and gammas. The penetration introduced into the reflector will lead to fast neutron streaming, which could potentially activate the system and generate additional heat in the linkages. Collisions with fast neutron flux, gamma radiation from neutron capture, and decay of activated products in the cryogenics all add additional radiation heating. A variety of configurations were simulated at proposed full power operations to determine the optimal balance of maximum cooling link cross-sectional area (for higher cooling power) and minimum radiation heating.

5.6.1   Attenuating the Neutron Flux incident on the Cryogenics

The position of the PT410 is at 50 cm vertical, and 50 cm horizontal from the center of the reflector to reduce the total neutron flux on the unit by 10^{-6} and keep it out of the line of sight of the target. The arrangement is shown in the as built configuration in Figure 5.22. The PT410 is linked to the moderator by a 99.999% pure aluminum

plate (high purity significantly increases heat conduction at low temperature) with a 90 degree bend to reduce the streaming flux incident on the unit. The primary structural material throughout the rest of the TMR is 6061 aluminum to keep long term activity in the moderator area low. The vertical void introduced above the moderator is filled with a pure polyethylene plug to compensate for the displaced water and to reduce fast neutron streaming.

The Monte Carlo calculations were performed in model geometries, then extended to realistic TMR configurations, to understand the basic properties of the neutron attenuation to arrive at the position at which to situate the PT410. The initial model is a very simple semi infinite slab of 5% (by number) borated poly with a cylindrical penetration with a 90 degree bend. The neutron source energy spectrum is that of the top surface of the moderator, which illuminates the poly through a uniform 60 degree arc.

This simple model facilitates quickly understanding the transport without having to account for extraneous elements of the TMR system, though we shall see it in fact agrees quite well with simulation in the full TMR geometry. Obtaining an accurate estimate of the neutron flux at the position of the PT410 requires variance reduction techniques due to the large reduction in flux compared to the moderator region. Finding the optimal variance reduction scheme can be a process of trial and error; it is far more efficient, both in altering input files and in computation speed, to optimize the variance reduction in the simple geometry. We can then import what we find into the complicated realistic case.

The variance reduction technique employed is called *geometry splitting*, where the slab model geometry is subdivided as in Figure 5.27 into several layers. In the Monte Carlo an incoming neutron track is split into N tracks upon entry into a subdivision in the geometry, each with track having $\frac{1}{N}$ of the weight of the initial

track to conserve probability. Splitting is not performed on entry into a void region to maintain independence of the tracks.

The optimized splitting scheme tracks as a function of the geometry is determined stochastically to be a factor of 2 doubling every 5 cm vertically. In regions of strong attenuation of the neutron flux, proper selection of the splitting function keeps the population of Monte Carlo tracks the similar in each cell, and the density of Monte Carlo tracks becomes biased toward regions of the geometry that are difficult to tally in reasonable amounts of cpu time. We must exercise caution however, as this also biases the random walk against regions of *presumed* low importance. Caution must be taken to ensure neglected regions do not contribute to the tally.

At the time these simulations were undertaken, TMR neutronic design work had progressed to the point where a realistic design model, see Figure 5.30 had been developed for an 11 MeV proton source (11 MeV proton source at 2.5 mA was later abandoned in favor of 13 MeV protons at 2.5 mA). The neutron energy spectrum of the neutron source term employed in the slab model is determined from this more realistic model, calculated at the exit surface of the moderator that illuminates the penetration. The results for the realistic case are shown in Figure 5.27 and are consistent with expectations from the simple model, where 6 orders of magnitude of reduction in total neutron flux has been achieved by locating the unit 50 cm vertically and 50 cm horizontally out of line of sight of the production target.

5.6.2   High Fidelity PT410 Flux Analysis

To check the effectiveness of the bend model, the PT410 was modeled at high resolution, see Figure 5.30, from the blueprints provided at the Cryomech website [107]. The results of the analysis show that the energy spectrum of the flux through the volume of the PT410 is given mainly by a weak fast neutron spectrum characteristic
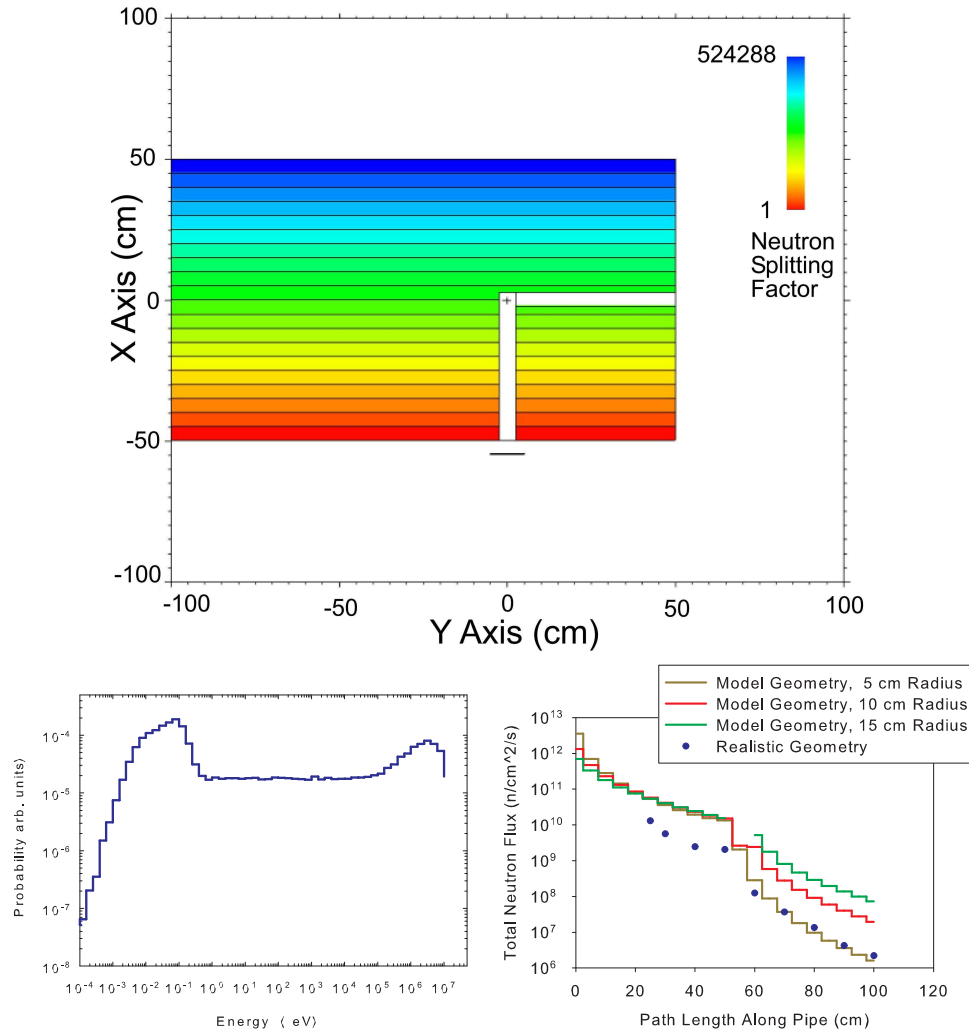
Figure 5.27: Geometry splitting model of neutron streaming in penetration. The is above a surface source of energy distribution modeled from the neutron flux at the moderator surface from a more realistic geometry. The neutrons illuminate the 5% by number borated poly shielding layer through an arc of 60 degrees. The point along the length of the hole at which the flux is sampled is plotted against total neutron flux, where we see attenuations of 10^{-6} are possible, and the bend greatly increases the attenuation. In addition, the realistic model (Figure 5.30) compares well with the simple model.

source flux that has transmitted directly to the unit, a strong slowing down component, and an ambient temperature thermalized part which is also very weak due to the boron loading of the polyethylene. The model geometry and results for integral regions of thermal, slowing down, and source flux are shown in Figure 5.30. Gamma

Figure 5.28: The realistic case geometry model. Orange and Purple: Borated Poly, Yellow: Lead, Green: Water, Light Blue: Methane Moderator, White: Void.
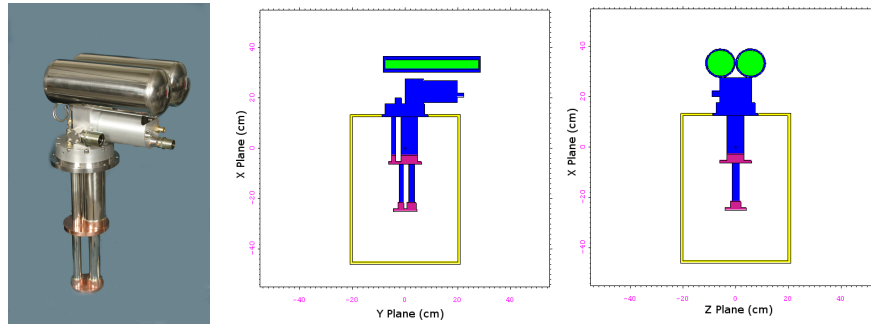
Figure 5.29: *Left:* Cryomech PT410 from [107]. *Center, Right:* Cryostat MCNP Model. Extending from the bottom up, copper linkages and stainless steel tubes form the bottom Stage I, which is attached to the similar Stage I. The topmost stage is connect to a Stainless Steel (SS) flange, pump housing, and helium pulse tubes on the top. Copper (red), Stainless Steel (blue), Helium (green).

flux shows strong lines at 477 keV from neutron capture in boron, 511 keV from pair production, and 2.2 MeV from neutron capture on hydrogen.

Deterministic transport was required to achieve a convergent tally, as indicated by the circles on in the geometry plot. The variance reduction method transports a particle to the surface of the sphere at every collision in the geometry, attenuating the weight by the transmission probability. Once the particle has been deterministically transported to the sphere, it begins a random walk once again, boosting the sampling of the geometry inside the region of the spheres. Two spheres are used, the first
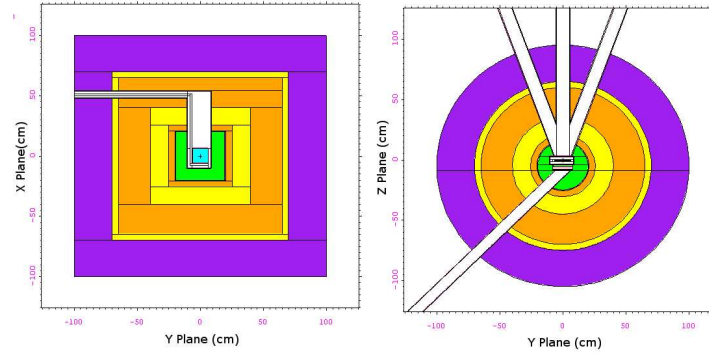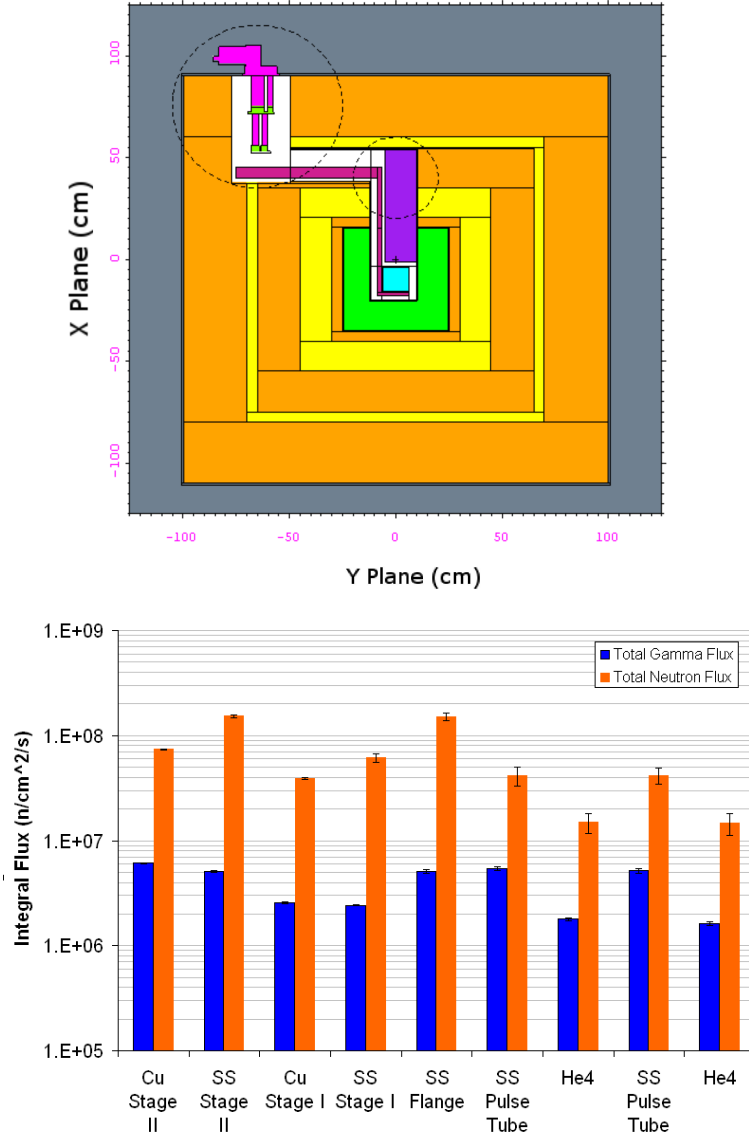
Figure 5.30: The realistic case geometry model. Orange and Purple: Borated Poly, Yellow: Lead, Green: Water, Light Blue: Methane Moderator, White: Void. 1e14 n/sec from source at 13 MeV (2 mA time ave)

transports particles to the bend, the second sphere transports particles to the pt410 region. Using 2 spheres in conjunction models more effectively samples streaming paths through the penetration.

The spectrum is assumed to be similar throughout the PT410, differing only by a scale factor for the the total flux in each component. We assume the copper stage
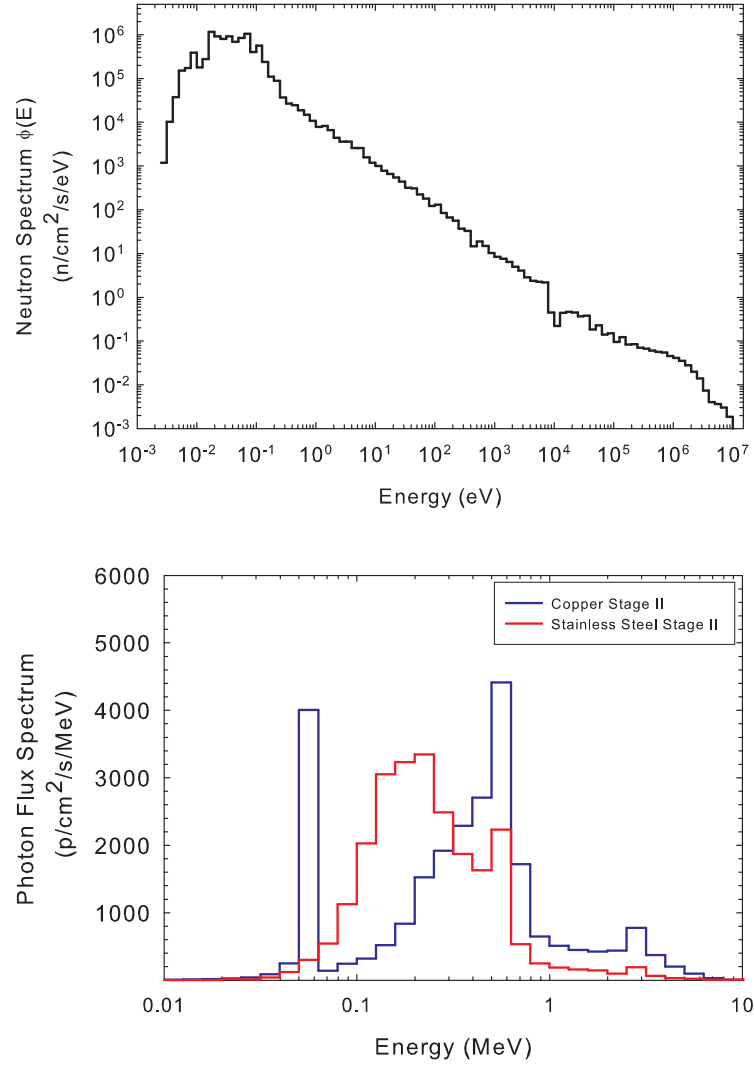
Figure 5.31: *Top:* Neutron flux through lowest copper segment. *Bottom:* Total photon flux in lowest stage.

II yield to represent the maximum possible copper activation, and use the stainless steel stage II to represent the maximum flux in both an aluminum and a stainless steel component. We may now estimate the saturation activity per unit mass , A_s, using the neutron spectrum in Figure 5.31 and the following equation

$$A_s = \frac{1}{\rho}\phi_t \int_0^\infty dE \Sigma(E)\phi(E) \tag{5.11}$$

where ρ is the material density and ϕ_t is given in the bar graph in Figure 5.30. The spectrum, $\phi(E)$, is normalized such that

$$\int_0^\infty dE \phi(E) = 1 \tag{5.12}$$

Results of this analysis for some sample nuclides are given in Table 5.6, and indicate that at full power very limited activities will build up in the PT410. The most susceptible parts would be Stage II components deep within the TMR shielding. Aluminum is found to stand out from a radionuclide standpoint among the other materials even at the PT410 location. The strong (n, γ) reaction in aluminum and its short half-life may lead to full saturation activity activities in TMR components during extended running. We estimate that TMR components, which of course should be always be handled carefully, can be accessed without remote handling after a decay period of 2 days.

Table 5.6: Activity estimation of PT410.

Cross-section, $\Sigma(E)$	Half Life	A_s (Bq/g)
^{27}Al(n, α)	14.96 Hours	567
^{27}Al(n, γ)	2.24 Minutes	35200
^{63}Cu(n, α)	5.27 Years	198
^{63}Cu(n, γ)	12.70 Hours	816
^{63}Cu(n, p)	100.10 Years	823
^{56}Fe(n, γ)	2.74 Years	197

5.6.3   Design Model Result for Radiative Heating

A configuration of 1.8×2.0 cm^2 in the cooling link gave total deposited power of 1.68 Watts (including decay activity). The estimated heat load on the cryogenics was calculated in MCNP by tallying energy deposition from neutrons and the gamma rays produced by neutron capture. The dominant source of gamma flux produced

by proton reactions in the beryllium target is the 3.5 MeV gamma ray from the ^{9}Be(p,α)^{6}Li reaction, and is modeled in a second simulation using an isotropic 3.5 MeV gamma ray source uniformly distributed throughout the target volume and normalized to 10% [41] of the primary neutron yield. In all cases, energy transferred to electrons is assumed to be deposited locally. Results from the MCNP analysis are given in Table 5.7. The Poly Plug and Thermal Shield are only in contact with the 1st stage of the refrigerator, which does not achieve 4 K temperatures but has a much higher cooling power than the 4 K 2nd stage. Thus, we compute that 595 mW goes into the 1st stage and only the remaining 895 mW is a load on the cryogenic elements related to moderator cooling.

Table 5.7: Contribution of various components of the radiative heating in the cryogenics and moderator.

Cryogenic Element	Neutron (mW)	Capture Photon (mW)	Target Photon (mW)
Methane	420	23.1	36.3
Moderator Vessel	83.0	0.0830	12.7
Fill Tube	7.7	18.8	26.3
Fill Tube Nib	0.3	1.18	1.12
Aluminum Bar	12.3	51.8	43.8
Fill Tube Segment	0.464	5.56	2.08
Fill Tube Segment	0.02	0.275	0.0585
Moderator Flange	0.767	3.53	2.71
Poly Plug	267	122	43.0
Thermal Shield	16.2	72.4	74.8
Total	**751**	**382**	**357**

Decay gamma and beta heating from activated aluminum is not included in the MCNP calculations, but was estimated from the calculated volume averaged fluxes in each element. At saturation, we expect this to be less than 182 mW of additional heating from the build up of radioactive products (dominated by the ^{27}Al(n,γ) reaction) over the course of long term running at full power.

5.7   Shielding Considerations

The leakage flux of neutrons and gamma rays not in the main beam is a source of background in measurements and potentially dangerous radiological dose. For LENS to succeed in achieving low backgrounds and safe operating conditions the TMR must be encased in neutron and gamma shielding. The sources of radiation are gamma rays produced in the target (predominantly 3.5 MeV) during proton bombardment, highly penetrating primary neutron flux, collided neutron flux (both slowing down and thermal), and gamma rays produced by neutron capture in the reflector and shielding. The vast majority of the gammas produced are from the reflector, but those may not be the only ones of importance to the instruments, since capture in the shielding may be more likely to send a gamma into the detector. Also, target gammas have a non-zero probability to transmit directly to the sample position. As we will discuss, neutrons are generally shielded by low Z materials, and gamma rays by high Z materials, leading to a matrix of boron loaded polyethylene and lead as the LENS radiation shield.

5.7.1   Calculation of Dose

The conversion of neutron flux to radiological dose is given by an integration of the neutron flux with the appropriate response function or kerma, $R(E)$,

$$D = \int_0^\infty dE R(E)\phi(E) \tag{5.13}$$

Several institutions, including ANSI, ASTM, IAEA, ICRU, ICRP, and NCRP maintain dose standards determined from measurement and calculation of the the effect of primary and secondary ionizing radiation on tissue and tissue phantoms. Kerma and response functions are tabulated by these groups which represent the equivalent

dose delivered to the entire body (whole body dose), to extremities such as the skin or the hands and feet, or even the dose delivered to electronics. We study whole body dose equivalent in these calculations, employing the ANSI 1977 standard for whole body neutron and gamma dose calculations, shown in Figure 5.32.
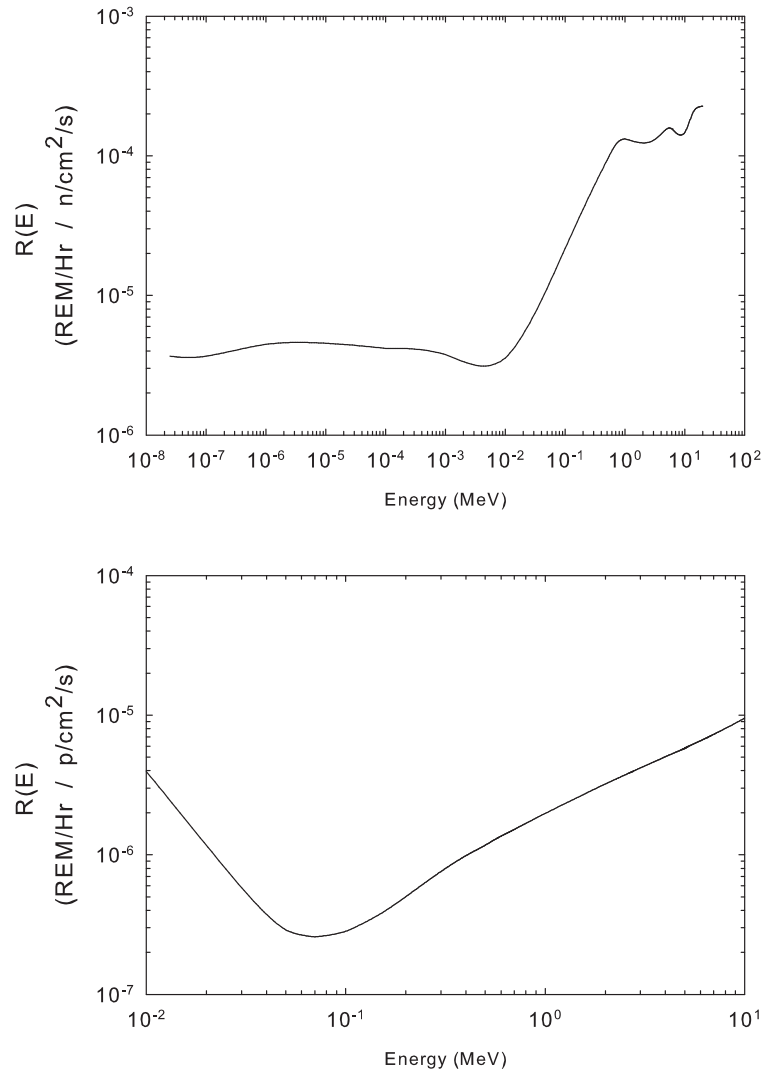

Figure 5.32: ANSI/ANS-6.1.1-1977 standards for *Top:* Neutron R(E) for whole body dose *Bottom:* Gamma R(E) for whole body dose.

5.7.2   Methods of Dose Reduction

Because MeV neutron flux is so much more damaging to tissue than slowing down or thermal neutron flux, the main consideration in the shielding of neutron flux is the attenuation of the highest energy neutrons. Also, because neutron cross-sections tend to increase as energy decreases, if one can effectively shield in the highest energy neutrons then the lower energy neutrons will be effectively shielded as well. Fast neutrons are highly penetrating, and due to the $\frac{1}{v}$ nature of neutron absorption, generally impossible to absorb directly. Thus, neutron shielding is multi step process.

We must place enough material of sufficiently short mean free path between the region to be shielded and the primary neutron source to attenuate the line of sight uncollided primary neutron flux. If the neutron energy is below the ~ 5 MeV, this is efficiently accomplished using hydrogenous materials, though for $\gtrsim 10$ MeV neutrons this requires materials such as steel or graphite. Iron alone is not a good fast neutron shield because of a "window" in the neutron cross section in the keV region, leading to very high transmission of slowing down neutrons through the shield at these energies.

Next, we must thermalize the collided neutron flux to both reduce its ability to damage tissue and to make it possible to absorb the neutrons. This is accomplished by using a hydrogenous material loaded with a thermal neutron absorber, such as borated polyethylene (borated poly). The choice of neutron absorber must be considered as well. Boron emits 477 keV gamma rays upon neutron capture, whereas lithium does not emit gamma rays when capturing a neutron. Thus, when shielding near a sensitive detector, lithium loaded materials may be considered. Also, when using a hydrogenous absorber one must consider that the fast and slowing down neutron flux in the absorber material will *not* be absorbed, and in fact the neutron density of detectable slowing down flux may *increase* in the region of the hydroge-
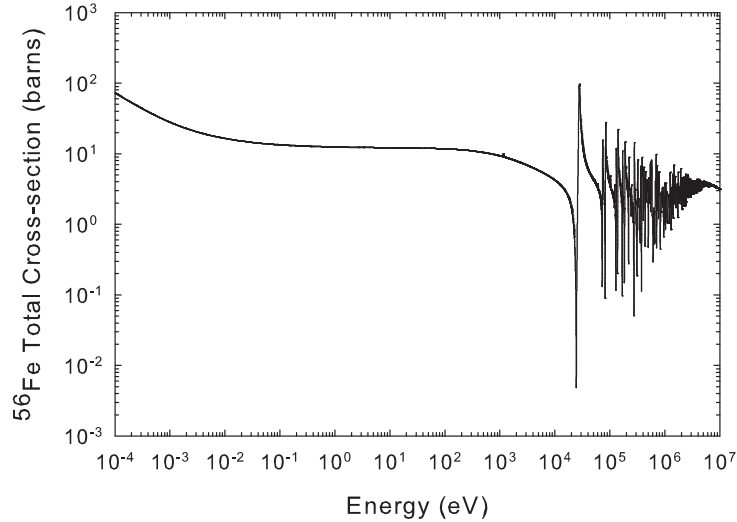
Figure 5.33: ^{56}Fe cross-section [65]. Note the window at 24.5 keV, making iron a poor fast neutron shutter. Neutrons slow down in the iron until reaching $\sim$25 keV, then transmit with very little attenuation.

nous shielding material. Thus, very near neutron detectors, hydrogenous absorbers should be avoided as they can become a source of background.

Finally, the gamma flux must be addressed. At LENS, this problem has many facets. We must attenuate the 3.5 MeV gamma rays from the target must as well as the 2.2 MeV gamma rays from neutron capture on hydrogen in the water reflector. The capture gamma rays produced in the borated shielding layers must be attenuated due to the phenomenon of *dose buildup* [108], shown in Figure 5.35. At certain depth in the neutron absorber, gamma dose from neutron capture (which is not strongly attenuated by the hydrogenous material) will actually exceed the neutron dose.

Gamma flux is attenuated by collisions with electrons, so high Z materials of heavy density are ideal. This means using steel or lead, both of which have issues of neutron activation with alloying atoms and impurities. High purity lead was employed because of its very high attenuation and the fact that lead of sufficient purity to reduce activation can be obtained at reasonable cost.

5.7.3   Shield Optimization

To study shielding configurations, 2 simulations are generally required. The first simulates the coupled neutron and capture gamma field for 13 MeV protons, and the second simulates the emission of 3.5 MeV gamma rays from the target. The 3.5 MeV source is approximated as an isotropic point source emitted uniformly from the target volume, normalized to 10% of the target's neutron yield. Albedo from scattering in air and concrete walls in the vault gives small additional dose on surface elements of the TMR and is included. The simulation goal is to achieve the optimal matrix of lead and borated poly for biological shielding and neutron background reduction. Various parameters were studied in detail (see LENS Reports 2,4-6,7,9-22,24,26), however we shall briefly discuss the most essential parameters and methods of calculation. The studied parameters include:

- Boron vs. lithium loaded poly

- Boron content in poly

- Neutron attenuation lengths of flux for candidate materials

- Dose buildup lengths for candidate materials

- Optimized geometry of shielding matrix subject to spatial constraints

- Impact of TMR neutronics on fast neutron flux

- Impact of streaming neutrons from cracks in shielding

It is most economical to place the shielding material as close to the source as possible, and arrangement commonly referred to as a *monolith*. The monolith is then to be enclosed by a concrete vault. The two main goals of the shield design (at 30 kW operation) were identified to be:

- Contact dose inside vault 1 REM/hr

- Contact dose outside vault < 1 mREM/hr.

The shield arrangement was optimized using borated poly and lead in a modular MCNP geometry shown in Figure 5.34. The optimized configuration is an initial thin borated layer to decouple the TMR water from the shielding. This *decoupler* layer reduces thermal neutron activation of the lead. Next, a thick lead layer attenuates target and TMR water capture gamma rays. A thick borated poly layer attenuates fast neutrons, which is interrupted by a thin lead layer to absorb the boron capture gamma flux. A final thick layer of borated poly attenuates the dose to 1 REM/hr on the leakage surface of the TMR. Results from NCRP Report 38 indicate a concrete vault of 1.22 m thickness should attenuate 1 REM/hr of 10 MeV neutron dose to 1 mREM/hr.
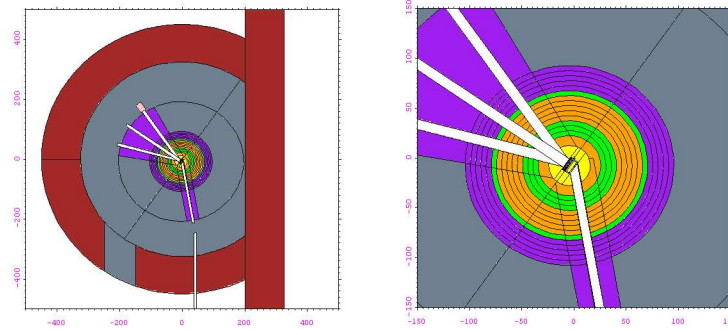
Figure 5.34: Modular MCNP geometry, including concrete vault, used for optimization of shielding layers. Concrete (red), Air (grey), Borated Poly (purple), Lead/Epoxy (green), Water (yellow), Borated Poly (orange).

Any penetration into the TMR leads to line of sight streaming to the production target. Thus, special care was taken to understand the radiation field at the neutron and proton beam lines. Additional shielding is called for at full power operations around these areas to ensure proper concrete wall thickness, but was not constructed

for the initial TMR. In addition, leakage flux from neutron beam lines requires beam line shielding to lower backgrounds and increase safety. Preliminary MCNP designs for this shielding were done, but not constructed for the initial TMR.

The sensitivity to boron loading in the poly is such that at 5% poly (by number) the total dose at the surface of the TMR saturates at a minimum value that is $\frac{1}{7}$ the dose without the boron loading. Increasing the boron loading does not strongly impact the leakage dose. Lithiated poly saturates at only 1% loading, but saturation is only $\frac{1}{4}$ times the unloaded value. Thus 5% borated poly is called for in the TMR design. In practice, shielding bricks of "caramel corn" [1] composed of poly pellets held together with boron loaded epoxy were constructed by B. Donnolly for the TMR monolith. The decoupler is made from a flexible commercial 9% borated poly taped to the outside of the water reflector can.

Figure 5.35 shows the buildup effect in a simulation of an isotropic point source of 15 MeV neutrons at the center of a sphere. The leakage dose at the surface of the sphere is plotted as a function of outer radius. By interrupting the dose build up of gamma flux with a lead layers and using boron loaded poly, we reduced leakage gamma dose by over a factor of 10 in the optimal configuration compared to a configuration that has pure poly layer without a thin lead layer.

Much of the "hot spot" neutron dose around the beam tubes is due to uncollided primary neutron flux, and the dose in these regions is 1000 times higher than on the optically thick sides of the TMR monolith. In addition, streaming from cracks in the shielding layers must also be controlled as the shielding is installed.

Shielding design work was completed by producing high spatial resolution maps of the dose produced by the optimized design model TMR and the surrounding areas, as shown in Figure 5.36. The primary goals of 1 REM/hr contact dose at TMR and 1 mREM/Hr at external concrete wall have been achieved in simulation of 13 MeV
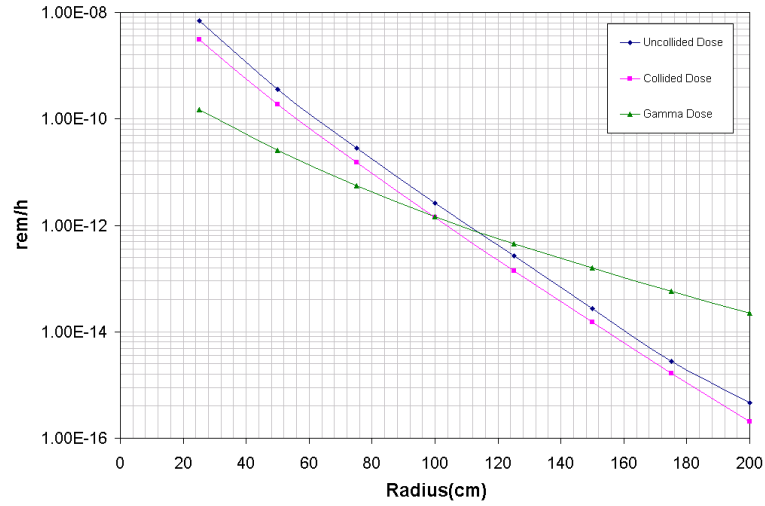
Figure 5.35: A simulated example of gamma dose buildup in 5% borated poly.
The dose is tallied at the surface of a sphere with an isotropic 15 MeV neutron
at the center. Note that at 200 cm gamma dose exceeds neutron dose by almost
an order of magnitude.

protons at 2.5 mA. We note, however, that at this full power level the dose level
within the main neutron beam can be as high as 5×10^3 R/Hr at the vault wall.

5.8   General Results for Instrument Design

General results are presented in this section for the *as built* configuration with 13
MeV proton beam. Results are intended to give general features of the LENS moder-
ator, such as energy, time, spatial, and angular distributions of the emitted neutron
flux, for use in instrument design work.

5.8.1   Neutrons per Photon

Some detection methods are sensitive to the gamma field in the main beam. The
number of neutrons per photon at the sample position at 570 cm on the central
beam line is quantified in Table 5.8. Target gamma production is modeled as an
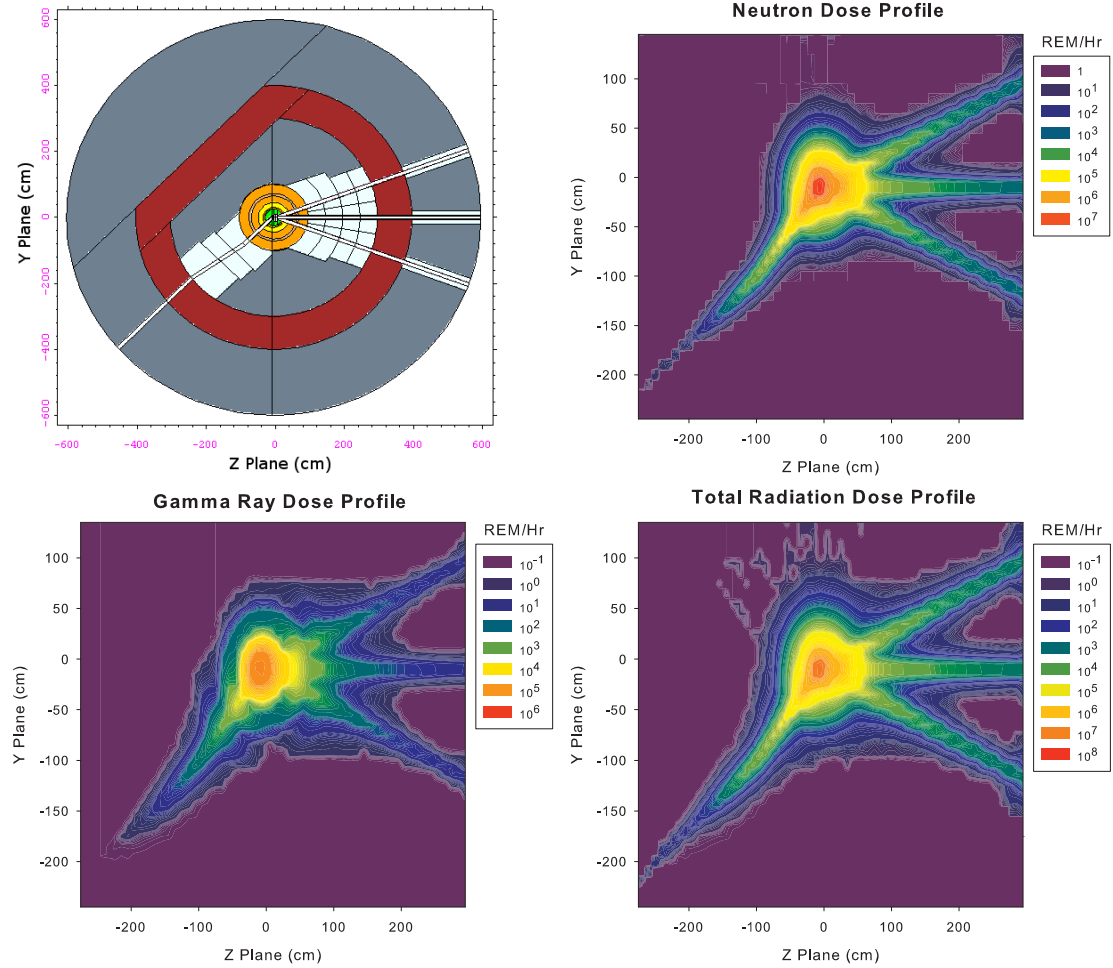
Figure 5.36: Contour map of the expected radiation levels during full power operation (13 MeV protons, 2.5 mA average current) of the optimized final model of the TMR.

isotropic volume source of 3.5 MeV gammas in the target normalized to 10% of the neutron normalization. The neutron flux, neutron capture gamma flux, and target gamma flux are simulated. The total number of neutrons in the main beam is dominated by fast neutrons, and the gamma spectrum is dominated by higher energy (E>500 keV) photons. Of primary interest to instrument design would be the ratio of thermal neutrons in the main beam to capture gamma radiation emitted from the TMR, which is (at sample position in the main beam) 0.63 at 7 MeV and

0.61 at 13 MeV. There are almost 2 photons emitted for every thermalized neutron.

The lifetime of the excited Li state is on the order of ns [109, 110], so target gamma flux will not plague thermal neutron measurements parasitically as they arrive at the detector at least a full millisecond before the thermal neutrons. However, a strong mixed field of gamma and fast neutron of the direct beam during target irradiation, called *gamma flash* or *target flash*, may saturate some types of detectors (notably ^{3}He based gas filled detectors). These detectors would require some time (generally a few ms) to recover before neutron detection is again possible. These calculations neglect neutron transport into the beam lines, which are assumed to absorb all neutrons with the generation of secondary radiation. Future beam line neutron transport calculations and design work should be careful to investigate the impact of neutron capture in beam line elements on the instruments.

Table 5.8: Neutrons per photon

Quantity	7 MeV	13 MeV
Total Neutrons per Photon	4.21	4.37
Thermal Neutrons ($E < 125meV$) per Photon	.12	.12
Fraction of Photon Flux $E > 500keV$	0.799	0.802
Total Neutrons per Capture photon	22.4	22.4
Thermal Neutrons per Capture photon	0.63	0.61
Thermal neutrons per > 500 keV capture photon	0.895	0.844

5.8.2 Angular distribution of flux on moderator surface

We would expect the thermalized neutron flux to be emitted from the instrument side of the moderator with uniform radiant intensity, a L'ambertian distribution. Any directionality of the incident source flux is completely washed away by repeated collisions in the reflector and moderator during thermalization. Fast neutrons should retain some directionality with respect to the moderator normal. In Figure 5.37 we tally the mean cosine of the angle between the neutron current, $\vec{j}$, and the instrument

face of the moderator normal as a measure of beam divergence. Tallies are made both in the forward (flux traveling towards instruments) and backward direction (flux entering the moderator), the quantity plotted is:

$$
< \mu >_{fwd} = \frac{\frac{1}{A} \int_0^1 d\mu \int_{E_i}^{E_i+\delta E} dE \vec{j}(E,\mu)}{\frac{1}{A} \int_0^1 d\mu \int_{E_i}^{E_i+\delta E} dE \vec{j}(E,\mu)/\mu} = \frac{\frac{1}{A} \int_{E_i}^{E_i+\delta E} dE \vec{j}_{fwd}(E)}{\int_{E_i}^{E_i+\delta E} dE \phi(E)} \tag{5.14}
$$

$$
< \mu >_{back} = \frac{\frac{1}{A} \int_{-1}^0 d\mu \int_{E_i}^{E_i+\delta E} dE \vec{j}(E,\mu)}{\frac{1}{A} \int_{-1}^0 d\mu \int_{E_i}^{E_i+\delta E} dE \vec{j}(E,\mu)/\mu} = \frac{\frac{1}{A} \int_{E_i}^{E_i+\delta E} dE \vec{j}_{back}(E)}{\int_{E_i}^{E_i+\delta E} dE \phi(E)} \tag{5.15}
$$

where A is the moderator surface area. The results show strong forward peaking ($\mu > .5$) for high energy flux tending to L'ambertian emission ($\mu = .5$) at lower energies as we expect. However, at 10-100 meV, there is a strong component of the flux that is highly divergent, which we discuss next.
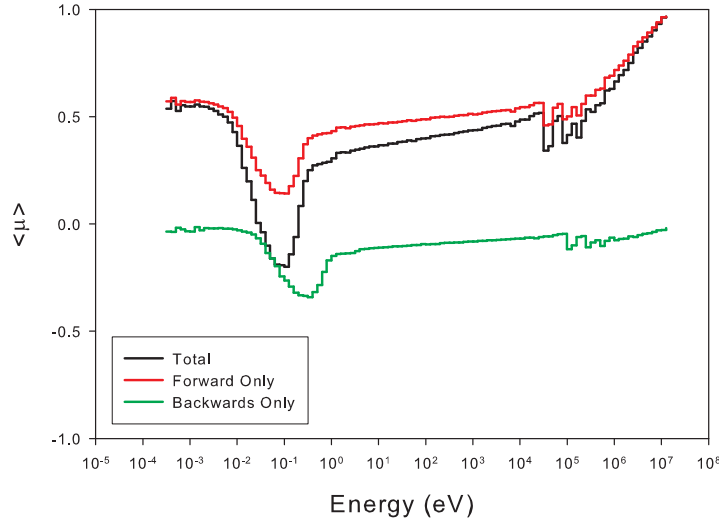
Figure 5.37: Mean cosine of flux passing over the moderator instrument face. A value of 0.5 indicates l'ambertian emission. The dips in the 10-100 meV regime indicate more flux is entering than exiting the moderator at these energies. This is due to the influx of thermal neutrons from the reflector.

An interesting result is present in the analysis of *backward* going flux over the moderator instrument face. This represents current traveling *towards* the TMR. Not

only is it non-zero on the leakage side of the moderator, there is a strong peaking of 10-100 meV flux from the water reflector impinging on the face of the moderator. Inelastic scattering dominates this energy regime in methane, but reflection via equation 4.24 could be expected to occur from the hydrogen in the methane. Also, it shows that return paths of thermalized neutrons into the moderator are important sources of cold flux.

We can see these effects in more detail by looking at integral regimes of cold, thermal, and epithermal neutron energy. The quantity plotted is

$$\phi(\mu) = \frac{1}{A} \frac{1}{2\pi\delta\mu} \frac{1}{\delta E} \int_{\mu_i}^{\mu_i+\delta\mu} 2\pi d\mu \int_{E_i}^{E_i+\delta E} dE \vec{j}(E,\mu) = \frac{1}{A} < \vec{j}(E,\mu) > \qquad (5.16)$$

As expected, for cold neutrons emission is linear in cosine and negligible for return paths. However, thermal and epithermal show isotropic emission for the forward direction ($\mu > 0$), but peaked emission at $\mu \sim 0.6$ for the return paths.
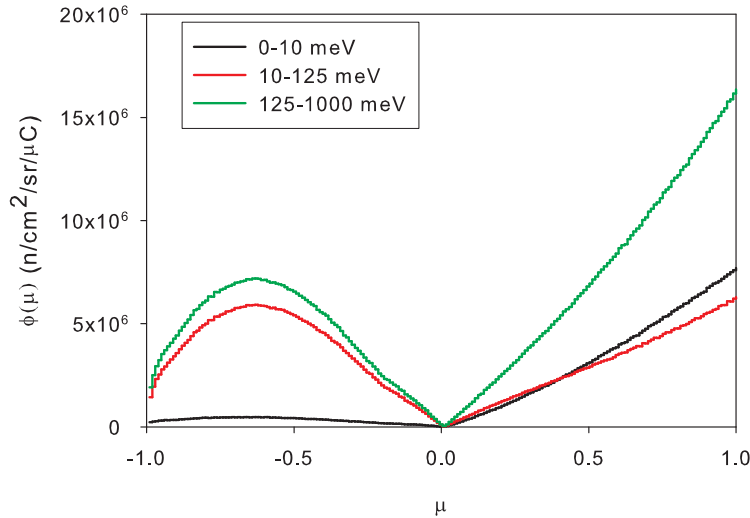
Figure 5.38: Angular distribution of low energy groups. Emission is l'ambertian (linear in cosine) in the forward direction and, negligible for backward for low energy. There are peaks in the thermal and epithermal flux regime from return paths into the moderator.

5.8.3   Spatial distribution of flux on moderator surface

The mean free path of cold neutrons in the methane is 1.5-2.0 mm, so most of the cold flux leakage is from a thin layer at the instrument face of the moderator. To investigate the spatial distribution of the flux over the moderator, we integrate the flux over the last 2 mm of the moderator instrument face in a 2 mm wide transects in the vertical (x plane) and horizontal (y plane) directions for several energy regimes. The quantity plotted, relative to the moderator instrument face center, is

$$\phi = \int_{E_i}^{E_i+\delta E} dE \int_{0.9cm}^{1.0cm} dz \int_{-0.1cm}^{0.1cm} dx \int_{-0.1cm}^{0.1cm} dy \phi(E,\vec{r}) \qquad (5.17)$$

We find that cold neutron flux is fairly uniform across the face of the moderator,
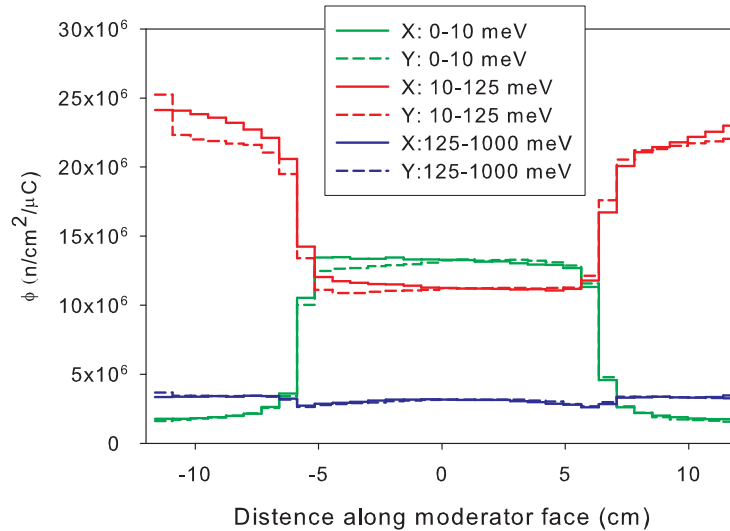
Figure 5.39: Spatial distribution of flux on the moderator surface. Cold moderator extends from -6 to 6 cm.

dropping to an intensity representative of the cold flux present in the tail of the water moderated ambient temperature flux off the moderator face. The thermal group is actually much lower *in* the moderator volume. This is because the thin LENS moderator is a sink of thermal flux as it cools the thermal flux to cold flux.

Finally, we see a small boost in intensity for epithermal flux as the methane has a higher hydrogen density and moderates more effectively than water. However, the epithermal flux has a mean free path on the order of 5.5 mm in the methane, compared to 2 mm to 3 mm for thermal flux, such that about 30% of the epithermal flux transmits through the moderator.

5.8.4   Emission time, Mean offset $\bar{t}(t)$

The emission time distribution is simulated by tallying the leakage of neutrons over the instrument side of the cold moderator face in a forward cone convolved in time with a 150 μs proton pulse square proton pulse as employed in the experiments. A fairly broad cone ($\cos\theta > 0.95$) is accepted in the calculation to enhance Monte Carlo statistics while still retaining some fidelity in representing the conditions of the experimental measurement.

Figure 5.44 shows the emission time distribution for several low energy neutron groups for a 150 μs proton pulse, and the FWHM is shown in Figure 5.12. The neutron emission rises during the proton pulse then decays over a time period that is consistent with the characteristic decay time in the large water reflector. The FWHM at high energy is dominated by the proton pulse width, then increases for $E < 0.1$ eV, as more collisions are required to slow the neutrons to lower energies. As the neutron energy becomes comparable to the moderator temperature (< 0.01 eV) the neutrons become equally likely to gain or to lose energy in a collision (quasi-equilibrium), and the emission time FWHM saturates at $\sim$325 μs. The lifetime of these neutrons in the TMR system saturates as the flux is attenuated by the mean absorption of the the quasi-equilibrium flux in the moderator and reflector.

Long emission times lead to an energy dependent offset in the mean time required to emit after the *start* of the proton pulse. We call this term $\bar{t}(t)$, calculated

in simulation via Equation 5.20 and 5.21.

$$E = \frac{1}{2}m\frac{L^2}{t^2} \tag{5.18}$$

$$\bar{E} = \frac{1}{2}m\frac{L^2}{(t-\bar{t})^2} \tag{5.19}$$

$$\bar{t} = t(1 - \sqrt{\frac{E}{\bar{E}}}) \tag{5.20}$$

$$\bar{E}(t_i) = \frac{\int_{t_{i-1}}^{t_i} dt \int_0^\infty dE\,\varepsilon(E)E\phi(E,t)}{\int_{t_{i-1}}^{t_i} dt \int_0^\infty dE\,\varepsilon(E)\phi(E,t)} \tag{5.21}$$

where t_i is the ith time channel upper bound, and ε is the detector efficiency, which in this case is given by the ^{3}He(n,p) reaction. $\bar{E}(t)$ is calculated at the position at which spectra are taken in the measurement, and $\Delta T = t_i - t_{i-1}$ is chosen to reflect the 100 μs channel width employed in the experiment. The inclusion of weighting the flux by detector efficiency controls whether the detector "sees" mean energies closer to the end or the beginning of the time channel. However, simulations of unit efficiency, $\frac{1}{v}$ efficiency, and high efficiency show less than 5% deviations between the resulting t_o for 570 cm, SANS beam line with 150 μs proton pulse, so we employ the $\frac{1}{v}$ efficiency result.

This approach was in fact suggested by Ikeda and Carpenter [76], but neglected in their analysis of IPNS pulse shapes because $v\bar{t}$ was $\leq$ 5 cm for total flight paths lengths of 7.55 m and 12.87 m. At LENS, $v\bar{t}$ is $\sim$ 90 cm for 200 meV neutrons, and $\sim$ 50 cm for 10 meV neutrons, both of which are significant fractions of the 570 cm flight path. Also, the correction changes factor changes rapidly in the 30-200 meV regime as the neutron pulse shapes transition from the 150 μs wide square pulses at higher energy to the longer "charging and discharging" pulses at low energy, as seen in Figure 5.44 and 5.12. However, we note that $\frac{\bar{t}}{t}$ for E < 1 meV is less than 3%
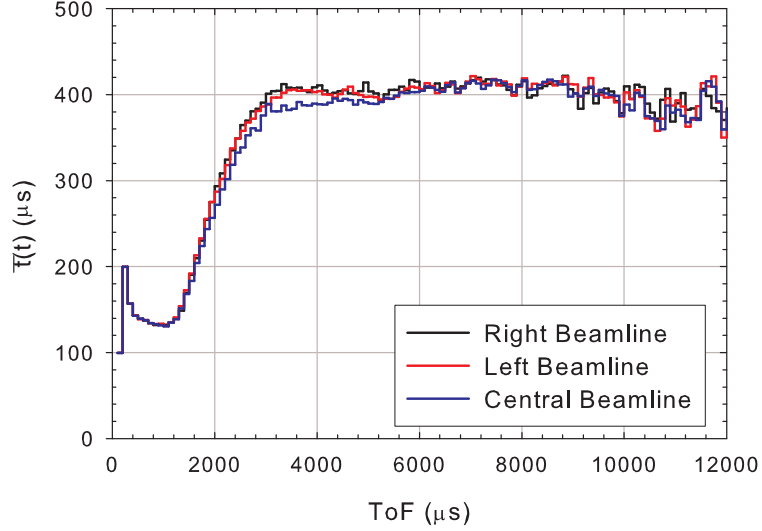
Figure 5.40: $\bar{t}(t)$ calculated in MCNP for 570 cm from the moderator on each beam line.

of the ToF, so at long time scales (low neutron energy) the impact of $\bar{t}$ is minimal. In the next Chapter 6 we will show how $\bar{t}$ perturbs the ToF-energy relationship in neutron spectroscopy measurements.

5.8.5   Neutron Spectrum and integral yields at full power

The neutron flux was simulated for each beam line at 570 cm at 13 MeV. The beam line characteristics are given in table 5.9. The -20 (SANS) degree beam line has ideally modeled 2 hole converging collimation given by 7.62 cm diameter at 140 cm, 1.27 cm diameter at 570 cm. Integral yields of neutrons are given for each beam line in Table 5.10

5.8.6   Comparison to IPNS

To gain experience with neutron spectroscopy measurements, we took data on several IPNS beam lines in coordination with the CD4 commissioning measurement at SNS

Table 5.9: Modeled beam line characteristics

Beam Line	Right	Left	Center
Angle to moderator normal (degrees)	+20	-20	0
Instrument	Radiography	SANS	Development
Modeled Collimation	None	Yes	None
Beam Line Geometry	Circular	Circular	Square
Beam Line Width	10 cm dia.	10 cm dia.	10×10 cm^2

Table 5.10: Table of simulated integral neutron yields on each beam line for 13 MeV protons. Units are $10^6 n/sr/\mu C$.

Energy Range	Wavelength Range (Å)	Right	Left	Center
< 0.20 meV	> 20	0.137 ± 0.0030	0.128 ± 0.003	0.202 ± 0.004
0.20-0.82 meV	10-20	2.447 ± 0.0169	2.281 ± 0.016	3.560 ± 0.020
0.82-3.27 meV	5-10	25.652 ± 0.069	23.564 ± 0.064	36.505 ± 0.084
3.27-10 meV	2.86-5	55.865 ± 0.112	51.022 ± 0.102	76.823 ± 0.138
10-125 meV	0.809-2.86	97.308 ± 0.185	82.602 ± 0.132	103.084 ± 0.186
125-550 meV	0.385-0.809	24.759 ± 0.104	21.612 ± 0.089	28.599 ± 0.109
1 eV coupling	0.286	18.178 ± 0.165	16.446 ± 0.171	22.241 ± 0.182

[50, 57]. Typical IPNS proton currents are 15 μA, which compare favorably here to 2.5 mA, 13 MeV proton currents at LENS. Figure 5.42 compares the LENS design to these measurements and shows that LENS design may achieve competitive neutron intensities at long wavelengths when full power operations begin.

5.8.7   Calculated As Built Performance for SANS Beam Line

Simulated neutron energy leakage spectra (Figure 5.43) are calculated for a beam port viewing the moderator at 20 degrees from the moderator surface normal for three cases of a) 7 MeV proton energy with an empty moderator vessel, b) 7 MeV proton energy with a 22 K methane moderator, and c) 13 MeV proton energy with 22 K methane moderator. The quantity calculated is:

$$EI(E) = \frac{L^2}{\dot{i}} E\phi(E) \tag{5.22}$$
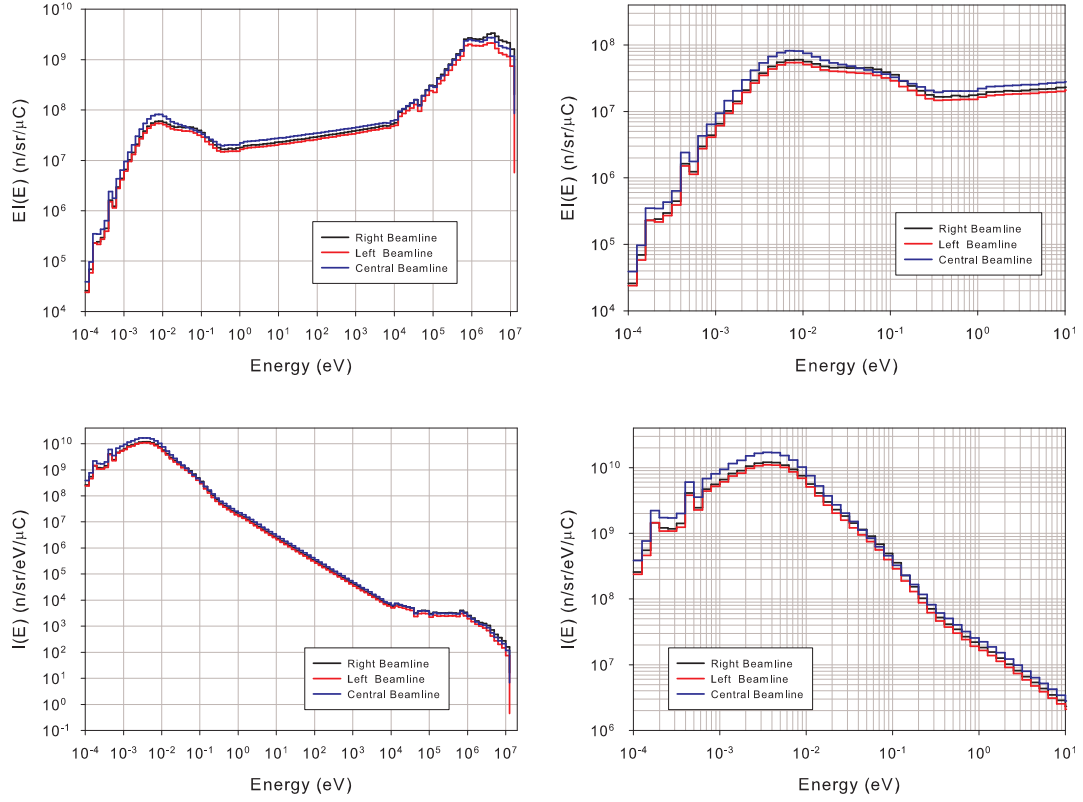
Figure 5.41: Simulated neutron spectra for 13 MeV protons on the three beam lines.

where E is the neutron energy, $I(E)$ is the luminous intensity in units of $n/sr/uC/eV$, L is the flight path length in units of cm, i is the time averaged proton current, and ϕ is the neutron flux in n/cm^2/s/eV. Calculations presented are for the prototype SANS beam line (-20 degree beam line), which has 2 pin hole collimation, and is where experiments were performed. The 2 hole collimation is modeled ideally in simulation as a 7.62 cm diameter hole at 140 cm from the moderator face, and a 2.54 cm diameter hole at 570 cm.

$EI(E)$ is the unit of flux if energy is expressed in terms of lethargy, $ln(\frac{E_o}{E})$, where E_o is a reference energy for moderator coupling, typically 1 eV [83]. It is advantageous to use this unit because lethargy is the natural unit in neutron slowing down theory and the relative height of each energy channel is proportional to the
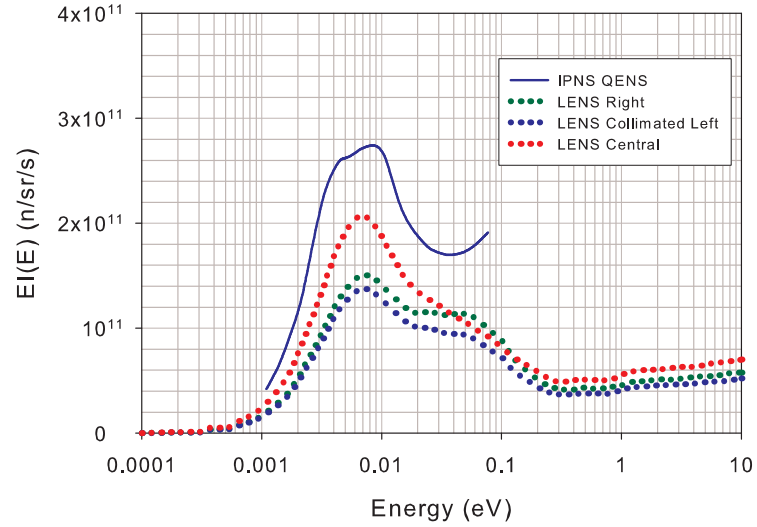
Figure 5.42: Comparison of LENS 13 MeV at 2.5 mA time average current to IPNS QENS, IPNS H Moderator at 15 μA time average current. The LENS moderator is modeled as $12 \times 12 \times 1$ cm^3 thick 22 K coupled methane slab, and the H moderator experimental measurement [50] is a $10 \times 10 \times 4.5$ cm^3 thick cadmium poisoned and decoupled 28 K methane slab.

integral number of neutrons in that channel. Integral yields, Y in units of $n/sr/\mu C$, are determined from equation 5.23 and given in Table 5.11.

$$Y = \frac{L^2}{i} \int_a^b \phi(E) dE = \int_a^b I(E) dE \qquad (5.23)$$

Table 5.11: Table of simulated integral neutron yields on collimated SANS prototype beam line. Units are $10^6 n/sr/\mu C$.

Proday Energy and Moderator	7 MeV Water	7 MeV 22K Methane	13 MeV 22K Methane
0.20-0.82 meV	0.0091 ± 0.005	$0.463 \pm .024$	2.28 ± 0.02
0.82-3.27 meV	0.304 ± 0.07	$6.35 \pm .09$	23.6 ± 0.06
3.27-10 meV	1.719 ± 0.053	$10.37 \pm .05$	51.0 ± 0.1
10-125 meV	44.30 ± 0.80	$19.03 \pm .18$	82.6 ± 0.13
1 eV Coupling	5.35 ± 0.09	3.29 ± 0.02	16.4 ± 0.2
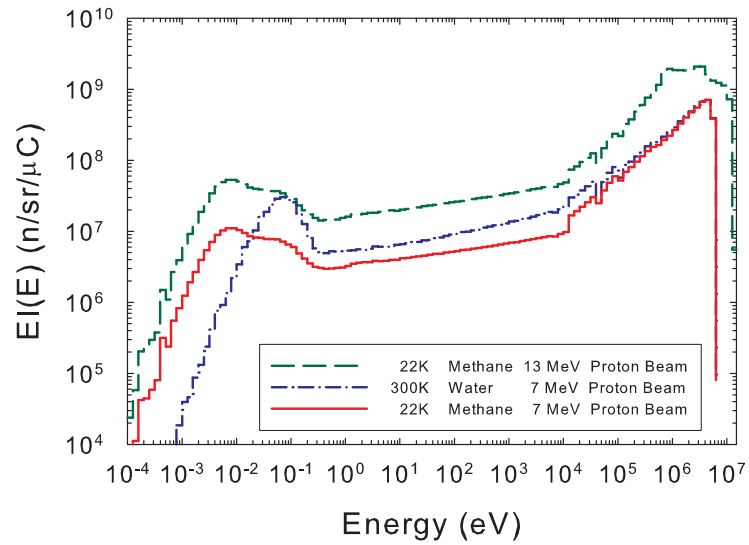
Figure 5.43: Neutron spectrum predicted by MCNP for different proton beam stages of the LENS project. Discontinuities in the 0.01-0.1 MeV range of the fast neutron spectrum are due to attenuation by strong resonances in aluminum. The source term begins at .01 MeV.
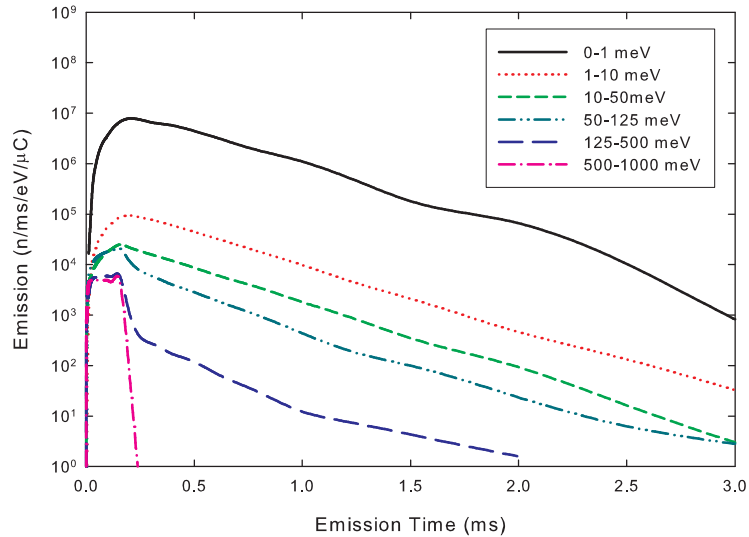
Figure 5.44: Neutron emission time distributions. The water reflector and coupled moderator create long emission times for all low energy neutron groups. The proton beam pulse shape defines pulse shapes of higher energy neutrons (500-1000 meV in this figure).

5.9 Conclusion

We have extensively modeled the LENS TMR. The design effort from 2004-2006 culminated in the construction of the prototype LENS TMR, SANS instrument, and radiography camera. Experimental measurements of neutron performance follow in the next section to validate the fidelity of the as built neutronic model.

Chapter 6

Experimental Benchmarks

> I have not failed.
> I've just found 10,000 ways that won't work.
>
> Thomas A. Edison

6.1   Overview

Experimental measurements of the neutronic performance include neutron time of flight energy spectroscopy measurements with gas filled detectors, foil activation measurements of integral flux, and emission time measurements with a time focussing crystal analyzer. In this section we compare the results of these measurements with expectations from simulation in the as built neutronic model.

6.2   First Neutrons

First neutrons were produced December 15, 2004, where a polyethylene moderator was employed place of the cryogenic gallery. Commissioning operations began afterwards, largely parasitically to accelerator development work and NRERP users.

Figure 6.1 shows the first neutron beam recorded on the SANS instrument area detector.
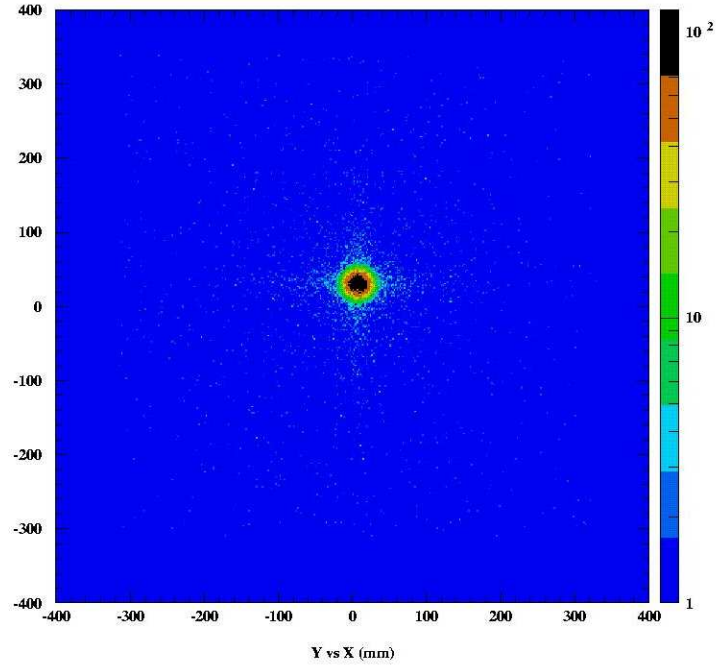
Figure 6.1: Beam spot on the SANS area detector from first neutrons at LENS, December 15, 2004.

6.3   Normalized Spectra

6.3.1   ToF Measurement

We use the standard technique [50, 111] for measuring moderator spectra, but with a slight modification to account for the longer pulses. In the standard technique, the count rate in the detector is related to the flux through:

$$C(t) = \Delta T A \varepsilon(E) \phi(E) \frac{dE}{dt} \tag{6.1}$$

where $C(t)$ is the counts per unit time at time t after the start of the proton bombardment of the target, A is the area of the neutron beam on the detector, ΔT is the time channel width, and $\phi(E)$ is the neutron flux. The neutron detector employed is a thin ^{3}He detector manufactured by LND [112]. The fill gas of the detector is 3 Torr ^{3}He with 38 Torr N_2 as a quench gas and 719 Torr ^{4}He as a buffer gas [1], with a 1.91 cm thick active region, and a detection area 10×10 cm^2. The detector efficiency is determined by the pressure and thickness of the ^{3}He absorber:

$$\varepsilon(E) = 1 - e^{-n\sigma \frac{\lambda}{\lambda_o} x} = 1 - e^{-k\lambda} \qquad (6.2)$$

where n is the number density of the neutron absorber, x is the detector thickness, λ is the neutron wavelength wavelength, σ is the absorption cross-section specified at λ_o. Efficiency is linear in wavelength when $k\lambda \ll 1$ (the "thin" detector condition),

$$\varepsilon(E) \sim k\lambda \qquad (6.3)$$

If a thin detector is employed and the conventional energy-time relationship is in place (see Equation 5.18) such that

$$\frac{dE}{dt} = \frac{2E}{t} \qquad (6.4)$$

Then the count rate in the detector is *directly* proportional to the lethargy flux,

$$C(t) = \kappa E \phi(E) \qquad (6.5)$$

where κ is a constant of proportionality.

The long neutron emission time of the coupled moderator and proton pulses have

---

[1]specification provided to LND, Inc. LND quotes tolerance on fill levels of 0.1 Torr.

an effect on the measured spectra, and this will perturb the energy-time relationship. The perturbation can be linked both to the initial proton pulse and the longer times required (in a coupled moderator) for a thermal neutron to diffuse into the moderator from the reflector. This amounts to an average delay in the origin of the time of flight, with respect to the of the start proton pulse, for any particular neutron to exit the moderator before beginning its flight to the detector. We take this into account by defining an average delay, $\bar{t}(t)$, in terms of the measured time of flight[2], t, to determine the correct mean energy for a ToF channel, $\bar{E}(t)$, as shown in Equation 6.6.

$$E = \frac{1}{2}m(\frac{L}{t})^2 \rightarrow \bar{E}(t) = \frac{1}{2}m(\frac{L}{t - \bar{t}(t)})^2 \qquad (6.6)$$

Due to the low power of the LENS source at present, emission time measurements are not yet available at LENS across the 3-4 orders of magnitude range in neutron energies required to fully determine $\bar{t}(t)$. Therefore, we rely on simulation to calculate the mean energy per ToF channel and provide an approximate value for $\bar{t}(t)$, as discussed in Section 5.8.4.

6.3.2   The Implication of $\bar{t}(t)$ for Measurements

The standard technique starts from the Equation 6.1 which itself is a special case of the most accurate representation.

$$C(t) = A \int_{t-\Delta T/2}^{t+\Delta T/2} dt \int_0^\infty dE\epsilon(E)\Phi(E,t) \qquad (6.7)$$

Equation 6.1 assumes the time dependence of $\Phi(E,t)$ in Equation 6.7 is such that *all* the neutron flux of energy E is emitted between $t - \Delta T/2$ and $t + \Delta T/2$. If we

---

[2]Strictly speaking, t is actually the time after the start of the proton pulse. If the emission time distribution were narrow and the proton pulse were short, then t would be the true ToF.

redefine $\Phi(E, t)$ such that the following is true for all energies

$$\Phi(E, t) = \phi(E)\tau(E, t) \tag{6.8}$$

$$\int_0^\infty dt\tau(E, t) = 1 \tag{6.9}$$

then Equation 6.1 is true if the emission time distribution described by $\tau(E, t)$ is very sharp,

$$\tau(E, t) = \delta(t - t(E)) \tag{6.10}$$

where

$$E(t) = \frac{1}{2}mL^2 t^{-2} \rightarrow t(E) = \sqrt{\frac{mL^2}{2E}} \tag{6.11}$$

and $\epsilon(E(t))\phi(E(t))$ in Equation 6.1 is in actuality the *average value* of the quantity, $< \epsilon(E(t))\phi(E(t)) >$, over the TOF channel.
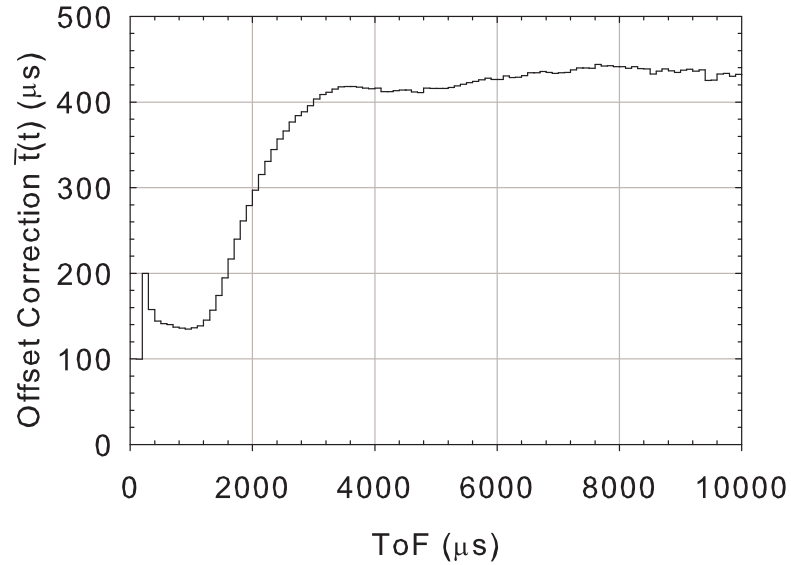

Figure 6.2: The offset term, $\bar{t}$, calculated in MCNP for 22 K methane to give the mean energy in a ToF channel for a detector at 570 cm, 20 degrees to the moderator normal.

Let us consider the case where

$$E \rightarrow \bar{E} = \frac{1}{2}mL^2(t - \bar{t}(t))^{-2} \tag{6.12}$$

and investigate the impact of the time perturbation on a measurement. The use of $\bar{t}(t)$ is a particularly simplified attempt to describe the impact of convolving the emitted neutron spectrum with the complicated emission time distribution.

We will now show how the correction term will impact both the vertical and the horizontal axis of a plot of E vs. $\phi(E)$ compared to an uncorrected plot. We can investigate the horizontal axis first by expressing the energy relationship in terms of the original energy function as

$$\bar{E} = E(1 - \bar{t}/t)^{-2} \tag{6.13}$$

Because $t > \bar{t}(t)$ for all t, $\bar{E}$ will always be greater than E. Thus, the effect of the correction on the horizontal axis will be to stretch the measured $\phi(E)$ in the direction of higher energies relative to uncorrected energies when $t \sim \bar{t}$ while leaving those energies where $t \gg \bar{t}$ largely unperturbed.

The vertical dependence is more complicated. First, we need to evaluate the derivative.

$$\frac{d\bar{E}}{dt} = \frac{dE}{dt}[(1 - \bar{t}/t)^{-2}(1 + \frac{\frac{d\bar{t}}{dt} - \frac{\bar{t}}{t}}{1 - \bar{t}/t})] \tag{6.14}$$

Next, we express Equation 6.1 more simply, as

$$C(t) = \kappa \frac{\phi(E)\frac{dE}{dt}}{\sqrt{E}} \tag{6.15}$$

where we have assumed a thin detector is employed, such that $\epsilon(E) = k\lambda =$
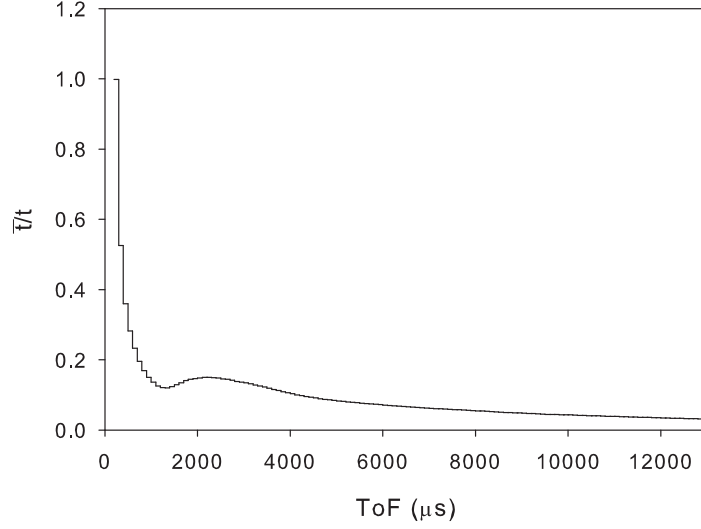
Figure 6.3: A plot of $\frac{\bar{t}(t)}{t}$ shows that for a 5.7 m flight path and 100 μs proton pulse $\bar{t}(t)$ is a significant fraction of the time of flight. Also note that $t > \bar{t}(t)$ for all t.

$k0.286/\sqrt{E}$

$$\kappa = 0.286A\Delta Tk \tag{6.16}$$

Likewise, we define $\bar{C}(t)$ as

$$\bar{C}(t) = \kappa\frac{\phi(E)\frac{d\bar{E}}{dt}}{\sqrt{\bar{E}}} \tag{6.17}$$

If we assume that $\phi(E)$ is slowly varying such that $\phi(E) \sim \phi(\bar{E})$, we have

$$\bar{C}(t) = \kappa\frac{\phi(E)\frac{d\bar{E}}{dt}}{\sqrt{\bar{E}}} \tag{6.18}$$

$$= \kappa\frac{\phi(E)\frac{dE}{dt}}{\sqrt{E}}(1 - \bar{t}/t)^{-2}(1 - 2\bar{t}/t + \frac{d\bar{t}}{dt}) \tag{6.19}$$

$$= C(t)(1 - \bar{t}/t)^{-2}(1 - 2\bar{t}/t + \frac{d\bar{t}}{dt}) \tag{6.20}$$

For the final result

$$\frac{C}{\bar{C}} = \frac{(1 - \bar{t}/t)^2}{1 - 2\bar{t}/t + \frac{d\bar{t}}{dt}} \tag{6.21}$$

$\bar{C}$ represents what we would measure if there is a $\bar{t}(t)$ term in the present in time-

energy relationship. However, recall that Equation 6.5 is directly proportional to $E\phi(E)$, such that our desire is to measure C, *not* $\bar{C}$. Therefore, a plot of t vs. $C/\bar{C}$ reveals the size of the correction required to return the measured $E\phi(E)$ to the true value. Thus, we have the following constraints on the effectiveness of this correction:

- $\bar{C}(t) > C(t)$ if $\bar{t}(t)$ has a sharp positive slope. This is the case in the ToF range corresponding to 1 eV to 30 meV, where in this analysis we would expect the measured intensity to be *less* than the actual intensity.

- If $\phi(E)$ is not slowly varying across a ToF channel such that $\phi(E) \neq \phi(\bar{E})$, the correction algorithm will fail. This is expected to occur for high energies ($\gtrsim 1$ eV).

- At long ToF, such that $t \gg \bar{t}(t)$, the correction should be negligible.
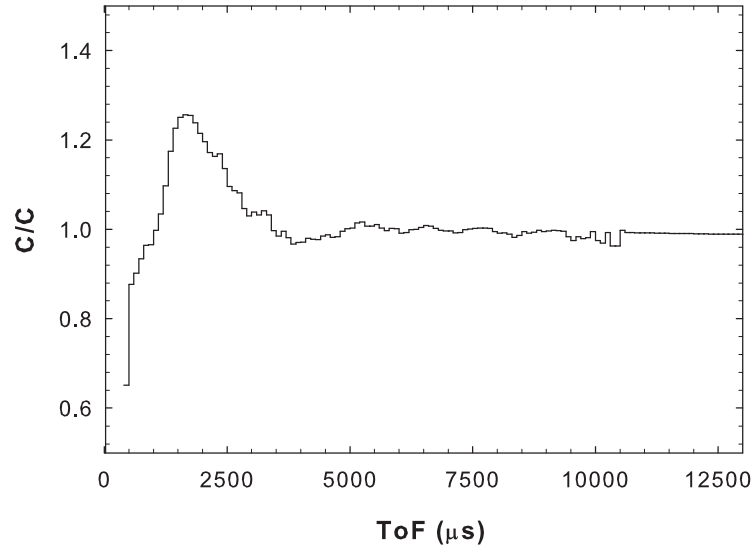
Figure 6.4: A plot of $C/\bar{C}$ shows the size of the expected deviation between the measured flux and the true flux calculated via Monte Carlo. At 3000 μs ($\sim$ 20 meV) the correction to the measured flux may be as large as a factor of 1.3. Because $\bar{E} > E$, the deviation between the measured and true value may be even larger when plotting $E\phi(E)$ due to the multiplication of the flux by the energy and the shift of the measured energy toward the higher energies.

We can check if the correction algorithm is valid by simulating the experiment in MCNP by calculating Equation 6.7. We may also calculate the time independent neutron energy distribution for the same neutron spectrum, which is given by

$$\phi(E) = \frac{1}{\Delta E} \int_{E-\Delta E/2}^{E+\Delta E/2} dE \int_0^\infty dt \Phi(E, t) = \frac{1}{\Delta E} \int_{E-\Delta E/2}^{E+\Delta E/2} dE \phi(E) \qquad (6.22)$$

where as usual we plot the result as

$$\frac{L^2}{i} E\phi(E) \qquad (6.23)$$

If we apply Equation 6.1 to the simulated $C(t)$, we will obtain an estimate of what we might expect in a ToF measurement of the neutron spectrum. If we then compute the measured flux using Equation 6.1 both with and without the correction term $\bar{t}(t)$ (Equation 6.12), and then look at the time-independent MCNP calculation of the same spectrum, we will have a check the effectiveness of the correction.

In simulation, $k = 1$ in the evaluation of κ in Equation 6.16, and ΔT is 100 μs. Results are shown in Figure 6.5, where the correction is successful below 200 meV for the cold moderator. The correction fails sooner than expected, beginning to undershoot the benchmark at 200 meV, corresponding to a ToF of 900 μs. The flux is indeed changing rapidly in this regime, for example if the channel ToF energy extends from 600-900 meV (430 to 530 μs) then the $1/E$ flux would by increase 150% from 900 to 600 meV.

The preceding analysis shows an approximate route for recovering $E\phi(E)$ (i.e. the correct count rate and time-energy relationship in the thin detector) in the presence of a finite emission time distribution. The most accurate method to account for the emission time dependence would be to perform a deconvolution, such as is
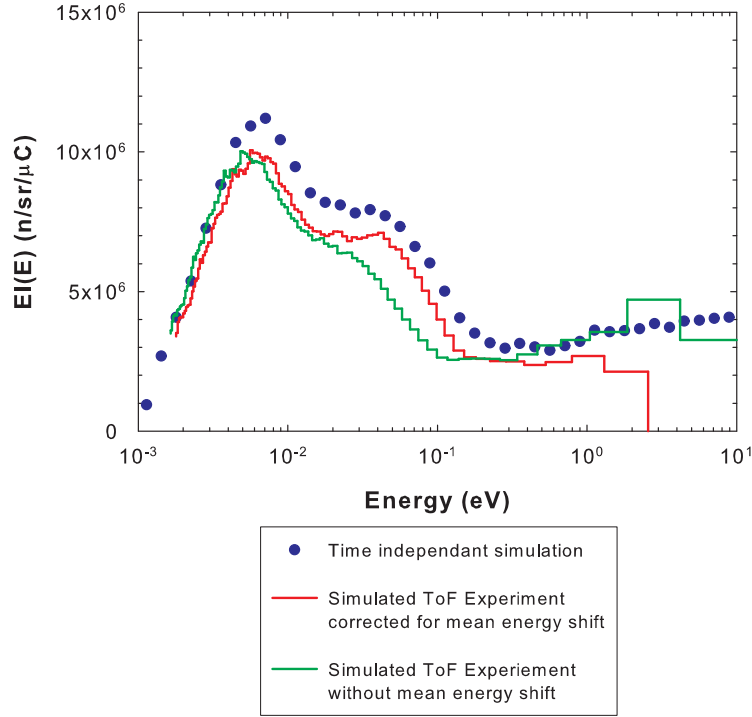
Figure 6.5: Simulation of the $\bar{t}$. Note the success of the correction below ~ 200 meV. Above 200 meV $\frac{d\bar{t}}{dt} < 0$, which is an indication that the condition that the flux is not slowly varying such that $\phi(E) = \phi(\bar{E})$ is *not* valid. *Blue:* Eqn. 6.22, *Red:* Eqn. 6.1 using $\bar{E}$ calculated via Eqn. 6.12, *Green:* Eqn. 6.1 using $E = \frac{1}{2}mL^2 t^{-2}$

shown below,

$$\int_0^\infty dt\tau^{-1}(E,t)C(t) = \int_0^\infty dt\tau^{-1}(E,t)A \int_{t-\Delta T/2}^{t+\Delta T/2} dt \int_0^\infty dE\epsilon(E)\phi(E)\tau(E,t) \tag{6.24}$$

$$\int_0^\infty dt\tau^{-1}(E,t)C(t) = A\epsilon(E)\phi(E) \tag{6.25}$$

Leaving us with the question of how exactly to define the emission time inversion, $\tau^{-1}(E,t)$. Lacking this function, we employ the $t \to (t-\bar{t})$ relationship and find that it appears successful in matching discrepancies between simulated measured data and MCNP time independent flux calculations below about 200 meV, and with more

marginal success from 200 meV to 1000 meV. Above this energy, the effectiveness of the correction in matching simulation and experiment is not as successful and a more advanced deconvolution algorithm would need to be developed.

6.3.3   Detector Efficiency Calibration

I   Bootstrap to SNS Detector Calibrated at IPNS

During the collaboration with the SNS CD4 measurement planning [50, 57], we also used the LENS detector. We strapped the LENS detector to the SNS detector during measurements on HRMECS. The HRMECS chopper could not be completely dephased to view the entire beam, so there are notches in the spectrum when the chopper was partially obscuring the beam. Results are shown in Figure 6.6

The efficiency of 3 Torr ^{3}He, as specified to LND for the LENS detector, is $5.47 \times 10^{-4} \overset{\circ}{A}{}^{-1}$. The calibrated efficiency of the SNS detector is $7.5 \times 10^{-4} \overset{\circ}{A}{}^{-1}$ at 1% accuracy. A factor of 6.36 was required to match the SNS detector to the LENS detector, for a LENS detector efficiency of $(4.77 \pm 0.50) \times 10^{-4} \overset{\circ}{A}{}^{-1}$, less than 15% off the specification. Because we must match both vertical scale and curve shape, error comes from the quoted 1% accuracy of the SNS detector calibration and a 10.4% mean residual, calcualted via Equation 6.26 between the LENS and the SNS detector.

$$MRD = \frac{1}{N} \sum_{i=0}^{N} \frac{|C_{SNS}(t_i) - C_{LENS}(t_i)|}{C_{LENS}(t_i)} \tag{6.26}$$

II   Simultaneous Gold Foil Activation

Bare and cadmium covered gold foils were activated at the detector position simultaneously with the spectral measurements to provide an independent and absolute calibration of the detector efficiency [50, 111]. The foil activity was measured with a $\beta - \gamma$ coincidence method. The foils were placed between a lithium-drifted ger-
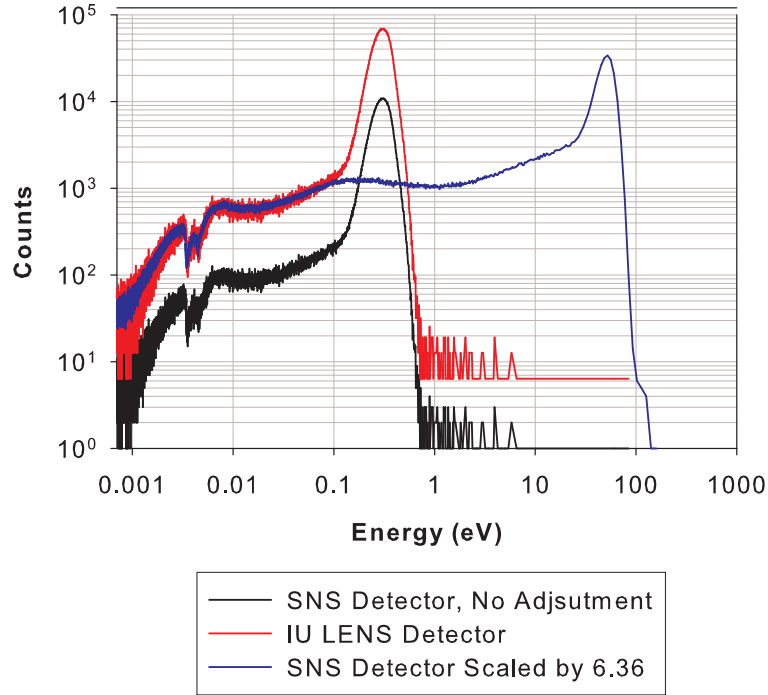
Figure 6.6: Comparisons of IU and SNS CD4 detector. The calibrated SNS detector is multiplied by a constant to match the uncalibrated LENS detector. The large spike at 0.1-1 eV and low count rate above 1 eV in the SNS detector at short ToF is due to dead time resulting from saturation of the detector from neutrons and gammas produced during target irradiation. This also occurs for the LENS detector, although we note the faster recovery of the IU detector, extending the ToF range of the measurement to ~1 eV. We attribute to the enhanced performance of the LENS detector to the use of nitrogen as the quench gas instead of Ar. Nitrogen which has a lower gamma cross-section than argon and only a slightly lower ionization potential, and so is less likely to saturate in a strong gamma field.

manium detector, used for γ detection, and a plastic scintillator coupled to a photo-multiplier tube used as the β detector. The γ background signal in the β detector was measured using aluminum filters and a high activity gold foil. With such an arrangement, the absolute efficiencies were about 4% in γ detection and about 13% in β detection. Single and coincidence counts were recorded in five minute time bins to detect any variation of the background. At the end of the 10 hour irradiation, the bare foil had activity around 3.7 Bq and the cadmium covered foil had activity around 1.0 Bq. The combined calculated uncertainty from these contributions is ap-

proximately 12% for the bare foil using the coincidence counting method and comes from counting statistics and background fluctuations. This uncertainty estimate is in good agreement with the variation in activities calculated independently using the absolute gamma and beta detector efficiencies.

Once the saturation foil activation has been determined with sufficient accuracy, we can use it to determine a detector efficiency. From Equation 6.1 we see the flux is related the energy dependant efficiency of the detector as follows:

$$\phi(E) = \frac{C(t)}{\Delta T A \varepsilon(E) \frac{dE}{dt}} \tag{6.27}$$

where $E \rightarrow < E >$ is used for the long pulse corrected energy. The foil activity is equal to the reaction rate at saturation (See flux def 3). We have for cadmium transmission

$$T(E) = 1 - e^{-\Sigma_{cd}(E)x} \tag{6.28}$$

The transmission function has a sharp cutoff at 550 meV (the *cadmium cutoff*), which allows us to use cadmium subtracted activity to account for the activation per unit volume, $\tilde{A}$, of the gold foil from neutrons above the cadmium cutoff in the analysis.

$$\tilde{A} = \tilde{A}_{bare} - \tilde{A}_{cd} = \int_0^\infty dE \sigma(E) T(E) \phi(E) \tag{6.29}$$

$$\tilde{A} = \int_0^\infty dE \sigma(E) T(E) \frac{C(t)}{\Delta T A \varepsilon(E) \frac{dE}{dt}} \tag{6.30}$$

Due to the use of time of flight, C(t) extends only up to a certain energy, E_{max} before the ToF overlaps the proton pulse width. However, we know from the physics arguments presented in Chapter 4 that we may assume a power law for the flux, $1/E^{1+\alpha}$.
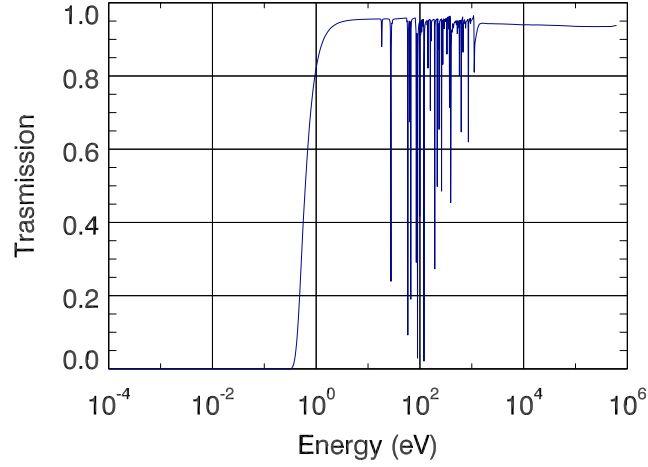
Figure 6.7: The Cadmium transmission function, calculated from Equation 6.28 for 0.058 mm (20 mil) thick cadmium [65].

The capture cross section for gold (shown in Figure 6.8) is dominated by a the 5 eV resonance, and follows a $\frac{1}{v}$ dependence below sufficiently below the resonance ($E \lesssim 500$ meV). Thus the influence of the fast neutrons and primary neutrons on the total activation is small, and even less for the cadmium-difference activation. We approximate the flux in the $1/E$ regime with a power law fit extending from E_{max} to the maximum proton energy (5.2 MeV for 7 MeV protons on beryllium), assuming deviations from $1/E$ energy spectrum at high energy ($E > 10$ keV) due to the primary source will have a small impact on the calculated activity.

The flux used in the numerical integration of Equation 6.30 is:

$$\phi(E) \quad = \frac{C(t)}{\Delta T A \varepsilon(E) \frac{dE}{dt}} \quad E < E_{max} \tag{6.31}$$

$$= \phi_s \frac{1}{E^{1+\alpha}} \quad E_{max} < E < 5.2 MeV \tag{6.32}$$

$$= 0 \quad E > 5.2 MeV \tag{6.33}$$

Where ϕ_s is a constant related to the magnitude of the thermal flux chosen such

that the flux is continuous. The total flux contained in the ϕ_s term is

$$\int_{E_{max}}^{5.2MeV} \phi(E) = \frac{\phi_s}{1+\alpha} E_{max}^{\alpha}(1 - (\frac{E_{max}}{5.2MeV})^{\alpha}) \sim \frac{\phi_s}{1+\alpha} E_{max}^{\alpha} \qquad (6.34)$$

The reader will note that $\frac{L^2 \phi_s}{i}$ is in fact the moderator coupling.
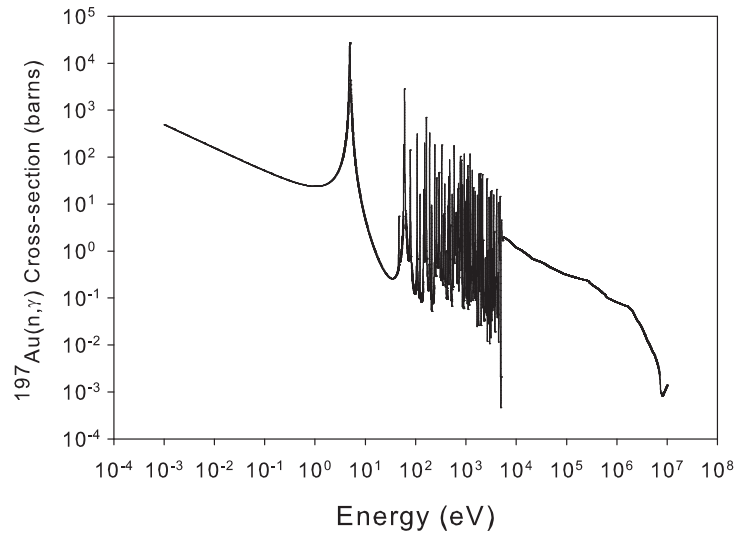
Figure 6.8: The gold (n, γ) activation cross-section. It is dominated by thermal neutron capture and the very pronounced resonance peak at 5 eV [65].

The value of k for a low efficiency detector is the absolute efficiency. For a low efficiency detector, this reduces to

$$k = \frac{\int_0^{E_{max}} dE\sigma(E)T(E)\frac{C(t)}{\Delta TA\lambda\frac{dE}{dt}} + \int_{E_{max}}^{5.2MeV} dE\sigma(E)T(E)\phi_s\frac{1}{E^{1+\alpha}}}{\tilde{A}} \qquad (6.35)$$

We found the influence of the second integral to be 22.2% of the total activity integral. The resulting value of k is $(4.40 \pm 0.88) \times 10^{-4} \mathring{A}^{-1}$. Error in the value is due primarily to the error in the gold foil activity. The detector efficiency results are summarized in Table 6.1.

Table 6.1: LENS LND Low Efficiency Detector Efficiency

Measurement	k ($\AA^{-1}$)
Specification	$(5.47 \pm 0.18) \times 10^{-4}$
SNS Bootstrap	$(4.77 \pm 0.50) \times 10^{-4}$
LENS Gold Foil	$(4.40 \pm 0.88) \times 10^{-4}$

6.3.4 Proton Dosimetry

At present, the LENS accelerator does not have true per pulse proton dosimetry. The addition of a Pearson Transformer after the current upgrade should resolve this in the future. Beam drop out is a serious issue for absolute flux measurements, where we seek the neutron flux per proton. For these measurements, the beam current was read out by directing the beam onto an instrumented beam stop and reading the peak current during the pulse, shown on the right in Figure 6.9.

There are 3 radiation monitors that record the radiation levels in the TMR vault once per minute. These monitors are a NaI gamma detector, a Bonner sphere [113] fast neutron detector, and a thermal neutron detector in direct beam on the central port at about 120 cm from the monitor face. One additional check on proton current for the low efficiency detector measuring the spectrum (which does not saturate during the flash) comes from the number of counts in the ToF channels corresponding to proton on target.

The fluctuation in the proton beam current during a measurement is quantified using the vault monitor detectors. Detector response is assumed to be directly proportional to proton beam current. We also assume that there is little fluctuation in the beam current during the first 10 minutes, such that the mean count rate during the first 10 minutes of the run represents the current read out on the beam stop. The average fraction, f, of that current delivered to the target during the run

is

$$f = \frac{\frac{1}{10}\sum_0^{10}\phi_i}{\frac{1}{i_{max}}\sum_0^{i_{max}}\phi_i} \tag{6.36}$$

where i_{max} is the time at which the measurement ends, and ϕ_i is the count rate in the vault monitor during the ith minute of the spectrum measurement. For the gold foil normalization run the current fraction is 0.73. Figure 6.9, left, shows a typical monitor response. When the beam is aligned with the target, the Bonner sphere peaks due to neutrons produced on the unshielded stop, which in line of sight of the detector bank. Also, during drop outs of the beam the gamma activity decays away slowly showing the impact of short lived isotopes produced in the TMR.
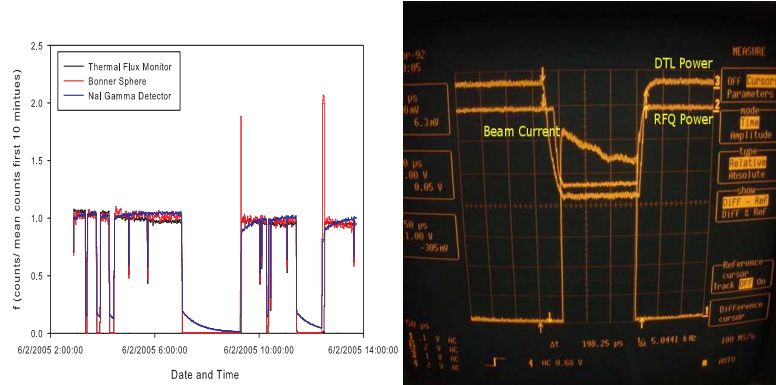
Figure 6.9: *Left:* Typical monitor response, showing dropouts of proton beam. *Right:* Typical beam current readout, this readout is for first neutrons Dec. 15, 2004.

6.3.5 Measured Neutron Energy Spectra

The collimation used to define the angular acceptance in all spectral shape experiments is established by two 20 cm long steel collimators clad with boron nitride. The collimators are 7.62 cm diameter at a distance of 140 cm from the moderator center face and 2.54 cm diameter at 570 cm. Integral flux yields and 1 eV coupling are given in Table 6.3.

Measurement of the energy spectrum from an empty moderator vessel depends

only on the moderation in the water reflector for which scattering kernels are well established. Results for this situation are shown in Figure 6.10. The measured integrated yields below 125 meV agree with the simulation if one corrects the observed spectra for the emission time delay from the moderator. The dominant sources of uncertainty in the these measurements are detector normalization, background determination, and proton current normalization.
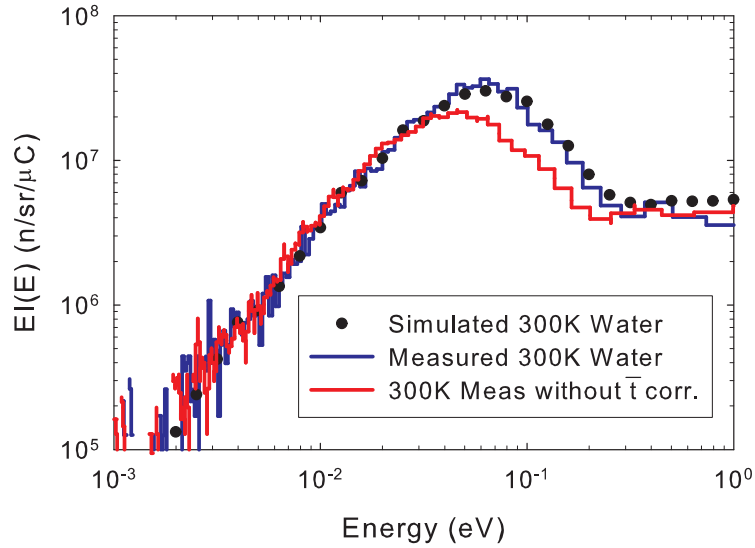
Figure 6.10: The water moderated absolute neutron flux, with and without the $\bar{t}(t)$ correction applied to the data compared to simulation.

The agreement for the 1 eV coupling is less impressive (Table 6.3), with the simulation overestimating the coupling by a little more than the experimental uncertainty. The most likely explanation for this difference is differences between the model and the experimental reality regarding the details of the water geometry between the target and the moderator. As indicated in Figure 5.25, slight changes to the thickness of this layer can significantly change the spectrum in this energy range even when the moderator is filled. Greater dependence of the flux at 1 eV on the thickness of this layer should be expected in the case when the moderator is empty

(since a small change in water thickness will be a greater fractional change in the total hydrogen content between the target and the detector). Another contribution to this discrepancy could be uncertainty in the background at these high energies as this was not fully characterized with our present temporary experimental setup.

The methane moderator is prepared by liquifying from the gaseous state in the moderator vessel. The methane is then cooled from liquid to the 4 K base temperature in about 2 hours, with no external heat applied during that time. Cold moderator neutron spectral data are taken on a high efficiency (20 atm ^{3}He) detector during the cool down in order to obtain spectral information in short exposure times. Once the 4 K base temperature is achieved, the gold foil measurement with thin detector is done in a 10 hour exposure. The high efficiency results at base temperature are scaled to the gold foil normalized thin detector measurement to provide the absolute normalization for the high efficiency detector.

With the exception of 1 eV coupling, agreement with simulation is not as good for the solid methane moderator yield, shown in Figure 6.11. The discrepancies in the methane moderated neutrons versus simulation may be related to the exclusion of essential physics from the scattering kernel, or from the condensed condition of solid methane system which might affect the neutron cross section. The scattering kernel physics is based upon a phonon expansion with 4 discrete modes to model the excitations of the hydrogen about the central carbon atom. New research to include the contribution from hindered rotation and spin state in the low temperature methane scattering law is progressing at IUCF [114]. We take note of the increase in flux at low energies (< 3 meV) upon reducing the moderator temperature from 25 K to 4 K.

Table 6.2: Table of experimental and simulated integral neutron yields for 7 MeV proton beam, 150μs wide proton pulse. Units of $10^6 n/sr/\mu C$.

Energy Group (meV)	300K Water (MCNP)	300K Water
0.20-0.82	0.0091 ± 0.0005	< 0.04
0.82-3.27	0.304 ± 0.001	0.22 ± 0.05
3.27-10	1.719 ± 0.009	1.64 ± 0.37
10-125	44.30 ± 0.07	47.6 ± 10.6
1 eV Coupling	5.35 ± 0.09	3.8 ± 0.9

Table 6.3: Table of experimental and simulated integral neutron yields for 7 MeV proton beam, 150μs wide proton pulse. Units of $10^6 n/sr/\mu C$.

Energy Group (meV)	22K Methane (MCNP)	25K Methane	4K Methane
0.20-0.82	$0.463 \pm .002$	0.18 ± 0.04	0.44 ± 0.09
0.82-3.27	6.37 ± 0.02	2.4 ± 0.5	3.3 ± 0.7
3.27-10	$10.40 \pm .01$	6.3 ± 1.2	6.2 ± 1.3
10-125	19.05 ± 0.01	14.1 ± 2.8	13.2 ± 2.7
1 eV Coupling	$3.25 \pm .02$	3.5 ± 0.7	4.0 ± 0.8
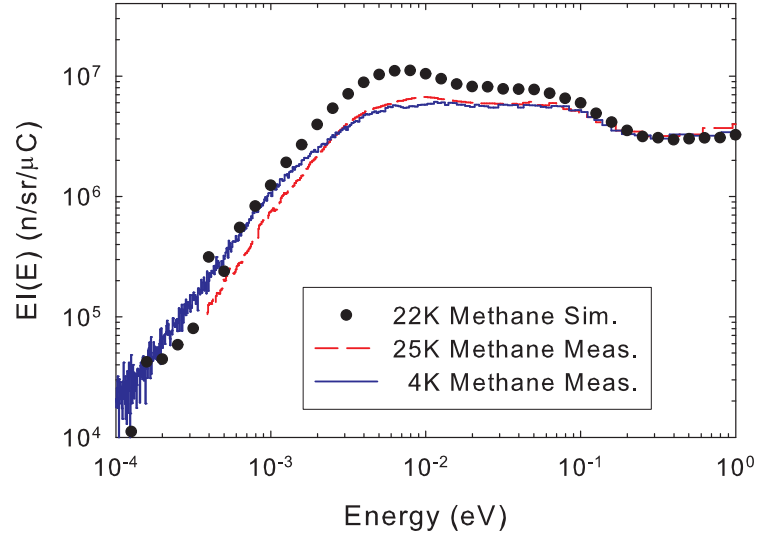
Figure 6.11: Solid methane at 25 K and the base 4 K temperature. The moderated neutron flux, with the t_o correction applied to the data, compared to simulation.

6.4 Spectrum as a function of moderator temperature

To see the impact of cooling the moderator on the neutron spectrum we began a series of experiments that observed the spectrum in real time as the moderator cooled. We then linked these spectra with moderator temperature instrumentation to determine the condition of the moderator. The moderator was held at 7 different temperatures above and below the phase II transition in methane by applying external heat to the refrigerator. The resulting data set of a neutron energy spectrum at a given temperature was fit with Equation 4.71.

6.4.1   Apparatus

The moderator instrumentation reads out the temperature of the top and bottom of the moderator every minute. The moderator instrumentation clock was synchronized with the multichannel scalar (MCS) clock. The MCS outputs binary files that contain the start time and the duration of the measurement. A script was run on the MCS to capture a spectrum every 10 minutes. To read out the detector in 10 minute frames, a high efficiency (k=.92 determined from 10 ATM ^{3}He pressure at 2.54 cm diameter) LND 25291 tube detector [112] was used. To avoid saturation, it was masked to a 4 mm diameter beam spot by boron nitride.

A program was written to determine the mean temperature of the moderator as function of time from calibrated Cernox temperature sensors placed at the top and bottom of the moderator vessel. Once the time frames of the stable temperatures were established, the code selected and averaged the neutron spectra which began and ended during that time frame. The code then computed the neutron spectrum and various integral yield metrics, including the integral yields and moderator coupling as shown in Table 6.3. Finally, the spectra were output as $EI(E)$ and fed to a non-linear least squares analysis code [115] for fitting with Equation 4.71 to determine the temperature of the fundamental neutron mode. The spectra were normalized by comparing the base temperature high efficiency results and finding the scale factor required to match it to the gold foil normalized low efficiency detector measurement.

6.4.2   Neutron Spectra Results

The basic spectra show a weak fundamental mode above the 20.4K phase transition in methane which is absent in the lower temperatures, and the spectrum assumes a "flat top" behavior. Integral counts in various wavelength ranges shown in Figure 6.13

reveal that the flux increases as temperature decreases, but at shorter wavelengths there is a discontinuity near the phase I-II ordering transition [102] in methane that does not appear in the long wavelength results. While it should be noted that there is a large degree of scatter in these plots, the change in slope at the phase transition is very intriguing. A plot of the neutron spectral temperature as a function of moderator temperature also shows a change in slope near the phase transition.

Extrapolation to zero moderator temperature for LENS implies the lowest achievable neutron temperature would be 26 K. These results do not show the lower spectral temperature from the Inoue [96] measurement for the limiting temperature of a methane moderator. The Inoue measurement employed a thick (20 cm radius, 20 cm height) reentrant cavity configuration coupled to a photoneutron source without a reflector, which appears to be able to achieve lower neutron temperatures than the slab geometry. This could be due to the increased effectiveness of the larger solid methane moderator (the Inoue solid methane appears to have been nearly as large as the LENS water reflector), or due to the reduced leakage paths of neutron deep inside the methane in their configuration. Results similar to Inoue have been recorded at IPNS for a grooved 7.6 cm thick methane moderator [116].

6.4.3 Fit to spectrum

Results of the fits from the spectral temperature analysis are given in Figure 6.14 and Tables 6.4, 6.5, and 6.6. Reduced chi-square values range from 0.93 to 6.56, with the exception of the 10 K measurement, which is likely due to the higher energy part not being strictly Maxwellian in shape and the impact of the $\bar{t}$ correction at >200 meV energies. Statistics are relatively poor for the 10 K methane temperature measurement, leading to higher chi-square values.

Table 6.4: Thermalized flux fit parameters, See Equation 4.71

Temp (K)	N_1 ($10^6 n/sr/\mu C$)	E_1(K)	N_2 ($10^6 n/sr/\mu C$)	E_2(K)
35	24.15	56.46	11.36	317.06
30	21.72	46.52	10.08	299.78
25	21.93	42.84	8.98	309.29
20	20.90	38.19	9.91	301.80
18	20.74	36.64	9.76	317.51
15	21.20	37.55	9.54	318.75
10	19.86	36.79	12.74	272.05
3	18.25	29.44	9.27	309.91

Table 6.5: Epithermal fit parameters. See Equation 4.71.

Temp(K)	ϕ_s ($10^6 n/sr/\mu C$)	α	a (eV$^{\frac{1}{2}}$)	b
35	3.85	-0.11	1.63	-11.92
30	3.62	-0.18	1.13	-9.22
25	3.58	-0.22	1.10	-9.01
20	3.72	-0.19	1.04	-9.32
18	3.69	-0.18	1.10	-10.01
15	3.61	-0.21	1.12	-9.74
10	4.35	-0.08	1.10	-10.16
3	3.61	-0.21	1.88	-8.92

Table 6.6: Reduced Chi-squared for fits. Statistics in the measurement taken at 10 K methane temperature have relatively poor statistics compared to the other spectra, leading to higher χ^2 values.

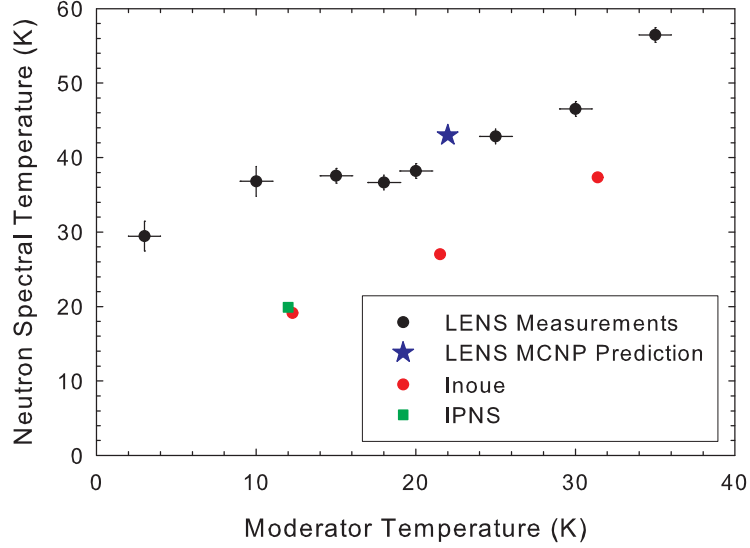| Temp(K)	Reduced χ^2
35	0.98
30	2.78
25	2.58
20	1.16
18	1.74
15	2.37
10	16.92
3	6.56

Figure 6.12: Effective temperature of low energy neutron flux at LENS, compared to results of Inoue [96]. Data is also shown for a grooved 7.6 cm thick methane moderator with aluminum foam (C moderator) at IPNS [116]. All 3 moderators are coupled and are not poisoned.

6.5   Emission Time

Although we were not able to measure the emission time distributions across an adequate energy range to fully correct our time-of-flight data, we were able to measure some time distributions, which provide additional quantities for comparison between our simulations and the LENS TMR system. The emission time distribution is measured using a time focused geometry technique, which cancels out instrumental resolution effects to first order [76, 97]. The equipment used at the Intense Pulsed Neutron Source (IPNS) in reference [76] was loaned to the LENS facility for these measurements. The crystal monochromator is a mosaic Ge[111] crystal, with first order reflection set for 2.74 meV, such that the 3rd order reflection falls at 24.3 meV. This focuses the analyzer on near the peaks of the 2 Maxwellian fit, and places the 3rd order reflection near the peak of an ambient temperature Maxwellian.

The proton pulse conditions were 150 μs square pulse, 7 mA peak current, 15
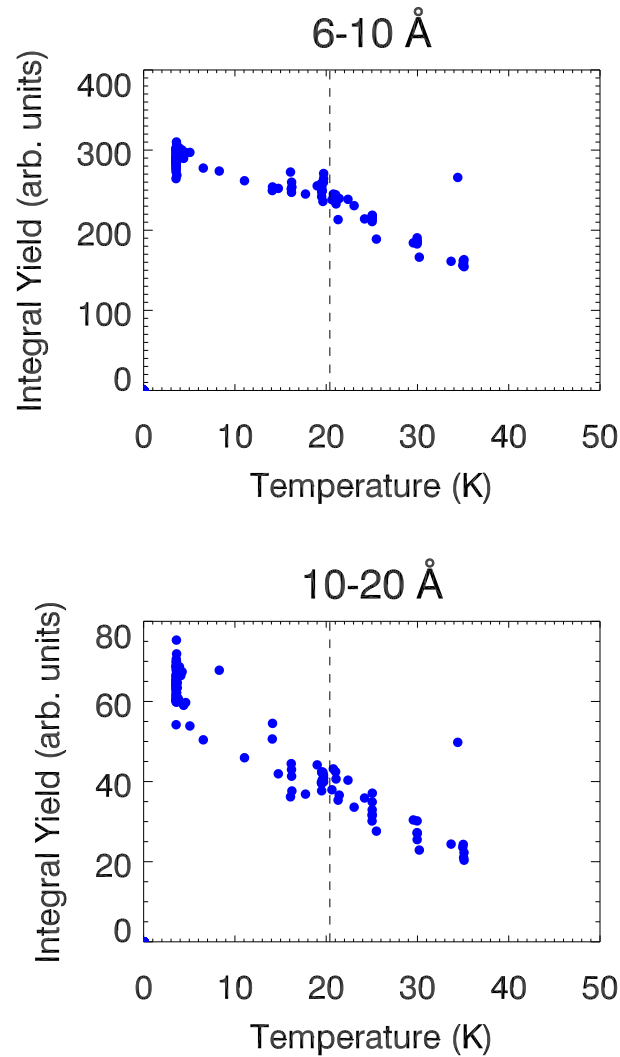
Figure 6.13: Integral yields in arbitrary units as a function of temperature.

Hz pulse rate (110 W total power). The analyzer was placed at 20 degrees to the moderator normal. The flight path ratio is $P = 0.1$ to have the detector and analyzer as close as possible to the cold source and to each other, for a total flight path of 6.6 meters from the moderator to the detector. The result of 12 hours of data collection is shown in Figure 6.15. Statistics are too low to gain information from the 3rd and 4th order reflections, but the first Bragg edge at 2.74 meV agrees well with an MCNP simulation convoluted with a 150 μs square pulse as shown in Figure 6.16. The time
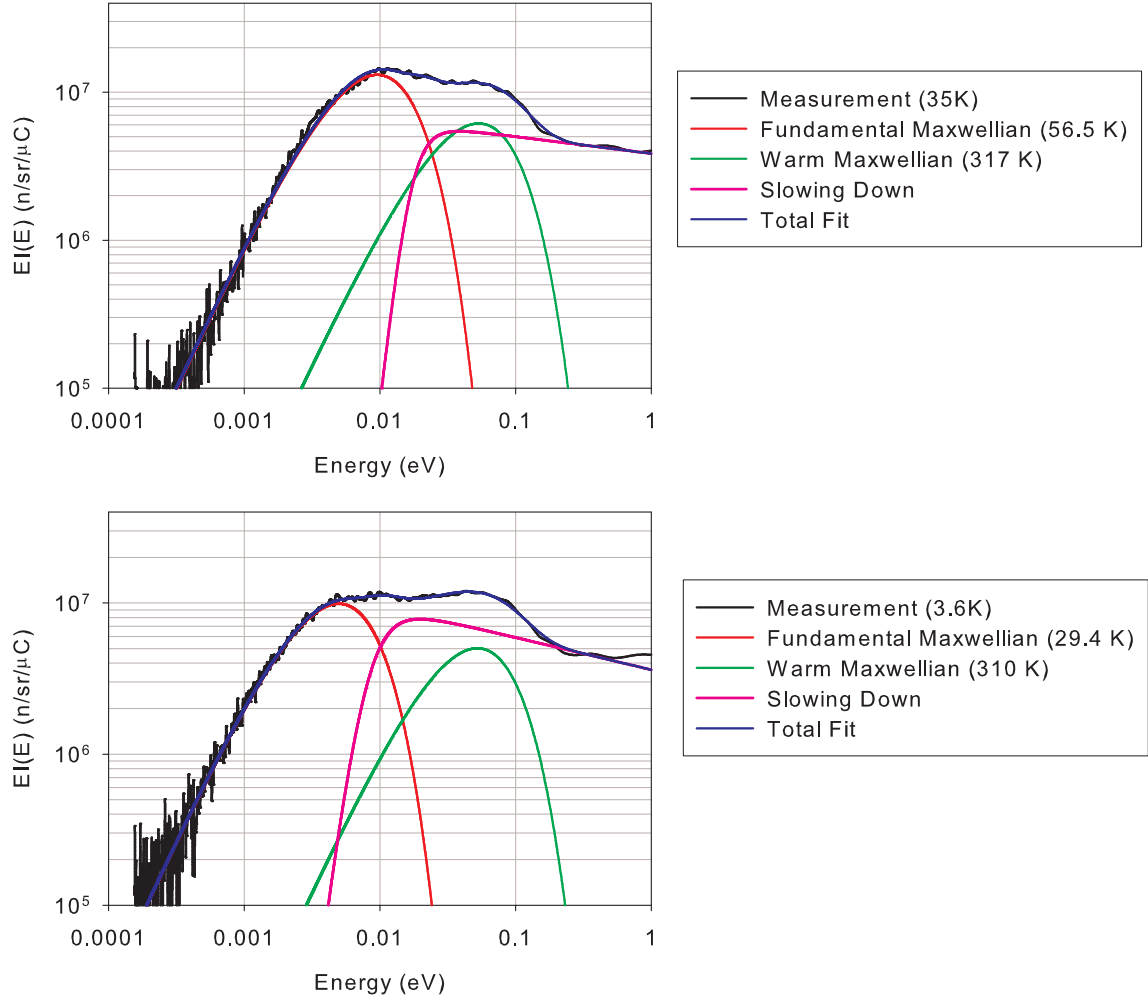
Figure 6.14: Results of nonlinear least squares fit of measured spectra, corrected for $\bar{t}$, to Equation 4.71

axis is shifted by 8.8 msec such that the neutron pulse begins at $t = 0$ (reduced time).

6.6   Core Flux Measurement with Activation Foils

In coordination with dosimetry efforts for NRERP, the core flux of the TMR was measured via activation foils. Pure ^{58}Ni foil, cadmium subtracted Gold foil, and
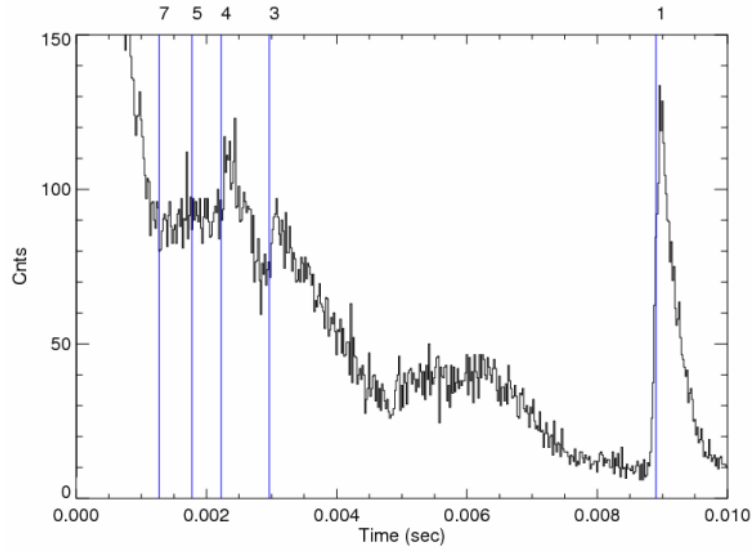
Figure 6.15: Time of Flight of bragg reflections from $Ge[111]$ crystal mosaic crystal, time focussed. The order of reflection is shown at top.
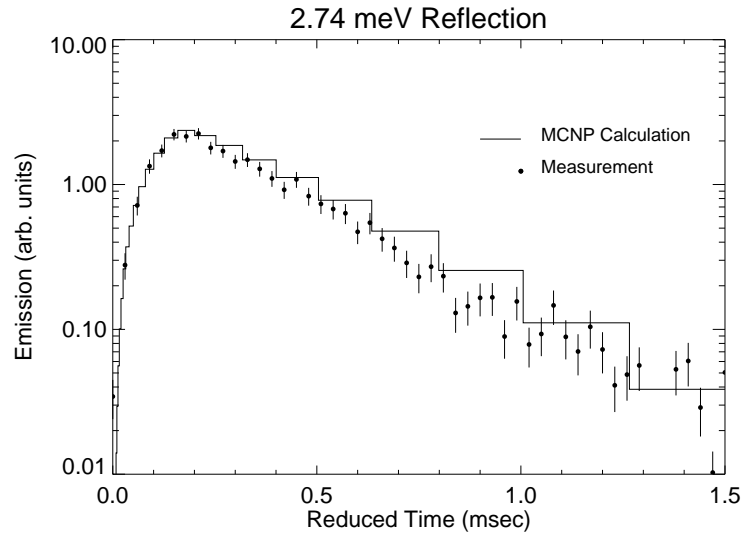
Figure 6.16: Pulse shape measurement compared with MCNP simulation convolved with 150 μs square pulse. Integral area is normalized to 1 for both curves.

pelletized ^{32}S were used. Activated nickel emits gamma radiation, which was detected on a high resolution Ge(Li) detector. S is a beta emitter, which were initially read out by P. Griffen at Sandia National Laboratory and later by B. Von Prezowski at

NRERP. Ni and S are sensitive to MeV neutrons, and Gold is sensitive to thermal neutrons.

The Ge(Li) detector is from Canberra, and employs a USB based MCA with the Canberra Genie 2000 software, which identifies peaks and determines their activity. We can then determine the saturation activity [117] and compare that activity to an MCNP calculation of the expected activity. The Ge(Li) was calibrated with a NIST traceable Isotope Products Laboratories gamma ray standard[3] containing ^{125}Sb,^{154}Eu, and ^{155}Eu which is actually a distributed source or radius 4.5 cm. To avoid error due to the size of the standard, calibration measurements were done 20 cm from the detector. During a calibration run, the measurement was paused and the standard was turned over half way through measurement before resuming to average out effects of the position of the radioactive material relative to the center of the standard.

The activity of a foil is related to the flux as usual as

$$\frac{\mathbb{R}}{N_a} = \int_o^\infty \sigma(E)\phi(E)dE \qquad (6.37)$$

where N_a is the number of atoms in the foil, and $\mathbb{R}$ is the activity of the foil in Bq. The Ni and S reactions selected are sensitive to only fast neutrons (see figure 6.6), which is highly sensitive to the energy spectrum of the external source of neutrons. For comparison to MCNP, we compare the calculated activity to the measured activity. Cadmium subtracted gold foil is sensitive to thermal neutrons. The NRERP measurements were conducted with the moderator empty, so the flux is considered to be well thermalized at ambient temperature. Assuming a Maxwellian form for the neutron flux, the *effective* thermal flux is directly related to the cadmium subtracted

---

[3]P.O. No. 20412-0063, Catalog No. EG-TN

Table 6.7: Core TMR foil activity measurements

Moderator	Measurement	Foil Activity	Simulation
Polyethylene	Gold Foil $(n/cm^2/\mu C)$	$(3.01 \pm .78) \times 10^6$	3.79×10^6
Empty Moderator	Gold Foil $(n/cm^2/\mu C)$	$(2.65 \pm .75) \times 10^6$	3.58×10^6
Empty Moderator	Nickel Foil $(Bq/atom/\mu C)$	$(1.17 \pm .19) \times 10^{-19}$	2.10×10^{-19}

gold foil activity [61, 75]

$$\phi_{th} = \frac{1}{\sigma_o} \frac{\mathbb{R}}{N_a} \tag{6.38}$$

where σ_o is the value of the activation cross-section at 25 meV.
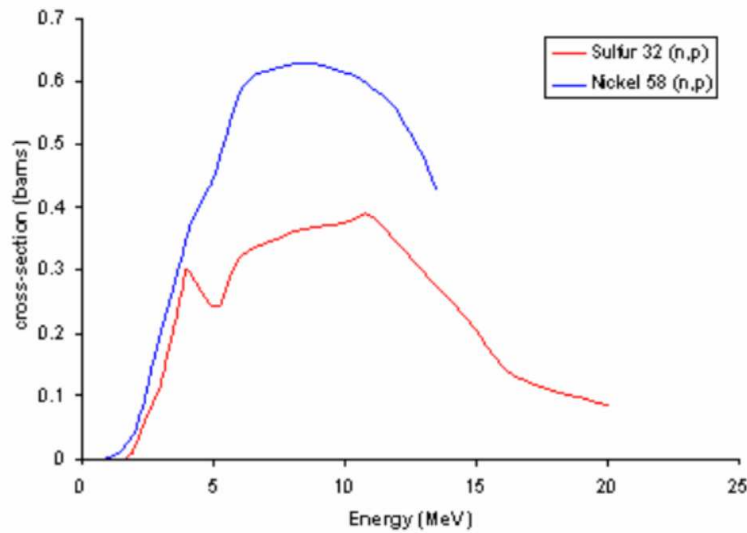
Figure 6.17: Nickel foil and sulfur pellet activation cross-sections for fast neutron measurement of core flux [65].

10 cadmium subtracted gold foil pairs were run from 2/18/05 to 10/27/05. The foils were affixed to a sample plate and inserted into the TMR via the central beam port to about 8 cm from the moderator surface for an ambient temperature moderator configuration. The results are divided into measurements done with the polyethylene moderator and those with empty cold moderator configuration. Simultaneously, sulfur pellets and Ni foils were affixed to the sample plate. Seven nickel foils were run. The weighted mean of the measurements is given in Table 6.7.

The main results from foil activation measurement confirm the as built config-

uration to the 30% level for thermal flux. Nickel activity is somewhat below this, which we attribute to the sensitivity of the nickel cross-section to the MCNP source term in this energy regime. While this result indicates the MCNP source term is inaccurate in this regime, the sensitivity of thermal and cold neutron production to the energy distribution of spectrum of the source is relatively weak. The TMR's ability to produce cold neutrons from 7 MeV proton beam is dominated by the source total neutron yield and amount of hydrogenous material around the source, so thermal flux results are more sensitive to total neutron yield and will not be affected strongly by this inaccuracy in the source term.

Fast neutron measurements also revealed a position dependence to the fast flux that was not observed for the thermal flux. NRERP sent the initial sulfur pellets to Sandia to be evaluated, and the results were returned in "Californium equivalent flux", but still show the position dependence. Results for foils placed at $\sim$5 cm from the center of the moderator are about a factor of 2 lower than foils placed near the center. Follow up simulation confirmed the presence of this effect, which is due to the angular distribution of the primary source term. Results of the simulation for thermal flux and nickel foil activity are shown in Figure 6.18.

6.7   Conclusion

The performance of the LENS target moderator reflector assembly has been evaluated through a series of measurements at low accelerator power. Measurements confirm that a beryllium target neutron yield strongly coupled to a light water reflector produces high cold neutron fluxes from a solid methane moderator. Yields of thermal neutrons at sample positions are commensurate with MCNP simulations, confirming the validity of the neutronic model. Cold neutron yield is significant,
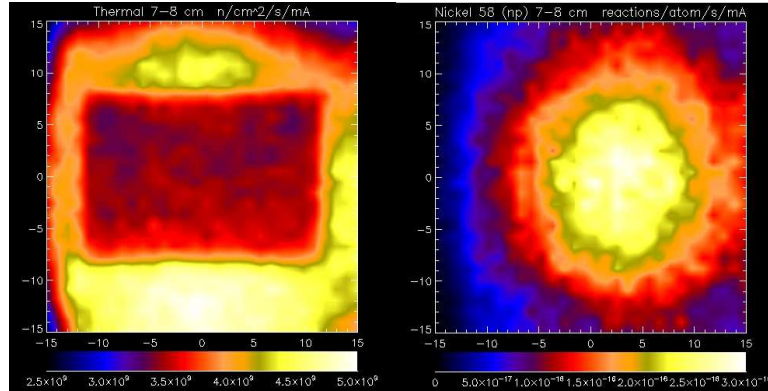
Figure 6.18: *Left:* Thermal neutron flux at 8 cm from the moderator face. The flux is uniform in the beam port, increasing dramatically in the water reflector above and below the beam port. *Right:* Nickel foil activity. Fast neutron activation is higher on the positive Y axis side of the beam port by almost a factor of 2. This side is more in line with the incident proton vector.

though not as high as expected from simulation. The variation in the spectral shape of the measured cold neutron flux near the temperature of the simulated scattering kernel indicates that there are deficiencies in the scattering law for methane. The neutron emission time distribution at 2.7 meV is in good agreement with expectations from simulation, which indicates the mean free path in the methane is modeled accurately. Thus, we propose the deficiencies to be related more to inaccurate modeling of the specific details of the energy exchange modes in methane than to inaccuracy in total cross-section or in the MCNP model itself.

Chapter 7

Advanced Neutronics

> Only put off until tomorrow
> what you are willing to die
> having left undone.
>
> ――――――――――――――
>
> Pablo Picasso

The fidelity of high resolution Monte Carlo methods have been verified in the course of this thesis. These results suggest the possibility of using MCNP to adapt recent ideas in neutronics [118, 119] and design reliable new neutronic configurations to the LENS source to boost the cold flux and reduce the spectral temperature of the fundamental mode.

7.1   Be Reflector and Reflector Filter

We have mentioned that at full power operations, which are still some years off, LENS could benefit from a beryllium reflector. However, the expense of machined beryllium suggests that its use be carefully optimized. Because Be works best on the highest energy flux, a combination of water and beryllium might prove a more efficient reflector geometry. At the larger radius, where the highest energy flux would

have its first interactions, beryllium could be employed as an effective moderator. Closer to the core, where mean neutron energies are lower, light or heavy water could be employed to achieve high densities of thermal flux near the moderator. However, while the exact nature of the optimization would determine the final configuration, it seems that it should be possible to optimize a reflector that retains the advantages of beryllium at reduced cost, and perhaps, greater effectiveness.

Muhrer and coworkers [118] have shown that it is possible to use beryllium not only as a low pass filter for low energy neutrons as in the He II measurements discussed in Chapter 1, but also simultaneously as a reflector. By placing sufficient thickness of beryllium into the beam port, an increase neutron flux reflected into the moderator may be possible. Gains of over 50% are reported, and it seems possible to realize similar gains at LENS. Muhrer has also shown that the reflector-filter can be optimized such that a single filter can service multiple beam lines in separate ways for an optimized configuration. In addition, a Be reflector/filter could also reduce leakage paths of fast neutrons into the scattering hall, reducing background.

7.2 Premoderator and Advanced Moderator Geometry

It was also shown [118] that beryllium premoderators enhance flux. We have shown the water gap thickness at LENS is not optimal at present, and demonstrated that the gap is important to achieving high brightness. It seems possible that an optimized selection of premoderator material and geometry could enhance the cold flux beyond the increases we have observed for an optimized water gap.

A major limiting factor in cold neutron flux is absorption in the methane. While the use of deuterated methane could be considered to reduce this, another method is

possible. If we can reduce the energy of the flux coupling to the moderator, we should be able to reduce the number of collisions required to reach a given energy, and reduce the self-absorption in the moderator. It is conceivable that LENS could achieve this by surrounding the moderator with polyethylene held at low temperature. Not only would this fill the vacuum gap, it may actually boost the cold flux.

Picton and coworkers [119] have detailed an optimization of a combined 2 piece methane and hydrogen moderator for ISIS. In this configuration, one serves as pre-moderator for the other. One striking feature of this work is that an optimized strongly coupled grooved moderator can produce greater than 200% more cold neutron flux than a simple slab. At LENS, we should consider attempting to achieve similar flux gains by employing a grooved or cavity type moderator. This, in coordination with advanced reflector and premoderator designs, could boost cold flux at LENS significantly at relatively little cost.

7.3   High Fidelity $S(\alpha, \beta)$

As we have noted, the present kernels for methane do not accurately predict the flux generated in a very low temperature methane moderator. In comparison to the measurements of Inoue, we have also seen that we have not achieved the lowest possible spectral temperature of the neutron flux. We have also seen in our measurements that the Phase I-II transition in methane may play a role in the moderation properties of the cryogenic solid. Experiments with moderator materials with similar phase transitions to methane, such as deuterated methane, CD_4, could also be used to probe the role of the phase transition in the moderation process.

Higher fidelity kernels for low temperature moderator materials would greatly enhance the design of cold sources. All of the methods suggested in this section thus

far suggest new ways to feed the moderator with ever greater intensities and better optimized energy of the incident flux. Naturally, the determination of the optimal incident flux depends on the scattering kernel employed.

Experimental work into generating better effective frequency spectra should be considered to update the 1967 work of Harker and Brugger which forms the basis of today's model [101, 120]. Muhrer and coworkers [121] have investigated ways of optimizing the phonon expansion methods of the present models with limited success. Perhaps new calculational methods, beyond the Gaussian representation employed in building current models, should be employed in the generation of $S(\alpha, \beta)$ tables. Promising work on the calculational aspects of this problem are being done by Shin [114] and Granada [122, 123]. We have shown that when the scattering laws are accurate, the neutronic model presented in this dissertation are quite accurate, such that LENS is an effective source for testing scattering laws. Future experiments at the LENS facility can reveal more insights into the generation of better scattering laws, which naturally will lead to better optimizations, greater reliability of transport codes, and higher brilliance in cold source designs.

7.4 Ultra Cold Neutron Production

The consideration of filling the beam port leads to an interesting opportunity for Ultra Cold Neutron (UCN) production. UCN's are produced rather inefficiently by single inelastic excitations in materials, such as superfluid He II or solid oxygen or solid deuterium. To generate a high density of UCNs in a UCN source, the flux entering the UCN producing material must be very high. If the modular LENS reflector unit is replaced with a unit that has very limited cryogenic penetration and no beam ports (such that leakage paths are virtually eliminated), then the flux trapped in the

reflector would be much higher than in the present configuration. Lower absorption reflectors, such as heavy water which were initially ruled out because of the emission time constraint, could also be employed to further enhance the flux. Proof of concept work carried out by Liu and coworkers [124] has shown that sufficient UCN density for fundamental physics could be achieved with an optimized moderator and nearly hermetic TMR.

7.5   Conclusion

We have taken some time in this chapter to discuss some future directions for LENS, including imaginative uses of beryllium, premoderators, reflector configurations, and advanced moderator geometries. In addition, new paradigms in cold scattering kernel calculation and experimental verification of those kernels would be widely applicable and of great value to the neutron scattering community. We hope that the the design methods and experimental benchmarks presented in the course of this dissertation work will provide a firm foundation from which to explore these and other new ideas, and the ideas we have not yet had time to envision.

Bibliography

[1] J. Carpenter, Technical Report No. ANL-02/16, ORNL/SNS-TM-2001/163, IPNS/SNS (2002).

[2] L. Van Hove, Physical Review **95**, 249 (1954).

[3] W. Yao *et al.*, J. Phys. G: Nucl. Part. Phys. **33**, (2006).

[4] G. Placzek and L. Van Hove, Physical Review **93**, 1207 (1954).

[5] L. Landau, Physical Review **60**, 356 (1941).

[6] L. Landau, Physical Review **75**, 884 (1949).

[7] R. K. Pathria, Statistical mechanics, 2nd ed. (Butterworth-Heinemann, Oxford ; Boston, 1996).

[8] R. P. Feynman and M. Cohen, Progress of Theoretical Physics **14**, 261 (1955).

[9] R. P. Feynman and M. Cohen, Physical Review **102**, 1189 (1956).

[10] M. Cohen and R. P. Feynman, Physical Review **107**, 13 (1957).

[11] H. Palevsky *et al.*, Physical Review **108**, 1346 (1957).

[12] D. G. Henshaw, Physical Review Letters **1**, 127 (1958).

[13] J. L. Yarnell, G. P. Arnold, P. J. Bendt, and E. C. Kerr, Physical Review Letters **1**, 9 (1958).

[14] J. L. Yarnell, G. P. Arnold, P. J. Bendt, and E. C. Kerr, Physical Review **113**, 1379 (1959).

[15] I. N. Serdyuk, Physica B: Condensed Matter **234-236**, 188 (1997).

[16] D. I. Svergun, Biophysical Journal **76**, 2879 (1999).

[17] C. G. Windsor, Journal of Applied Crystallography **21**, 582 (1988).

[18] D. I. Svergun and K. H. Nierhaus, Journal of Biological Chemistry **275**, 14432 (2000).

[19] J. Frank *et al.*, Nature **376**, 441 (1995).

[20] N. W. Ashcroft and N. D. Mermin, Solid state physics (Holt, New York, 1976).

[21] M. K. Wu *et al.*, Physical Review Letters **58**, 908 (1987).

[22] Z. X. Zhao *et al.*, Kexue Tongbao **32**, 661 (1987).

[23] A. R. Moodenbaugh *et al.*, Physical Review B **38**, 4596 (1988).

[24] J. M. Tranquada *et al.*, Physical Review Letters **60**, 156 (1988).

[25] Y. Maeno, N. Kakehi, M. Kato, and T. Fujita, Physical Review B **44**, 7753 (1991).

[26] M. K. Crawford *et al.*, Physical Review B **44**, 7749 (1991).

[27] J. D. Axe *et al.*, Physical Review Letters **62**, 2751 (1989).

[28] J. M. Tranquada *et al.*, Nature **375**, 561 (1995).

[29] L. F. Curtiss, An introduction to neutron physics (Van Nostrand, Princeton, N.J., 1959).

[30] M. M. R. Williams, The slowing down and thermalization of neutrons (North-Holland Pub. Co., Amsterdam, 1966).

[31] Californium User Facility for Neutron Science Website, 2006, http://www.ornl.gov.

[32] J. M. Carpenter, Nuclear Instruments and Methods **145**, 91 (1977).

[33] C. Allardice and E. R. Trapnell, The first pile (U.S. Atomic Energy Commission. Technical Information Division, Oak Ridge, Tennessee, 1949).

[34] Nuclear News **49**, 37 (2006).

[35] R. W. Peelle and F. C. Maienschein, Physical Review C **3**, 373 (1971).

[36] F. Pleasonton, R. L. Ferguson, and H. W. Schmitt, Physical Review C **6**, 1023 (1972).

[37] V. V. Verbinski, H. Weber, and R. E. Sund, Physical Review C **7**, 1173 (1973).

[38] C. L. Hollas, C. Goulding, and W. Myers, NIM A **543**, 559 (2005).

[39] P. C. Fisher and L. B. Engle, Physical Review **134**, B796 (1964).

[40] E. Iverson, Private Communication, 2007.

[41] J. Guzek *et al.*, NIM B **139**, 471 (1998).

[42] R. L. Cappelletti *et al.*, J. Res. Natl. Inst. Stand. Technol. **106**, 187 (2001).

[43] NIST, NIST Center for Neutron Research Accomplishments and Opportunities, Special Publication 1045, 2005.

[44] H. J. Prask, J. M. Rowe, J. J. Rush, and I. G. Schroder, J. Res. Natl. Inst. Stand. Technol. **98**, 1 (1993).

[45] NIST, NIST Center for Neutron Research Accomplishments and Opportunities, Special Publication 993, 2002.

[46] E. Kulagin, S. Kulikov, V. Melikhov, and E. Shabalin, NIM B **215**, 181 (2004).

[47] J. M. Carpenter, Nature **330**, 358 (1987).

[48] P. Kopetka, R. Williams, and J. M. Rowe, NIST NCNR Advanced Cold Source Technical Report (unpublished), 2006.

[49] D. J. Hughes, Neutron optics (Interscience Publishers, New York, 1954).

[50] B. J. Micklich *et al.*, in ICANS-XVII, edited by G. Russell and J. Rhyne (Los Alamos, Santa-Fe, 2005), Vol. II, pp. 463–472.

[51] K. C. Littrell, J. W. Richardson, J. M. Carpenter, and B. S. Brown, Physica B-Condensed Matter **311**, 112 (2002).

[52] J. Carpenter, High Intensity, Pulsed Thermal Neutron Source (U.S. Patent No. 3,778,627), 1973.

[53] E. B. Iverson, J. M. Carpenter, and E. J. Hill, Physica B: Condensed Matter **241-243**, 33 (1997).

[54] K. Skold and D. L. Price, Neutron scattering, Methods of experimental physics ; (Academic Press, Orlando, 1986).

[55] C. K. Loong, S. Ikeda, and J. M. Carpenter, NIM A **260**, 381 (1987).

[56] D. F. R. Mildner and J. M. Carpenter, NIM A **484**, 486 (2002).

[57] E. B. Iverson *et al.*, in ICANS-XVII, edited by G. Russell and J. Rhyne (Los Alamos, Santa-Fe, 2005), Vol. II, pp. 436–446.

[58] A. Lawler, Science **279**, 470 (1998).

[59] U. S. O. of Science and T. Policy., Interagency working group on neutron science : report on the status and needs of major neutron scattering facilities and instruments in the United States (Executive Office of the President, Office of Science and Technology Policy, Washington, D.C., 2002).

[60] D. V. Baxter *et al.*, NIM B **241**, 209 (2005).

[61] Measurement of neutron flux and spectra for physical and biological applications, NCRP Report 23 (U.S. Dept. of Commerce National Bureau of Standards, Washington, 1960).

[62] J. Breimeister, MCNP4c2 (2001).

[63] P. F. Zweifel, Reactor physics (McGraw-Hill, New York, 1973).

[64] G. L. Squires, Introduction to the theory of thermal neutron scattering (Dover Publications, Mineola, N.Y., 1996).

[65] T-2 Nuclear Information Service, http://t2.lanl.gov/.

[66] S. F. Mughabghab, R. R. Kinsey, C. L. Dunford, and S. F. Mughabghab, Neutron cross sections series, [4th ed. (Academic Press, New York, 1981).

[67] Neutron News **3**, 29 (1992).

[68] R. E. MacFarlane, LA-12639-ms: New Thermal Neutron Scattering Files for ENDF/B-VI Release 2, 1994.

[69] F. Reif, Fundamentals of statistical and thermal physics (McGraw-Hill, New York, 1965).

[70] B. Davison, Neutron transport theory (Clarendon Press, Oxford, 1957).

[71] R. K. Osborn and S. Yip, The foundations of neutron transport theory, Monograph series on nuclear science and technology (Gordon and Breach, New York, 1966).

[72] W. H. Press and N. R. S. (Firm), Numerical recipes in FORTRAN, 2nd ed., v2.0. ed. (Cambridge University Press, New York, N.Y., 1992).

[73] O. Gasnault *et al.*, Geophys. Res. Lett. **28**, 37973800 (2001).

[74] C. Westcott, AECL-1101: Effective Cross Section Values for Well-moderated Thermal Reactor Spectra (Atomic Energy of Canada Limited, Chalk River, Ontario, 1960).

[75] ASTM, Annual Book of ASTM Standards: Vol. 12 Standard E262 (ASTM, West Conshohocken, PA, 1997).

[76] S. Ikeda and J. M. Carpenter, NIM A **239**, 536 (1985).

[77] R. M. Pearce and J. M. Kennedy, Nuclear Science and Engineering **19**, 102 (1964).

[78] MCNP5 - a general monte carlo n-particle transport code (2005).

[79] D. L. Friesel and W. Hunt, in <u>XIX International Linac Conference</u> (JA-CoW.org, Chicago, IL, 1998), pp. 61–63.

[80] V. Derenchuk *et al.*, in <u>LINAC 2006</u> (JACoW.org, Knoxville, TN, 2006).

[81] D. Friesel, V. Derenchuk, T. Sloan, and E. Stephenson, in <u>EPAC 2000</u> (JA-CoW.org, Vienna, Austria, 2000), pp. 539–541.

[82] V. P. Derenchuk *et al.*, in <u>PAC 2005</u> (JACoW.org, Knoxville, Tennessee, 2005), pp. 3200–3202.

[83] J. M. Carpenter and W. Yelon, <u>Methods of Experimental Physics, Vol. 23A</u> (Academic Press, Orlando, 1986).

[84] <u>CRC handbook of chemistry and physics</u> (CRC Press, Cleveland, Ohio, 1984), Vol. 65.

[85] M. A. Atta and M. C. Scott, Journal of Nuclear Energy **27**, 875 (1973).

[86] M. A. Lone, A. J. Ferguson, and B. C. Robertson, NIM **189**, 515 (1981).

[87] J. Raisanen, T. Witting, and J. Keinonen, NIM B **28**, 199 (1987).

[88] M. A. Lone *et al.*, NIM **143**, 331 (1977).

[89] P. Chen, W. Wu, B. G. Jones, and T. A. Newell, in <u>2006 Internation Congress on Advances in Nuclear Power Plants (ICAPP '06)</u> (ICAPP, Reno, NV, 2006).

[90] H. Nann, Private Communication, 2006.

[91] M. Lone *et al.*, <u>AECL-7413: Low Energy 7Li(p,n)7Be Neutron Source (CANUTRON)</u> (Chalk River Nuclear Laboratories, ADDRESS, 1982).

[92] F. Ajzenberg-Selove, Nuclear Physics A **413**, 1 (1984).

[93] H. J. Brede *et al.*, NIM A **274**, 332 (1989).

[94] W. B. Howard *et al.*, Nuclear Science and Engineering **138**, 145 (2001).

[95] W. Whittemore and A. McReynolds, Technical Report No. Ga-2503, General Atomic Division of General Dynamics (unpublished).

[96] K. Inoue, Y. Kiyanagi, and H. Iwasa, NIM **192**, 129 (1982).

[97] K. F. Graham and J. M. Carpenter, NIM **85**, 163 (1970).

[98] K. Inoue, Y. Kiyanagi, H. Iwasa, and K. Jinguji, in <u>ICANS-V</u> (ICANS, Julich, 1981).

[99] J. M. Carpenter, in <u>International Workshop on Cold Moderators for Pulsed Neutron Sources</u>, edited by J. M. C. Iverson and E.B. (OECD OCDE, Argonne National Laboratory, 1997), p. 13.

[100] Nuclear News **49**, 1 (2006).

[101] R. E. MacFarlane, in <u>International Workshop on Cold Moderators for Pulsed Neutron Sources</u>, edited by J. M. C. Iverson and E.B. (OECD OCDE, Argonne National Laboratory, 1997), pp. 221–231.

[102] S. Grieger *et al.*, J. Chem. Phys. **109**, 3161 (1998).

[103] M. A. Lone and H. Nann, TMR Neutronics L0 - Neutronic performance of the TMR (Internal IUCF Technical Report), 2003.

[104] Y. Kiyanagi *et al.*, Physica B **213-214**, 857 (1995).

[105] Y. Kiyanagi, N. Watanabe, and H. Iwasa, NIM A **312**, 561 (1992).

[106] Y. Kiyanagi *et al.*, Physica B **213-214**, 854 (1995).

[107] Cryomech, (2006).

[108] J. K. Shultis and R. E. Faw, <u>Radiation shielding</u> (American Nuclear Society, La Grange Park, IL, 2000).

[109] P. Paul, J. B. Thomas, and S. S. Hanna, Physical Review **147**, 774 (1966).

[110] W. I. McAlexander, E. R. I. Abraham, and R. G. Hulet, Physical Review A **54**, R5 (1996).

[111] E. B. Iverson, J. M. Carpenter, and E. J. Hill, Physica B **241-243**, 33 (1998).

[112] LND, http://www.lndinc.com/.

[113] R. L. Bramblett, R. I. Ewing, and T. Bonner, Nuclear Instruments and Methods **9**, 1 (1960).

[114] Y. Shin *et al.*, in <u>ICANS-XVII</u>, edited by G. Russell, J. Rhyne, and B. V. Maes (Los Alamos Neutron Science Center, Santa Fe, new Mexico, 2005), Vol. II, pp. 542–550.

[115] D. V. Baxter, Private Communication, 2005.

[116] G. H. Lander and J. M. Carpenter, Physica B+C **137**, 373 (1986).

[117] G. F. Knoll, <u>Radiation detection and measurement</u>, 2nd ed. (Wiley, New York, 1989).

[118] G. Muhrer, E. Pitcher, and G. Russell, NIM A **536**, 154 (2005).

[119] D. Picton, S. Bennington, T. Broome, and T. Beynon, NIM A **545**, 363 (2005).

[120] Y. Harker and R. Brugger, J. Chem. Phys. **46**, 2201 (1967).

[121] G. Muhrer, A. Stupnik, and E. Schachinger, NIM A **528**, 707 (2004).

[122] F. Cantargi, J. R. Granada, S. Petriw, and M. M. Sbaffoni, Physica B: Condensed Matter **385-386**, 1312 (2006).

[123] S. Petriw *et al.*, Physica B: Condensed Matter **385-386**, 1309 (2006).

[124] P. McChesney, in APS 2006 Division of Nuclear Physics Annual Meeting (APS, Nashville, Tennessee, 2006), p. Abstract 3A.0051.

<div align="center">

Christopher M. Lavelle
Curriculum Vitae

Indiana University Cyclotron Facility
2401 Milo. B. Sampson Lane
Bloomington, In 47408

Email: chlavell@indiana.edu
Office: (812) 855-1435

</div>

Personal Information:

Born in Rochester, Minnesota, May 23, 1978 (U.S. Citizen)
Married to Erin Lane Buccicone August 20, 2005
One child, Salvatore Edward Lavelle, born November 1, 2006

Education:

B.S. University of Minnesota-Duluth (Honors Physics), 2001
B.A. University of Minnesota-Duluth (English Literature), 2001
M.S. Indiana University (Physics), 2003
Ph.D. Indiana University (Condensed Matter Physics), 2007
       Defense date: January 12, 2007
       Advisor: Dr. David V. Baxter
       Thesis: Neutronic Performance of the Low Energy Neutron Source
           (LENS) Target/Moderator/Reflector (TMR)

Experience:

Graduate Assistant, LENS Project 2002-2006
Graduate Assistant, Charge Symmetry Breaking Experiment 2001-2002
REU, IUCF Polarized Ion Source project (CIPIOS), 1999
Undergraduate Research Assistant, Reflectance Spectroscopy and
       Remote Sensing 1999-2001

Areas of Research:

- Development of high brilliance cold neutron moderators
- Neutron transport Monte Carlo methods
- Extensive MCNP and MCNPX experience
- Cold neutron scattering kernels
- Absolute neutron flux measurements
- Investigation of the role of molecular energy levels in the neutron moderation process

Teaching:
- Discussion Section Leader for P202, Spring 2004
- Supervised undergraduate Patrick McChesney's MCNP research on UCN production at LENS
- Supervised undergraduate honors thesis project of John Horton, "High Energy Neutron Detection for Lens," (B.S. 2005)
- Taught Undergraduate laboratories at University of Minnesota 1999-2001
- Public and private tutoring for high school and college students 1999-2006

Scholarships and Awards:
- Graduate MCNPX Intermediate Course with John Hendrix, 9/2004
- Indiana University COAS Travel Grant Support, 4/2005
- UMD Physics Project of the year 2001
- UMD Student of the Year 2001
- UMD Chancellor Award 1997,1998,1999

Professional Societies:
- American Physical Society Student Member
- American Nuclear Society Student Member
- Neutron Scattering Society of America

Committees:
- Indiana University Department of Physics Graduate Recruitment Committee 2005-2006
- Graduate Student and Professional Organization Physics Representative 2001
- UMD Executive Committee of College of Science Student Representative 2000-2001
- UMD Committee of College of Science Physics Student Representative 2000-2001

Refereed Journals:
1. "Neutronic Design and Experimental Benchmarking of the IUCF Low Energy Neutron Source (LENS) Performance" C.M. Lavelle, D.V. Baxter *in preparation for submission*
2. "Deuteron-deuteron elastic scattering at 231.8 MeV", A.M. Micherdzinska, P.V. Pancella, E.J. Stephenson, A.D. Bacher, C.E. Allgower, A.C. Fonseca, C.M. Lavelle, H. Nann, J. Olmsted, M.A. Pickar, and A. Smith *Submitted to Physical Review C.*
3. "Status of the Low Energy Neutron Source at Indiana Univeristy", D.V. Baxter, J.M. Cameron, V.P. Derenchuk, C.M. Lavelle,M.B. Leuschner, M.A. Lone, H.O. Meyer, T. Rinckel, W.M. Snow. NIM B241 (2005) 209-212
4. "LENS: A New Pulsed Neutrons Source for Research and Education", M. Leuschner, D.V. Baxter, J.M. Cameron, V. Derenchik, C. Lavelle, A. Lone, H. Hann, T.Rinckel, and W.M. Snow. J. Res Natl. Inst. Stand. Technol. 110, 153-155 (2005)

5. "Observation of the Charge Symmetry Breaking $d + d \rightarrow {}^4He + \pi^o$ Reaction Near Threshold." E. J. Stephenson, A. D. Bacher, C. E. Allgower, A. Gardestig, C.M. Lavelle, G. A. Miller, H. Nann, J. Olmsted, P.V. Pancella, M. A. Pickar, J. Rapaport, T. Rinckel, A. Smith, H.M. Spinka, and U. van Kolck. Phys. Rev. Letters 91 (2003) 14 142302

Invited Talks:

1. "LENS: Neutronic Aspects and Recent Experimental Results with a 4 K Methane Moderator" Spallation Neutron Source (SNS), Oak Ridge Tennessee. April 10, 2006
2. "LENS: Neutronic Aspects and Recent Experimental Results with a 4 K Methane Moderator" Lujan Center (LANSCE), Los Alamos New Mexico. June 1, 2006
3. "Neutronic Aspects and Recent Experimental Results with Methane Moderators at IUCF Low Energy Neutron Source (LENS)" NIST Center For Neutron Research (NCNR), Gaithersburg MD. July 6, 2006.

Conference Proceedings:
1. "Indiana University Cyclotron Facility Low Energy Neutron Source: Simulation and Measurement of Neutronic Performance", American Conference on Neutron Scattering (ACNS) 2006. C. M. Lavelle, D. V. Baxter, H. Kaiser, M. B. Leuschner, W. R. Lozowski, N. B. Remmes, T. Rinckel, M. A. Lone, and P. E. Sokol
2. "Neutronic Performance of the LENS TMR", 17th meeting of the international collaboration on advanced neutron sources (ICANS-XVII). C.M. Lavelle, D.V. Baxter, M.B. Leuschner, M.A. Lone, W. Lozowski, H. Nann, N. Remmes, T. Rinckel, Y.Shin, W.M. Snow, and P.E. Sokol.
3. "LENS Status and Prospects – a Facility Talk," 17th meeting of the international collaboration on advanced neutron sources (ICANS-XVII).
4. "Cold Neutron Scattering Kernels," 17th meeting of the international collaboration on advanced neutron sources (ICANS-XVII)
5. "Absolute Flux measurements at IPNS," 17th meeting of the international collaboration on advanced neutron sources (ICANS-XVII).
6. "CD4 Experiment Planning for SNS," 17th meeting of the international collaboration on advanced neutron sources (ICANS-XVII).
7. "Neutron Radiation Effects Program at LENS," 17th meeting of the international collaboration on advanced neutron sources (ICANS-XVII).
8. "The Neutron Radiation Effects Program (NREP) at Indiana University Cyclotron Facility" B. von Przewoski, D. V. Baxter, A. Bogdanov, S. Clark, V. P. Derenchuk, T. Ellis, C.M. Lavelle, M. B. Leuschner, N. Remmes, T. Rinckel, P.E. Sokol and T. Turflinger NSREC 2006
9. International Conference on Precision Measurements with Slow Neutrons, NIST April 5-7 2004, Gaithersburg, MD. "Design and Simulation of a Solid Methane Moderator at the LENS Neutron Source" Yunchang Shin, Chris Lavelle, William Michael Snow, David Baxter, Mark Leuschner, Aslam Lone.

Presentations and Posters
1. *Preparing Future Faculty Conference, IU 2/9/2007*
2. "Neutronic Performance of LENS" Poster Presentation, 17th meeting of the international collaboration on advanced neutron sources (ICANS-XVII). C.M. Lavelle, D.V. Baxter, M.B. Leuschner, M.A. Lone, W. Lozowski, H. Nann, N. Remmes, T. Rinckel, Y.Shin, W.M. Snow, and P.E. Sokol.
3. "UCN Production by moderation" IU Physics Journal Club, 10/2005 with Dr. M. W. Snow
4. *"LENS Shielding Considerations" External LENS Review Committee 10/2003*

Internal IUCF Laboratory Reports and Presentations
1. *LENS L-Series Reports (L1 – L26)* M.A. Lone, H. Nann, and C.M. Lavelle Coauthored a series of 26 Internal research reports from 2002-2004 detailing the essentials results of the LENS MCNP simulation and design work.
2. "LENS – A University Based Pulsed Neutron Source", NSF Review Committee Meeting, 6/2004
3. "Cold Moderator Flux at LENS" IUCF Lunch Time Talk 2005 with Dr. M. Leuschner
4. "Neutron Shutter Design Simulations" LENS Group Meeting 2004
5. "LENS: Design, Commissioning and New Directions," For A. Barzilov and P.E. Sokol. 6/2005